

Exploitation of hyperspectral satellite data for the detection of fluorescence originating from biological sources

Dissertation

von

ALEKSANDRA WOLANIN



Institut für Umweltphysik
Fachbereich Physik/Elektrotechnik
Universität Bremen

Juli 2015

Exploitation of hyperspectral satellite data for the detection of fluorescence originating from biological sources

Dissertation

von

ALEKSANDRA WOLANIN

zur Erlangung des akademischen Grades
eines Doktor der Naturwissenschaften (Dr.rer.nat.)
vom Fachbereich Physik und Elektrotechnik der Univerität Bremen

1. Gutachter: Prof. Dr. Astrid Bracher
Alfred-Wegener-Institut Helmholtz-Zentrum für Polar- und Meeresforschung
2. Gutachter Prof. Dr. J.P. Burrows
Institut für Umweltphysik, Universität Bremen

Datum des Kolloquiums: 01.09.2015

Institut für Umweltphysik
Fachbereich Physik/Elektrotechnik (FB 1)
Postfach 33 04 40
D-28334 Bremen

Ich versichere, dass ich die Dissertation selbstaendig verfasst und keine anderen als die angegebenen Quellen und Hilfsmittel benutzt habe.

Bremen, Juli 2015

Moim kochanym rodzicom

Acknowledgments

This thesis is the result of the work, which has only been possible with the help and support which I received during the years of my PhD research. Therefore I would like to express my gratitude to my mentors, colleagues, friends, family and institutions. Without them, this thesis could not have come to existence.

In the first place I would like to thank my supervisor, Astrid Bracher, for the opportunity to carry out my PhD research in the Phytooptics group. She provided me with guidance and assistance, and encouraged me to think independently and follow new ideas. Thank you very much for your support, trust and understanding, and for sharing your vision on the scientific world, which I could relate to.

John P. Burrows has welcomed me as a PhD student and as a guest scientist at IUP, which had provided me with an excellent and stimulating atmosphere for my work. I'm thankful for the inspiring and challenging discussions, for a lot of scientific insight, for the patience, and for the time he found for me in his busy schedule. Thank you also for just enough British humor to make sure I don't treat myself or my work too seriously.

Vladimir Rozanov has been an indescribable help during all the phases of my PhD work. He has always welcome me with a warm smile, and dedicated long hours to answer all the physics questions I dared to ask, as well as to improve my simulations, retrievals and manuscripts. Thank you for your advice and time you took to support me.

I am grateful to my current and past colleagues of the Phytooptics group: Tilman Dinter, Mariana Soppa, Sonja Wiegmann, Rafael Gonçalves Araujo, Alexandra Cherkasheva, Wee Cheah, Alireza Sadeghi and Bettina Taylor. They have created a wonderful atmosphere in which I enjoyed both working and other, more relaxing activities. Thank you also for the feedback and discussions, which have improved my work and provided me with new ideas.

Hella van Asperen and Matthias Buschmann have helped me in all sorts of circumstances, which are now too many to list here. Thank you that you were always there, ready to save me.

Funding of my work was provided by the Earth System Science Research School (ESSReS), an initiative of the Helmholtz Association of German research centers (HGF) at the Alfred Wegener Institute for Polar and Marine Research. Many thanks go to the ESSReS coordinators, Klaus Grosfeld, Ludvig Löwemark and Helge Meggers, and to Stefanie Klebe, for their support during these years. ESSReS provided a great space for discussion,

exchange, and interdisciplinary work. I am especially grateful to my Bremen ESSReS colleagues, (in alphabetical order) Leonardo Alvarado, Hella van Asperen, Lena Brinkhoff, Matthias Buschmann, Marcus Huntemann, Jia Jia, Stefan Schreier, Johannes Sutter, and Yufang Ye, who have become my good friends.

I am also grateful to Eva-Maria Nöthig for creating the possibility to let me participate in the Polarstern expedition. I also would like to thank the captain, the crew, the principal investigator and the scientists onboard RV Polarstern for their support during the ARKXXVII-1 cruise.

I am especially grateful to Mariana Soppa, Hella van Asperen, Matthias Buschman and Luis Guanter for reading parts of this thesis.

During all my PhD time I was surrounded by wonderful colleagues both at IUP in Bremen and at AWI in Bremerhaven. Thank you all for your kindness. Special thanks go to (in alphabetical order) Faiza Azam, Heinrich Bovensmann, Stefan Bötzel, Klaus Bramstedt, Martin Budde, Michael Buchwitz, Kai-Uwe Eichmann, Konstantin Gerilowski, Andreas Hilboll, Thomas Krings, Luca Lelli, Elpida Leventidou, Patricia Liebing, Linlu Mei, Andreas Meier, Christian Melsheimer, Stefan Noël, Nabiz Rahpoe, Maximilian Reuter, Andreas Richter, Alexei Rozanov, Marco Vountas, Katja Weigel. I also would like to thank Kai-Uwe and Elpida for taking care of me during lunch time, even if it meant taking a detour.

I am grateful to Petra Horn, Geraldine Schmiechen and Birgit Teuchert for their administrative support.

I thank Heiko Schellhorn and Heiko Schröter for providing technical support whenever needed.

I am thankful to DLR and ESA for SCIAMACHY Level-1 data. I also acknowledge the MODIS mission scientists and associated NASA personnel for the production and distribution of the MODIS satellite data. Part of the MODIS data, which was used in this study, was produced with the Giovanni online data system, developed and maintained by the NASA GES DISC.

Finally, I want to thank my family and close friends, whose love, trust and support were a never-ending source of motivation. I especially thank my dear parents, who have encouraged me to follow the scientific path.

Abstract

Oxygenic photosynthesis is responsible for virtually all of the biochemical production of organic matter, and regulates atmospheric carbon dioxide and oxygen concentrations, which profoundly affects both climate and biogeochemical cycles. Observations of biomass, health and productivity of ocean and land ecosystems are crucial for monitoring changes in the Earth system. Here, space-borne hyperspectral data, mainly of the SCIAMACHY instrument (onboard ENVISAT), have been investigated in terms of application to global observations of marine and terrestrial primary producers.

This study focuses primarily on retrieving inelastic processes from the natural waters: CDOM and chlorophyll (chl) *a* fluorescence. Originally, the chl *a* fluorescence retrieval was developed in its red peak and for the ocean application only. However, it was further extended to the far-red peak of chl *a* fluorescence, and subsequently applied to terrestrial scenes. All retrievals are based on the Differential Optical Absorption Spectroscopy (DOAS), and involve fitting spectral features of the filling in of the Fraunhofer lines by fluorescence processes. The reference spectra of chl *a* and CDOM fluorescence, used in the DOAS fits, were calculated with the ocean-atmosphere coupled radiative transfer model SCIATRAN. Furthermore, a simple algorithm to retrieve a chl proxy of terrestrial vegetation was developed.

The retrievals were developed with the use of simulated radiances, and subsequently applied to SCIAMACHY data. Although the original aim of the SCIAMACHY instrument was to monitor atmospheric composition, its unique spectral characteristics (namely broad spectral range from 240 nm to 2380 nm, and high resolution of 0.2 nm to 1.5 nm) have enabled previously other novel retrievals to be developed. These included observations of inelastic processes (rotational and vibrational Raman scattering), and marine phytoplankton. In this thesis, the chl *a* fluorescence and chl proxy retrievals were applied to eight years of the SCIAMACHY data (2004-2011). In addition to presenting yearly composites and monthly climatologies of the obtained results, monthly averages were applied to study the seasonality of both, marine phytoplankton and terrestrial vegetation.

Modeling studies of CDOM fluorescence, followed by preliminary retrievals applied to SCIAMACHY data, have not been successful in retrieving CDOM fluorescence from hyperspectral satellite data. On the other hand, the obtained chl *a* fluorescence results showed good spatial agreement with other datasets. Marine observations of the red peak of chl *a* fluorescence captured successfully the phytoplankton seasonal cycles and interannual variability for two studied regions: a subregion of the Indian Ocean near Madagascar, and the equatorial Pacific. Good agreement with multispectral ocean color products

(MODIS nFLH and MODIS Chl *a*) was obtained. Response of phytoplankton to climate fluctuations, as expressed by Multivariate ENSO Index, was observed for the equatorial Pacific.

In case of land observations, all retrieved parameters (red and far-red chl *a* fluorescence, and chl proxy) followed the seasonal cycles of vegetation for five regions representing different biomes worldwide (croplands in the North America, evergreen needleleaf forest in Euroasia, evergreen broadleaf forest in Central Africa, woody savannas in Central Africa and savannas in Southern Africa). However, the three SCIAMACHY datasets did not show exactly the same seasonal pattern, and their relationship varied over time and among biomes. This proves that the retrieved parameters do not carry the same information on vegetation, and hence suggests that they all should be used simultaneously for observations of vegetation dynamics. The calculated ratio and the difference of the two peaks of chl *a* fluorescence, followed the increase of chl content and canopy development, which supports previous findings by *in situ* measurements and models.

The red and far-red chl *a* fluorescence and chl proxy algorithms have enabled simultaneous retrievals of multiple parameters of marine phytoplankton and terrestrial vegetation. While the application of the SCIAMACHY results is still constrained (mainly by the noisiness of the results and spatio-temporal resolution of the satellite measurements), the developed retrievals and their successful application to studies of ocean and land phenology have advanced the prospects of observations of phytoplankton and terrestrial vegetation with hyperspectral satellite instruments.

List of publications

Parts of this thesis (including text passages, figures, and tables) have been previously presented in various research articles, conference talks, and conference posters.

Peer-reviewed publications

As first author

Wolanin, A., Rozanov, V., Dinter, T., and Bracher, A. (2015a). Detecting CDOM fluorescence using high spectrally resolved satellite data: A model study. In Lohmann G., Meggers H., Unnithan V., Wolf-Gladrow D., Notholt J., & Bracher A. (Eds.), *Towards an Interdisciplinary Approach in Earth System Science* (pp. 109-121). Cham: Springer International Publishing.

Wolanin, A., Rozanov, V., Dinter, T., Noël, S., Vountas, M., Burrows, J.P., and Bracher, A. (2015b). Global retrieval of marine and terrestrial chlorophyll fluorescence at its red peak using hyperspectral top of atmosphere radiance measurements: Feasibility study and first results. *Remote Sensing of Environment*, 166, 243-261. doi:10.1016/j.rse.2015.05.018.

Wolanin, A., Rozanov, V., Burrows, J.P., & Bracher, A. Observations of the seasonality of photosynthetic activity of vegetation using SCIAMACHY data. Manuscript in preparation for publication in *Remote Sensing*.

As a co-author

Rozanov V.V., Dinter T., Rozanov A.V., **Wolanin, A.**, Bracher A., and Burrows, J.P. Radiative transfer through terrestrial atmosphere and ocean including inelastic scattering processes: Software package SCIATRAN. Manuscript in preparation.

Proceedings

Wolanin, A., Dinter, T., Rozanov, V., Noël, S., Vountas, M., Burrows, J.P., and Bracher, A. (2014a). Marine Fluorescence from High Spectrally Resolved Satellite Measurements and its Terrestrial Application. Proceedings of 5th International Workshop on Remote Sensing of Vegetation Fluorescence, Paris, France, 22-24 April 2014.

Wolanin, A., Dinter, T., Rozanov, V., Noël, S., Vountas M., Burrows, J.P., Vountas M., and Bracher A. (2014b) Marine chlorophyll fluorescence from high spectrally resolved satellite data. Proceedings of Ocean Optics XXII. Portland, ME, USA, 26-31 October 2014.

Conference contributions

Oral Presentations

Wolanin, A., Bracher, A., Dinter, T., Rozanov, V. Remote sensing of marine CDOM and chlorophyll fluorescence using high spectrally resolved satellite data. Seminar 'Ocean, Ice, and Atmosphere' at the Institute of Environmental Physics, University of Bremen, 29th May 2012, Bremen, Germany.

Bracher, A., Dinter, T., Sadeghi, A., **Wolanin, A.**, Altenburg Soppa, M., Taylor, B., Rozanov, V., Vountas, M., Röttgers, R. and Peeken, I. Ocean color products from hyperspectral satellite sensor SCIAMACHY compared to products from the multispectral sensors MERIS, MODIS and SeaWiFS., Sentinel-3 OLCI/SLSTR & MERIS/(A)ATSR Workshop, 15-19 October 2012, ESA-ESRIN, Frascati, Italy.

Wolanin, A., Dinter, T., Rozanov, V., Noël, S., Vountas, M., Burrows, J.P., Bracher, A. Marine chlorophyll fluorescence from high spectrally resolved satellite measurements. Ocean Optics XXII, 26-31 October 2014, Portland (ME), USA.

Wolanin, A., Dinter T., Rozanov V., Noël S., Vountas, M., Burrows, J.P., Bracher, A. Global observations of chlorophyll fluorescence from space. ESSReS Retreat, 21st November 2014, Bremerhaven, Germany.

Wolanin, A., Bracher, A., Dinter, T., Rozanov, V. Marine chlorophyll fluorescence from high spectrally resolved satellite measurements. Seminar 'Ocean, Ice, and Atmosphere' at the Institute of Environmental Physics, University of Bremen, 9th December 2015, Bremen, Germany.

Posters

Wolanin, A., Rozanov, V., Rozanov, A., Burrows, J.P., Dinter, T., and Bracher A. Application of coupled ocean-atmospheric RTM SCIATRAN to retrieve chlorophyll and CDOM fluorescence from space: first results. International Radiation Symposium, 6-10 August 2012, Berlin, Germany.

Dinter T., Rozanov V., Sadeghi A., **Wolanin, A.**, Taylor, B., and Bracher, A.. Retrieval of oceanic phytoplankton with a combined Phytodoas-RTM method utilizing hyper spectral satellite measurements. 44th International Liège Colloquium On Ocean Dynamics, 7-11 May 2012, Liège, Belgium.

Dinter, T., Rozanov, V., **Wolanin, A.**, Taylor, B., Sadeghi, A., Bracher, A. Sensitivity Study for the retrieval of oceanic Phytoplankton by PhytoDOAS using the full atmosphere-ocean radiative transfer model SCIATRAN. Sentinel-3 OLCI/SLSTR & MERIS/(A)ATSR Workshop, 18 October 2012, ESA-ESRIN, Frascati, Italy.

-
- Wolanin, A.**, Rozanov, V., Rozanov, A., Burrows, J.P., Dinter, T., and Bracher A. Application of coupled ocean-atmospheric RTM SCIATRAN to retrieve chlorophyll and CDOM fluorescence from space: first results. ESSReS Retreat, 30 November 2012, Bremerhaven, Germany.
- Wolanin, A.**, Dinter, T., Rozanov, V., Noël, S., Vountas, M., Burrows, J.P., Bracher, A. Marine Fluorescence from High Spectrally Resolved Satellite Measurements and its Terrestrial Application. Proceedings of the 5th Int. Ws. on Remote Sensing of Vegetation Fluorescence, 22-24 April 2014, Paris, France.
- Wolanin, A.**, Dinter, T., Rozanov, V., Noël, S., Vountas, M., Burrows, J.P., Bracher, A. Marine fluorescence from high spectrally resolved satellite measurements. EGU General Assembly 2014, 27 April-2 May 2014, Vienna, Austria.
- Wolanin, A.**, Dinter, T., Rozanov, V., Noël, S., Vountas, M., Burrows, J.P., Bracher, A.. Marine chlorophyll fluorescence from high spectrally resolved satellite measurements. AWI PhD Days, 5-8 May 2014, Helgoland, Germany.
- Bracher, A., Dinter, T., **Wolanin, A.**, Rozanov, V., Burrows, J.P., Soppa, M. (2015) Ocean color products from hyper-spectral satellite data of SCIAMACHY using Differential Optical Absorption Spectroscopy and coupled atmospheric-ocean radiative transfer modelling. International Ocean Color Science (IOCS) Meeting, San Francisco, June 2015.

Contents

| | |
|--|-----------|
| Abstract | 9 |
| List of Publications | 11 |
| 1 Introduction | 19 |
| 1.1 Motivation and goals of the study | 19 |
| 1.2 Thesis outline | 24 |
| 2 Scientific Background | 25 |
| 2.1 Basic principles of satellite observations of ocean color | 25 |
| 2.2 Natural fluorescence of biological sources | 28 |
| 2.2.1 CDOM fluorescence | 28 |
| CDOM and its optical properties | 28 |
| Satellite remote sensing of CDOM | 33 |
| 2.2.2 Chlorophyll <i>a</i> fluorescence and its relationship to photosynthesis | 35 |
| Basic mechanism of photosynthesis | 35 |
| Fluorescence at the molecular level | 38 |
| Linking fluorescence at PS II and photosynthesis | 40 |
| PSI and PSII fluorescence | 40 |
| 2.2.3 Chlorophyll <i>a</i> fluorescence in the marine environment | 42 |
| The variability of chl <i>a</i> fluorescence signal | 42 |
| <i>In situ</i> measurements of marine chlorophyll chl <i>a</i> fluorescence | 43 |
| Remote sensing of marine chlorophyll fluorescence: normalized Fluorescence Line Height | 44 |
| 2.2.4 Chlorophyll <i>a</i> fluorescence of terrestrial vegetation | 45 |
| A. WOLANIN | 15 |

| | |
|---|-----------|
| Variability of chl <i>a</i> fluorescence signal | 45 |
| <i>In situ</i> measurements of terrestrial chlorophyll <i>a</i> fluorescence | 47 |
| Remote sensing of terrestrial chlorophyll <i>a</i> fluorescence with hyper- spectral instruments | 48 |
| 3 Modeling of fluorescence processes | 49 |
| 3.1 Principles of radiative transfer | 49 |
| 3.2 The SCIATRAN radiative transfer model | 52 |
| 3.3 Fluorescence in natural waters modeled by the ocean-atmosphere coupled radiative transfer model SCIATRAN | 52 |
| 3.3.1 Modeling of CDOM fluorescence | 53 |
| CDOM as mixture of humic and fulvic acids | 53 |
| Excitation-emission matrices and PARAFAC approach | 54 |
| 3.3.2 Modeling of marine chl <i>a</i> fluorescence | 56 |
| 3.4 Terrestrial fluorescence in SCIATRAN | 57 |
| 4 Development of satellite retrievals of fluorescence and chlorophyll proxy | 59 |
| 4.1 Overall retrieval approach | 59 |
| 4.1.1 Retrieval technique: DOAS | 59 |
| 4.1.2 Reference spectra | 60 |
| 4.1.3 Hyperspectral satellite data | 61 |
| SCIAMACHY | 61 |
| GOME-2 | 62 |
| Future missions | 62 |
| 4.2 Retrieval of CDOM fluorescence | 63 |
| 4.2.1 Reference spectra of CDOM fluorescence | 63 |
| 4.2.2 Spectral windows of the retrieval | 65 |
| 4.3 Retrieval of the red chl <i>a</i> fluorescence peak | 67 |
| 4.3.1 Reference spectrum of red chl <i>a</i> fluorescence and selection of spectral window of retrieval | 67 |
| 4.3.2 Retrieval technique of the red peak of chl <i>a</i> fluorescence | 69 |
| 4.3.3 Accounting for effects of water vapor absorption and Raman scattering | 71 |
| 4.3.4 Conversion scheme to fluorescence emission (SCIAMACHY FLH) | 74 |

| | | |
|----------|--|------------|
| 4.3.5 | Conversion from SCIAMACHY FLH into SCIAMACHY snFLH . . . | 76 |
| 4.4 | Retrieval of the far-red chl <i>a</i> fluorescence peak | 77 |
| 4.4.1 | Reference spectrum of far-red chl <i>a</i> fluorescence and selection of spectral window of retrieval | 77 |
| 4.4.2 | Offset correction | 81 |
| 4.4.3 | Conversion scheme into fluorescence emission | 84 |
| 4.5 | Retrieval of the chl proxy | 86 |
| 4.5.1 | Reference spectrum of chlorophyll | 86 |
| 4.5.2 | Spectral window of retrieval | 87 |
| 5 | Observations of CDOM fluorescence with hyperspectral data | 91 |
| 6 | Observations of chlorophyll <i>a</i> fluorescence and absorption | 97 |
| 6.1 | Observations of the red peak of chlorophyll <i>a</i> fluorescence | 97 |
| 6.1.1 | Marine chl <i>a</i> fluorescence | 97 |
| | Chl <i>a</i> fluorescence observed with SCIAMACHY | 97 |
| | Comparison to MODIS Chl <i>a</i> and MODIS nFLH | 104 |
| | Temporal variations in SCIAMACHY marine chl <i>a</i> fluorescence . . . | 111 |
| | Chl <i>a</i> fluorescence observed with GOME-2 | 113 |
| 6.1.2 | Terrestrial chl <i>a</i> fluorescence | 114 |
| | Chl <i>a</i> fluorescence observed with SCIAMACHY | 114 |
| | Chl <i>a</i> fluorescence observed with GOME-2 | 117 |
| | Comparison to other fluorescence retrievals and MODIS EVI | 118 |
| 6.1.3 | Global observations of the red peak of chl <i>a</i> fluorescence | 120 |
| 6.2 | Observations of the far-red peak of chl <i>a</i> fluorescence | 121 |
| 6.2.1 | Chl <i>a</i> fluorescence observed with SCIAMACHY | 121 |
| 6.2.2 | Comparison with previous results | 125 |
| 6.3 | Observations of the terrestrial chl proxy with SCIAMACHY | 128 |
| 7 | Observations of the seasonality of photosynthetic activity of vegetation using SCIAMACHY data | 133 |
| 7.1 | Vegetation seasonality | 133 |
| 7.2 | Vegetation Indices | 136 |

CONTENTS

| | | |
|----------|---|------------|
| 7.3 | Chl <i>a</i> fluorescence application for vegetation observations | 137 |
| 7.4 | Biomes determination | 139 |
| 7.5 | Observations of seasonality of photosynthetic activity for different biomes . | 141 |
| 7.5.1 | Croplands in North America (region C) | 142 |
| 7.5.2 | Evergreen needleleaf forest in Euroasia (region ENF) | 145 |
| 7.5.3 | Evergreen broadleaf forest in Central Africa (region EBF) | 147 |
| 7.5.4 | Woody savannas in Central Africa (region WS) | 150 |
| 7.5.5 | Savannas in Southern Africa (region S). | 150 |
| 7.6 | Discussion and Summary | 151 |
| 8 | Summary, conclusions and outlook | 155 |
| | List of abbreviations | 159 |
| | Bibliography | 163 |

Chapter 1

Introduction

1.1 Motivation and goals of the study

Anthropogenic pressure on aquatic and terrestrial ecosystems has never been as high as it is now (MEA, 2005; IPCC, 2013). Rapid increase of human population accompanied by, among others, development of technology, global agriculture practices, production of energy and extraction of natural resources, have been changing the Earth system. Lately, the value of natural ecosystems has been increasingly acknowledged, and it has been recognized that ecosystem goods and services benefit human population with its economic value estimated to be on average 33 trillion US\$ per year globally (Costanza et al., 1997). The exponential growth of human pressures has reached a point where humanity is close to transgressing planetary boundaries, within which humanity is expected to be able to operate safely (Rockström et al., 2009). Such transgression destabilizes critical biophysical systems and triggers abrupt or irreversible environmental changes that would be deleterious or even catastrophic for human well-being (Rockström et al., 2009). Rockström et al. (2009) defined nine such planetary boundaries, which include climate change, ozone depletion, ocean acidification, interference in the global nitrogen and phosphorus cycles, land-use change, global freshwater use, biosphere integrity, air pollution, and novel entities (such as organic pollutants, radioactive materials, nanomaterials, and micro-plastics) (Fig. 1.1). All these boundaries are directly related to or mitigated by the Earth's biosphere. Earth's ecosystems change has been driven by humans to such an extent, that a new geologic chronological term, the anthropocene, has been employed to denote the current epoch, which began when human activities started to have a significant global impact on the Earth's ecosystems (Crutzen, 2002; Zalasiewicz et al., 2008). With global changes happening fast and worldwide, the need for accurate assessment, observation and modeling of the Earth's ecosystems has clearly become urgent.

All organisms on Earth (with only a very few exceptions) depend upon photosynthesis as their food and energy source, which is also the source of the oxygen, which we, humans, breathe. In both land and ocean components of the biosphere, oxygenic photosynthesis is responsible for virtually all of the biochemical production of organic matter (Field, 1998), and regulates atmospheric carbon dioxide and oxygen concentrations, by which it

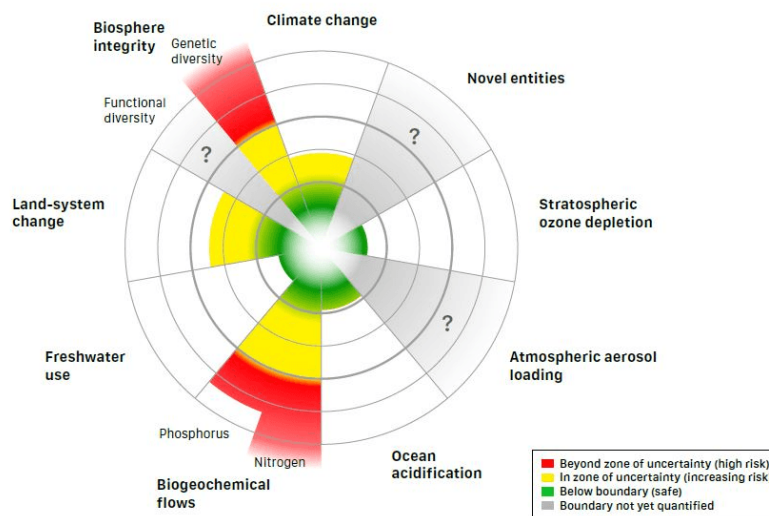


Figure 1.1: The nine planetary boundaries identified by Rockström et al. (2009): climate change, ozone depletion, ocean acidification, interference in the global nitrogen and phosphorus cycles, land-use change, global freshwater use, biosphere integrity, air pollution, and novel entities. Illustration: Steffen et al. 2015 (<http://www.stockholmresilience.org/>).

profoundly affects climate and biogeochemical cycles (Chavez et al., 2011) (Fig. 1.2).

Plants and phytoplankton fix carbon dioxide (CO_2) as organic compounds, generating a carbon flux, also known at the ecosystem level as gross primary production (GPP). GPP diminished by the respiration of the primary producers amounts to net primary production (NPP). Global terrestrial and marine NPP has been estimated to be approximately on the order of 50 PgC per year each (Field, 1998). Although oceanic producers are responsible for nearly half of the biospheric NPP, they represent only 0.2% of global primary producer biomass. This is a consequence of the more than three orders of magnitude faster turnover rate of plant organic matter in the oceans (average of 2 to 6 days, Falkowski & Raven 2007) than on land (average of 19 years, Thompson & Randerson 1999). In addition, GPP is one of the major processes controlling land-atmosphere CO_2 exchange, providing the capacity of terrestrial and marine ecosystems to partly offset anthropogenic CO_2 emissions (Beer et al., 2010).

Satellite observations

The global satellite-based observations of terrestrial vegetation and aquatic phytoplankton, which are commonly used for estimates of global primary production, have traditionally been focused on the standing stocks of chlorophyll (chl) *a*. Chl *a* concentration is the main product of multispectral ocean color instruments. In case of land, vegetation is commonly characterized using chl-related indices, usually based on the steep increase in vegetation reflectance in the VIS/NIR region (also called ‘the red edge’). However, in addition to chl *a* absorption, another optical signal can provide supplementary information on photosynthetic processes (Fig. 1.3). This signal is chl *a* fluorescence, which constitutes of red and far-red light photons that are emitted by chl *a* pigments after the absorption of

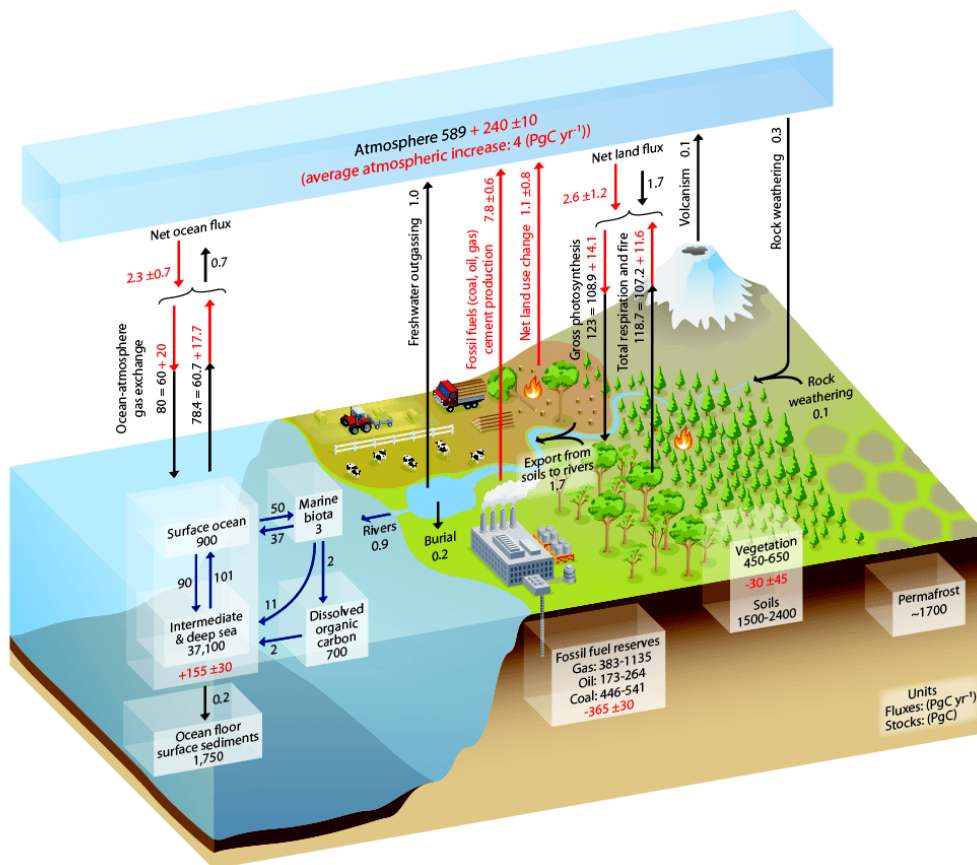


Figure 1.2: Simplified schematic of the global carbon cycle. Numbers represent reservoir mass, also called ‘carbon stocks’ (in PgC) and annual carbon exchange fluxes (in PgC yr⁻¹). Black numbers and arrows indicate reservoir mass and exchange fluxes estimated for the time prior to the Industrial Era, around year 1750. Red arrows and numbers indicate annual ‘anthropogenic’ fluxes averaged over the 2000–2009 time period. Source: IPCC 2013

light. Chl *a* fluorescence originates from two different photosystems (complexes in which light absorption and primary electron transfer take place), which is also reflected in the two-peak spectral shape of the signal (see more in Section 2.2.2).

The chl *a* fluorescence signal has been recently gaining more attention for its potential to be, in addition to chl absorption observations, a new source of information on both, aquatic and terrestrial ecosystems. Regarding space-borne platforms, chl *a* fluorescence has been retrieved from ocean in the form of Fluorescence Line Height, firstly from MODIS (Abbott & Letelier, 1999), and subsequently from other multispectral instruments, MERIS (Gower et al., 2004) and GOCI (O’Malley et al., 2014). For the case of land, latest efforts with respect to the observations of chl *a* fluorescence involve the proposal of the Earth Explores 8 Mission FLEX (Moreno, 2006), which aims for the global observation of the chl *a* fluorescence signal at its two peaks in the oxygen absorption bands. CarbonSat, the other Earth Explores 8 Mission candidate, is aimed at observations of CO₂ and methane (CH₄), but could also perform measurements of the far-red peak of chl *a* fluorescence (Buchwitz et al., 2013). In the meantime, chl *a* fluorescence signal originating from land has been

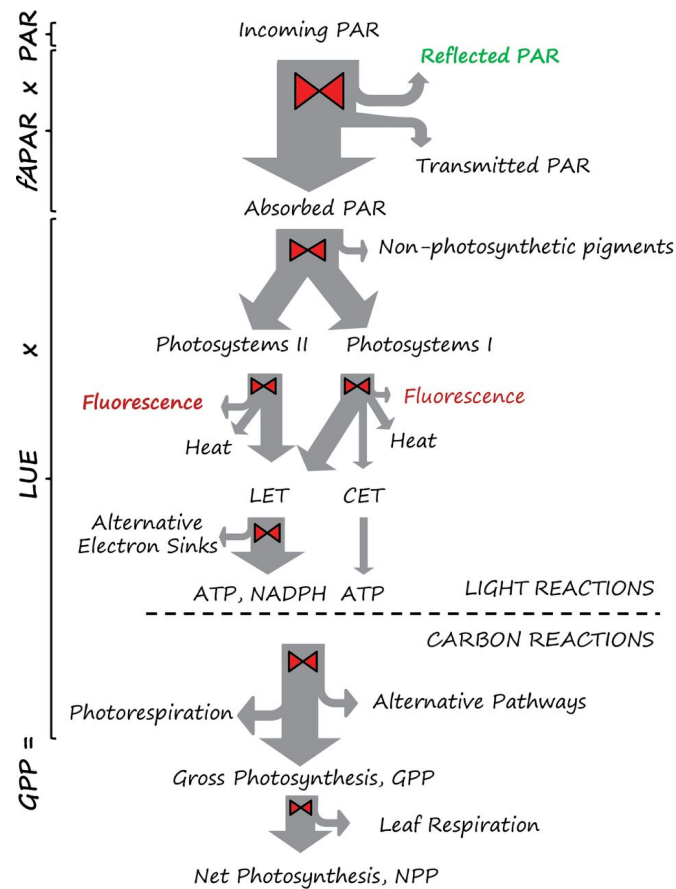


Figure 1.3: Photosynthetic energy partitioning at the leaf level. Grey arrows represent the flow of energy. Red valve symbols indicate the action of regulatory mechanisms which adjust the energy partitioning between pathways (grey arrows). Optical signals available to remote sensing include properties of reflected light (shown in green) and chlorophyll a fluorescence (shown in red). LET, linear electron transport; CET, cyclic electron transport; LUE, light use efficiency; GPP, gross primary production; fAPAR, fraction of absorbed photosynthetically active radiation; PAR, photosynthetically active radiation. Source: Porcar-Castell et al. (2014).

retrieved with the use of the current satellite hyperspectral instruments, primarily aimed at the atmospheric chemistry observations: GOSAT and GOME-2 (e.g., Frankenberg et al., 2011b; Joiner et al., 2011; Guanter et al., 2012; Joiner et al., 2013).

These atmospheric instruments have poorer spatial resolution, but an order of magnitude better spectral resolution, as compared to multispectral spectrometers, which are primarily designed for observations of the Earth's surface. They also often cover a broad range of wavelengths. Hence, novel and experimental algorithms, other than originally planned products, can be developed for and tested on the hyperspectral radiance measurements. It is especially important, because the upcoming space missions will have improved spectral and spatial resolution, and increased number of channels, which will also enable application of new and improved algorithms. Hyperspectral spectrometers can resolve narrow Fraunhofer lines, which can be used for observations of inelastic processes, such as fluorescence

(of chl *a*, but also other compounds), and vibrational and rotational scattering (e.g., Vountas et al., 1998; Vasilkov, 2002).

In addition to chl *a*, the fluorescent part of the the dissolved organic matter (DOM) comprise other fluorescent compounds of the natural waters. DOM is a significant element in the carbon cycle, and ~ 700 PgC is bound in DOM in the world's oceans (Fig. 1.2). Absorption of colored DOM (CDOM) has been commonly measured *in situ*, and is one of the main error sources in satellite retrievals of chl *a*. CDOM absorption is also retrieved together with other optical water properties by the semi-empirical ocean color algorithms (e.g. QAA (Lee et al., 2002) and GSM (Garver & Siegel, 1997; Maritorea et al., 2002)).

Overall, the hyperspectral observations from space platforms data are a new exciting source of the top of atmosphere radiance signal, which can be used for novel algorithms to retrieve key parameters of both marine and terrestrial ecosystems. In addition to the retrieval of the inelastic scattering, space-borne hyperspectral instruments have previously been used to retrieve marine chl and different phytoplankton functional types (e.g., Bracher et al., 2009). In this thesis, fluorescence signals originating from CDOM and chl *a* have been observed at multiple spectral windows, with the aim of studying CDOM distribution and composition, and of obtaining information on photosynthetic activities of primary producers. The retrievals of these inelastic processes are developed with use of the radiative transfer model SCIATRAN and applied mainly to data from SCIAMACHY instrument. SCIAMACHY data were also further exploited in terms of chl observations, but in the context of terrestrial vegetation. A chl proxy is retrieved by using its absorption in the blue range of electromagnetic spectrum, which is complementary to typical red-edge algorithms. Since this retrieval does not require such high spectral resolution, it is interesting for future multispectral missions dedicated to land measurements, which might have sufficient spectral resolution.

The main objectives of this study were:

1. to model and investigate the fluorescence signal from different sources (chl *a*, CDOM) by using the radiative transfer model SCIATRAN (Rozanov et al., 2014), and asses the potential to retrieve fluorescence from hyperspectral space-borne instruments;
2. to retrieve from high spectrally resolved satellite data:
 - (a) the CDOM fluorescence signal from the ocean,
 - (b) the chl *a* fluorescence signal originating both from ocean and land, and at both (red and far-red) fluorescence peaks,
 - (c) terrestrial chl absorption signal in the blue region of the electromagnetic spectral region,
3. to test the applicability of the retrieved datasets for the global observation of aquatic phytoplankton and terrestrial vegetation.

1.2 Thesis outline

The structure of the thesis, which contains eight chapters, is as follows. In Chapter 1 the general motivation and the objectives of the study are introduced. Chapter 2 summarizes the relevant scientific background information. The basic principles of satellite measurements of ocean color are introduced. The natural fluorescence processes of CDOM and chl *a* in marine environment are discussed. Chl *a* fluorescence of the terrestrial vegetation is also briefly considered. In Chapter 3, the fundamentals of radiative transfer modeling and the radiative transfer model SCIATRAN are introduced. All the radiative transfer simulations used in this study were performed with the SCIATRAN model. The implementation of fluorescence processes in water (CDOM and chl *a*) and land (chl *a*) in the SCIATRAN model are described. In Chapter 4 the retrieval method and the hyperspectral satellite data, to which retrievals were applied (and could be applied potentially in future), are presented. Algorithms designed to retrieve CDOM fluorescence, red and far-red peak of chl *a* fluorescence and chlorophyll proxy, are described in detail. The encountered challenges and implemented solutions for each retrieval are discussed. In Chapter 5, the results of the preliminary trial retrievals of CDOM fluorescence are presented. The implications for the remote sensing, challenges and possible future improvements of the retrievals are discussed. These results, regarding the implementation of CDOM fluorescence into the radiative transfer model, and the investigation of the feasibility of retrieving different CDOM fluorescent components from hyperspectral satellite-borne instruments, were published in Wolanin et al. (2015a). They are also a part of a larger manuscript, Rozanov et al., (in prep), which explains the implementation of various inelastic processes into the ocean-atmosphere coupled radiative transfer model SCIATRAN. Observations of chl *a* fluorescence for both marine and terrestrial realms, and chl proxy for land vegetation, are presented in Chapter 6. Results of the red peak of chl *a* fluorescence are presented, firstly for oceans and subsequently for land, and finally globally. Marine fluorescence results are compared to MODIS products, and are applied to study the seasonal variability in phytoplankton community and its response to climate fluctuations for chosen regions. Land fluorescence results are discussed and compared with previous GOME-2 fluorescence observations and MODIS EVI product. The results for the red peak of chl *a* fluorescence were published in (Wolanin et al., 2015b). Observations of the far-red peak of chl *a* fluorescence are shown with a major focus on land observations. The results of terrestrial vegetation chl proxy are briefly discussed. All terrestrial parameters, retrieved with SCIAMACHY, are applied to observations of photosynthetic activity of terrestrial vegetation for different biomes, which is shown in Chapter 7. The differences between various parameters and biomes are discussed. The retrievals of far-red chl *a* fluorescence and chl proxy, together with their application to study vegetation dynamics of different biomes, are a part of a manuscript Wolanin et al., which is now in preparation. Finally, a summary in Chapter 8 brings together main results and findings of this work. An outlook describing the perspectives for future studies and identifying remaining knowledge gaps are discussed.

Chapter 2

Scientific Background

2.1 Basic principles of satellite observations of ocean color

The discipline of research concerned with observations of the ocean using satellite- or aircraft-borne spectrometers, within selected spectral regions in the visible and near-infrared domains of the electromagnetic spectrum, is commonly called ocean color radiometry or ocean color remote sensing.

Passive ocean color remote sensing has been possible from space since 1978, when NASA launched the first satellite sensor to monitor ocean color, the Coastal Zone Color Scanner (CZCS). At that time, the goals of the mission were to measure water-leaving radiance

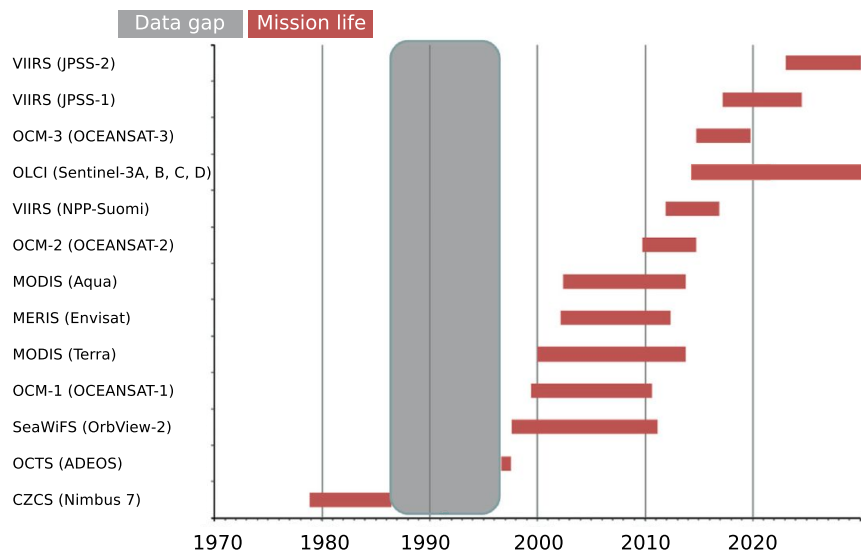


Figure 2.1: Timeline 1970–2030 illustrating past, current, and future global ocean-color satellite missions. Missions after 1999 were extracted from the online CEOS Earth Observation Handbook (<http://www.eohandbook.com/>). Satellite platforms are indicated. Adapted from Blondeau-Patissier et al. (2014).

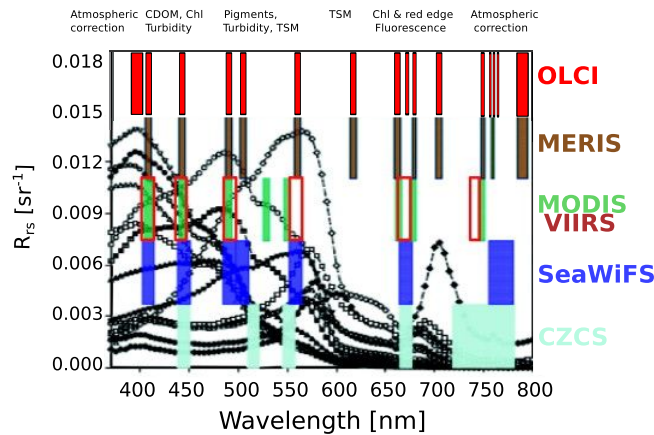


Figure 2.2: Comparison of the spectral band positions for six ocean color sensors: CZCS, SeaWiFS, MERIS, MODIS, VIIRS and OLCI. The potential applications for each spectral region are indicated. Near-infrared bands used for atmospheric correction are not indicated beyond 800 nm. Examples of measured spectral remote-sensing reflectance (R_{rs}) from various waters around the world (Lee et al., 2007) are shown in the background. Adapted from Blondeau-Patissier et al. (2014), who adapted it from Lee et al. (2007).

at a limited number of wavebands in the visible domain, and to infer from these data the chl *a* concentration of top layers of the water column (Esaias et al., 1986). Since the initial success of CZCS, many following sensors have been developed and launched, with increasing numbers of spectral bands. Past, current, and future global ocean-color satellite missions are shown in Fig. 2.1. Simultaneously, mission goals have extended far beyond measuring chl *a* concentration. The details of the progress, advantages and limitations of the algorithms, used with the multi-spectral ocean color sensors (CZCS, SeaWiFS, MODIS and MERIS), have been recently discussed in Blondeau-Patissier et al. (2014). The comparison of the spectral band positions for these four ocean color sensors and VIIRS (the most recently launched instrument) is shown in Fig. 2.2.

Conceptually, passive ocean remote sensing instruments retrieving information about the constituents of natural waters, their corresponding inherent optical properties (IOPs), the bottom type and depth, from the electromagnetic radiation reaching the sensor. However, the instruments measure the upwelling radiance that includes contributions by the atmosphere, the water surface and the water column (Fig. 2.3). Main contributions to the measured signal are as follows (Sathyendranath, 2000):

- light reaching the sensor after scattering of photons in the atmosphere;
- light reaching the sensor after reflection of direct sunlight at the sea surface, e.g., in sun glint, from whitecaps or foam, which will be attenuated by scattering and absorption in the atmosphere before reaching the detector;
- light upwelling from the sea surface after back-scattering in water, which will be also attenuated in the atmosphere before reaching the detector.

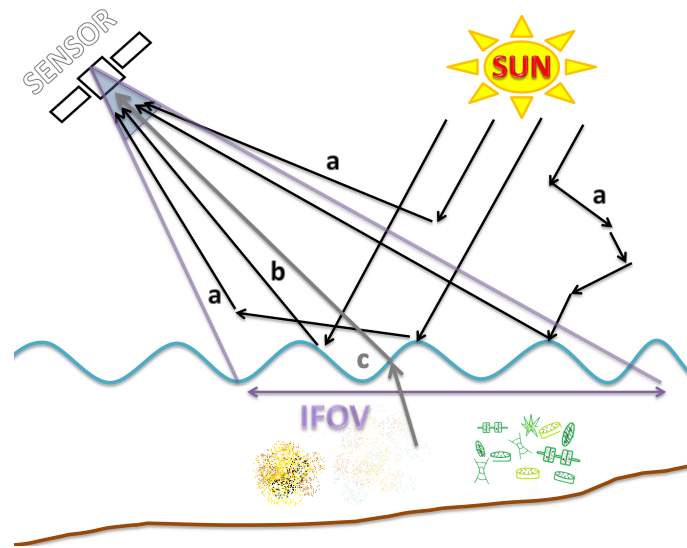


Figure 2.3: Pathways of light reaching the remote sensor. Adapted from Sathyendranath (2000). (a) Light scattered in atmosphere. (b) Specular reflection of direct sunlight at the sea surface. (c) Upwelling light leaving the water surface and traveling in the direction of the sensor. Instantaneous field of view (IFOV) is determined by the geometry of the sensor, its altitude and its viewing angle.

The only radiometric component of the measured signal, which carries useful information about the water body, is the upwelling radiance from the sea surface. Thus, the atmospheric contribution and the light directly reflected at the surface (e.g., in sun glint, or from whitecaps or foam) have to be corrected for. They are typically removed in the ocean color atmospheric correction procedure. However, highly glint or cloud contaminated scenes are routinely screened out. The atmospheric signal, which includes, among others, the Rayleigh and aerosols components, can contribute up to 90% of the detected signal. It also changes with the geometry of illumination and observation as well as with the aerosol type and optical depth. Hence, small errors in the estimated atmospheric contribution can cause significant biases in the estimation of the water components.

Upwelling water leaving radiance is influenced by several factors. Direct sunlight and scattered sky light that penetrate the sea surface may be absorbed or scattered within the water column. In-water constituents that affect light optical properties are traditionally grouped into the following components (Mobley, 1994):

- sea water (pure water + inorganic dissolved materials),
- phytoplankton,
- CDOM (colored dissolved organic matter),
- non-phytoplankton organic particles (sometimes referred to as detritus or tripton),
- inorganic particles,
- bubbles.

In shallow waters, a significant part of the light from the sun may also reach the bottom and be reflected from it. Ocean color remote sensing analyses the variations in magnitude and spectral dependence of the water-leaving radiance to derive information on the type and concentration of substances present in the water. The retrievals of the different IOPs and biogeochemical components of the water are performed with bio-optical algorithms (e.g. Lee, 2006).

2.2 Natural fluorescence of biological sources

2.2.1 CDOM fluorescence

CDOM and its optical properties

CDOM is part of the dissolved organic matter (DOM) pool, which significantly absorbs light in the UV and blue spectral region. Hence, it has a yellowish color, which is why CDOM is also referred to as gelbstoff, gilvin or yellow substance. The term 'dissolved' refers to its solubility in the water, but it is generally defined operationally as the filtrate of the mechanical separation by filtration through 0.2- μm pore size filter. CDOM is ubiquitous in all natural waters and covers a wide range of compounds of different chemical structures that are of biological origin. Additionally, part of the CDOM pool also fluoresces.

CDOM is an important component of aquatic systems and plays an important role for many physical, chemical and biological processes. First of all, CDOM strongly influences the light field in water: it reduces UV radiation, which is potentially harmful to aquatic organisms, within the water column. On the other hand, when abundant, it limits the amount of light available for photosynthesis and decreases the light penetration depth. CDOM absorption may also influence the vertical distribution of radiant heating in the upper ocean and thus alter stratification, mainly in coastal waters where CDOM is most abundant (Granskog et al., 2007).

CDOM is the principal abiotic photoreactive constituent in marine waters and undergoes photoprocesses, during which its average molecular weight is reduced and products are formed, e.g., reactive oxygen species (ROS) and a number of trace gases, like CO_2 , CO and carbon sulfide (COS) (Blough, 2001). Reducing molecular weight leads to the formation of biologically available low molecular weight organic compounds and to the release of available forms of nitrogen, thereby providing important compounds for growth of microorganisms. Furthermore, the biological availability of some metals can be altered by CDOM: directly through photochemistry or indirectly through reactions with the ROS or sea-air exchange of trace gases by redox reactions of some trace metals mediated by CDOM (Coble, 2007, and references therein).

DOM is a significant element in the carbon cycle - in fact, DOM is arguably the most important intermediate component in global carbon cycling (Battin et al., 2008). The amount of carbon bound in DOM in the world's oceans is similar to the amount bound as atmospheric CO_2 (~ 700 PgC) (Siegenthaler & Sarmiento, 1993). Estimates of the

contribution of CDOM to total dissolved organic carbon (DOC) in the ocean range from 20% to 70%, with highest estimates for river-dominated coastal regions and lowest estimates for the open ocean (Coble, 2007, and references therein). Besides CDOM being a useful proxy for dissolved carbon, it is also an indicator of water exchange and mixing. CDOM can be used as water mass tracer as it displays conservative behavior on the time scales of physical mixing. It can be helpful in tracing inputs of rivers or pollutants, distinguishing between waters of different origin and verifying exchange of ballast waters in the ocean-going vessels (Coble, 2007, and references therein).

Optical parameters of CDOM are often used to characterize it both qualitatively and quantitatively. The absorbance and fluorescence of CDOM are frequently measured locally and globally to examine the water quality, the chemical composition of dissolved organic matter, trace water masses and to study dynamical processes involving CDOM.

Absorption: CDOM absorbs strongly in UV and short-VIS wavelengths, with an exponential decrease towards longer wavelengths (almost negligible above 550 nm) and without any discernible peaks in the absorption spectrum. The CDOM absorption spectrum is usually described by an exponential model (Jerlov, 1976; Shifrin, 1988):

$$a_{cdom}(\lambda) = a_{cdom}(\lambda_0) \cdot e^{-S(\lambda-\lambda_0)} \quad (2.1)$$

where $a_{cdom}(\lambda_0)$ is the absorption of CDOM at the reference wavelength λ_0 , and S is the spectral slope coefficient of the exponential, which determines the shape of the absorption curve. Value of $a_{cdom}(\lambda_0)$ is a proxy of concentration, and S is often used as an index for changes in the composition of CDOM, reflecting the complexity and diversity of compounds, marine or terrestrial origin of CDOM or ratio of humic to fulvic acids (Carder et al., 1989; Green & Blough, 1994). Bricaud et al. (1981) suggested that the model as in Eq. 2.1 can reasonably describe CDOM absorption in the near-UV-visible domain (350-700 nm) and that S is independent of the choice of λ_0 . On the contrary, more recent studies show that S values are highly dependent on the wavelength range used for the calculation. Both λ_0 and range over which S is calculated varied in previous studies (Twardowski et al., 2004, and references therein).

As an alternative to the exponential model, Twardowski et al. (2004) proposed a hyperbolic model to describe $a_{cdom}(\lambda)$:

$$a_{cdom}(\lambda) = a_{cdom}(\lambda_{412}) \cdot \left(\frac{\lambda}{\lambda_{412}} \right)^{-\gamma} \quad (2.2)$$

where $a_{cdom}(\lambda_{412})$ is the reference absorption of CDOM at 412 nm, and γ is the hyperbolic slope that was assumed by Twardowski et al. (2004) to be 6.92. Though this model has the convenience to depend on one parameter only and can be considered to be a better descriptor of CDOM absorption spectra than the exponential model by Bricaud et al. (1981), it still inadequately accounts for the CDOM variability in a wide range of natural

waters (Shanmugam, 2011). Hence Shanmugam (2011) has proposed a new exponential form with two slope parameters:

$$a_{cdom} = a_{cdom}(\lambda_i) \cdot e^{-S(\lambda-\lambda_0)-\gamma^0} \quad (2.3)$$

where $a_{cdom}(\lambda_i)$ is absorption of CDOM at 350 nm and the γ^0 is an additional parameter, independent of S, which takes into account the large variability of CDOM in coastal and ocean waters. The model was developed for satellite remote sensing and showed very good agreement between the absorption spectra estimated by that model and the spectra measured by spectrophotometer of discrete water samples (Shanmugam, 2011).

Regardless of CDOM composition and the model used to describe its absorption spectrum, the CDOM absorption spectra lack sharp features. This can possibly be explained by the complex chemical composition of CDOM, with its various compounds that have overlapping absorption spectra, and with no single compound dominating (Coble, 2007). Del Vecchio & Blough (2004) argued that CDOM absorption spectrum cannot solely result from a simple linear superposition of the spectra of numerous independent chromophores, but it might rather arise from a continuum of coupled states resulting from intermolecular interactions.

Despite the invention and application of new models to describe the shape of the absorption spectrum, the most commonly used models are still single absorption models (as in Eq. 2.1). S is sometimes considered a constant for specific applications (usually between 0.014 to 0.016 nm⁻¹), although in several studies its value varied from 0.003 to 0.0247 nm⁻¹ (Twardowski et al., 2004, and references therein). Changes in S have been attributed to different compositions of CDOM; its marine or terrestrial origin and degradation; photo-oxidation; bacterial remineralization; and water masses mixing. The slope of the absorption curve is usually lower in freshwater and coastal environments than in marine environments (Coble, 2007). Relationships between the spectral slope coefficient and the absorption coefficient have been used to differentiate between terrestrial and marine origin of CDOM (Kowalczyk et al., 2005; Stedmon & Markager, 2001).

Fluorescence: Fluorescence of CDOM is one of several imperfect inelastic scattering processes in natural waters, which include vibrational Raman scattering and chl *a* fluorescence. Fluorescence occurs when a molecule absorbs a photon, where loosely held electron is excited to a higher energy level, and then shortly after it emits a photon of a different wavelength as the electron returns to its original energy level. Between processes of absorption and emission some energy is dissipated as heat, so the energy emitted is lower than the energy absorbed (the Stoke's shift). The wavelengths at which a photon is absorbed and emitted depends primarily on the molecule itself (Lakowicz, 1999).

Fluorescent CDOM (FDOM) is a subgroup of CDOM (Fig. 2.4), and is (analogously to CDOM) a complex mixture of many fluorescent compounds. Due to the difficulty of identifying individual fluorophores (compounds that fluorescence) in natural waters, two major types of FDOM are usually separated (Coble, 2007): humic-like, and protein-like or amino acid-like (usually specifically tryptophan-, tyrosine- or phenylalanine-like). In

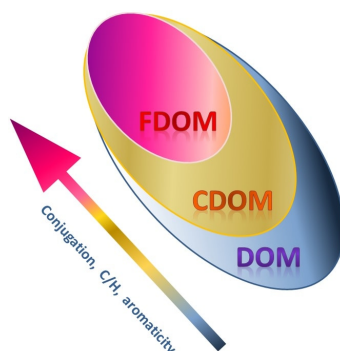


Figure 2.4: Colored and fluorescent DOM (CDOM and FDOM, respectively) represented as a subfraction of the total DOM pool. Based on Stedmon & Álvarez Salgado (2011).

general, humic-like fluorescence displays broader fluorescence peak with emission wavelengths typically above 400 nm, whereas protein-like display narrower peaks with emission wavelengths below 400 nm.

Typically, humic substances are sub-divided into three categories, which are chemically defined by the solubility at different pH: humic acids are insoluble in aqueous solution at pH lower than 2, but soluble at higher pH; fulvic acids are soluble in water under all pH conditions and humins are insoluble in water under any pH conditions (Aiken G.R., 1985). Fluorescent humic-like fluorophores are also usually divided into terrestrial and marine origin. Terrestrial humic-like compounds display red-shifted fluorescence. This means that they show excitation and emission maxima at longer wavelengths, which is probably due to higher molecular weight.

The main components of protein-like FDOM are three fluorescent amino acids: tryptophan, tyrosine and phenylalanine. Tryptophan-like and tyrosine-like fluorescence has been repeatedly observed (e.g. Coble, 1996, 2007; Nieto-Cid et al., 2005; Yamashita & Tanoue, 2003; Stedmon et al., 2007). Their fluorescence spectra show similarities to fluorescence signals of pure tryptophan and tyrosine. Natural water samples display a blue shift to shorter wavelengths because amino acids behave differently in different microenvironments (Determann et al., 1998). Phenylalanine fluorescence has also been observed (Jørgensen et al., 2011), and showed a good agreement with the phenylalanine standard.

Besides being dependent on the molecule itself, fluorescence depends also on environmental factors, which can affect both the wavelengths at which fluorescence is emitted and its intensity. Fluorescence generally increases with increasing pH. However, in aquatic systems where the pH ranges normally between 5-9, the intensities of fluorophores are found to change only by about 10% and hence pH has a much lower effect on fluorescence than the DOM molecular character (Hudson et al., 2007). These changes in fluorescence result from conformational changes in molecules (Hudson et al., 2007), which are exposing or hiding fluorescent parts of molecules. Low pH causes the molecule to coil, while raising pH extends the molecule (Hudson et al., 2007).

The presence of metals through the formation of organo-metal complexes can either quench or enhance CDOM fluorescence in a certain spectral region (Hudson et al., 2007,

2. SCIENTIFIC BACKGROUND

Table 2.1: Fluorescence properties: excitation maxima Ex_{max} and emission maxima Em_{max} , for major fluorescent components of CDOM in seawater, after Coble (1996)

| Peak | $Ex_{max}[nm]$ | $Em_{max}[nm]$ | |
|------|----------------|----------------|-------------------------------|
| B | 275 | 310 | Tyrosine-like, protein-like |
| T | 275 | 340 | Tryptophan-like, protein-like |
| A | 260 | 380-460 | Humic-like |
| M | 312 | 380-420 | Marine humic-like |
| C | 350 | 420-480 | Humic-like |

and references therein). However, quenching by metals is not likely in natural waters (Hudson et al., 2007). Fluorescence can also be quenched by increase in temperature, as a rise in temperature increases the likelihood that an electron will come back to its ground state by a radiationless process. Measurements of thermal quenching were also suggested to provide another way to analyze CDOM composition or to fingerprint DOM pollutants from different sources (Baker, 2005). Hence, CDOM fluorescence measurements are conventionally taken under constant temperatures in order to avoid the influence of thermal quenching of fluorescence (Baker, 2005).

The dominant process for FDOM (and CDOM) removal from natural waters is photo-bleaching, with microbial decomposition of lesser importance (Coble, 2007, and references therein). Photodegradation alters both intensity and peak position of fluorescence. DOM may be degraded by direct alteration of the DOM structure or indirect chemical changes through reactions with free radicals created by the application of light (Hudson et al., 2007, and references therein), with both its optical and chemical properties altered.

Fluorescence of CDOM has been observed for a long time in natural waters, but its measurement has become relatively fast and easy only for the last 20 years. This is mainly resulting from the excitation emission matrix fluorescence spectroscopy (EEMS), which nowadays enables synchronous scanning of excitation, emission and fluorescence intensity. As a result, a 3-D plot of fluorescence excitation wavelength, emission wavelength and intensity is obtained (see example in Figure 3.4). This technique allows to perform analysis over a vast array of available data. Fluorescence data reveal more details and provide more information on CDOM composition than the smooth absorption spectra. The first method to analyze EEMs of DOM and identify fluorescent compounds was proposed by Coble (1996) and was rather descriptive and involved manual identification of peaks in EEMs. Coble (1996) based the characterization of FDOM on 3-D plots, contour plots, number of fluorescence peaks, position of emission maxima at fixed excitation wavelengths, fluorescence intensities and position of wavelength-independent fluorescence maxima, and ratio of the two humic-like peaks. As a result, five major fluorescent components were identified and designated by letters (Table 2.1). The nomenclature introduced by Coble (1996) has since then been commonly used and referred to in the literature.

To extend our understanding of the character of fluorophores, by utilizing such large amount of data and separating contributions of individual fluorophores, which usually have spectral overlap, multivariate and statistical methods have been applied to extract the most information from the EEM data. Such methods include the Analysis of Variance

(ANOVA), Partial Least Squares regression (PLS), Principal Component Analysis (PCA) and Parallel Factor Analysis (PARAFAC) (Hudson et al., 2007, and references therein). PARAFAC has turned out to be especially useful, as under some circumstances, it enables a so-called mathematical chromatography to be performed; that is, to separate the mixture of measurements into the contributions from the underlying individual chemical analytes. For each analyte, the pure excitation and emission spectra are obtained as well as their relative concentrations (Bro & Vidal, 2011). The PARAFAC model has its origin in psychometrics. However, over the past thirty years it has successfully been applied to decompose EEMs of complex mixtures into their fluorescent components, and it has been used to analyze CDOM and fluorescence for over ten years (Stedmon et al., 2003). Lately, the PARAFAC method has been frequently used for CDOM fluorescence analysis and has proven itself to be a useful and quite a reliable tool (e.g. Guéguen et al., 2011; Jørgensen et al., 2011; Murphy et al., 2008; Singh et al., 2010; Stedmon et al., 2003; Stedmon & Markager, 2005; Stedmon et al., 2007; Yamashita et al., 2010).

Satellite remote sensing of CDOM

Due to its optical properties, CDOM can in principle be estimated by ocean color algorithms. In the last decades, many algorithms have been developed to assess CDOM concentration (IOCCG, 2006). The algorithms have been developed for a variety of sensors, water types, input parameters, etc. Most of these algorithms aim at estimating the CDOM absorption coefficients at 440 or 443 nm, which is widely accepted as the proxy of CDOM content. Most of them (e.g. QAA, Lee et al. 2002, and GSM, Garver & Siegel 1997; Maritorena et al. 2002) produce the combined absorption coefficient of detritus and CDOM (a_{dg}), as satellites cannot discriminate between dissolved and particulate material. However, the effect of using such a hybrid coefficient is viewed as negligible when applied to clear waters, where detrital materials are usually at very low concentrations (Nelson & Siegel, 2013).

Empirical approaches relate a combination (e.g. ratio) of radiances at several wavelengths to the desired parameter. In this case it is usually a CDOM absorption coefficient, and sometimes additionally a spectral slope parameter S (e.g. Swan et al., 2013). Another example is the CDOM index (Morel & Gentili, 2009), which reflects the relative anomalies in the relationship between CDOM and chl a concentrations as compared to chl a for the mean conditions of bio-optical model developed for Case 1 waters. These empirical relationships are usually developed from *in situ* data sets, where radiometric measurements and CDOM absorption have been collected simultaneously or in a narrow period of time. Hence, the obtained relationships may be valid only for the specific locations, for which the input data was available, and not appropriate globally. On the other hand, semi- or quasi-analytical algorithms (e.g. QAA and GSM) make us of both empirical parameters (the way the IOPs are parameterized i.e. how their variations and spectral shapes are formulated), and bio-optical models relating radiometric parameters and IOPs (generally absorption and backscattering coefficients). The inversion usually allows simultaneous retrieval of several variables contained in the IOP terms. Alternative approaches have also been suggested, e.g. an artificial neural network (aNN) inversion procedure, which was developed for the MERIS instrument (Doerffer & Schiller, 2007).

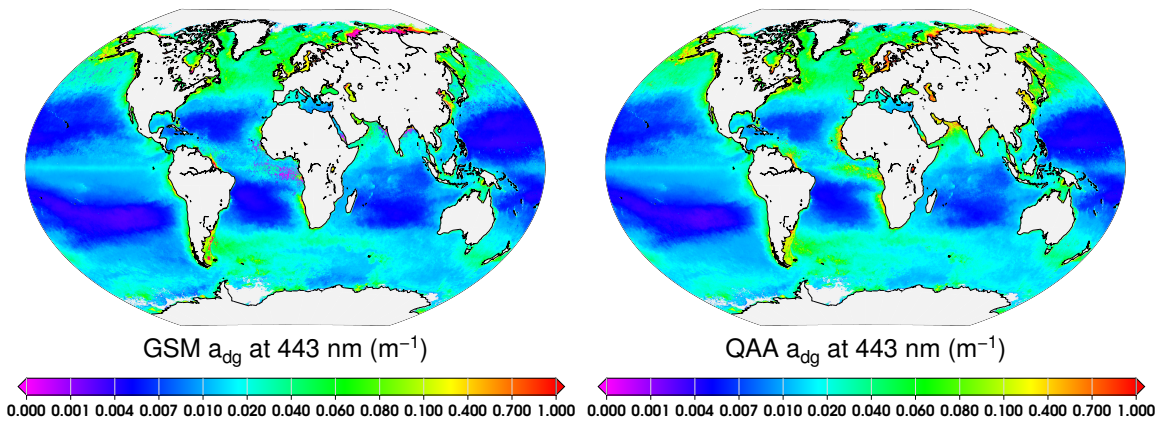


Figure 2.5: Dissolved and Detrital Organic Matter Absorption Coefficient at 443 nm (a_{dg}) from MODIS-Aqua for year 2009, derived with GSM model (left panel) and QAA algorithm (right panel). Data source: the Ocean Color Data Portal, <http://oceandata.sci.gsfc.nasa.gov/>.

In principle, the most widely used algorithms, GSM and QAA, partition the satellite-determined reflectance spectra into, among others, a_{dg} . One of the biggest drawback of these methods is the assumption of a constant spectral slope of colored detrital material (CDM, i.e. CDOM and detrital particulate combined), despite the known spatial and seasonal variability of the slope (Bricaud et al., 2012).

Recently, the GSM model was used for studies of the global surface ocean distribution of CDOM by Nelson & Siegel (2013), and authors stated that alternative bio-optical models give largely similar results. The mean global surface distributions of a_{dg} at 443 nm from MODIS-Aqua using the GSM model and QAA algorithm are compared in Fig. 2.5 (data freely available at the Ocean Color Data Portal at <http://oceandata.sci.gsfc.nasa.gov/>). Global distribution of the satellite-derived CDM illustrates an oceanic pattern that clearly mirrors the chl a distribution, with low values in the oligotrophic waters of the subtropical gyres, and high values in the subpolar regions and regions of persistent upwelling. Values of a_{dg} in the North Atlantic are often up to 0.1 m^{-1} , while values found in the South Pacific Gyre are often an order lower, and around 0.01 m^{-1} . These pattern largely reflect the distribution estimated from *in situ* observations of CDOM (Nelson & Siegel, 2013, and references therein). Enhanced values are also observed in the coastal areas, where big rivers (e.g., Amazon or Congo) discharge into the ocean. Despite overall good agreement between the two products, some discrepancies can still be observed: e.g., in the equatorial Atlantic and especially Arctic Ocean (Fig. 2.6), where unexpectedly low values are observed in case of GSM product, while at the same time QAA a_{dg} values are remarkably high.

As mentioned above, CDOM fluorescence varies with the types of CDOM and with the environmental conditions. However, fluorescence of CDOM only becomes an important component of water leaving radiance for regions with very high CDOM concentration (Conmy et al., 2014, and references therein). Furthermore, high CDOM waters are typically near-shore or inland water bodies, which are usually masked within the data processing in order to avoid land reflectance contamination, which further complicates

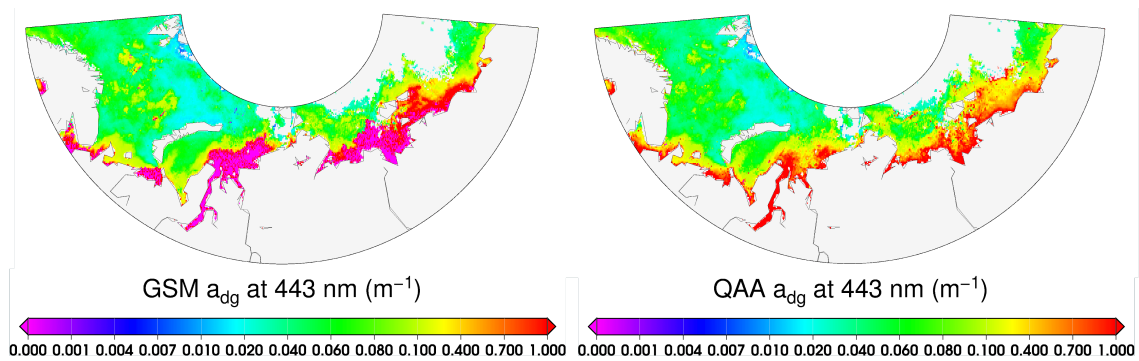


Figure 2.6: Dissolved and Detrital Organic Matter Absorption Coefficient at 443 nm (a_{dg}) from MODIS-Aqua for year 2009, derived with GSM model (left panel) and QAA algorithm (right panel), shown for a subregion in the Arctic. Data source: the Ocean Color Data Portal, <http://oceandata.sci.gsfc.nasa.gov/>.

possible satellite remote-sensing measurements. Additionally, a fluorescence signal fills in Fraunhofer lines, which offers another potential remote sensing application. Although some studies have shown promising results (Vodacek et al., 1994), sun-induced CDOM fluorescence is a very weak signal and its emission spectrum might be too broad to enable passive remote sensing of FDOM (Conmy et al., 2014), which was also supported by this study (see Section 5).

2.2.2 Chlorophyll *a* fluorescence and its relationship to photosynthesis

Basic mechanism of photosynthesis

Photosynthesis is a biological process whereby light energy is captured and stored by an organism, and the stored energy is used to drive energy-requiring cellular processes (Blankenship, 2002). The most common form of photosynthesis involves chl-type pigments and operates by using light-driven electron transfer processes. The light used for photosynthesis that drives a series of chemical reactions, comes from the Sun. The solar spectrum, along with absorption spectra of some photosynthetic organisms, is shown in Fig. 2.7.

In eukaryotic photosynthetic cells, photosynthesis is localized in subcellular structures known as chloroplasts. The chloroplasts contain all the chl pigments and, in most organisms, carry out all the main phases of the photosynthesis process. In prokaryotic photosynthetic organism, the early steps of photosynthesis take place in specialized membranes, which are derived from the cell's cytoplasmic membrane. In these organisms, the carbon metabolism reactions take place in the cell cytoplasm, along with all the other reactions that make up the cell's metabolism.

For convenience, photosynthesis can be divided into four phases (Blankenship, 2002):

1. light absorption and energy delivery by antenna systems,

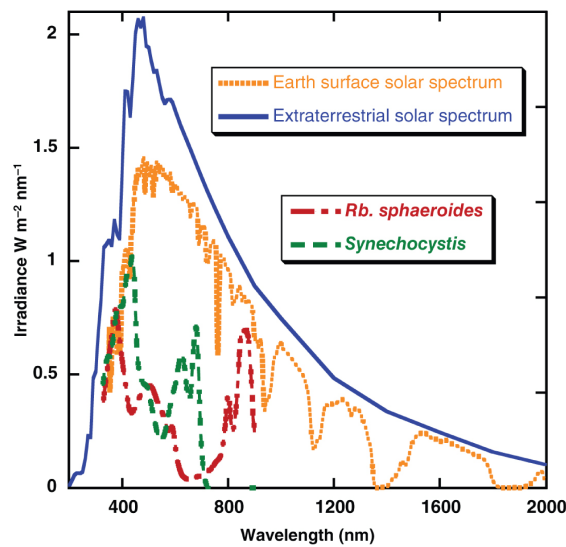


Figure 2.7: Solar irradiance spectra (blue and orange) and absorption spectra of photosynthetic organisms (*Rhodobacter sphaeroides* in red and *Synechocystis* PCC 6803 in green). The spectra of organisms are in absorbance units (scale not shown). Source: Blankenship (2002).

2. primary electron transfer in reaction centers,
3. energy stabilization by secondary processes,
4. synthesis and export of stable products.

Traditionally, the first three phases make up the so-called ‘light reactions’, while the fourth encompasses the so-called ‘dark reactions’.

Photosynthesis starts with absorption of light by one of the pigments associated with the photosynthetic apparatus. Not every pigment carries out photochemistry: the vast majority functions as antennas, collecting light and then delivering energy to the reaction center, where the photochemistry takes place. In the reaction center, the energy of excited states is transformed into chemical energy. The essence of photosynthetic energy storage is the transfer of an electron from an excited chl-type pigment to an acceptor molecule in the reaction center. The primary electron transfer event is then followed by a rapid series of secondary chemical reactions (Blankenship, 2002).

Most of photosynthetic organisms have two photochemical reaction center complexes that work together in a non-cyclic, linear electron transfer chain (LET) (Fig. 2.8). The two reaction center complexes are called photosystem (PS) I and PS II, which operate in series in the opposite order, so that electrons are transferred from PS II to PSI. PSII removes electrons from water, which is oxidized to molecular oxygen, which is then released as a waste product. The electrons extracted from water are transported via a quinone and the cytochrome b_6f complex to PS I and, after a second light-driven electron transfer step, eventually reduce an intermediate electron acceptor, NADP^+ , to form NADPH. During the process, photons are also transported across the membrane and into the thylakoid lumen, creating a protonmotive force, which drives the ATP synthesis.

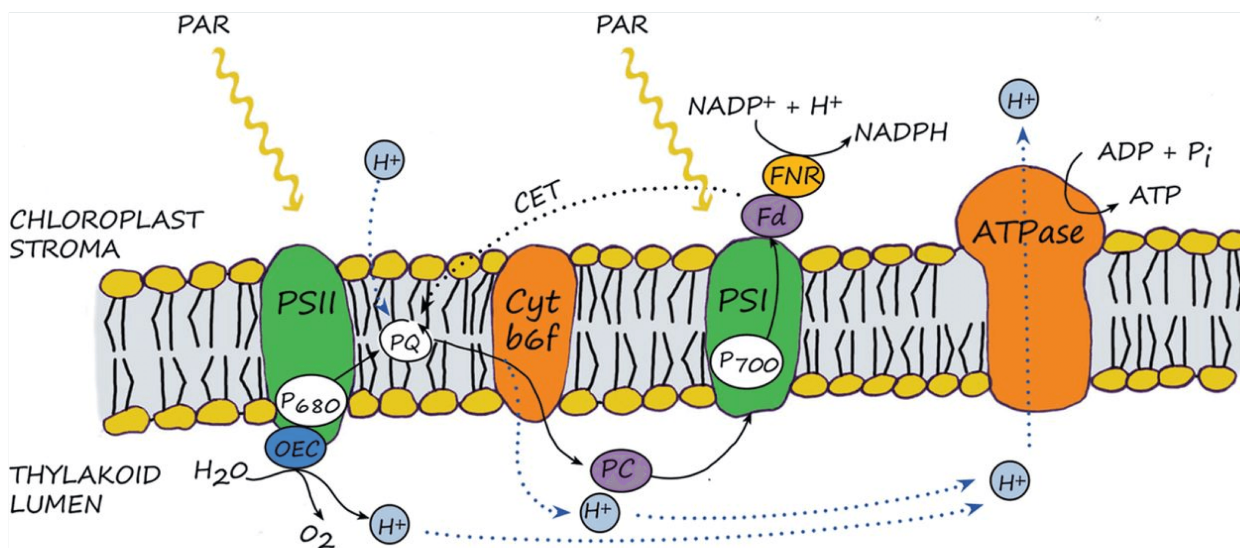


Figure 2.8: Schematic diagram of the photosynthetic linear electron transfer (LET) chain. In LET, excitation energy from absorbed photons in PSII is used to reduce the plastoquinone pool ('PQ') and pump protons from the chloroplast stroma into the thylakoid lumen via the cytochrome (Cyt) b6f complex. Energy from absorbed photons in PSII is also used to operate the oxygen-evolving complex (OEC) by which water molecules are split yielding further protons. Simultaneously, the energy from photons absorbed by PSI is used, via ferredoxin (Fd), by ferredoxin-NADPH reductase (FNR) to reduce NADP^+ to NADPH. The oxidized PSI reaction centre P700^+ is reduced back to P700 using an electron donated by plastocyanin (PC), originally from PSII. In the cyclic electron transport (CET), an electron is passed from Fd back to the PQ pool and again to PSI via PC. This results in pumping of protons to the lumen but no NADPH synthesis. Protons accumulated in the lumen (from either LET or CET) are used by ATP synthase (ATPase) to synthesize ATP. Source: Porcar-Castell et al. (2014).

The final phase of photosynthetic energy storage involves the production of stable high-energy molecules and their utilization to power a variety of cellular processes. This phase uses the intermediate reduced compound, NADPH, generated by PS I, along with the phosphate bond energy of ATP to reduce carbon dioxide to sugars. In eukaryotic photosynthetic organisms, phosphorylated sugars are then exported from the chloroplasts. The carbon assimilation and reduction reactions are enzyme-catalyzed processes that take place in the chloroplast stroma.

As light and carbon reactions exhibit different sensitivities to environmental factors (e.g. light, temperature, water stress), the production of ATP and NADPH by light reactions do not always match the consumption of these metabolites by the carbon reactions. As energy absorbed in excess by the light reactions can damage the photosynthetic apparatus (for example in very sunny but cold environment), photosynthetic organisms use regulatory mechanisms to adjust the energy balance between light and dark reactions. Thus the performance of light reactions tend to emulate that of carbon reactions, which establishes a link between optical data (related to the light reactions) and primary production. This is potentially useful for remote sensing of photosynthesis (Porcar-Castell et al., 2014).

2. SCIENTIFIC BACKGROUND

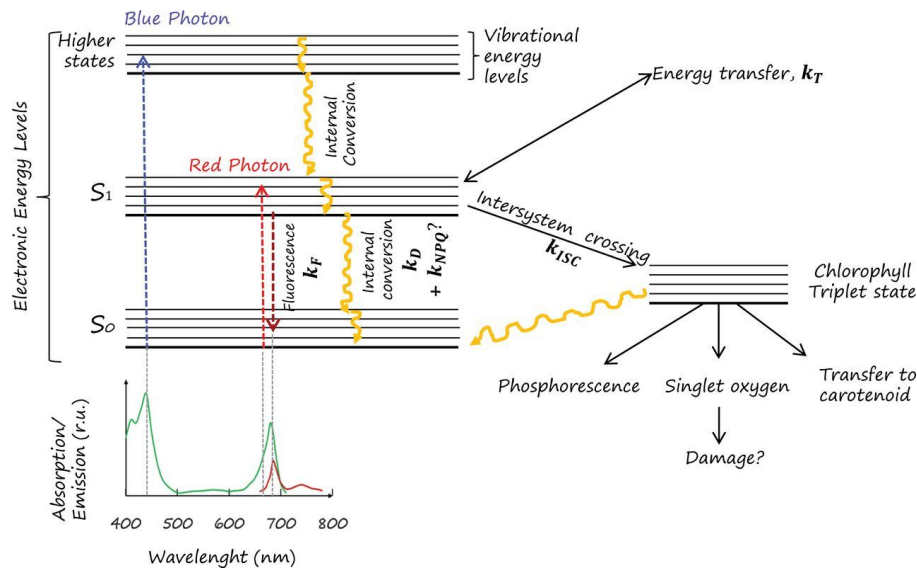


Figure 2.9: Idealized Jablonski diagram illustrating the energy partitioning of absorbed photons in a chl *a* molecule. Source: Porcar-Castell et al. (2014).

However, there are several processes that can interfere with this relationship. A scheme of the partitioning of photosynthetic energy at the leaf level with the regulatory mechanisms is shown in Fig. ???. The regulatory mechanisms adjust energy partitioning between different different pathways of energy flow are indicated in Fig. 1.3 as red valves.

Fluorescence at the molecular level

Unlike CDOM, chl *a* is not dissolved in water, but located within living cells, which alters its spectral properties and fluorescence efficiencies. An idealized Jablonski diagram of the energy levels and possible dissipation pathways for a chl *a* molecule embedded in a photosynthetic antenna, from which most of the chl *a* fluorescence originates, is shown in Fig. 2.9. Even though energy levels are quantized, chl *a* molecules display continuous absorption and emission spectra due to superposition of vibrational energy levels on each electronic energy level. Because photosynthetic pigments *in vivo* are tightly packed into a protein matrix, the vibration of the chemical bonds in the pigment-protein complex add additional variability to the absorption and emission spectra of pigments *in vivo*. Due to this phenomenon, also known as inhomogeneous broadening, pigments display different spectral shapes *in vivo* (Vassiliev & Bruce, 2008), but not when isolated. Vibrational energy is associated with vibrations of atoms around their equilibrium positions in the molecule, while rotational energy is associated with the rotation of the molecule around its axis, which is negligible in the solid state.

Chl *a* absorbs light in the blue and red part of the visible electromagnetic spectrum (Fig. 2.10 left). The red absorption band (which is centered at 661 nm when chl *a* is dissolved in diethyl ether), corresponds to an electronic transition from the ground state directly to the first excited state (S_1) of the chl *a* molecule (Fig. 2.9). The blue absorption band (centred at 429 nm in diethyl ether) corresponds to an electronic transition from the

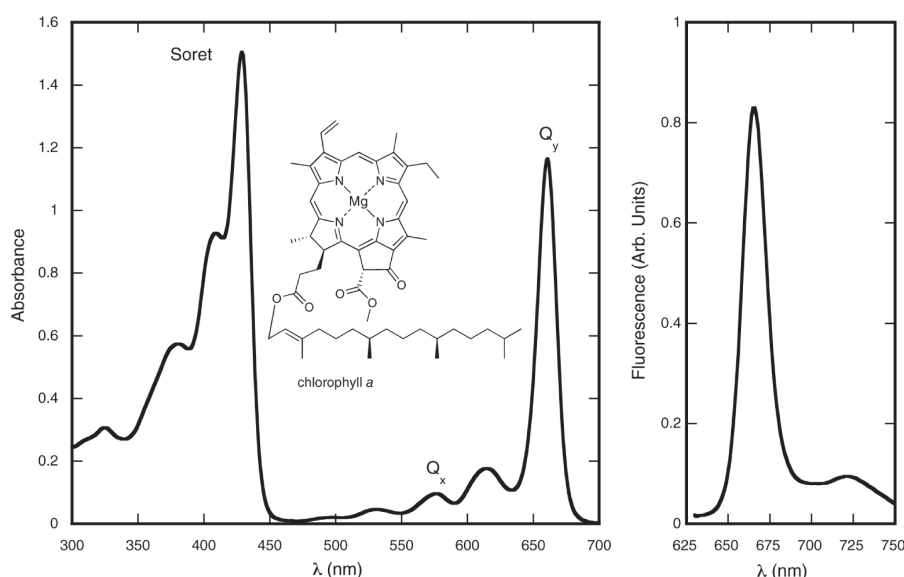


Figure 2.10: Absorption (left) and fluorescence (right) spectra of chlorophyll *a* dissolved in diethyl ether. The Soret and Q_y absorption bands of chl *a* are indicated. Source: Blankenship (2002).

ground state to the second excited state. Because vibrational energy levels from higher excited states overlap with those of the S_1 level, excited states can switch to the vibrational manifold of the S_1 level, and the vibrational energy is again rapidly dissipated. Hence, the difference in excitation energy between blue and red photons is almost always dissipated as heat.

For S_1 level vibrational states, lifetimes of excitations are a thousand times longer as compared to higher energy levels, and their energy can be used for other processes besides internal conversion (Porcar-Castell et al., 2014). For a chl *a* molecule embedded in a photosynthetic antennae, in the non-stressed conditions, most of the energy is effectively transferred to other pigments or to the reaction center pigments, which is a pathway to perform photosynthesis. Excitation energy can also be re-emitted as fluorescence. Additionally, via the process of inter-system crossing, a long-lived chlorophyll triplet state can be formed. The triplet state is long lived and can relax either by reacting with oxygen to produce reactive singlet oxygen, by transfer of energy to a carotenoids (what is their photoprotective function, next to photosynthetic) or by emission of a phosphorescence photon. As formation of singlet oxygen can cause oxidative damage to the pigments, lipids and proteins of the photosynthetic thylakoid membrane, the triplet state is potentially dangerous. One photoprotective mechanism to counter this problem is the so-called non-photochemical quenching (NPQ), which is a physiology regulated component of thermal dissipation.

The fluorescence spectrum of chl *a* peaks at slightly longer wavelengths than the absorption maximum (Fig. 2.10). It is usual that a fluorescence spectrum has a characteristic ‘mirror image’ relationship to the absorption spectrum. This is because those molecular vibrations that are activated during electronic absorption are also likely to be activated upon fluorescence emission. However, in this case, prior to photon re-emission, some energy is

lost first in the internal conversion process and the initial state is the ground vibrational state of the excited electronic state, while the final state is the excited vibrational state of the ground electronic state. This causes a shift of the emission to the longer-wavelength side of the main transition, which is known as the Stokes shift (Blankenship, 2002).

Chl *a* dissolved in ether is highly fluorescent, with quantum yield of 30%, in contrast to quantum yield of fluorescence *in vivo*, which has typical values of 0.5–3%, and does not exceed 10%. This difference is due to photochemical and non-photochemical quenching of excitation energy in the photosynthetic antennae (Porcar-Castell et al., 2014, and references therein).

Linking fluorescence at PS II and photosynthesis

The processes that control the energy partitioning in PS II are crucial for relating chl *a* fluorescence with photosynthesis and primary productivity. Energy absorbed by pigments of PSII can be used for photochemistry, dissipated non-radiatively as heat or re-emitted as fluorescence. Because of dynamic and physiology-regulated non-radiative energy dissipation, a unique relationship between fluorescence and photochemical efficiency cannot be established. In low light and no stress environment, most energy is effectively used for photochemistry and excitation lifetime in the antenna of PS II τ_{PSII} is short (in the order of hundreds of picoseconds). Hence, the fluorescence yield is low. This de-excitation pathway is called photochemical quenching (PQ). If light intensity increases, the carbon fixation reactions and electron transport chain gradually become light saturated, which causes an increase in τ_{PSII} , and results in increasing fluorescence yield (Porcar-Castell et al., 2014). The sudden increase of fluorescence is especially well observed when dark-acclimated photosynthetic organisms (terrestrial plant or phytoplankton) are exposed to strong light after previous dark acclimation, which is then followed by a sudden decrease. This process is collectively called the Kautsky effect (e.g., Govindje 1995, first observed by Kautsky & Hirsch 1931). These dynamic changes reflect the rapid reduction and re-oxidation of PS II electron acceptors and their influence on τ_{PSII} .

Increase in τ_{PSII} raises the chance of the formation of hazardous chlorophyll triplet states. Hence, plants and phytoplankton use a number of regulatory mechanisms that are capable of dissipating the excess quanta as heat in order to minimize τ_{PSII} , while still allowing electron transfer, hence photosynthesis, to take place. These mechanisms lead to a decrease in the excitation lifetime in the antenna and subsequently a decrease in fluorescence yield as well as PQ, and are collectively termed non-photochemical quenching (NPQ). The primary modes of NPQ are antennae quenching (qE) and reaction center quenching (qI) (Krause & Jahns, 2004). Antennae quenching functions by intercepting energy transfer from the outer antennae to the PS II core, while qI is associated with damaged or down regulated PS II and heat dissipation at the core.

PSI and PSII fluorescence

Chl *a* fluorescence originates from chl *a* pigments associated with one of the photosystems (PSI or PSII), which co-operate in the electron transfer during photosynthesis. The

reaction center of PSI and PSII contains a special dimer of pigments that is the primary electron donor for the electron transfer cascade (Blankenship, 2002). These pigments are chemically nearly identical to the chlorophylls that form antenna pigments, but their environment in the reaction center protein gives them unique properties. The pigments are called P####, with '###' after the wavelength maximum of their Q_y absorbance band (see Fig. 2.10), which is 680 nm for PSII (P680) and 700 nm for PSI (P700). Because of this, the two photosystems show different spectroscopic properties (Fig. 2.11). At room temperature, chl *a* fluorescence from PSI presents a peak at 730 nm and a shoulder at 690 nm, whereas fluorescence from PSII peaks at \sim 685 nm and has vibrational satellite bands at wavelengths $>$ 700 nm, overlapping with PSI fluorescence (Porcar-Castell et al., 2014, and references therein).

In contrast to PSII, the lifetime of excitation in PSI, τ_{PSI} , does not seem to be affected by photochemical or non-photochemical quenching processes (at least on short time scales), possibly because its reaction center is very efficient at quenching excitation energy in the oxidized state. The primary electron transfer rate (Blankenship, 2002) is slowed down upon accumulating reduced quinone A acceptor (Q_A^-) in PS II, which is the major effect that gives rise to the fluorescence increase in PS II. Electrostatic repulsion of Q_A^- inhibits the charge separation process and promotes the back transfer of the excitation to the bulk antenna system, where fluorescence takes place. Some of the increase is also due to recombination luminescence, in which the charge-separated state of P680 and pheophytin, the primary electron acceptor of PSII, ($P680^+Pheo^-$), recombines to form excited state $P680^*$, followed by the back transfer of the excitation to the antenna system. Under most circumstances, $P680^+$ is never found, because it is such a strong oxidizer that there is usually species to reduce it. Therefore it does not enter into the normal phenomenon of fluorescence induction in PS II.

PS I has several important differences in comparison to PSII, which contribute to low variable fluorescence (Blankenship, 2002). First, the electron transfer process is largely irreversible, due to the steeper redox gradient on the acceptor side of PS I. This rapidly removes the electron that is transferred further from P700, compared to the situation in PS II. This effect greatly reduces the probability of recombination luminescence due to charge recombination. In addition, the larger distance of the electron acceptor diminishes the electrostatic effect of the reduced acceptor on the primary electron transfer. Finally, a significant amount of $P700^+$ is present under conditions of steady-state electron flow through PSI. $P700^+$ quenches antenna excited states just as effectively as does P700, although the mechanism is quite different. Probably, $P700^+$ quenches the antenna by forming an excited state of the $P700^+$ complex ($P700^{+*}$), which then rapidly decays by nonradiative pathways (Blankenship, 2002). All these effects lead to a semi-constant pace of excited states quenching at PSI antenna pigments and hence low variability of fluorescence yield.

Differences in yield and spectral properties between photosystems lead to variable contribution of each of them to the total fluorescence signal. It is generally assumed, that in natural conditions most of the fluorescence signal originates from PS II (Franck et al., 2002). PSI fluorescence contributes from 0 up to 50% of total fluorescence, depending on the method, measuring conditions, species, and especially the spectral region (Porcar-

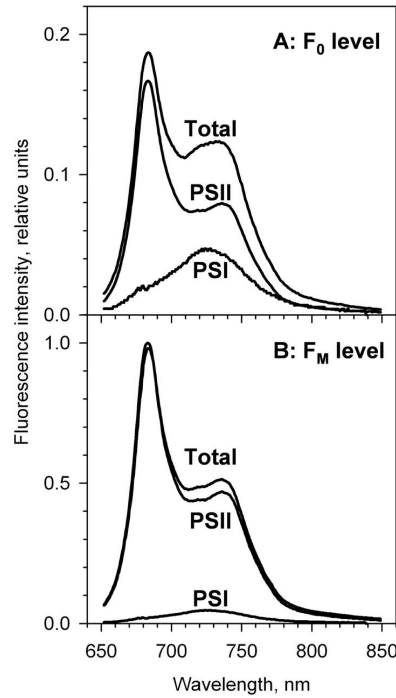


Figure 2.11: The relative spectral contributions of PSI and PSII fluorescence to the total emission spectrum in (A) barley leaves at the minimal (F_0) and (B) maximal F_M fluorescence levels. Fluorescence is normalized to the peak in F_M . Source: Porcar-Castell et al. (2014), redrawn from Franck et al. (2002).

Castell et al., 2014). The contributions of PSI fluorescence has its maximum in the near infrared and is considered insignificant in red wavelengths (Fig. 2.11).

2.2.3 Chlorophyll *a* fluorescence in the marine environment

The variability of chl *a* fluorescence signal

The in vivo fluorescence flux emitted by an elementary volume (F) is often modeled as a product of photosynthetically available radiation (PAR), chl *a* concentration (C), the mean chl *a*-specific absorption coefficient $\bar{a}^*(\lambda)$, fluorescence intracellular reabsorption factor (Q_a^*) and quantum yield of in vivo fluorescence ϕ_F (Falkowski & Kiefer, 1985; Babin et al., 1996; Babin, 2008):

$$F = PAR C \bar{a}^*(\lambda) Q_a^* \phi_F . \quad (2.4)$$

Eq. 2.4 reflects basic factors that influence fluorescence emission. As it implies, the fluorescence that is measured does not dependent solely on fluorescence efficiency. In nature, the variables that vary the most are PAR and C . PAR varies with changing sun elevation, which depends on the location, the season and the time of day. It also varies within the water column, and in response to atmospheric conditions (e.g., clouds). Changes

in C can cover four orders of magnitude, with smallest values less than 0.03 mg m^{-3} in oligotrophic waters and highest of 30 mg m^{-3} and more in eutrophic waters (Babin et al., 1996). Nevertheless, the remaining terms are also largely variable and change in response to environmental conditions.

The mean chl *a*-specific absorption coefficient $\overline{a^*}(\lambda)$ is the chl *a*-specific absorption coefficient of phytoplankton $a^*(\lambda)$, weighted by the irradiance spectrum. In nature, $a^*(\lambda)$ is always influenced by accessory pigments present within algae. Therefore, $a^*(\lambda)$ is highly dependent on a phytoplankton species, but also changes with environmental conditions, to which algae adjust their pigment concentration and composition. Additionally, with an increase in chl concentration, molecular self-shading decreases $a^*(\lambda)$ from its maximum value. This phenomenon is usually called ‘package effect’.

Fluorescence is partly reabsorbed within the phytoplankton cell, since the chl *a* fluorescence emission spectrum overlaps the absorption spectrum of chl. The fraction reabsorbed varies spectrally and depends on the absorption efficiency of the cell and, therefore, on its size and internal pigment content (e.g. Morel & Bricaud, 1981; Collins et al., 1985). The portion of emitted fluorescence, which is not reabsorbed within the cell is characterized by the factor Q_a . Theoretically, Q_a can vary between 0 and 1, but was found to usually range between 0.66 to 1 (Collins et al., 1985).

Besides these primary factors forming the fluorescence signal, chl *a* fluorescence changes in response to phytoplankton physiology, which in consequence could help to monitor these changes and characterize photosynthesis, health and the productivity of oceans at global scale (Lichtenthaler & Rinderle, 1988; Babin et al., 1996). For example, fluorescence variability can reflect the effect of nutrient limitations, e.g. macro-nutrients (Schallenberg et al., 2008; Abbott & Letelier, 1999) or iron (Behrenfeld et al., 2009). Chl *a* fluorescence also depends on species composition (MacIntyre et al., 2010) and growth irradiance, i.e. irradiance that phytoplankton has experienced during the growth phase of the cells and hence to which it is acclimated (e.g. Morrison & Goodwin, 2010; O’Malley et al., 2014).

***In situ* measurements of marine chlorophyll chl *a* fluorescence**

The measurement of chl *a* in vivo fluorescence was introduced in oceanography by Lorenzen (1966) to monitor changes in phytoplankton biomass. However, chl *a* fluorescence measurements have expanded into a variety of measurement protocols, used for different purposes, meant for different spatial and temporal scales, and from different platforms. The most common use of in vivo chl *a* fluorescence in oceanography, is for an instantaneous estimation of the phytoplankton biomass. The basic assumption for this principle is that a product of $\overline{a^*}(\lambda) Q_a^* \phi_F$ is constant. Hence, having a constant light source to generate PAR, then F is proportional to C, following Eq. 2.4.

The excitation and emission spectra of fluorescence are often measured by spectrofluometers. The excitation spectrum is commonly used to derive the absorption spectrum of photosynthetic pigments. Some of the most recent fluorescence measurement techniques are based on measuring variable fluorescence, i.e. the measurements of maximum and minimum fluorescence by changing the illumination of the water samples. There are three

different protocols to measure variable fluorescence (Huot & Babin, 2010): pulse amplitude modulation fluorometry (PAM), pump-and-probe fluorometry (P&P), and fast repetition rate fluorometry (FRR).

In vivo emission of chl *a* fluorescence by phytoplankton typically creates a peak at 685 nm in the spectra of downward and upward irradiance measured in natural waters. With increasing depth, the amplitude of the fluorescence peak observed in the upward light increases relative to its background. At greater depths, due to high absorption of liquid water in this spectral region, the scattering itself is greatly reduced, while inelastic scattering is still relatively strong as a result of lower light attenuation within the water column at the excitation wavelengths (Huot & Babin, 2010). The measurement of so-called ‘natural’ fluorescence (Kiefer et al., 1989; Huot & Babin, 2010) are actually measures of vertical profiles of nadir radiance around 685 nm and of PAR. This radiance can be measured with underwater spectrometers that enable measurements of broader spectra, from which a fluorescence signal can be extracted. More on *in situ* fluorescence measurements can be found in Huot & Babin (2010).

Remote sensing of marine chlorophyll fluorescence: normalized Fluorescence Line Height

The marine chl-*a* fluorescence has been retrieved from space by ocean color retrievals. The fluorescence line height algorithm (FLH), designed for MODIS (Abbott & Letelier, 1999) and later also applied to the MERIS instrument (Gower et al., 2004), derives the strength of the fluorescence signal by comparing radiance in the fluorescence channel to the background radiance. MODIS and MERIS are high spatial resolution low spectral resolution instruments, both having bands in the visible spectral region dedicated to fluorescence measurements (Figure 2.12). For MODIS, the radiances are measured in three channels in 10 nm windows, two of which are used to account for other effects (backscatter and Raman scattering) by calculating the ‘baseline radiance’ for fluorescence through interpolation of measurements at 667 nm (band 13) and 748 nm (band 15), the latter one being far from fluorescence emission due to water vapor absorption lines near 730 nm. The third band, the fluorescence band, is centered at 678 nm (band 14). This band does not cover the maximum of the fluorescence signal at 685 nm in order to avoid oxygen absorption features (Abbott & Letelier, 1999). Because of these limitations on bands placement, the measured MODIS FLH responds to only 57% of the actual fluorescence signal (Gower et al., 2004). In case of the MERIS instrument, the FLH algorithm uses bands 7, 8 and 9, located at 665 nm, 681 nm and 709 nm, respectively, and hence measured MERIS FLH responds to 78% of the actual fluorescence signal (Gower et al., 2004). FLH is calculated with use of water leaving radiances, while nFLH (normalized FLH) uses normalized water leaving radiances. The schematic of the algorithm and corresponding positions of relevant MODIS and MERIS bands are shown in Figure 2.12. Using the following algorithm, nFLH for MODIS is calculated as follows:

$$nFLH = L_{WN,14} - L_{WN,15} + (L_{WN,13} - L_{WN,15}) * [(\lambda_{15} - \lambda_{14}) / (\lambda_{15} - \lambda_{13})], \quad (2.5)$$

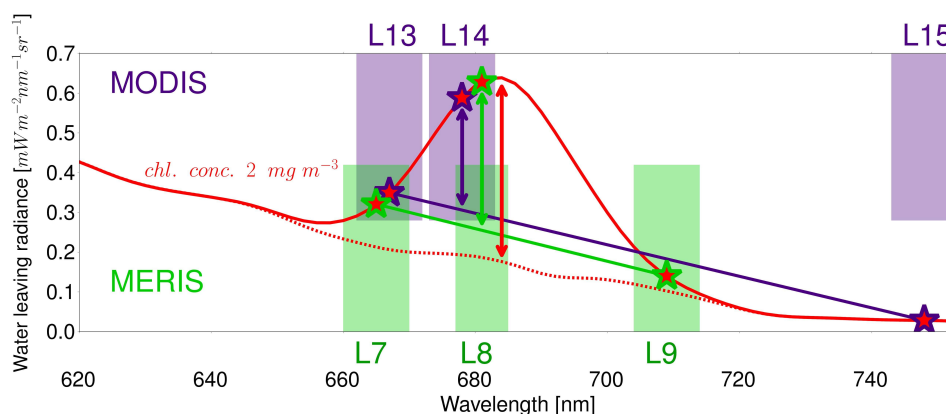


Figure 2.12: A schematic of the FLH algorithm, showing positions of MODIS and MERIS bands. The actual fluorescence signal, as well as FLH theoretically retrieved by MODIS and MERIS are shown with arrows (red, purple and green, respectively). Water leaving radiances, including (red solid line) and excluding (red dashed line) chl *a* fluorescence were calculated with the radiative transfer model SCIATRAN for a chl *a* concentration of 2 mg/m³.

where L_{WN} are the normalized water leaving radiances of the MODIS band number given by subscript; nFLH is currently a MODIS Level 3 standard product (available online at <http://oceancolor.gsfc.nasa.gov/cgi/l3>).

MODIS nFLH delivered the first global picture of marine fluorescence and initiated global studies on phytoplankton physiology and productivity (Behrenfeld et al., 2009; Morrison & Goodwin, 2010; McKibben et al., 2012; Huot et al., 2013; Westberry et al., 2013). However, detecting a weak fluorescence signal accurately is challenging. Atmospheric corrections applied to multispectral data are based on several assumptions about the atmospheric effects on different wavelength regions. The nFLH algorithm assumes the spectral shape of the fluorescence. Further problems may arise from backscattered light by particulate matter that scatters light in the red wavelengths and from which some nFLH signal originates (Abbott & Letelier, 1999). Negative values of nFLH were observed during blooms of some cyanobacteria species (Wynne et al., 2008), which was later used for a cyanobacterial bloom forecast system in Lake Erie (Wynne et al., 2013a).

2.2.4 Chlorophyll *a* fluorescence of terrestrial vegetation

Variability of chl *a* fluorescence signal

For terrestrial vegetation, there are additional factors that need to be considered when linking chl *a* fluorescence and photosynthesis on a leaf or canopy level. Similar to the marine environment, the fluorescence signal is strongly reabsorbed by chlorophylls. Additionally, in case of terrestrial chl *a* fluorescence, the effect is differently modulated for the two peaks of fluorescence, and interactions between leaf anatomy and the wavelength of light determine the shape of absorption profiles (Vogelmann & Evans, 2002; Porcar-Castell et al., 2014, and references therein). Red light penetrates deeper into the leaf, where it is more scattered than blue light (Figure 2.13). This is primarily due to the carotenoids

2. SCIENTIFIC BACKGROUND

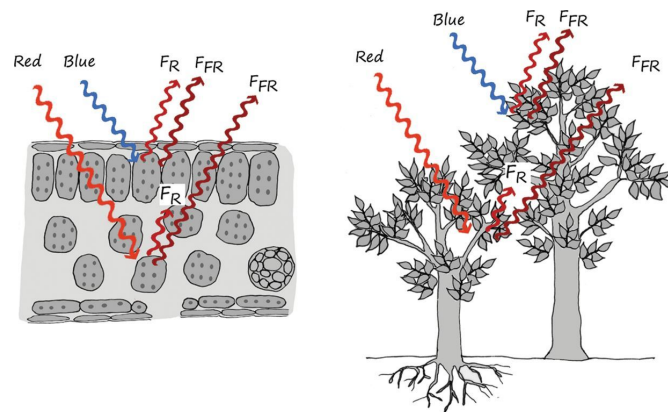


Figure 2.13: Wavelength dependency of light penetration and fluorescence reabsorption within a leaf and a plant canopy. Source: Porcar-Castell et al. (2014).

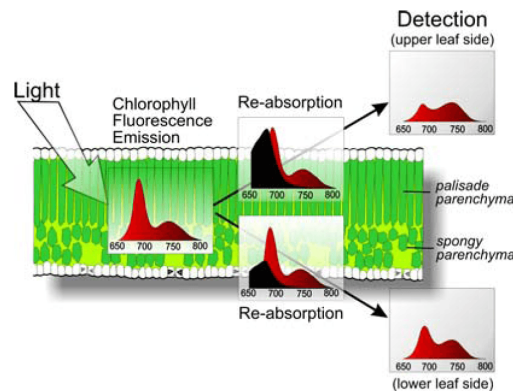


Figure 2.14: Emission and detection of light-induced chl *a* fluorescence with a scheme indicating the re-absorption of primarily the red chl *a* fluorescence band by the in vivo absorption bands of chl inside a bifacial leaf. Source: Buschmann (2007).

absorbing strongly in blue (but not red) light in the upper layers of the leaf (Buschmann & Lichtenthaler, 1998). On the other hand, scattering in mesophyll tissue (the primary location of photosynthesis in the plant), which increases the pathlength and hence the probability of light absorption, is larger for red than blue light (Vogelmann & Evans, 2002). Furthermore, like in case of phytoplankton, because of the overlap of absorption and fluorescence spectra, red fluorescence has a large probability (up to 90 % within the leaf, Gitelson et al. 1998) of being reabsorbed by chl within the leaf or canopy.

As a result, far red fluorescence might have stronger contribution from a deeper part of the leaf or canopy layer, and is, in general, less reabsorbed by chlorophylls, producing a stronger signal. These differences are important to consider when interpreting the fluorescence data in which signals are obtained from different spectral regions, which carry information originating from different layer of the leaves and the canopy (Porcar-Castell et al., 2014). The original chl fluorescence emission spectrum of a leaf, and how it is modified by re-absorption, is shown in Figure 2.14.

The chl *a* fluorescence signal is also modified by physiological and thermodynamic effects (Porcar-Castell et al., 2014, and references therein). For example, a fluorescence emission spectrum is known to change with temperature, and the range of temperature at which observations are made can exceed 60 °C. Fluorescence yield also has shown to respond to water stress. However, other processes, such as photorespiration, may undermine the possibility of tracking plant stress under certain conditions. Satellite-derived fluorescence has been shown to have a significant relationship to modeled GPP (Frankenberg et al., 2011b; Joiner et al., 2013; Guanter et al., 2012), although this strong dependence was not confirmed by the modeling study of Mohammed et al. (2014). Hyperspectral measurements of fluorescence above the canopy, and especially red fluorescence, were also shown to improve the daily empirical model of GPP when used together with Photochemical Reflectance Index (Cheng et al., 2013). More on the link between chl *a* fluorescence and photosynthesis, with focus on remote sensing application, can be found in the recent review by Porcar-Castell et al. (2014).

***In situ* measurements of terrestrial chlorophyll *a* fluorescence**

In situ measurements of chl *a* fluorescence can be divided into active and passive methods (retrievals of sun-induced fluorescence). In general, active methods are applied at leaf level, and passive methods are typically used at the canopy level and beyond.

In one of the active instruments, pulse amplitude-modulated fluorescence (PAM) fluorometers, a weak and pulsed measuring light is used to excite fluorescence. In PAM fluorometers, the fluorescence signal measured shortly before or after an active pulse is subtracted from the fluorescence signal measured during the active pulse. In this process, virtually all non-PAM fluorescence signal is eliminated from the measurement. By using a number of assumptions, and additionally performing PAM measurements on dark-acclimated leaves, a number of parameters can be obtained using PAM fluorometry, e.g., quantum yield of photochemistry in PSII, electron transport rate, the maximum quantum yield of photochemistry, regulated non-photochemical quenching or photochemical quenching. While they need to be handled with careful consideration, PAM fluorometers can be an effective tool for tracking the photoacclimation of photosynthesis (Porcar-Castell et al., 2014).

With passive methods, it is possible to measure chl *a* fluorescence that originates from excitation by sunlight photons. Sun-induced fluorescence can be measured passively from a leaf-scale to satellite remote sensing. In principle, passive techniques use retrievals based on observations of filling-in of the Fraunhofer lines by chl *a* fluorescence. Changes in the fractional depths of Fraunhofer lines at several wavelengths are used to compute sun-induced fluorescence. In contrast to PAM methods, where the light source is known, here the adequate qualification of incident radiance is needed. Additionally, atmospheric absorption and scattering need to be accounted for. Physiological interpretation of the fluorescence signal depends also on the spectral window chosen (Porcar-Castell et al., 2014).

Remote sensing of terrestrial chlorophyll *a* fluorescence with hyperspectral instruments

Remote sensing of terrestrial chl *a* fluorescence has been investigated in several studies, by use of ground-based, airborne and spaceborne platforms (Meroni et al. 2009, and references therein; Frankenberg et al. (2011b); Joiner et al. (2011); Guanter et al. (2012); Joiner et al. (2013)). For the last few years, chl *a* fluorescence received a lot of attention and has been extensively studied. The development of techniques applied to spaceborne instruments until now is briefly presented here. Such techniques utilized the filling in of Fraunhofer lines and telluric absorption lines, and hence were applied to hyperspectral instruments.

First global observations of terrestrial chl *a* fluorescence were performed on the data from the Fourier Transform Spectrometer on-board the Japanese Greenhouse Gases Observing Satellite (GOSAT) (Frankenberg et al., 2011b; Joiner et al., 2011; Guanter et al., 2012). GOSAT-FTS has very high spectral resolution (~ 0.025 nm), which enables observations of the in-filling of Fraunhofer lines. The proposed retrievals focus on the use of a strong K line around 770 nm (Joiner et al., 2011), or additional use of a spectral region around 757 nm (Frankenberg et al., 2011b; Joiner et al., 2011), which contains several Fraunhofer lines. These spectral regions are not much affected by atmospheric absorption. These wavelengths are located close to the far-red peak of chl *a* fluorescence emission. While GOSAT-FTS has excellent spectral resolution, it has poor spatial sampling and a relatively high retrieval noise. Therefore, new algorithms have been developed for instruments with better spatial sampling, e.g. GOME-2 (Joiner et al., 2013). The new proposed retrieval extends the data-driven approach of Guanter et al. (2012) to a broader spectral range, which is then also more affected by atmospheric absorption. In such case, interactions of fluorescence signal not only with Fraunhofer lines, but also with telluric absorption lines, need to be taken into consideration within the retrieval.

Chapter 3

Modeling of fluorescence processes

3.1 Principles of radiative transfer

The radiative transfer equation (RTE) governs the behavior of radiance within the medium, which in the case here is the natural water body. RTE expresses conservation of energy written for a collimated beam of radiance transferring through an absorbing, scattering and emitting medium (<http://www.oceanopticsbook.info/>, accessed at 20th May). For convenience, light can be depicted in the form of many beams of photons of various wavelengths passing in all directions through each point of space, and possibly altered underway. A single beam of radiance L , which is propagating in some direction (θ, ϕ) and has a wavelength λ is illustrated in (Fig. 3.1). The following six processes, which are affecting it, and need to be considered in RTE, are (Mobley, 1994):

1. loss of photons from the beam through annihilation of photons and conversion of radiant energy to nonradiant energy (absorption),
2. loss of photons from the beam through scattering to other directions without change in wavelength (elastic scattering),

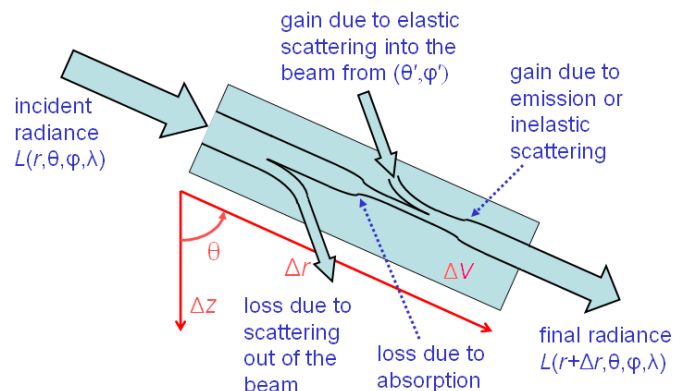


Figure 3.1: Illustration of a single beam of radiance and the processes that affect it as it propagates a distance Δr . Source: <http://www.oceanopticsbook.info>.

3. loss of photons from the beam through scattering with change in wavelength (inelastic scattering),
4. gain of photons by the beam through scattering from other directions without change in wavelength (elastic scattering),
5. gain of photons by the beam through scattering with a change in wavelength (inelastic scattering),
6. gain of photons by the beam through creation of photons by conversion of nonradiant energy into radiant energy (emission).

These six processes that change the radiance as the beam travels a short distance Δr in passing through a small volume ΔV of water (represented by the blue rectangle of Fig. 3.1), are quantitatively formulated below (Mobley, 1994).

Processes 1 and 3. The change in radiance L , while traveling distance Δr , due to absorption can be assumed to be proportional to the incident radiance, which can be expressed as:

$$\frac{L(r + \Delta r, \theta, \phi, \lambda) - L(r, \theta, \phi, \lambda)}{\Delta r} = \frac{\Delta L(r + \Delta r, \theta, \phi, \lambda)}{\Delta r} = -a(r, \lambda)L(r, \theta, \phi, \lambda) . \quad (3.1)$$

Here $\Delta L(r + \Delta r, \theta, \phi, \lambda)$ denotes the change in L between r and $r + \Delta r$. The proportionality constant $a(r, \lambda)$ in Eq. 3.1 is the absorption coefficient. Absorption at the wavelength λ of interest accounts for both energy converted to non-radiant form ("true" absorption) and for energy that is redistributed from wavelength λ to a different wavelength (inelastic scattering). Either process leads to a loss of energy from the beam at wavelength λ (Mobley, 1994).

Process 2. Analogously, the loss of radiance due to elastic scattering can be written as:

$$\frac{\Delta L(r + \Delta r, \theta, \phi, \lambda)}{\Delta r} = -b(r, \lambda)L(r, \theta, \phi, \lambda) , \quad (3.2)$$

where $b(r, \lambda)$ is the scattering coefficient.

Process 4. Ambient radiance may be scattered from other directions into the beam direction (θ, ϕ) (Fig. 3.2). The scattering along Δr from direction (θ', ϕ') into the direction (θ, ϕ) corresponds to scattering angle ψ as shown in Fig. 3.2. The contributions from all directions can be integrated as follows:

$$\frac{\Delta L(r + \Delta r, \theta, \phi, \lambda)}{\Delta r} = \int_0^{2\pi} \int_0^\pi L(\theta', \phi', \lambda)\beta(\theta', \phi' \rightarrow \theta, \phi; \lambda) \sin(\theta')d\theta'd\phi' , \quad (3.3)$$

where $\beta(\theta', \phi' \rightarrow \theta, \phi; \lambda)$ is the spectral volume scattering function.

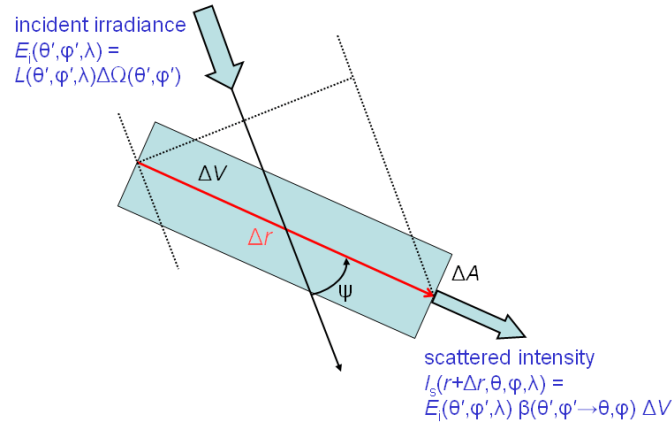


Figure 3.2: Illustration of a beam of radiance in direction (θ', ϕ') generating radiance in the direction of interest (θ, ϕ) by elastic scattering. Source: <http://www.oceanopticsbook.info>

Processes 5 and 6. For simplification, processes 5 and 6, can be included in the RTE as a generic source function S , which represents the creation of radiance by any inelastic scattering or emission process, without specifying the mathematical form of S :

$$\frac{\Delta L(r + \Delta r, \theta, \phi, \lambda)}{\Delta r} = S(r, \theta, \phi, \lambda). \quad (3.4)$$

Each process, e.g., Raman scattering or fluorescence, requires a separate mathematical formulation to specify S , which for fluorescence processes will be discussed further in this chapter.

In summary, changes in radiance with distance along a given beam direction can be related to the optical properties of the medium and the ambient radiance in other direction. This relationship can be expressed as the net change in radiance due to all six mentioned radiative processes. By taking Δr as infinitesimally small ($\Delta r \rightarrow \delta r$), it can be expressed as:

$$\begin{aligned} \frac{dL(r, \theta, \phi, \lambda)}{dr} = & - [a(r, \lambda) + b(r, \lambda)]L(r, \theta, \phi, \lambda) \\ & + \int_0^{2\pi} \int_0^\pi L(r, \theta', \phi', \lambda)\beta(r; \theta', \phi' \rightarrow \theta, \phi; \lambda) \sin \theta' d\theta' d\phi' + S(r, \theta, \phi, \lambda). \end{aligned} \quad (3.5)$$

In oceanography, a coordinate system with the depth z being normal to the mean sea surface and positive downward is often used. Changes in r are related to changes in z as $dr = dz/\cos\theta$ (see Fig. 3.1). Assuming that the ocean is horizontally homogeneous, one obtains:

$$\begin{aligned} \cos \theta \frac{dL(z, \theta, \phi, \lambda)}{dz} = & - [a(z, \lambda) + b(z, \lambda)]L(z, \theta, \phi, \lambda) \\ & + \int_0^{2\pi} \int_0^\pi L(z, \theta', \phi', \lambda)\beta(z; \theta', \phi' \rightarrow \theta, \phi; \lambda) \sin \theta' d\theta' d\phi' + S(z, \theta, \phi, \lambda). \end{aligned} \quad (3.6)$$

3.2 The SCIATRAN radiative transfer model

The ocean-atmosphere coupled radiative transfer model SCIATRAN was used within the scope of this work (Rozanov et al., 2014). SCIATRAN was developed at the University of Bremen to analyze measurements performed by the hyperspectral instrument SCIAMACHY onboard ENVISAT.

SCIATRAN is a comprehensive software package for the modeling of radiative transfer processes in the atmosphere and ocean in the spectral range from the ultraviolet to the thermal infrared (0.18–40 μm) including multiple scattering processes, polarization, thermal emission and ocean–atmosphere coupling. The software is capable of modeling spectral and angular distributions of the intensity or the Stokes vector (describing the polarization) of the transmitted, scattered, reflected, and emitted radiation assuming either a plane-parallel or a spherical atmosphere. Simulations are done either in scalar or in vector mode (i.e. accounting for the polarization) for observations from multiple platforms and in various viewing geometries (e.g. nadir, limb, occultation). All significant radiative transfer processes are included. These are, e.g. Rayleigh scattering, scattering by aerosol and cloud particles, absorption by gaseous components, absorption of chl and CDOM in water, inelastic processes of Raman scattering and fluorescence, bidirectional reflection by an under-lying surface including Fresnel reflection from a flat or roughened ocean surface. The software package contains an extensive database, and a specific module for solving inverse problems (Rozanov et al., 2014).

The SCIATRAN software package along with a detailed User’s Guide is freely available for non-commercial use via the webpage of the Institute of Environmental Physics, University of Bremen at <http://www.iup.physik.uni-bremen.de/sciatran>.

3.3 Fluorescence in natural waters modeled by the ocean-atmosphere coupled radiative transfer model SCIATRAN

The implementation of inelastic processes (such as vibrational Raman scattering, VRS, and chl *a* fluorescence) was performed in SCIATRAN following Haltrin & Kattawar (1993). The verification of VRS implementation was achieved by comparing the calculated VRS reference spectra with model data (Kattawar & Xu, 1992), as well as with VRS spectra, obtained from hyperspectral ship-borne measurements of the solar radiation reflected from the ocean surface (Peters et al., 2014). The accuracy of the implementation of chl *a* or CDOM fluorescence has not been verified by a dedicated study, but the method is similar to that used for VRS and gives very good results.

Fluorescence is an additional component in the RTE equation, and can be expressed as the source function S of fluorescent process F (Eq. 3.4 and 3.5), which is called hereafter

S_F . The source term S_F can be expressed as (Mobley, 1994):

$$S_F(z, \theta, \phi, \lambda) = \int_0^\infty \int_0^{2\pi} \int_0^\pi L(z, \theta', \phi', \lambda) \beta_F(z; \theta', \phi' \rightarrow \theta, \phi; \lambda' \rightarrow \lambda) \sin \theta' d\theta' d\phi' d\lambda', \quad (3.7)$$

where $\beta_F(z; \theta', \phi' \rightarrow \theta, \phi; \lambda' \rightarrow \lambda)$ is the spectral volume inelastic scattering function of the fluorescence process F ; and λ' and λ are an excitation and emission wavelength respectively.

Function $\beta_F(z; \theta', \phi' \rightarrow \theta, \phi; \lambda' \rightarrow \lambda)$ was implemented following Mobley (1994):

$$\beta_F(z; \theta', \phi' \rightarrow \theta, \phi; \lambda' \rightarrow \lambda) = a_F(z; \lambda') R_F(\lambda' \rightarrow \lambda) \tilde{\beta}_F(\theta', \phi' \rightarrow \theta, \phi) \quad [m^{-1} sr^{-1} nm^{-1}], \quad (3.8)$$

where $a_F(z; \lambda')$ is an absorption coefficient of a fluorescent substance at the depth z and wavelength λ' , usually expressed as a product of a specific absorption coefficient of a fluorescent substance $a_F^*(\lambda')$ and concentration of that substance $C_F(z)$. $R_F(\lambda' \rightarrow \lambda)$ is a wavelength redistribution function which describes the energy transport out of excitation wavelength λ' to emission wavelength λ . $\tilde{\beta}_F(\theta', \phi' \rightarrow \theta, \phi)$ is a phase function and is assumed to be isotropic for both CDOM and chl a fluorescence (Mobley, 1994).

3.3.1 Modeling of CDOM fluorescence

The CDOM fluorescence was implemented into the SCIATRAN radiative transfer model on the base of two different approaches as described below.

CDOM as mixture of humic and fulvic acids

Hawes (1992) assumed that fulvic and humic acids comprise the sum of total CDOM (although it contains also amino acid-like components, see Section 2.2.1). Hawes (1992) isolated humic and fulvic acids from several samples and measured their absorption and fluorescence properties. Specific absorption coefficient of CDOM, $a_{\text{CDOM}}^*(\lambda')$, and spectral fluorescence quantum efficiency functions $\eta_{\text{CDOM}}(\lambda' \rightarrow \lambda)$ were parameterized into mathematical functions with linear regression, in order to be used afterwards in optical models. Hawes (1992) calculated $\eta_{\text{CDOM}}(\lambda' \rightarrow \lambda)$ (units of numbers of photons), from which $R_{\text{CDOM}}(\lambda' \rightarrow \lambda)$ (units of energy) was obtained, following Mobley (1994):

$$R_{\text{CDOM}}(\lambda' \rightarrow \lambda) = \eta(\lambda' \rightarrow \lambda) \frac{\lambda'}{\lambda} \quad [nm^{-1}]. \quad (3.9)$$

For the purpose of this study, absorption and fluorescence parameters of samples numbered FA7 (of fulvic acids) and HA6 (of humic acids) from Hawes (1992) were used (of a total of four fulvic acid and seven humic acid samples, for which $\eta_{\text{CDOM}}(\lambda' \rightarrow \lambda)$ was determined by Hawes 1992). Specific absorption spectra and fluorescence quantum efficiency functions for components FA7 and HA6 are shown in Fig. 3.3.

3. MODELING OF FLUORESCENCE PROCESSES

CDOM abundance is typically quantified by its absorption coefficient at a given wavelength (e.g. 443 nm, see Section 2.2.1). For most of the ocean, $a_{CDOM}(443 \text{ nm})$ is below 0.1 m^{-1} (Morel & Gentili, 2009), but can be much higher for coastal waters. In European coastal waters $a_{CDOM}(443 \text{ nm})$ ranges approximately between 0.01 and 1 m^{-1} (Babin, 2003). In case of the data used here, 1 g m^{-3} of fulvic or humic acids corresponds to $a_{CDOM}(443 \text{ nm})$ of 0.075 m^{-1} for FA7 and 0.011 m^{-1} for HA6.

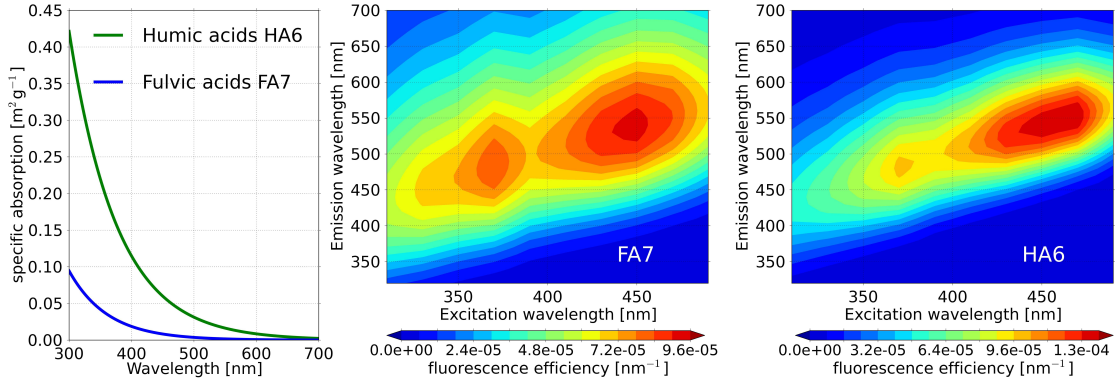


Figure 3.3: Specific absorption spectra and fluorescence quantum efficiency functions for samples numbered FA7 (of fulvic acids) and HA6 (of humic acids). Redrawn from Hawes (1992).

Excitation-emission matrices and PARAFAC approach

A PARAFAC (PARALLEL FACTOR analysis) model was used in the second approach of implementing CDOM fluorescence into SCIATRAN. Nowadays, PARAFAC is widely applied to EEMs and enables qualitative and quantitative characterization of CDOM samples (Ishii & Boyer, 2012).

The PARAFAC model is similar to PCA (principal component analysis), but decomposes the data matrix into a set of trilinear terms and a residual array as follows:

$$x_{ijk} = \sum_{n=1}^N b_{in}c_{jn}d_{kn} + \varepsilon_{ijk}, \quad (3.10)$$

$$i = 1, \dots, I; j = 1, \dots, J; k = 1, \dots, K$$

According to Stedmon et al. (2003), when applying the PARAFAC model to EEMs, x_{ijk} is the intensity of fluorescence for the i th sample at emission wavelength j and excitation wavelength k ; b_{in} is directly proportional to the concentration of the n th component in sample i ; c_{jn} is linearly related to the fluorescence quantum efficiency of the n th component at emission wavelength j , d_{kn} is linearly proportional to the specific absorption coefficient at excitation wavelength k . N defines the number of components in the model, and a residual ε_{ijk} represents the variability, which is not accounted for by the model. The parameters of the PARAFAC model are found by the least-square minimization.

For this study, the PARAFAC data from Jørgensen et al. (2011) were used. Jørgensen et al.

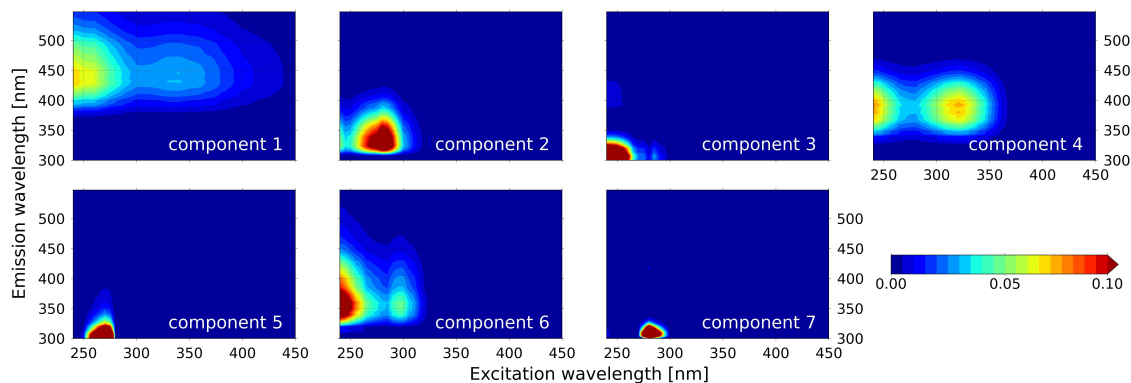


Figure 3.4: Fluorescence characteristics of the seven components identified by the PARAFAC analysis and included into radiative transport model SCIATRAN. Redrawn from Jørgensen et al. (2011)

(2011) conducted a broad analysis of CDOM fluorescence samples collected worldwide and identified seven components with the PARAFAC model, with use of split half analysis for validation (introduction to the PARAFAC technique and description of its application to CDOM fluorescence are presented in more detail in Stedmon & Bro 2008). Jørgensen et al. (2011) characterized these components by comparing their spectral characteristics to components identified in earlier studies as well as pure fluorophores (fluorescent chemical compounds). Spectral characteristics (product of matrices \mathbf{c} and \mathbf{d}) of seven PARAFAC components are shown in Fig. 3.4. Jørgensen et al. (2011) identified components 1 and 4 as humic-like FDOM. Components 2, 3, 5 and 7 were characterized as amino acid-like FDOM, which had spectral similarity to phenylalanine, tryptophan and tyrosine. Component 6 had characteristics similar to both humic- and amino acid-like groups.

Since, it is not known, in principle, what the fluorescent components exactly are, the molar absorbance, quantum efficiency and concentration cannot be calculated explicitly. Hence, the terms of the PARAFAC model are only proportional to the molar absorbance, quantum efficiency and concentration. As the optical properties of CDOM vary spatially and temporally, the matrices were scaled in order to obtain values that are realistic and comparable to the first approach that was used for CDOM modeling. Although the applied scaling is not explicitly correct, it is sufficient for the feasibility study of CDOM fluorescence modeling and retrieval, as presented here. Fluorescence quantum yields of CDOM were previously reported to range from 0.005 up to 0.025 (Green & Blough, 1994). The values obtained by Hawes (1992), used in the first approach of modeling CDOM fluorescence, vary within these limits (0.009 to 0.019). In order to obtain fluorescence yields of the same order for the PARAFAC components, matrix \mathbf{c} was scaled by a factor of 0.001, after which the fluorescence yields varied between 0.009 and 0.024.

The absorption of the PARAFAC components is calculated as a product of matrices \mathbf{b} and \mathbf{d} . These matrices were scaled so that the absorption obtained was similar to the first modeling approach. In case of humic and fulvic acids, their concentrations were set to 1 g m^{-3} and 10 g m^{-3} , and the sum of 1 g m^{-3} of fulvic and 1 g m^{-3} of humic acids lead to the absorption of 0.086 m^{-1} at 443 nm. To be consistent, the product of matrices was scaled so that the final absorption of all components at 443 nm would be similar. In fact,

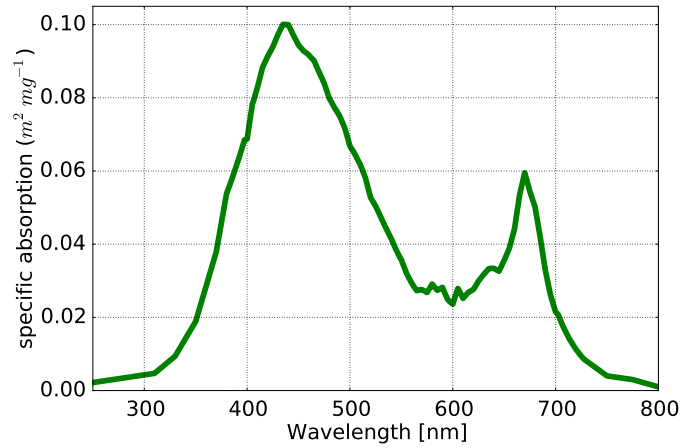


Figure 3.5: The chl *a*-specific phytoplankton absorption coefficient, as used in this study. Source of data: Prieur & Sathyendranath (1981); Haltrin (2006).

it is only component 1 of PARAFAC model that absorbs at this wavelength region, and after scaling was applied its absorption equaled 0.088 m^{-1} at 445 nm. The scaled matrices were used to calculate $R_{CDOM}(\lambda' \rightarrow \lambda)$, with which the form of spectral volume inelastic scattering function $\beta_{CDOM}(z; \theta', \phi' \rightarrow \theta, \phi; \lambda' \rightarrow \lambda)$ was derived (Eq. 3.8). It is important to bear in mind, that matrices could only be scaled to the values similar to the previous approach, but their correct values remain unknown.

3.3.2 Modeling of marine chl *a* fluorescence

The chl *a*-specific phytoplankton absorption coefficient used in the calculations (Prieur & Sathyendranath, 1981; Haltrin, 2006) is shown in Fig. 3.5. The wavelength redistribution function for chl *a* fluorescence $R_{chl}(\lambda' \rightarrow \lambda)$, was calculated analogously to CDOM fluorescence according to Eq. 3.9, from spectral fluorescence quantum efficiency function for chl *a* fluorescence $\eta_{chl}(\lambda' \rightarrow \lambda)$, which here is described as:

$$\eta_{chl}(\lambda' \rightarrow \lambda) = \Phi_{chl}(\lambda') f_{chl}^{ex}(\lambda') f_{chl}^{em}(\lambda) \quad [nm^{-1}], \quad (3.11)$$

where $\Phi_{chl}(\lambda')$ is a quantum efficiency (or quantum yield) of chl *a* fluorescence, which is defined by

$$\Phi_{chl}(\lambda') = \frac{\text{the number of photons emitted at all wavelengths } \lambda}{\text{the number of photons absorbed at } \lambda'}. \quad (3.12)$$

The chl *a* fluorescence excitation function $f_{chl}^{ex}(\lambda')$ is defined as a unitless function that specifies the interval over which light is able to excite chl *a* fluorescence, and $f_{chl}^{em}(\lambda)$ as the chl *a* fluorescence wavelength emission function.

For chl *a* a fluorescence of marine phytoplankton, $\Phi_{chl}(\lambda')$ ranges from less than 0.01 to 0.10, with 0.01 to 0.05 being typical (Mobley, 1994). $\Phi_{chl}(\lambda')$ depends in a complicated manner on a number of parameters, which include phytoplankton species and physiological

state, as well as environmental conditions such as the ambient irradiance, availability of nutrients, or the presence of toxic pollutants (see Section 2.2.2 and 2.2.3). In the case of simulations performed in this study, $\Phi_{chl}(\lambda')$ was assumed to be 0.02, which is within the range of the typical yield.

The chl *a* fluorescence excitation function, $f_{chl}^{ex}(\lambda')$ was implemented in Mobley (1994) as:

$$f_{chl}^{ex}(\lambda') = \begin{cases} 1, & \text{if } 370 \leq \lambda' \leq 690 \text{ nm}, \\ 0, & \text{elsewhere.} \end{cases} \quad (3.13)$$

The emission function $f_{chl}^{em}(\lambda)$ was modeled by a Gaussian (Mobley, 1994):

$$f_{chl}^{em}(\lambda) = \frac{1}{\sqrt{2\pi}\sigma_1} \exp\left[-\frac{(\lambda - \lambda_1^0)^2}{2\sigma_1^2}\right], \quad (3.14)$$

where $\lambda_1^0 = 685$ nm is the wavelength of maximum emission and $\sigma_1 = 10.6$ nm is the standard deviation of the Gaussian, which corresponds to a value of 25 nm for the full width at half maximum of the emission band.

3.4 Terrestrial fluorescence in SCIATRAN

Terrestrial vegetation fluorescence can be included in the SCIATRAN model in the form of a known emission spectrum, which is considered in the model as an emission source located at the lower boundary level. It is assumed that the fluorescence emission is unpolarized and isotropic (uniform in all orientations).

Top of canopy fluorescence spectra can vary significantly, depending on the light conditions, vegetation type, canopy structure, pigment composition, soil type, etc. Following Joiner et al. (2011, 2012), fluorescence emission was assumed to be spectrally constant within the narrow windows (of few nanometers) that were used in the retrievals developed in this study. Since the shape of filling-in structures within such narrow windows are mostly driven by the depth and width of Fraunhofer lines, such approach expected to have no influence on the retrieval.

Chapter 4

Development of satellite retrievals of fluorescence and chlorophyll proxy

4.1 Overall retrieval approach

4.1.1 Retrieval technique: DOAS

In order to retrieve the fluorescence signal from high spectrally resolved satellite data, a modified approach, based on the Differential Optical Absorption Spectroscopy (DOAS) technique (Perner & Platt, 1979) was used. DOAS was originally developed for active long path remote sensing (Perner & Platt, 1979), but was subsequently extended to passive remote sensing ground-based observations (e.g., Eisinger et al., 1997). The DOAS retrieval approach utilizes the separation of high frequency from low frequency spectral features in wavelength space. Variants of this approach have been applied for several years for remote sensing of atmospheric trace gases (e.g., Burrows et al., 1999; Richter et al., 2005), and has been lately extended to the aquatic domain as PhytoDOAS (Vountas et al., 2007, Bracher et al., 2009, Sadeghi et al., 2012). A theoretical consideration of the relationships between different DOAS algorithms is given by Rozanov & Rozanov (2010). The family of DOAS algorithms exploit the fingerprint spectral features in backscattered solar radiance spectra that are caused by i) molecular absorption by atmospheric constituents (e.g., Richter et al., 2005), ii) spectral re-distribution features that are induced by inelastic processes in the atmosphere and ocean and fill in the solar Fraunhofer lines (e.g., Vountas et al., 1998; Vasilkov, 2002; Vountas et al., 2007; Dinter et al., 2015), iii) absorption features from terrestrial plants and marine phytoplankton (e.g., Wagner et al., 2007; Bracher et al., 2009; Sadeghi et al., 2012).

Inelastic processes (Raman scattering, Brillouin scattering and fluorescence) lead to a redistribution of solar backscattered electromagnetic radiation, and shift of the frequency toward higher or lower energies. Inelastic scattering by molecules in the air (mostly N_2 and O_2) is called rotational Raman scattering (RRS). In lakes, rivers and oceans there are two

dominant inelastic processes: vibrational Raman scattering (VRS) by water molecules, and fluorescence (of phytoplankton pigments, mainly chl *a*, and CDOM). The effect of those processes on the backscattered radiation at the top of atmosphere is possibly identified in the filling-in of Fraunhofer lines (spectrally narrow and often saturated absorption features in the solar spectrum), known as the Ring effect after its discoverer James Ring (Grainger & Ring, 1962). The spectral shift due to Brillouin scattering, which also may fill in Fraunhofer lines, is typically smaller than the spectral resolution of the hyperspectral instruments such as SCIAMACHY and GOME-2, and is not considered further here. The discussion of the impact of Brillouin scattering on the spectral structure of the radiation reflected from the ocean surface can be found in Peters et al. (2014).

The DOAS method determines the amount of molecular absorbers along the effective optical light path by fitting and scaling spectra within a given wavelength window. The broad-band effects (e.g., Rayleigh and Mie scattering) are removed by a low-degree polynomial that is also fitted. The fitting in the DOAS method is formalized as a least-squares minimization and is described by the following equation:

$$\left\| \tau(\lambda) - \sum_{i=1}^N \sigma_i(\lambda) S_i - \sigma_R(\lambda) S_R - \sigma_V(\lambda) S_V - \sigma_f(\lambda) S_f - \sigma_p(\lambda) S_p - \sum_{k=0}^K a_k \lambda^k \right\|^2 \rightarrow \min. \quad (4.1)$$

Here, $\tau(\lambda) = -\ln \frac{I(\lambda)}{I_0(\lambda)}$ is the so-called slant optical density, $I(\lambda)$ and $I_0(\lambda)$ are the measured backscattered radiance and extraterrestrial irradiance, respectively, $\sigma_i(\lambda)$ is the absorption cross-section of the i th atmospheric absorber, N is the number of absorber, $\sigma_p(\lambda)$ is a specific phytoplankton absorption spectrum, $\sigma_R(\lambda)$, $\sigma_V(\lambda)$, and $\sigma_f(\lambda)$ are reference spectra of RRS, VRS and chl *a* fluorescence, respectively, $\sum_{k=0}^K a_k \lambda^k$ is the low order polynomial, typically of the order $K \leq 4$. The ratio of $I(\lambda)$ and $I_0(\lambda)$ is taken in order to make the retrieval less sensitive to absolute radiometric calibration.

The minimization is carried out with S_i , S_R , S_V , S_f , S_p and polynomial coefficients as the fitted parameters. The parameter S_i is the integrated number density of the i th atmospheric absorber along the slant optical path, which is generally related to the concentration of a given absorber, while the parameter S_p is generally related to the chl *a* concentration. S_R , S_V , and S_f parameters are called scaling or fit factors and carry information about the strength of the corresponding inelastic process. The method can be applied to SCIAMACHY and GOME-2 data or data sets of similar instruments, which take measurements of both extraterrestrial radiation, $I_0(\lambda)$, as well as backscattered radiation, $I(\lambda)$, with sufficient spectral resolution.

4.1.2 Reference spectra

In order to perform the retrievals with the DOAS method, adequate reference spectra have to be determined for use as *a priori* information. Because the effect of inelastic processes on the top of atmosphere radiation can be modeled, the reference spectra for fluorescence

processes were calculated, following Vountas et al. (2003), as:

$$\sigma_j(\lambda) = \ln \frac{I^+(\lambda)}{I^-(\lambda)}, \quad j = R, V, f, \quad (4.2)$$

where $I^+(\lambda)$ and $I^-(\lambda)$ are the modeled radiances at the top of atmosphere accounting for the j th inelastic process and neglecting all other inelastic processes, respectively.

The radiances $I^+(\lambda)$ and $I^-(\lambda)$ have been calculated using the coupled ocean-atmosphere radiative transfer model SCIATRAN (Rozaanov et al., 2014; Blum et al., 2012). The details of the solution and the verification of the radiative transfer equation, including the rotational Raman scattering in the atmosphere, can be found in Vountas et al. (1998) and Rozaanov & Vountas (2014).

All reference spectra were determined using average conditions, namely the pressure, temperature, and water vapor profiles were set to default in the model for April and a latitude of 45° , according to a climatological data base obtained using a 2D chemical transport model developed at the University of Bremen (Sinnhuber et al., 2009).

Reference spectra for all components (described in Eq. 4.1) involved in the DOAS fitting process were pre-calculated with high spectral resolution (0.01 nm). To account for the different spectral resolution of the instruments, the simulated spectra needed to be convolved with the appropriate slit function. A Gaussian type slit function was used, of which the full width at half maximum (FWHM) parameter was optimized with respect to the chi-square errors (χ^2) for each retrieval for a sample dataset (odd days of January 2009). The process was done for each instrument separately (SCIAMACHY, GOME-2). Additionally, the simulated data of top of atmosphere radiances, that were used for development of the retrievals, were also convolved with a Gaussian type slit functions, with appropriate FWHM corresponding to each instrument.

4.1.3 Hyperspectral satellite data

SCIAMACHY

SCIAMACHY (Scanning Imaging Absorption Spectrometer for Atmospheric Chartography) is a grating spectrometer measuring transmitted, reflected and scattered sunlight in three different viewing geometries: nadir, limb, and both solar and lunar occultations (Burrows et al., 1995; Bovensmann et al., 1999). In addition, it measures solar irradiance. SCIAMACHY performs measurements of the upwelling radiation at the top of the atmosphere in nadir and in limb viewing geometries from 214 to 2380 nm in eight spectral channels, continuously from 214 to 1750 nm at relatively high resolution (0.2 nm to 1.5 nm). The channels with high spectral resolution have a variable ground scene footprint, which is typically 30 km x 60 km, but varies for different clusters. The instrument was launched in February 2002 on board the ENVISAT satellite into a sunsynchronous orbit in descending node having a 10:00 am equator crossing time. ENVISAT was in operation until April 2012 when ESA unexpectedly lost contact. Each nadir measurement is followed by a limb measurement, which leads to intermittent nadir scans along-track. The swath

width for both measurement cycles is 960 km. SCIAMACHY's primary objective was to measure trace gases in the atmosphere; however, part of the detected radiation is influenced by absorption and scattering from the surface layer of the ocean or land. This characteristic was already used to estimate vibrational Raman scattering by water (e.g., Vountas et al., 2007) and identify different phytoplankton groups (e.g., Bracher et al., 2009).

GOME-2

GOME-2 are a series of three identical instruments operating from polar orbiting meteorological satellites MetOps (Callies et al., 2000; Munro et al., 2006). The data used here are from the first GOME-2 instrument, which was launched in October 2006 onboard Metop-A, which flies in a sun-synchronous orbit having an equator crossing time of 9:30 a.m. It measures the Earth's backscattered radiance and the solar irradiance at wavelengths between 232 nm and 793 nm. In comparison to SCIAMACHY, GOME-2 has a larger footprint (40 km x 80 km) and a large nominal scan swath width (1920 km), though approximately once a month a narrow swath mode (320 km) is used. GOME-2 has a near daily global coverage whereas SCIAMACHY, with its alternating limb and nadir viewing geometry coupled with a swath width of 960 km, achieves global coverage in only six days at the equator. Moreover, as the second GOME-2 onboard Metop-B was launched in September 2012, from July 2013 onwards the Metop-B/GOME-2 instrument replaced the Metop-A/GOME-2 in a default swath mode, and Metop-A/GOME-2 is now in a reduced swath mode, which means that the swath is reduced to 960 km and pixel size is 40 x 40 km. The third satellite, Metop-C, is scheduled for launch at the end of 2017.

Future missions

The retrieval methods presented here are generic, and in future can be applied to other hyperspectral instruments with similar (or better) spectral and radiometric performance. New space missions will provide better spatial, temporal and spectral resolution and hence better coverage of hyperspectral data, on which fluorescence retrievals can be performed.

Orbiting Carbon Observatory-2 (OCO-2), was successfully launched in July 2014. Like other hyperspectral missions, its primary purpose is to investigate atmospheric chemistry (mainly CO₂), but its spectral resolution allows retrieving chl *a* fluorescence near wavelengths 750 nm (Frankenberg et al., 2014).

Upcoming ESA Sentinel missions, under the Copernicus Programme, will also provide better coverage and continuity of previous hyperspectral spectrometers. TROPOMI, on-board Sentinel 5P, planned for launch early 2016, and future Ultraviolet Visible Near-infrared (UVN) spectrometer on-board Sentinel 5 planned for launch in 2020 will have spatial resolution of 7 km x 7 km, and the UVN spectrometer on geostationary Sentinel 4 mission, planned for launch in 2020, will have 10 km x 10 km spatial resolution.

GOSAT, the instrument, from which chl *a* fluorescence was retrieved for the first time in 2011 (Joiner et al., 2011; Frankenberg et al., 2011b), is planned to have its successor

GOSAT-2. GOSAT-2 is planned for launch in 2018 and will provide further opportunity to estimate chl *a* fluorescence.

Besides hyperspectral spectrometers, primarily designed to monitor atmospheric chemistry, the FLEX mission (Moreno et al., 2006) is specially designed to map chl *a* fluorescence at high spatial and temporal resolution. FLEX is now in competition with CarbonSat (Bovensmann et al., 2010) in the latest stage of evaluation for ESA's Earth Explorer 8 mission. CarbonSat, the other candidate aimed at observations of CO₂ and CH₄, is a hyperspectral instrument that would also enable measurements of the far-red peak of chl *a* fluorescence (Buchwitz et al., 2013). Such combined and simultaneous CarbonSat measurements of CO₂, hence possibly of CO₂ uptake, and chl *a* fluorescence could further improve the knowledge on productivity of different ecosystems and their role in the carbon cycle. The final decision on Earth Explorer 8 mission is expected to be announced by ESA by the end of year 2015.

4.2 Retrieval of CDOM fluorescence

4.2.1 Reference spectra of CDOM fluorescence

Reference spectra for fulvic and humic acids (according to Hawes, 1992) and for seven PARAFAC components identified by Jørgensen et al. (2011), were calculated according to Eq. 4.2. The simulated radiances were convolved with a Gaussian type slit function with a FWHM of 0.4 nm.

The spectral characteristics of different CDOM components were investigated, particularly in terms of their possible application in the DOAS satellite retrieval. In particular, the narrow and sharp features resulting from filling-in of Fraunhofer lines were studied. For the investigation of CDOM fluorescence, which was performed in the broad spectral range, concentrations of fulvic and humic acids were set separately to 1 g m⁻³ and 10 g m⁻³ in the 100 m deep water column. For narrow-band modeling in the spectral region of Fraunhofer line H β at 486 nm concentrations of fulvic and humic acids were set simultaneously to 1, 10, 50 and 100 g m⁻³ for four different modeling scenarios.

Reference spectra for fulvic and humic acids and PARAFAC components, calculated according to Eq. 4.2, are presented in Fig. 4.1a, b and c. The noticeable sharp and narrow features correspond to filling-in of Fraunhofer lines or telluric absorption lines. In general, reference spectra of amino acid-like components have much smaller amplitude (up to three orders of magnitude) than the humic-like (Fig. 4.1b). Amino acid-like components exhibit the fluorescence excitation at shorter wavelengths, usually below 300 nm (Jørgensen et al., 2011). Due to this, the fluorescence signal is strong when measured with active techniques, but it is much weaker in natural conditions as there is little electromagnetic radiation reaching the ocean surface in this wavelengths region. One reason is the shape of the solar spectrum, which has its maximum irradiance in longer wavelengths near 500 nm (Fig. 2.7), and is rapidly decreasing towards shorter wavelengths. The second reason is the strong absorption of ozone in the UV region. Humic-like components of CDOM show stronger fluorescence features under natural conditions, as their spectral excitation region

4. DEVELOPMENT OF SATELLITE RETRIEVALS

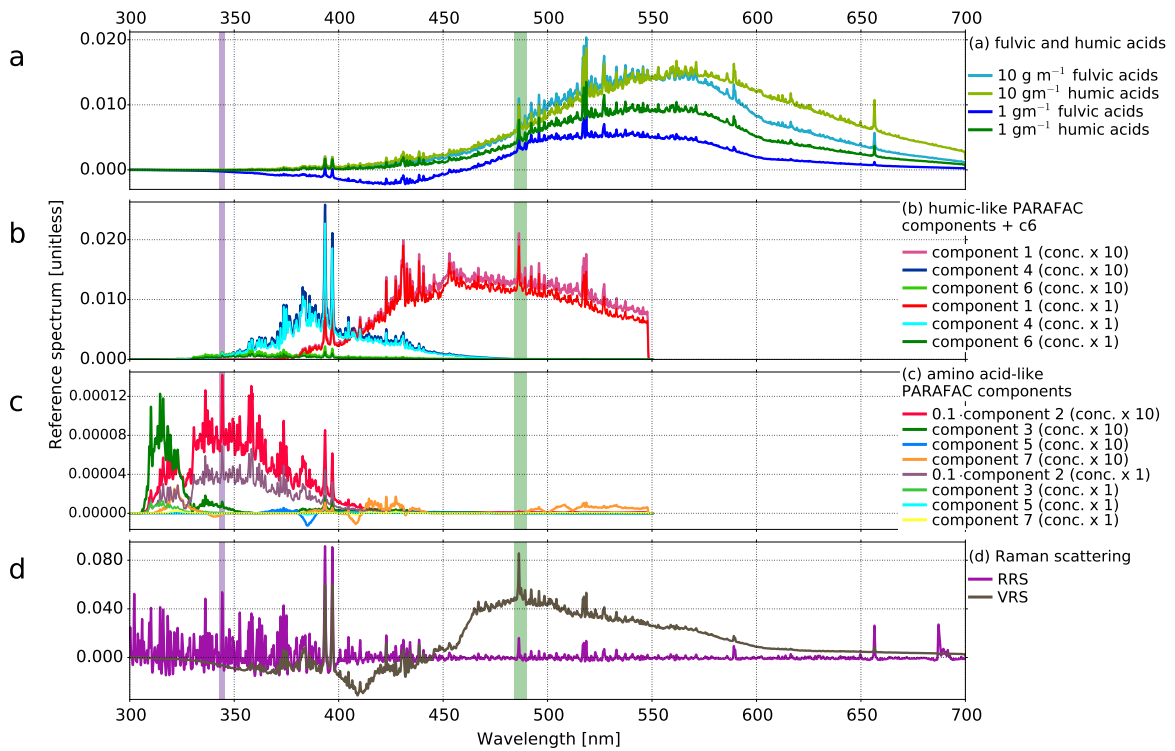


Figure 4.1: Calculated reference spectra for: (a) fulvic and humic acids (Hawes, 1992), (b,c) PARAFAC components (Jørgensen et al., 2011), (d) RRS and VRS. The shaded areas cover the wavelength regions used in the retrievals (fit windows).

is at longer wavelengths, above 300 nm, where more light is available in the water column. Among the amino acid-like PARAFAC components (Fig. 4.1c), fluorescence of component 2 is noticeably stronger than the others at wavelengths above 310 nm. This component was identified by Jørgensen et al. (2011) as tryptophan-like. Components 3 and 7 have very weak fluorescence, and component 5 did not produce any observable fluorescence signal.

The spectral shape of humic-like PARAFAC components differs significantly from the two spectra of humic and fulvic acids obtained using the Hawes (1992) approach (Fig. 4.1a). In case of the latter, their fluorescence emission starts in longer wavelengths and reaches further up to 700 nm, which is not the case for the PARAFAC measurements. This difference can be due to the techniques used by Hawes (1992) to separate and measure humic and fulvic acids absorption and fluorescence. It was shown in previous studies that CDOM extracted with C-18 cartridges (which were used in this case) did not always retain the optical properties of the original water sample (e.g., Vodacek, 1989). This conclusion is supported by the results of Green & Blough (1994), which indicate that this isolation procedure preferentially extracts longer wavelength absorbing and fluorescing material that also exhibits higher quantum yields. However, EEMs from oligotrophic waters might also underestimate absorption and fluorescence at longer wavelengths. According to the performed simulations, a ten fold increase in the concentration of CDOM leads to a much smaller increase in filling-in of Fraunhofer lines. This is true in case of both modeling

approaches.

4.2.2 Spectral windows of the retrieval

Two simple DOAS retrievals were performed, to test applicability of the DOAS method to CDOM fluorescence observations, in the two following wavelength regions:

- 343 - 345.5 nm, around Fe I lines at 344 nm (<400 nm, corresponding to strong amino acid-like fluorescence),
- 484 - 490 nm, H β line at 486 nm (>400 nm, corresponding to strong humic-like fluorescence).

These spectral windows are highlighted in Fig. 4.1, along with the calculated reference spectra. The Fe I and H β Fraunhofer lines are ones of the strongest within the wavelength regions of amino acid-like and humic-like fluorescence emission, respectively. Additionally, Fraunhofer line H β at 486 nm lies close to the CDOM fluorescence maximum reported in previous studies at 490 nm (e.g., Vodacek et al., 1994; Pozdnyakov et al., 2002).

The relative contribution of the inelastic processes to filling in of Fe I and H β Fraunhofer lines, was studied by comparing the reference spectra of CDOM, VRS and RRS (Fig. 4.2). RRS produces especially strong features in the short wavelength region, the region of amino acid-like fluorescence. Amino acid-like fluorescence is generally weak (Fig. 4.1). However, one has to bear in mind that the PARAFAC components were calculated using a scaling (introduced in this study) and hence the obtained estimations might deviate from the correct values. The differential part (after subtracting the polynomial in the spectral region of interest) of the reference spectra, for different inelastic processes is shown in Fig. 4.2. The contributions from all defined components of either approach of CDOM fluorescence modeling (CDOM concentration of 1 g m⁻³ of fulvic and 1 g m⁻³ of humic acids, and corresponding PARAFAC concentrations) were summed up for the presented CDOM spectra. Filling-in of those Fraunhofer lines due to the CDOM fluorescence is relatively weak when compared to filling in resulting from Raman scattering (RRS, VRS for clear water) for both spectral ranges. For the short-wave fluorescence of amino acid-like components (Fe I lines at 344 nm), the strength of RRS is absolutely dominant over all other inelastic processes (Fig. 4.2, left panel).

In case of longer wavelengths (H β at 486 nm), all processes lead to filling-in of the strength of the same order (Fig. 4.2, right panel). The impact of varying concentration of fulvic and humic acids (from none to 100 g m⁻³ each) on the differential reference spectra of CDOM and VRS is investigated in Fig. 4.3. In this wavelength region it is more likely to observe CDOM fluorescence with satellite measurements than in the shorter wavelengths (<400 nm). In clear waters, the VRS signal is dominant, but it weakens with increasing CDOM concentrations (Fig. 4.3 middle panel). In case of CDOM concentration of 1 g m⁻³ fulvic and 1 g m⁻³ humic acids, both CDOM fluorescence and VRS lead to similar filling-in. In case of CDOM being a mixture of 50 g m⁻³ of fulvic and 50 g m⁻³ humic acids, VRS signal is one order of magnitude weaker than CDOM fluorescence,

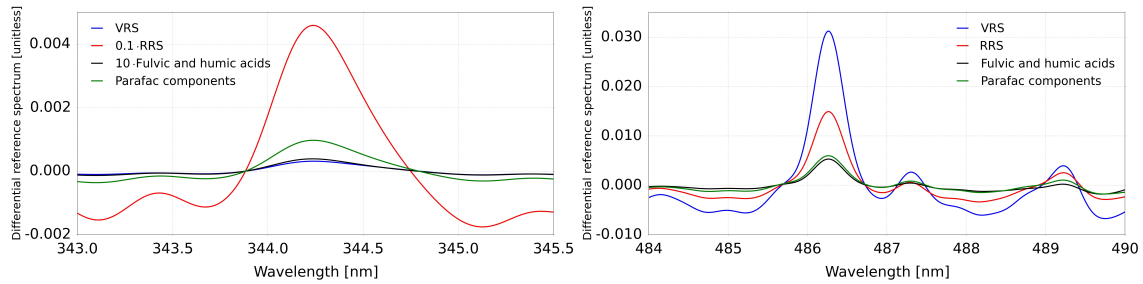


Figure 4.2: The differential part of the reference spectra calculated according to Eq. 4.2 for different inelastic processes in the spectral region of Fraunhofer lines Fe I at 344 nm (left panel) and H β at 486 nm (right panel). The contributions from all defined components of either approach of CDOM fluorescence modeling (CDOM concentration of 1 g m^{-3} of fulvic and 1 g m^{-3} of humic acids, and corresponding PARAFAC concentrations) were summed up for the presented CDOM spectra. VRS spectrum was calculated for clear water. In the left panel, RRS and fulvic and humic acids spectra were scaled for the clarity of the figure.

and for 100 g m^{-3} of fulvic and 100 g m^{-3} of humic acids, the VRS signal is negligible (Fig. 4.3). However, the filling-in due to CDOM fluorescence itself remains almost constant throughout all the scenarios of various CDOM concentrations. This is due to the fact that with increasing CDOM concentration, light is almost completely absorbed stronger within the top surface layers and does not penetrate that deep into the water column. Hence, the bulk CDOM fluorescence signal originates from thinner surface layers of the ocean and is not significantly higher for very large CDOM concentrations.

The results obtained here agree with the previous studies by Pozdnyakov et al. (2002), who showed that VRS is negligible for waters with high CDOM concentrations. Their results also indicate that the CDOM fluorescence signal does not increase substantially with much higher CDOM concentrations, even though it becomes relatively more significant, as in general, the upwelling radiance decreases with increase of CDOM. However, contrary to their results, in this study the VRS in clear water was found to be stronger than CDOM fluorescence in water of high CDOM concentration. These discrepancies might be due to the fact that while here the impact of inelastic process is investigate in terms of the filling-in of Fraunhofer lines at the top of the atmosphere, Pozdnyakov et al. (2002) focused on the water volume reflectance (where atmosphere contribution is corrected for). Furthermore, the coupled ocean-atmosphere radiative transfer model is applied here, while Pozdnyakov et al. (2002) used simple hydro-optical models, and calculated the volume reflectance arising from CDOM fluorescence directly from optical properties of water and CDOM. For scenarios of simultaneous CDOM fluorescence and VRS, the combined filling-in signal is overall getting weaker with increasing CDOM concentration (Fig. 4.3 right panel).

Hence, filling-in signals due to CDOM fluorescence and VRS are coupled: when there is no CDOM, the VRS signal is strongest. On the other hand, when CDOM concentrations are high, VRS signal is very weak and a significant CDOM fluorescence signal can be observed. It follows, that the filling-in can be due either strong CDOM fluorescence or strong VRS. However, VRS has generally higher impact on filling-in of Fraunhofer lines.

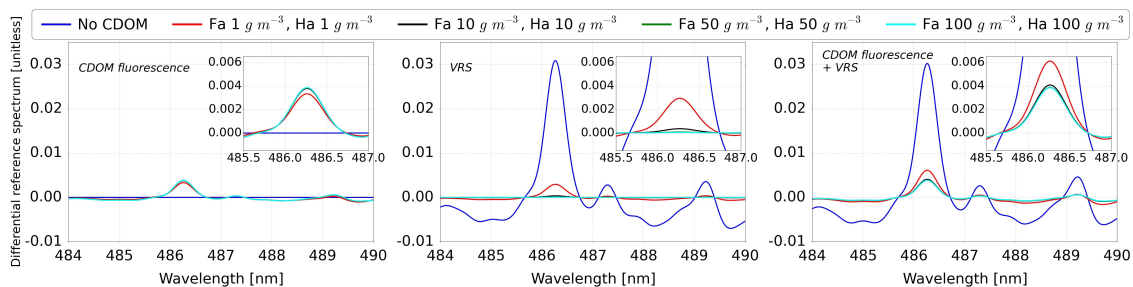


Figure 4.3: The differential part of the reference spectra calculated according to Eq. 4.2 in the spectral region of Fraunhofer line $H\beta$ at 486 nm calculated for different concentrations of humic and fulvic acids (see legend above) and for different inelastic processes: CDOM fluorescence (left panel), VRS (middle panel), CDOM fluorescence and VRS simultaneously (right panel). Here, only fulvic and humic acids approach was applied.

CDOM fluorescence emitted from the ocean surface does not increase with increasing CDOM concentration enough to produce a signal of filling-in, which would be higher than a VRS signal for clear waters. As a result, with increasing CDOM concentration it is expected to observe weakening of filling-in of Fraunhofer lines, due to decreasing light penetration depth, and hence a decreasing VRS signal.

4.3 Retrieval of the red chl *a* fluorescence peak

4.3.1 Reference spectrum of red chl *a* fluorescence and selection of spectral window of retrieval

The DOAS retrieval technique, generally and as implemented in this study, is sensitive to errors resulting from correlations between the reference spectra in the fit, i.e. the fit algorithm will not be able to distinguish between similar spectral features originating from different sources. Unfortunately, all inelastic processes have similar spectral behavior, as they all lead to the filling-in of Fraunhofer lines. Hence, some of the retrieved signal does not originate from fluorescence, but from Raman scattering. As in the wavelength region where chl *a* fluoresces, Raman scattering is not negligible, an optimal selection of the spectral region is essential. Ideally, a window where fluorescence is at its strongest and Raman scattering is relatively weak, is required. The choice of the fitting wavelength region is also limited by strong atmospheric absorption features of O_2 and water vapor. These regions are avoided because they attenuate the solar radiation, and for that matter, the fluorescence. The selection of an optimal spectral fitting window is especially critical for the retrieval performance because the marine fluorescence itself is a very weak signal (Neville & Gower, 1977, Abbott & Letelier, 1999).

The deepest Fraunhofer lines in the chl *a* fluorescence emission region, which lead to the strongest features of filling-in, are $H\alpha$ and Fe I. Although the Fraunhofer $H\alpha$ line at 656 nm is the strongest, it was not used in this work, because it is located in a spectral region of weak fluorescence and where rotational and vibrational Raman scattering is relatively

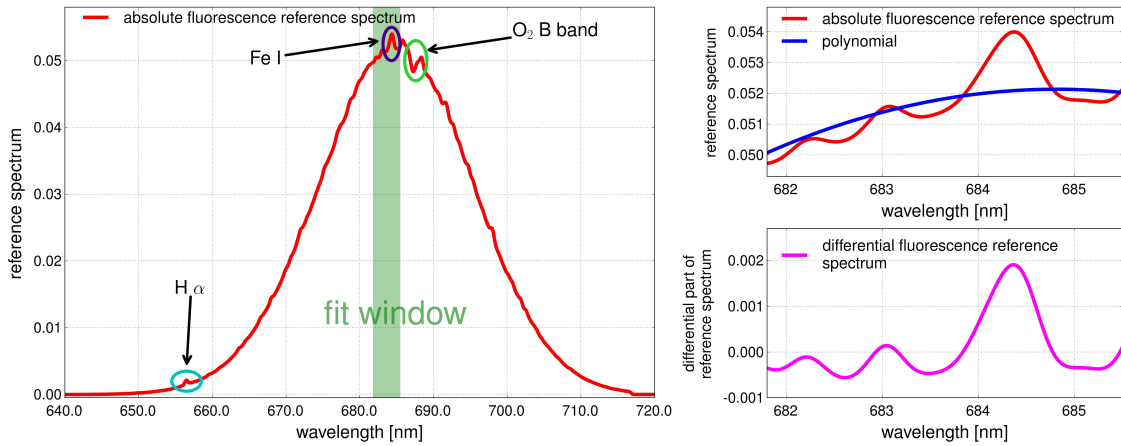


Figure 4.4: Left panel: simulated reference spectrum of chl *a* fluorescence for a concentration 1 mg/m^3 . Locations of the oxygen B band and Fraunhofer lines H α and Fe I are also shown. The green area covers the wavelength region used in the retrieval (fit window) and is shown expanded in the right panel. Right upper panel: polynomial (blue) subtracted from the absolute reference fluorescence spectrum (red). Right lower panel: the fluorescence differential fluorescence spectrum (magenta).

strong. This wavelength region is also substantially affected by water vapor absorption. The second deepest Fraunhofer line is the Zeeman triplet line Fe I at 684.3 nm, which is located close to the maximum of the fluorescence emission peak and was thus chosen for this study. The DOAS fit was carried out in the wavelength window 681.8 - 685.5 nm, which is close to, but outside of the oxygen-B band. This spectral region exhibits features originating from other inelastic processes and weak water vapor absorption, but to a much lesser extent than the region around the Fraunhofer H α line.

The reference spectrum of chl *a* fluorescence calculated according to Eq. 4.2, is shown together with the selected fit window in the left panel of Figure 4.4. In order to demonstrate the differential structure of the obtained reference spectrum within the selected fit window, the reference spectrum before and after polynomial subtraction is shown in the right panels of Figure 4.4.

As pointed above, in the selected fit window not only the contribution of inelastic processes, but also the absorption by water vapor, is accounted for. Because water vapor cross-sections depend on temperature and pressure, it was decided not to choose one absorption cross-section for a given temperature and pressure, but to calculate the reference spectrum for water vapor analogously to the reference spectra for inelastic processes. Specifically, the reference spectrum for water vapor was calculated according to Eq. (4.2), where $I^+(\lambda)$ and $I^-(\lambda)$ are modeled radiances at the top of atmosphere calculated including and excluding the absorption by water vapor, respectively.

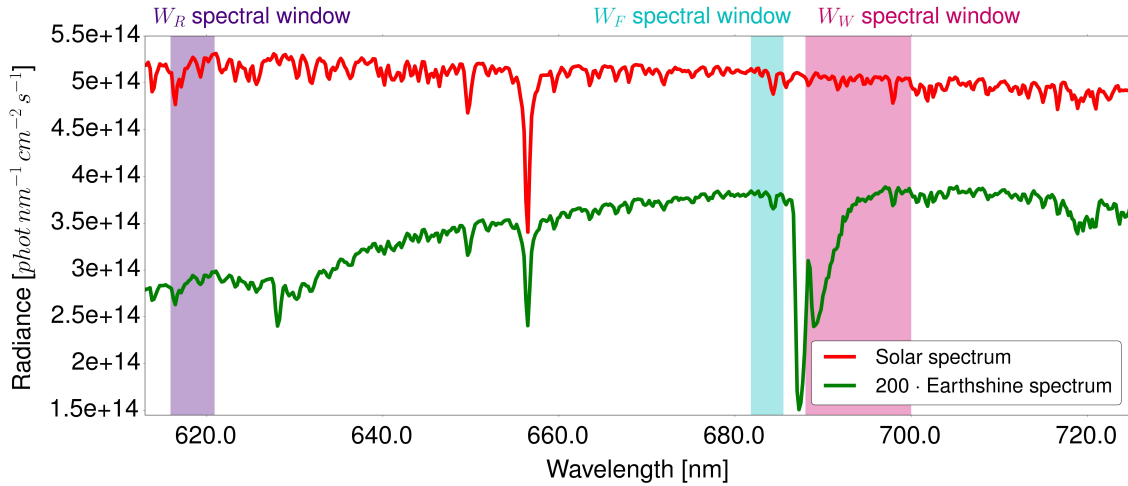


Figure 4.5: The locations of all the spectral windows used in the DOAS chl *a* fluorescence retrieval. SCIAMACHY measurements (9th April 2009; lat = 47° S, lon = 40° E) of extraterrestrial irradiance (red line) and scaled backscatter radiance (green) correspond to the sample DOAS fit shown further in Figure 6.1.

4.3.2 Retrieval technique of the red peak of chl *a* fluorescence

Using the information and settings described in the previous Section 4.3.1, the DOAS algorithm used for the retrieval of chl *a* fluorescence in the spectral window 681.8 - 685.5 nm, which will be referred to hereafter as W_F spectral window, is formulated as follows:

$$\left\| \tau(\lambda) - \sigma_w(\lambda)S_w - \sigma_f(\lambda)S_e - \sum_{k=0}^K a_k \lambda^k \right\|^2 \rightarrow \min, \quad (4.3)$$

where $\sigma_w(\lambda)$ and S_w are the water vapor reference spectrum and scaling parameter, respectively, S_e is the effective scaling parameter of the fluorescence reference spectrum, which in fact accounts for the filling-in of the Fe I Fraunhofer line caused by all inelastic processes.

Despite the fact that water vapor is fitted in the fluorescence DOAS fit, numerous numerical experiments have shown that the retrieved fluorescence fit factors are still to some extent sensitive to changing water vapor concentrations. As the fluorescence retrieval is additionally sensitive to the Raman scattering, additional corrections for these processes were applied. In order to estimate the influence of water vapor absorption and the contribution of Raman scattering, two additional DOAS retrievals were performed in spectral windows 688.0 - 700.0 nm and 615.9 - 620.9 nm, respectively. Hereafter these spectral windows will be referred to as W_W and W_R spectral windows. The W_W spectral window has been used by Noël et al. (2005, 2008) to retrieve water vapor from SCIAMACHY. The locations of all the spectral windows are shown along the example of a sample SCIAMACHY measurement in Figure 4.5.

By performing the DOAS retrieval on the simulated data in the fluorescence, water vapor,

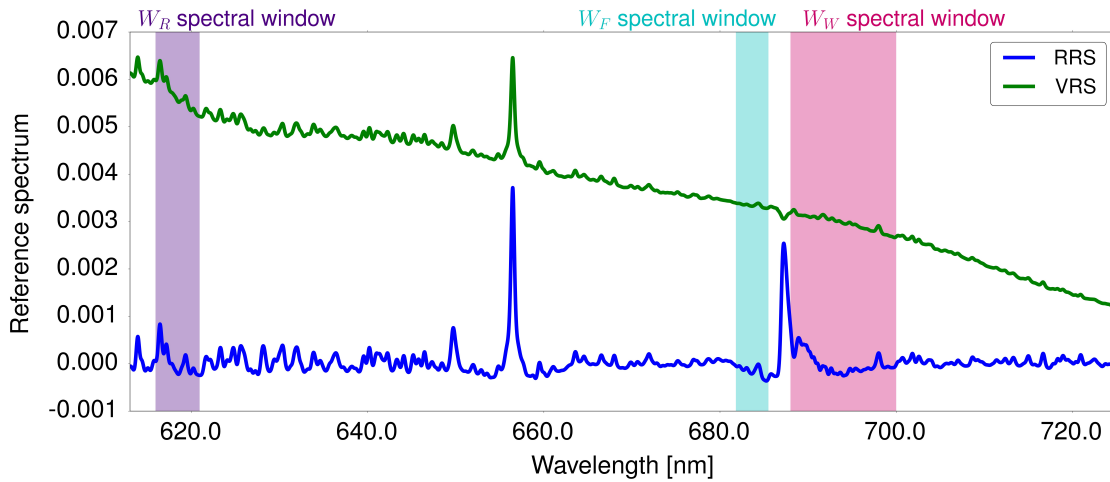


Figure 4.6: Simulated reference spectra of RRS and VRS and the locations of all the spectral windows used in the DOAS chl *a* fluorescence retrieval.

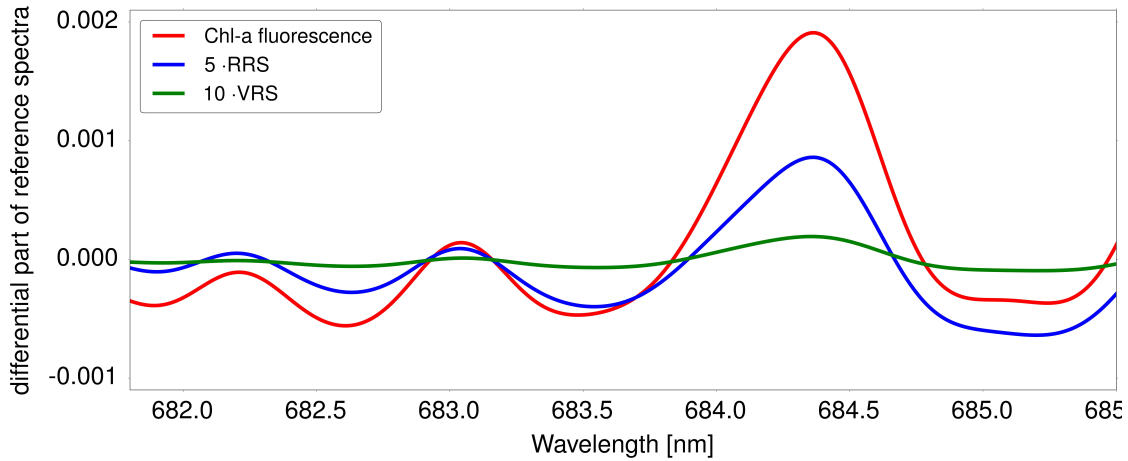


Figure 4.7: Differential spectra for chl *a* fluorescence, RRS and VRS in the spectral window W_F . Spectra of RRS and VRS were scaled by factors 5 and 10, respectively, for the clarity of the picture.

and Raman scattering spectral windows for the different atmospheric scenarios and solar zenith angles, the correction scheme was derived for the obtained fluorescence fit factors. The specific corrections are explained in detail below.

The FWHM functions used for convolving simulated radiances were 0.4 nm and 0.488 nm for SCIAMACHY and GOME-2, respectively, for the main fluorescence and water vapor correction retrievals; those values have already been previously used in other DOAS retrievals at W_W spectral window (Noël et al., 2005, Noël et al., 2008). For the Raman scattering simulations (important for further correction of the fluorescence results as detailed below), the radiances were convolved with a Gaussian of the FWHM of 0.3 nm for SCIAMACHY and 0.4 nm for GOME-2. Those values were based on the difference between the optimized FWHM for the reference spectra for fluorescence and the Raman scattering.

4.3.3 Accounting for effects of water vapor absorption and Raman scattering

Water vapor correction To obtain the water vapor correction, the uncoupled version of the radiative transfer model SCIATRAN was used. In this case, the fluorescence emission was set in the window W_F to a number of specific constant values at the surface and hence it was not further dependent on other environmental parameters such as solar zenith angle (SZA), chl *a* absorption, light penetration depth, etc. The simulations were performed for the aerosol free atmosphere and the following scenarios:

- the water vapor vertical column was set to 0.1, 1.0, 2.0, 3.0, 4.0, and 5.0 [g cm⁻²];
- fluorescence emission at the surface was set to 0.1, 0.5, 1.0, and 2.0 [mW m⁻²sr⁻¹nm⁻¹];
- SZA varied from 20° to 70° with 10° step;
- the surface albedo was set to a constant value of 0.1 (following Noël et al. 2004).

The water vapor fit factors were obtained solving two following minimization problems:

$$\left\| \tau(\lambda) - S_{wf} \sigma_w(\lambda) - \sigma_f(\lambda) S_e - \sum_{k=0}^K a_k \lambda^k \right\|^2 \rightarrow \min, \quad W_F \in [681.8, 685.5], \quad (4.4)$$

$$\left\| \tau(\lambda) - S_{ww} \sigma_{ww}(\lambda) - S_{O_2} \sigma_{O_2}(\lambda) - \sum_{k=0}^K a_k \lambda^k \right\|^2 \rightarrow \min, \quad W_W \in [688.0, 700.0], \quad (4.5)$$

where S_{wf} and S_{ww} are the water vapor fit factors in W_F and W_W spectral windows, respectively, $\sigma_{ww}(\lambda)$ and $\sigma_{O_2}(\lambda)$ are reference spectra of the water vapor and O₂-B absorption band in the W_W window calculated in the same way as described above for water vapor reference spectrum in the W_F window.

The results obtained show that the retrieved S_{wf} values are much noisier than S_{ww} , as the water vapor absorption is smaller in W_F window. Moreover, the retrieved fluorescence fit factors are still sensitive to the variation of the water vapor concentrations. To mitigate the impact of water vapor on the fluorescence fit factors, the following correction algorithm was used:

$$\hat{S}_e = S_e - \Delta_{ww}, \quad (4.6)$$

where \hat{S}_e is a corrected fluorescence fit factor. The function Δ_{ww} was calculated as a difference between the retrieved fluorescence fit factors S_{fw} and S_{f0} obtained for the case of simulations with and without water vapor in the atmosphere, respectively. The function was described best in a least-squares sense by a second order polynomial:

$$\Delta_{ww} = S_{fw} - S_{f0} = 0.0160 S_{ww}^2 + 0.0029 S_{ww} + 0.0024. \quad (4.7)$$

The introduced correction enables the obtained fluorescence fit factor to be extrapolated to the case of a water vapor free atmosphere using the retrieved water vapor fit factor S_{ww} .

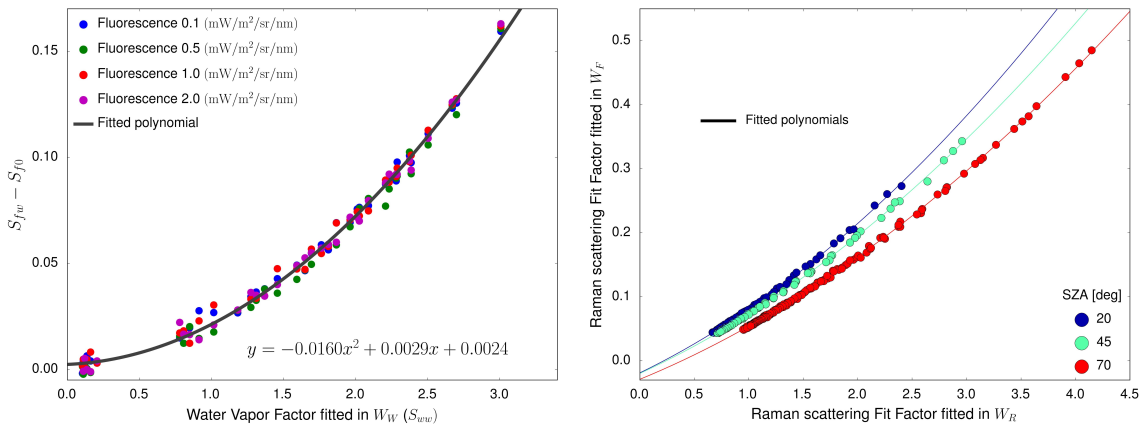


Figure 4.8: Corrections applied to original fluorescence fit factors based on modeled data. Left panel: water vapor correction. Right panel: Raman scattering correction.

It follows from the left panel of Figure 4.8 that the relationship between Δ_{ww} and S_{ww} does not change significantly with respect to SZA (different angles were not highlighted) and chl a fluorescence emission, even though water vapor and fluorescence fit factors themselves are dependent on these parameters. It should be noted that due to the weak dependence of the water vapor correction factor on the surface albedo, only a single albedo value was used for performing these radiative transfer simulations (Noël et al., 2004). This allows employing the same correction factor for the fluorescence retrieval over both ocean and land. It is assumed that this approximation is suitable in the framework of this study and can easily be improved in the future.

Raman scattering correction In order to account for Raman scattering, its contribution to filling-in of Fraunhofer lines was separated from filling-in originating from fluorescence. The reference spectra of all inelastic scattering processes show similar spectral structures mirroring the spectral structures of the solar irradiance spectrum, even though within the broad spectral range they exhibit significant differences (Fig. 4.6). However, within a narrow spectral range, as used in this study, after polynomial subtraction they differ only by a scaling factor (Fig. 4.7). From the mathematical point of view this means that in the fluorescence fit window the Raman scattering reference spectrum can be represented by a scaled fluorescence reference spectrum, i.e.,

$$\sigma_R(\lambda) \approx C \sigma_f(\lambda). \quad (4.8)$$

It follows that the effective scaling parameter S_e introduced in Eq. (4.3) can be represented as a linear combination

$$S_e = S_f + CS_R. \quad (4.9)$$

Thus, to correct the impact of Raman scattering on the filling-in of the selected Fraunhofer line, CS_R needs to be estimated and subtracted from the effective parameter S_e .

For this purpose, Raman scattering was retrieved in the W_R window using the DOAS

algorithm. This wavelength region is already outside, but it is still close to the fluorescence emission band. This assures that the relationship between the Raman scattering fit factors obtained in W_R and W_F spectral windows does not change significantly with respect to atmospheric/aquatic conditions.

The modeled radiances at the top of atmosphere were calculated including the rotational Raman scattering, but neglecting the water vapor absorption and fluorescence emissions. The DOAS fit can be formulated under these assumptions in the form of two following minimization problems:

$$\left\| \tau(\lambda) - x \sigma_x(\lambda) - \sum_{k=0}^K a_k \lambda^k \right\|^2 \rightarrow \min, \quad W_R \in [615.9, 620.9], \quad (4.10)$$

$$\left\| \tau(\lambda) - y \sigma_R(\lambda) - \sum_{k=0}^K a_k \lambda^k \right\|^2 \rightarrow \min, \quad W_F \in [681.8, 685.5], \quad (4.11)$$

where $\sigma_x(\lambda)$, x and $\sigma_R(\lambda)$, y are the Raman scattering reference spectra and fit factors from W_R and W_F spectral windows, respectively.

The simulations of RRS were performed for the following atmospheric scenarios:

- aerosol optical thickness at 650 nm was set to 0, 0.05, and 0.12;
- SZA varied from 20° to 70° with 5° step;
- the surface albedo varied from 0.01 to 0.5 with 0.01 step.

Preliminary simulations showed that VRS leads to minor filling-in as compared to RRS, what can also be seen in the comparison of the amplitudes of their differential reference spectra (Fig. 4.7). As a result, the impact of VRS for only a limited set of conditions was modeled. VRS was modeled using the ocean-atmosphere coupled version of SCIATRAN for the aerosol free atmosphere, the wind speed of 5 m/s, and the following scenarios:

- chl *a* concentration was set homogeneously to 0, 1 and 10 mg/m³ ;
- SZA varied from 20° to 70° with the step 10°.

As expected, VRS leads to negligible filling-in, as compared to RRS. As a result the correction was calculated based on RRS simulations only. Having solved the minimization problems given by Eqs. 4.10 and 4.11 for different SZAs, it was found that the relationship between RRS fit factors in both spectral windows can be represented in the form of the following regression:

$$y = a(\vartheta_0) x^2 + b(\vartheta_0) x + c(\vartheta_0), \quad (4.12)$$

where coefficients a , b and c depend slightly on SZA ($a \in [0.0116, 0.0182]$, $b \in [0.0701, 0.0849]$, $c \in [0.0138, 0.0288]$).

A subset of these resulting relationships for three SZAs is shown in the right panel of Figure 4.8. The fit factor values determined from the Raman scattering fit in the W_R window are subtracted from the retrieved fluorescence fit factors, according to the following equation:

$$\hat{S}_e = \hat{S}_e - C(y), \quad (4.13)$$

where \hat{S}_e is the fluorescence fit factor calculated according to Eq. 4.6, C is the factor obtained by scaling of the reference fluorescence spectrum according to Eq. 4.8; y is calculated according to Eq. 4.12 for a given SZA of the measurement, and for SZAs not used in the simulations, the y value is interpolated between the two nearest SZAs.

Taking the above corrections into account in order to remove the interference of water vapor and Raman scattering in fitting of the Fraunhofer Fe I line in the 681.8 nm - 685.5 nm spectral window, the retrieved fluorescence emission fit factor S_f is calculated as follows:

$$S_f = S_e - (0.0160 S_{ww}^2 + 0.0029 S_{ww} + 0.0024) - C [a(\vartheta_0) S_R^2 + b(\vartheta_0) S_R + c(\vartheta_0)], \quad (4.14)$$

where, the parameters S_e , S_{ww} , and S_R are obtained performing multi-window DOAS fit in W_F , W_W , and W_R spectral window, respectively.

4.3.4 Conversion scheme to fluorescence emission (SCIAMACHY FLH)

The fluorescence DOAS fit factor S_f obtained as a solution of the corresponding minimization problem is readily recalculated in the form of the absolute fluorescence emission spectrum. To demonstrate this, the fluorescence reference spectrum given by Eq. 4.2 can be and rewritten in the following form:

$$\sigma_f(\lambda) = \ln \frac{I^+(\lambda)}{I^-(\lambda)} = \ln \frac{I^-(\lambda) + \Delta I(\lambda)}{I^-(\lambda)} \approx \frac{\Delta I(\lambda)}{I^-(\lambda)}, \quad (4.15)$$

where it was taken into account that the variation of radiance at the top of atmosphere, $\Delta I(\lambda)$, caused by the fluorescence emission is much smaller than the elastic radiance, i.e., $\Delta I(\lambda) \ll I^-(\lambda)$. Assuming further that the *a priori* absolute fluorescence emission spectrum at the surface is $e_a(\lambda)$, it can be written

$$\Delta I(\lambda) = C_a e_a(\lambda), \quad (4.16)$$

where the factor C_a depends on the environmental conditions, i.e., $I^-(\lambda)$.

Comparing Eqs. (4.15) and (4.16), it can be stated that for the elastic radiance $I^-(\lambda)$:

$$e(\lambda) = S_f e_a(\lambda), \quad (4.17)$$

i.e., the fluorescence DOAS fit factor S_f is also the scaling factor of the *a priori* absolute fluorescence emission spectrum; $e(\lambda)$ is then the resulting fluorescence emission spectrum at the surface.

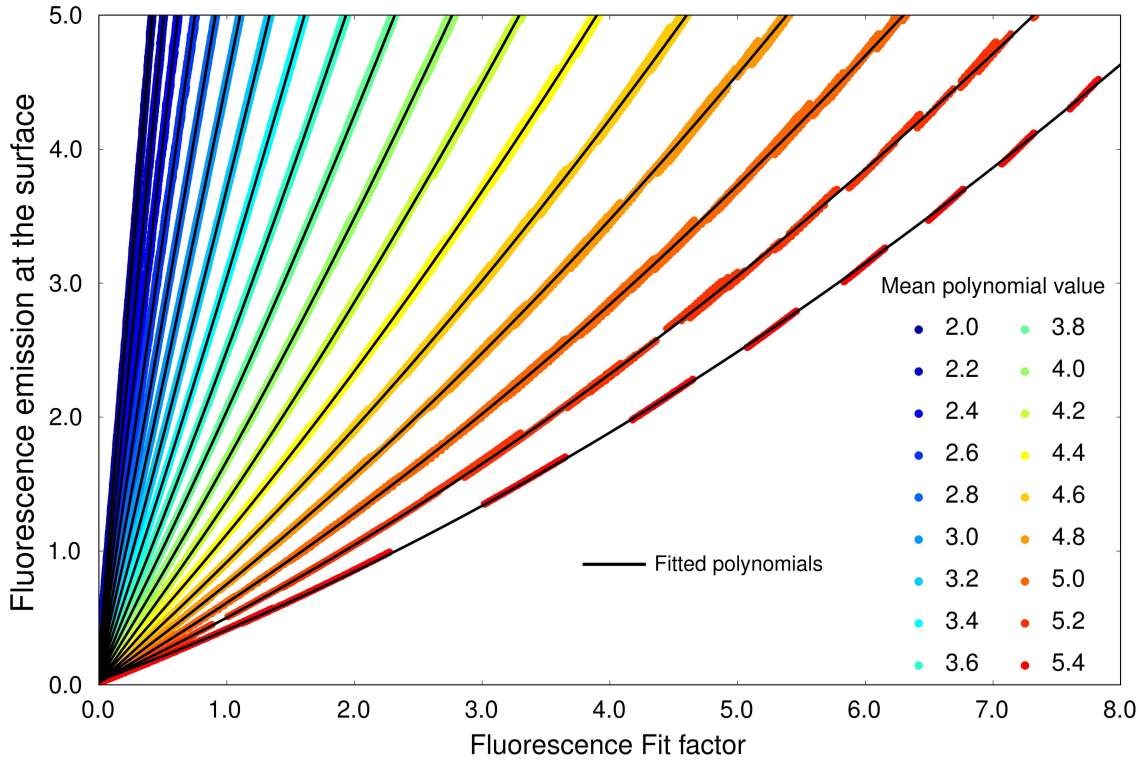


Figure 4.9: Conversion scheme for red chl *a* fluorescence between retrieved fluorescence fit factors S_f and the fluorescence emission at the surface, for a subset of calculated mean polynomial values.

The elastic scattering varies over an orbit and is not constant for the satellite measurements. As a result, the conversion from retrieved S_f into fluorescence emission at the surface is a function of $I^-(\lambda)$. As explained in Section 4.1.1, and seen in Eq. 4.1, the polynomial carries the information about the background signal and broad-band effects. To address this issue, a conversion scheme from S_f to absolute fluorescence emission was developed, which is dependent on the measured radiance, i.e., on the mean value of the polynomial fitted in the W_F spectral window. In order to simulate a variety of atmospheric and surface conditions and hence different background radiances and different polynomials obtained in the DOAS fitting, the following simulations were performed for a water-vapor free and excluding RRS atmosphere:

- three atmosphere scenarios: no aerosols and Rayleigh optical thickness at 600 nm amounting to 0.07 or 0.1; aerosol optical thickness at 650 nm amounting to 0.3 with Rayleigh optical thickness at 600 nm amounting to 0.07;
- fluorescence emission at the surface varying from 0.01 to 5 $\text{mW m}^{-2}\text{sr}^{-1}\text{nm}^{-1}$ with 0.01 $\text{mW m}^{-2}\text{sr}^{-1}\text{nm}^{-1}$ step;
- SZA varying from 17° to 70° with 1° step;
- the surface albedo varying from 0.01 to 0.5 with 0.01 step.

The top of atmosphere radiances were simulated for all the combinations of these parameters (4'050'000 combinations). The fluorescence retrieval was performed on simulated data for which the mean value of the polynomial fitted within the spectral window was calculated. It was obtained that the relationship between the absolute fluorescence emission and the fluorescence fit factor S_f can be represented in the following form:

$$e = a S_f^2 + b S_f + c, \quad (4.18)$$

where the polynomial coefficients depend on the mean radiance value, i.e., on the mean value of the polynomial fitted within the spectral window W_F . Coefficients a , b , and c in Eq. 4.18 were calculated for the mean polynomial values between 2.2 and 5.4 with 0.01 step. As the obtained results of marine chl a fluorescence are compared with MODIS data (see Section 6.1.1), the resultant absolute fluorescence emission will be called a fluorescence line height for SCIAMACHY (FLH) for the Fe I Fraunhofer line. The latter is given by:

$$FLH = S_f e_a(W_F). \quad (4.19)$$

4.3.5 Conversion from SCIAMACHY FLH into SCIAMACHY snFLH

The standard MODIS chl a fluorescence product is available in the form of nFLH. According to Gordon & Voss (2004) and Gordon & Clark (1981) the following relationship between nFLH and FLH can be easily derived:

$$nFLH = FLH \frac{F_0(\lambda_{14})}{E_d(0^+, \lambda_{14})}. \quad (4.20)$$

Here, $F_0(\lambda_{14})$ is the solar irradiance at the top of atmosphere and $E_d(0^+, \lambda_{14})$ is downwelling irradiance just above the surface, both measured in MODIS band 14. It follows that the quantitative comparison requires the calculation of $E_d(0^+, \lambda_{14})$, which depends on the aerosol optical thickness and solar zenith angle among others. $E_d(0^+, \lambda_{14})$ can be calculated running any coupled ocean-atmosphere radiative transfer model. However, this is a very time-consuming process requiring the global information of all atmospheric and oceanic parameters. Vice versa, the MODIS Terra Level 1 data in combination with SeaDAS software (<http://oceancolor.gsfc.nasa.gov/seadas/>) can be used to calculate MODIS FLH for each single measurement point. However, to obtain yearly composite average values, which are needed for comparison, a very large number of MODIS Level 1 data has to be reprocessed.

In order to estimate the expected quantitative relationship between FLH and nFLH representation of fluorescence emission, the measurements for an arbitrary chosen day (20th January 2009) of MODIS Terra FLH and nFLH were compared. For this purpose the Level 1 data were downloaded and processed with SeaDAS software. The default setting for atmospheric corrections and standard flags as in the Level 3 nFLH product were used. The obtained results show that nFLH values are on average ~ 1.5 times larger than FLH. However, they are up to four times different for low FLH values and highest solar zenith angles (data not shown).

Having this in mind, the SCIAMACHY results were additionally presented in the form of simplified nFLH (snFLH), in which case at least the SZA dependence could be accounted for. Hence, for the purpose of this study, snFLH is defined as follows:

$$snFLH = FLH \frac{F_0(W_F)}{E_{d,s}(0^+, W_F)}. \quad (4.21)$$

where $E_{d,s}(0^+W_F)$ is a simplified downwelling radiance, calculated with the SCIATRAN radiative transfer model with $F_0(W_F)$ as extraterrestrial irradiance, in the wavelengths of fluorescence fit window W_F . It is called simplified, as only the changes in the SZA are accounted for. Since the main goal of this study is to demonstrate the applicability of the DOAS approach to derive information about chl *a* fluorescence, this study was restricted to the qualitative comparison of SCIAMACHY FLH and snFLH with MODIS nFLH data. For snFLH calculations, the aerosol optical thickness τ_a and Rayleigh optical thickness τ_R were set to constant values for all scenarios (τ_R was set to 0.04, following Bodhaine et al. 1999 and τ_a was set to 0.05 after Halthore & Caffrey 2006). Halthore & Caffrey (2006) investigated τ_a at remote Pacific Ocean locations, and found a minimum τ_a of 0.017 at 670 nm for the Coconut Island measurements. However, for most presented measurements, the common values were ~ 0.05 , and this value was chosen for this study. The aerosol distribution varies over oceans, and is highest in the Atlantic Ocean next to the Sahara, the Arabian Sea and the Bay of Bengal. However, this study focused solely on SZA dependency. For these SCIATRAN calculations, the Bidirectional Reflectance Distribution Function was used as surface reflection type, and the wind speed was set to 5 m/s.

4.4 Retrieval of the far-red chl *a* fluorescence peak

4.4.1 Reference spectrum of far-red chl *a* fluorescence and selection of spectral window of retrieval

Chl *a* displays a double-peak fluorescence spectrum, with a second, far-red peak located near 740 nm (Fig. 2.11). The far-red peak is located in the vicinity of the oxygen A-band (Fig. 4.10), which is commonly used in remote sensing for the determination of cloud and aerosol properties (e.g., Sanders & de Haan, 2013; Geddes & Bösch, 2015). Hence, this spectral region is often measured by satellite-borne spectrometers with good spatial and spectral resolution.

As in the case of the retrieval of the red peak of chl *a* fluorescence at 685 nm, the fit window was chosen to stay outside of the oxygen absorption band in order to focus solely on the filling-in Fraunhofer lines. To stay within a cluster of a good spatial resolution of SCIAMACHY data, the wavelength region was limited to a very close proximity to the O₂-A band, where the cluster of the best spatial resolution was available. Here, a very narrow spectral window of around 4 nm in the wavelength boundaries of 754.0 - 758.1 nm (O₂-A band is located between 759 and 770 nm) was chosen. Similarly to the DOAS fit for red chl *a* fluorescence, the fit window is outside of main water vapor absorption, but the

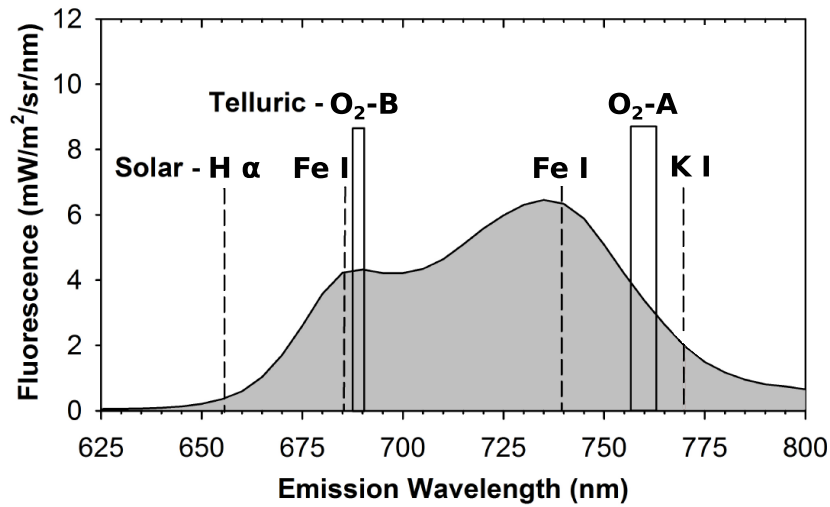


Figure 4.10: Emission spectrum of simulated chl *a* fluorescence with locations of oxygen absorption bands and several solar Fraunhofer lines (at leaf level). Adapted from Joiner et al. (2011).

retrieval is still slightly affected by its weak features. Hence, besides fluorescence, water vapor reference spectrum was also fitted in the DOAS fitting procedure.

The reference spectrum of fluorescence in this spectral region was calculated as before according to Eq. 4.2, with the simulated radiances convolved with a Gaussian type slit function with a FWHM of 0.42 nm. However, the ocean-atmosphere coupled version of SCIATRAN was not used for calculating chl *a* fluorescence spectrum in this case. Instead, chl *a* fluorescence was modeled as an emission source of $1 \text{ mW m}^{-2} \text{sr}^{-1} \text{nm}^{-1}$ at the surface. Albedo was set to 0.1, while the atmosphere was assumed to be free of aerosols and the SZA was set to 45° . As the fit window is very narrow, it was not additionally accounted for the spectral dependency of fluorescence. Hence, fluorescence emission was modeled as a spectrally constant additional signal, following Joiner et al. (2011, 2012). The obtained reference spectrum is clearly reflecting the Fraunhofer structures of the solar spectrum (Fig. 4.11).

To investigate the effect of other inelastic processes, namely VRS and RRS, on the retrieved fluorescence, VRS and RRS spectra were additionally calculated and later compared for this wavelength region. In case of VRS, its spectra were calculated with the use of the ocean-atmosphere coupled version of SCIATRAN, so no albedo value was defined a priori. Instead, two scenarios were modeled with a homogeneous chl *a* concentration in the water column of 0 and 1 mg/m^3 . RRS spectra were calculated with the uncoupled SCIATRAN version for surface albedo of 0.01 and 0.5, and additionally with the ocean-atmosphere coupled SCIATRAN version for waters with no chl.

The spectra calculated for chl *a* fluorescence, RRS and VRS are compared in Fig. 4.12. According to the previous SCIATRAN simulations, VRS was already very weak for the region of shorter wavelengths used in the retrieval of the red peak of chl *a* fluorescence (see Section 4.3.3). Here, in case of longer wavelengths, VRS effect gets even smaller. In similar retrievals of far-red chl *a* fluorescence, RRS was previously neglected as generally

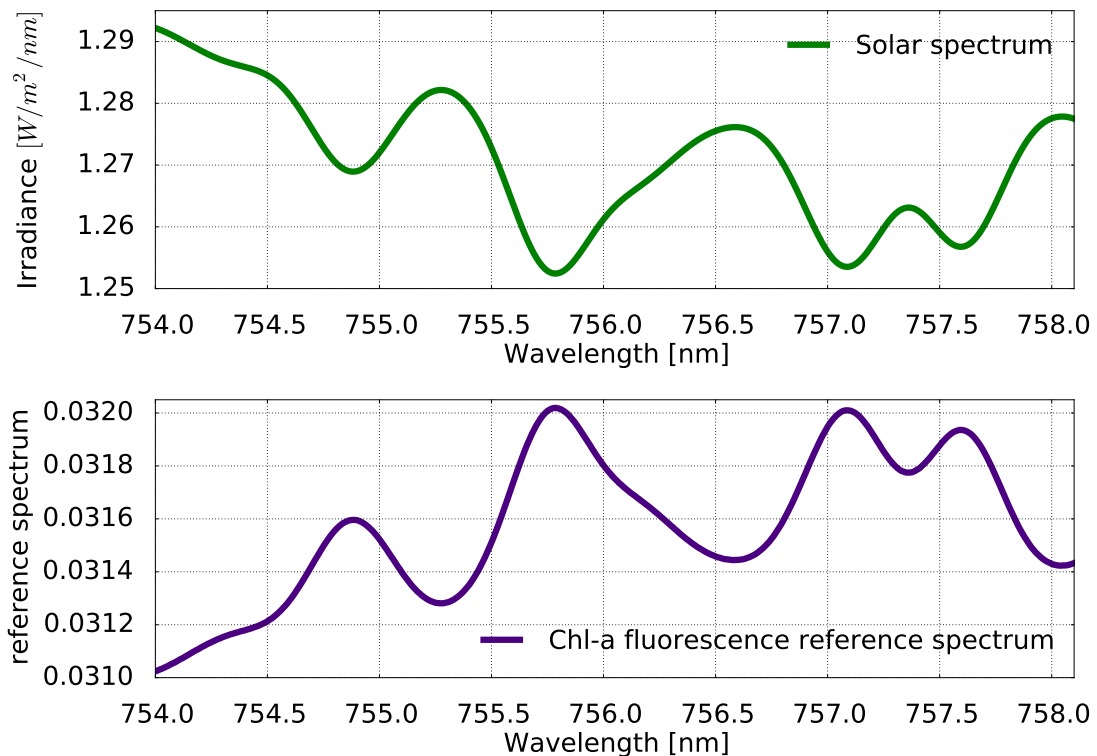


Figure 4.11: The solar spectrum (top panel), and the obtained reference spectrum (bottom panel), which is clearly mirroring the Fraunhofer structures of the solar spectrum, calculated from RTM simulations with SCIATRAN.

small, even though it was found to be a non-negligible effect (e.g., Joiner et al., 2013).

Nevertheless, the calculated VRS and RRS spectra are compared for this specific application. For comparison of chl *a* fluorescence and RRS, the spectra were calculated for those two surface albedo values representing the extreme values of very low and high albedo: 0.01 and 0.5. The spectra were calculated for two different albedo values, because, as in the previous retrieval, the spectra depend on the surface reflectance. Very low albedo is typical for oceans, as liquid water absorbs very strongly in this wavelength region. This spectral region is typically used as the ‘black pixel’ for atmospheric correction in ocean color algorithms for multispectral instruments. In contrast, a high albedo corresponds to high reflectivity of vegetation in the near infrared (Fig. 4.13). The reflectivity of the vegetation surface in NIR is mainly determined by the properties of the leaf tissues: their cellular structure and the air-cell wall-protoplasm-chloroplast interfaces (Kumar & Silva, 1973). It is further affected by environmental factors such as soil moisture, nutrient status, soil salinity, and leaf stage (Ma et al., 2001). Even bar soils or other unvegetated surface reach in the far-red a quite albedo >0.33

The reference spectra calculated for VRS, RRS and chl *a* fluorescence for different surface scenarios are shown in Fig. 4.12. Filling-in of Fraunhofer lines due to RRS is similar to the filling in originating from fluorescence emission of $0.3 \text{ mW m}^{-2}\text{sr}^{-1}\text{nm}^{-1}$ for the surface albedo of 0.01, or $0.1 \text{ mW m}^{-2}\text{sr}^{-1}\text{nm}^{-1}$ for the surface albedo of 0.5 (Fig. 4.12

4. DEVELOPMENT OF SATELLITE RETRIEVALS

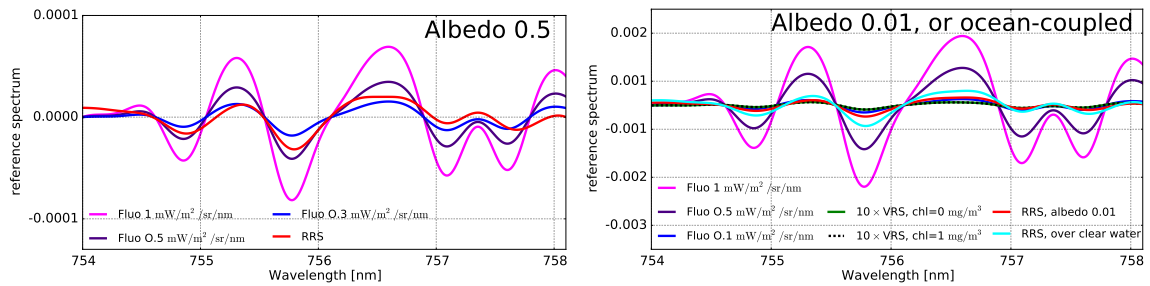


Figure 4.12: The reference spectra calculated for chl *a* fluorescence, RRS and VRS. Left panel: RRS and chl *a* fluorescence spectra calculated for albedo 0.5, and different fluorescence emissions. Right panel: RRS and chl *a* fluorescence spectra calculated for albedo 0.01, and different fluorescence emission. VRS was calculated with the coupled ocean-atmosphere SCIATRAN version for chl *a* concentrations of 0 and 1 mg/m³, respectively.

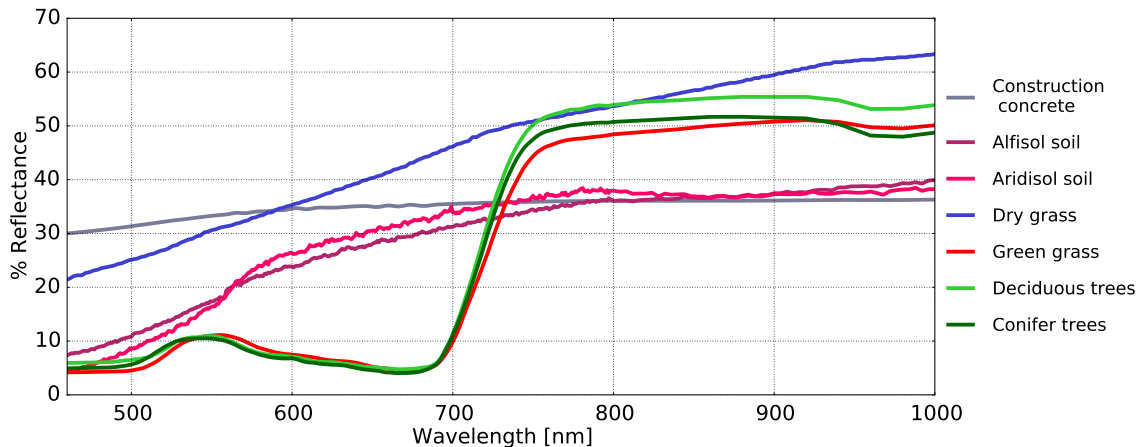


Figure 4.13: Typical spectra of different surface covers. Data source: ASTER Spectral Library (Baldrige et al., 2009).

left panel). These estimations are of the same order as the study of Vasilkov et al. (2013), who compared the impact of RRS and chl *a* fluorescence on the O₂-A and -B bands. RRS impact also depends on SZA, surface albedo and pressure, aerosol loading, as well as the spectral resolution of the instrument (Vasilkov et al., 2013).

VRS impact on filling-in of Fraunhofer lines is small, even if there is no chl in the water (Fig. 4.12 right panel). It is around fifteen times weaker than the effect of fluorescence of 0.1 mW m⁻²sr⁻¹nm⁻¹ calculated for an albedo of 0.01. In case of RRS, an additional spectrum was calculated in the ocean-atmosphere coupled SCIATRAN version for the purpose of comparison with VRS (for condition with no chl *a* in the water). VRS spectrum is twenty times smaller than RRS spectrum for albedo of 0.01, and as much as forty times smaller for the ocean-atmosphere coupled scenario. This also shows, that even an albedo as small as 0.01 is even higher than the ocean albedo calculated within the ocean-atmosphere coupled model.

To conclude, Raman scattering causes only small filling-in of Fraunhofer lines. Impact of

VRS is found to be particularly weak and even for clear waters it is of a few percent of RRS only. Hence, Raman scattering was not taken further into account in the development of the far-red chl *a* retrieval. Other potential sources of filling-in include luminescent minerals in soil and/or rocks (e.g., fluorite compounds) or emission from flaming fires and volcanoes (Joiner et al., 2012), which are out of scope of this study.

4.4.2 Offset correction

Already in previous studies, a zero-level offset was identified in the data, which is probably caused by instrumental effects. The issue was first discussed by Frankenberg et al. (2011a), who suggested that its source can be stray-light in case of grating spectrometers (such as SCIAMACHY), or detector signal non-linearity in case of FTS systems (such as GOSAT). Various correction schemes were applied in previous studies in order to account for this effect. In case of GOSAT retrievals, Frankenberg et al. (2011b) proposed an empirical correction of the offset by calibrating measured radiance as a function of the average radiance over Antarctica. This idea was followed by Guanter et al. (2012), who additionally included numerous vegetation-free spectra to generate corrections curves on a monthly basis. A different idea was proposed by Joiner et al. (2012), who suggested to use ocean spectra with similar background radiance to reduce the errors from instrumental effects. In the following algorithms developed for GOME-2, Joiner et al. (2013) used a statistical approach, which uses spectral principal components measured above vegetation-free pixels. In such case, calculated principal component probably also compensate for the zero offset.

In order to investigate the issue of zero offset in this retrieval, ocean and non-vegetated land scenes of the SCIAMACHY data for years 2004-2011, for which no fluorescence is predicted, were examined. No observable fluorescence signal is expected above any ocean scenes. If emitted, the chl *a* fluorescence signal is completely re-absorbed within the water column due to a very strong liquid water absorption. Nevertheless, for this investigation three oligotrophic regions of ocean gyres were chosen, where the chl *a* concentration remains very low for the whole year (Fig. 4.14). In case of land scenes, a subregion of Greenland (with some pixels being partly in the water) and a part of the Sahara desert were chosen (Fig. 4.14). Both regions have very little or no vegetation during the whole year. The pixels were filtered only for SZA ($<70^\circ$), which means that a complete variety of cloud contamination was included, ranging from cloud-free scenes to a complete cloud cover. Therefore, the scenes represent a variety of solar zenith angles and background radiances, as shown in the histograms in Fig. 4.15 (the background radiance, or the brightness of measured scene, correspond to the optical depth or polynomial fitted in the DOAS fitting procedure). Especially ocean scenes represent a full spectrum of pixel brightness: water is almost black in this wavelength range, but scenes can be much brighter when the ocean surface is covered with waves and foam, or if the pixels are cloud- or glint- contaminated.

These regions, for which it is not expected to observe any fluorescence signal, were investigated in terms of retrieved fluorescence fit factors. Analyzing histograms of fluorescence fit factors retrieved over them, a broad distribution of values around the mean value of ~ 1 is seen (Fig. 4.15 top panels), despite the fact that no fluorescence signal is expected. This shifted position of the mean value corresponds to the systematic, zero error of the

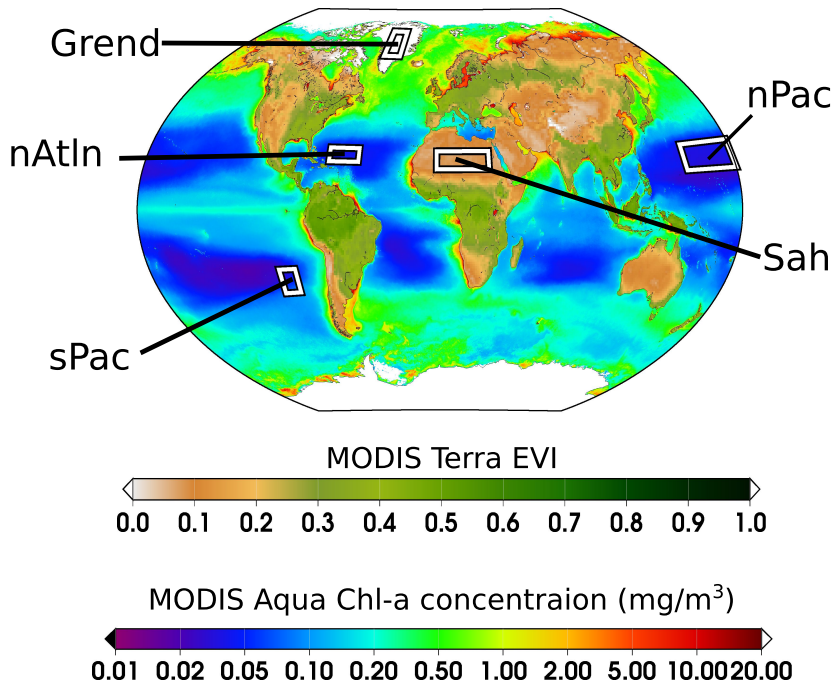


Figure 4.14: Locations of chosen ocean and non-vegetated land regions, on which the offset corrections were based. Ocean regions: nAtln (north Atlantic), nPac (north Pacific) and sPac (south Pacific). Land regions: Greenland (Grend) and Sahara (Sah).

retrieval, while the bell curve of the distribution of fluorescence fit factors reflects the effect of the random noise. The scatter is larger for ocean regions, for which pixel brightness extends over a wider value range. However, the dependency of the fluorescence fit factors on the mean polynomial value is not easy to notice, even though the scatter is broadened with the increase of the mean polynomial value, which corresponds to the darkening of scenes (Fig. 4.16). For darker scenes higher chi-square values (χ^2) are also observed, which is related to a weak signal arriving at the detector over dark ocean pixels (Fig. 4.17).

In order to investigate the dependency of retrieved fit factors on the scene brightness, the data were divided into subgroups based on the mean polynomial value. For each subgroup, a mean value of the retrieved fit factors was calculated. After such averaging, a dependency of the fluorescence fit factors on the mean polynomial value can be better identified (Fig. 4.18). First of all, the mean fluorescence factor values exponentially increase for the dark scenes where the polynomial equals five or more (Fig. 4.18 left panel). On the other hand, polynomial values below two represent exceptionally bright scenes (note that such values are not common, even not for Sahara and Greenland, Fig. 4.15 middle panel), which would be screened out as clouds or ice and hence excluded from the measurements in the data processing of the retrieval. Therefore, the offset correction was defined for the mean polynomial value between two and four only, for which a simple monotonic function can be fitted. A second order polynomial function that relates the retrieved mean polynomial value to the expected value of the offset, $S_{f, \text{offset}}$, was fitted (Fig. 4.18). Eventually, from

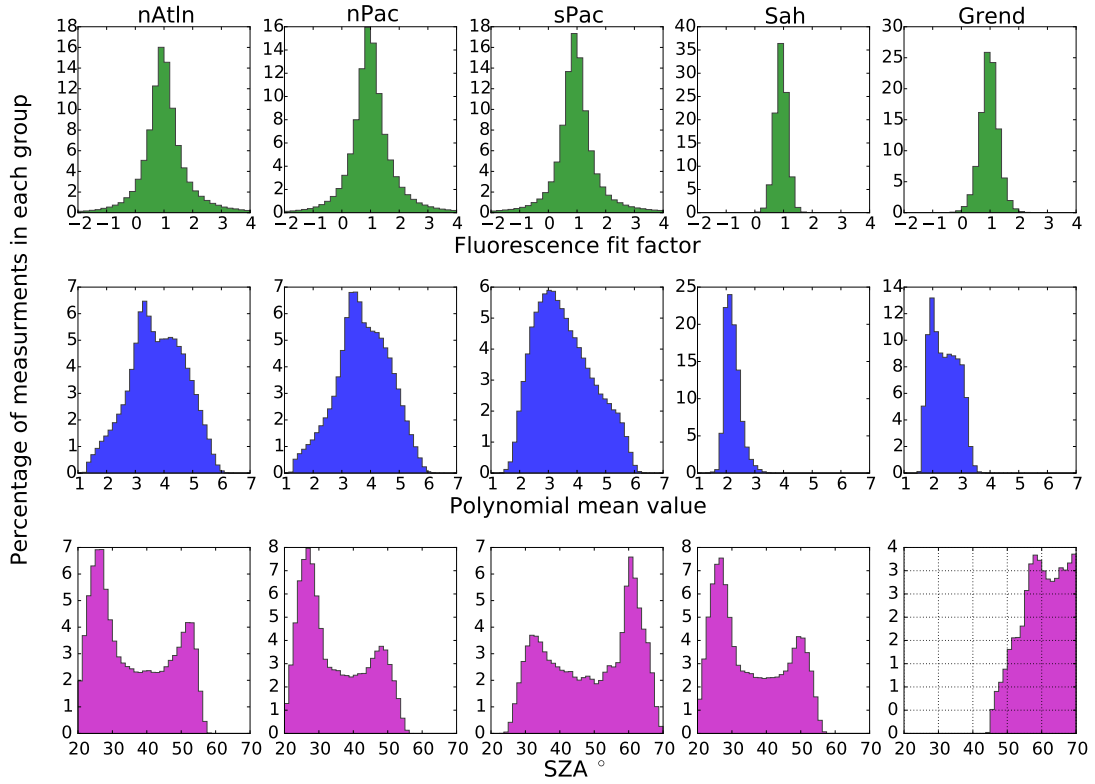


Figure 4.15: Histograms of retrieved fluorescence fit factors, mean polynomial values and SZAs over selected areas.

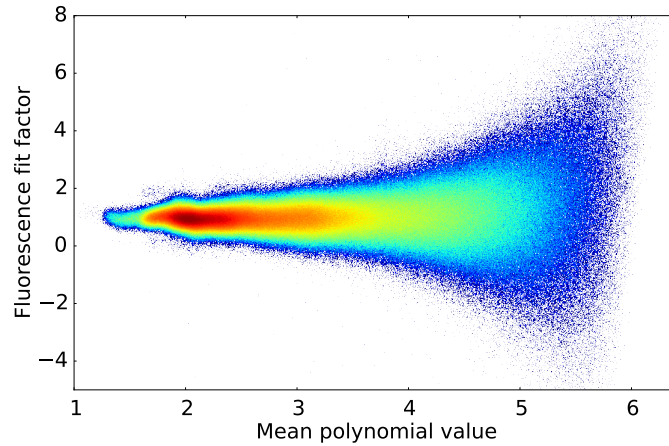


Figure 4.16: 2D histogram of eight years (2004-2011) of SCIAMACHY measurements for a range of retrieved fluorescence fit factors and mean polynomial values.

each retrieved fluorescence fit factor S_f a calculated $S_{f, \text{offset}}$ is subtracted:

$$S_{f, \text{corrected}} = S_f - S_{f, \text{offset}} = S_f - (-0.0061x^2 - 0.0056x + 0.9122), \quad (4.22)$$

where the independent variable x is a mean polynomial value.

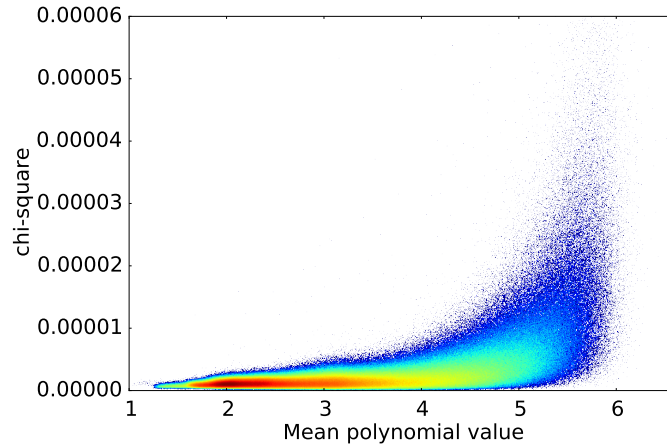


Figure 4.17: 2D histogram of eight years (2004-2011) of SCIAMACHY measurements for a range of chi-square and mean polynomial values.

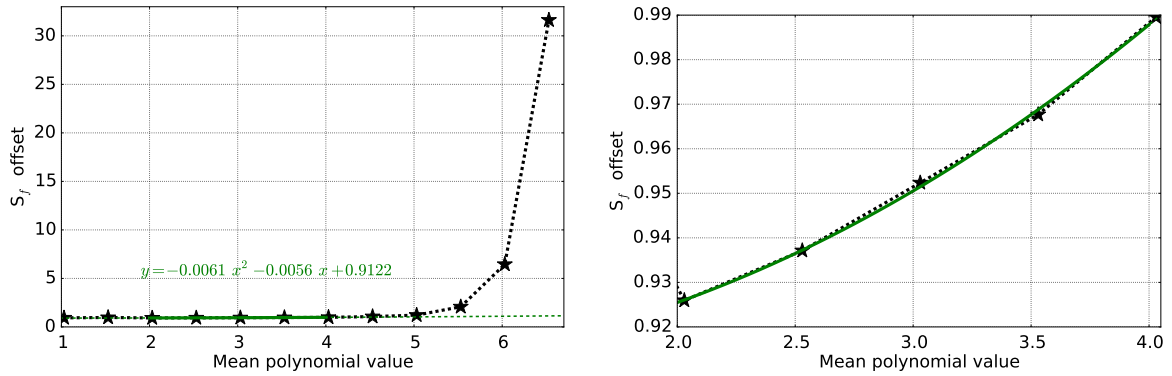


Figure 4.18: Relation between the offset value $S_{f, \text{offset}}$ and retrieved mean polynomial value for the regions defined in Fig. 4.14, for the whole range of data points (left panel), and for the limits within the offset correction function is defined (right panel).

4.4.3 Conversion scheme into fluorescence emission

Retrieved and offset-corrected fluorescence DOAS fit factor $S_{f, \text{corrected}}$ can be recalculated in the form of the absolute fluorescence emission spectrum at the surface, analogously to the approach introduced for red peak of chl a fluorescence (Section 4.3.4). The conversion scheme is based on the radiative transfer simulations with SCIATRAN. As compared to the red chl a fluorescence retrieval, a number of scenarios simulated with SCIATRAN was decreased in case of the far red chl a fluorescence retrieval in order to minimize the computational cost. The simulations with following settings were performed in the aerosol-free, Rayleigh atmosphere:

- fluorescence emission at the surface varying from 0 to 3 $\text{mW m}^{-2}\text{sr}^{-1}\text{nm}^{-1}$ with 0.1 $\text{mW m}^{-2}\text{sr}^{-1}\text{nm}^{-1}$ step;
- SZA varying from 17° to 70° with 1° step;

- the surface albedo varying from 0.01 to 0.5 with 0.01 step.

A conversion scheme for the far-red peak of chl *a* fluorescence was developed similarly to the red peak of chl *a* fluorescence. However, here the conversion factor is not dependent on the mean polynomial value, but depends directly on the mean value slant optical density within the spectral window of the retrieval (slant optical density defined as $\tau(\lambda) = -\ln \frac{I(\lambda)}{I_0(\lambda)}$, see Eq. 4.1). Based on the SCIATRAN simulations, it was found that this change leads to obtaining linear functions (instead of polynomials of second degree). Using linear functions is important for the retrieval in the far-red peak of chl *a* fluorescence, because of the observed zero-offset and introduced zero-offset correction. In case of a second order conversion function, the error introduced by a not fully corrected offset would lead to much higher differences in the absolute values. To further minimize the error introduced by the offset correction, the conversion scheme was applied to the mean gridded values of the offset-corrected fluorescence fit factors, based on mean gridded slant optical densities (on 0.5° grid).

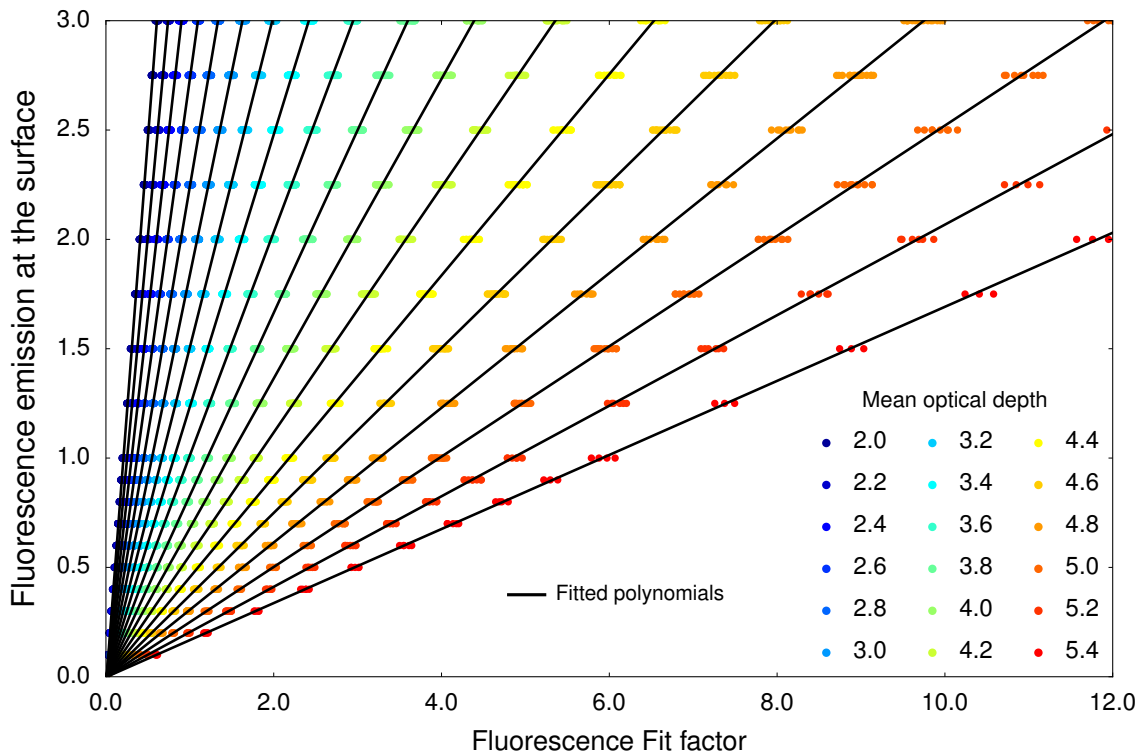


Figure 4.19: Conversion scheme for far-red chl *a* fluorescence between retrieved and offset-corrected fluorescence fit factors $S_{f, \text{corrected}}$ and the fluorescence emission at the surface, for a subset of calculated mean slant optical density values. Each color refers to the mean optical depth value in the range starting from a value as indicated in the legend, to this value incremented by 0.05. The larger spread of values as compared to Fig. 4.9 is due to a smaller number of simulations and a smaller number of different ranges of values for which different functions were calculated.

The relationship between the absolute fluorescence emission at the surface and the corrected fluorescence fit factor $S_{f,\text{corrected}}$ can be expressed in the following form:

$$e = a S_{f,\text{corrected}} + b, \quad (4.23)$$

where the polynomial coefficients a and b depend on the mean slant optical density within the fit window. Coefficients a and b in Eq. 4.23 were calculated for the mean slant optical density values between 2.0 and 5.4 in 0.05 step increments, based on simulated radiances. Since the number of simulations is lower than in the case of red chl a fluorescence, the step increments are bigger in order to ensure enough data points to fit the function. The obtained linear functions of the conversion scheme for far-red chl a fluorescence for a subset of calculated mean slant optical density values are shown in Fig. 4.19.

4.5 Retrieval of the chl proxy

By adding a chl a -specific absorption spectra of phytoplankton to the DOAS fit, the DOAS method was previously extended to PhytoDOAS and applied to global observations of phytoplankton overall and group-specific biomass (Vountas et al., 2007; Bracher et al., 2009; Sadeghi et al., 2012). The basic idea of this approach is also adequate for observations over land. Earlier applications of DOAS to terrestrial vegetation by Wagner et al. (2007) focused on the analysis of weak narrow-band reflectance structures of three types of vegetation (conifers, deciduous trees, grass) in the red spectral range. Wagner et al. (2007) found that some vegetation features are also retrieved from ocean pixels, especially with respect to the retrieval of conifers. Here, the application of the DOAS method was extended to observations of the global terrestrial vegetation by adding a chl absorption spectrum characteristic for terrestrial plants to the DOAS fit. The absorption features were retrieved in the blue spectral region, which covers the Soret band of chl absorption (see Fig. 2.10).

4.5.1 Reference spectrum of chlorophyll

Modeling simulations are not needed to calculate the absorption spectra used as the reference in the DOAS retrievals, as no wavelength shift needs to be simulated (which is the case for inelastic processes). Hence, in case of a chl absorption spectra, an *a priori* known spectrum can be directly used. However, chl absorption exhibits different spectra when isolated, as when it is embedded in a photosynthetic antenna (Section 2.2.2). Furthermore, there are always other pigments than chlorophylls present in the photosynthetic organism, which all together create the specific absorption spectra. Hence, a chl a absorption spectrum as shown in Fig. 2.10, was not used in the developed retrieval. Instead, a chlorophylls ($a+b$) absorption spectrum, which is also used in a widely-used leaf directional-hemispherical reflectance and transmittance model, PROSPECT-5 (Jacquemoud & Baret, 1990; Feret et al., 2008), was adopted. To calculate the specific spectral absorption coefficients, Feret et al. (2008) used a Gaussian approximation proposed by Maier (2000), which models the absorption of pigments located in antenna complexes, assuming a

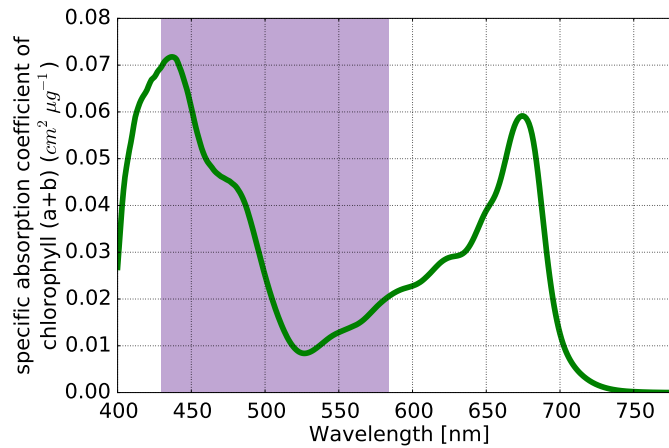


Figure 4.20: A chlorophylls (a+b) absorption spectrum used in the chl proxy retrieval (Maier, 2000; Feret et al., 2008), with the wavelength region of the DOAS chl proxy retrieval highlighted.

chlorophyll *a*:*b* ratio of about three, which is typical for terrestrial plants (Maier et al., 1999; Feret et al., 2008, and references therein). The specific absorption spectrum of chlorophylls, which is used in the retrieval, is shown in Fig. 4.20.

4.5.2 Spectral window of retrieval

The applicability of the DOAS retrieval for estimating chl concentration, in the blue spectral region of chl absorption (Soret band, Fig. 2.10) was investigated. This is a similar spectral region as used in earlier studies of marine phytoplankton (Vountas et al., 2007; Bracher et al., 2009; Sadeghi et al., 2012). Wagner et al. (2007), on the other hand, focused on the spectral region of the Q_y absorption band (see Fig. 2.10 for chl absorption bands). Most of the widely used vegetation indices are also designed to exploit the spectral reflectance in the red edge wavelengths (e.g., NDVI, MTCI, see Section 7.2). In this sense, since the algorithm developed here retrieves a chl proxy in a different spectral region, it provides additional and independent information on the vegetation biomass. The summary of spectral regions used in the previous DOAS applications focused on biosphere observations is shown in Table 4.1.

Because of the slowly-varying shape of the chl absorption spectrum, the fit window needs

Table 4.1: Spectral regions previously used in DOAS retrievals of marine phytoplankton and land vegetation.

| Reference | spectral region | phytoplankton/vegetation retrieved |
|---------------------|------------------|------------------------------------|
| Vountas et al. 2007 | 428 – 496 nm | phytoplankton |
| Bracher et al. 2009 | 429 – 495 nm | diatoms & cyanobacteria |
| Sadeghi et al. 2012 | 429 – 521 nm | diatoms & coccolithophores |
| Wagner et al. 2007 | 605 – 683 nm | conifers, deciduous, grass |
| this study | 429.2 - 583.8 nm | terrestrial vegetation |

to be broader in order to capture chl-specific features. As only certain wavelength clusters of SCIAMACHY instruments have high spatial resolution (e.g., O₂ A-band), the need of using a broader fit window leads to a decrease of spatial resolution, since the measurements within the clusters of higher spatial resolution are binned. Eventually, the final spatial resolution is the worst one of all the included clusters. Here, the chl proxy retrieval was performed in the spectral window of 429.2 - 583.8 nm, which covers four SCIAMACHY clusters of the channel three. Hence, the pixels spatial resolution is 240 km across track and along track 30 km, for most of the years. The spectral window is also highlighted in Fig. 4.20.

As in the previous DOAS retrievals, in addition to the chl absorption spectrum, atmospheric components, which absorb within the selected fit window, must be included in the DOAS fitting procedure. Since in contrast to the application of DOAS to the fluorescence retrievals, here a broad fit window was used for the chl proxy retrieval, a higher number of strong atmospheric absorbers dominate the spectral features within the wavelength window (Fig. 4.21 top panel). Additionally, the reference spectra of inelastic scattering processes (RRS, VRS) are shown in Fig. 4.21, bottom panel. For the chl proxy retrieval, the absorption spectra of O₃, O₄, NO₂, water vapor and the reference spectrum of RRS were fitted. Since it was not aimed here to retrieve chl over the ocean, VRS was not considered in this DOAS fit.

In principle, most satellite vegetation products are given in form of indices (e.g., most commonly used NDVI, which is based on the contrast between the maximum absorption in red and the maximum reflection in near-infrared, Curran e.g., 1980). The retrieved values of chlorophyll fit factors were not converted into physical values (e.g., chl content), as such a conversion would need to take into account that the radiance originating from the top of the canopy results from photon interactions within the whole canopy, the canopy surface included. Important features that must be considered to estimate the canopy radiation regime include (Knyazikhin et al., 1998):

- the architecture of individual plants and the entire canopy,
- optical properties of vegetation elements (leaves, stems) and soil, the former also depend on physiological conditions (water status, pigment concentration, etc.),
- atmospheric conditions, which determine the incident radiation field.

Since the aim of this study was to test the feasibility of the global application of the DOAS method for terrestrial chlorophyll observations, no specific biome type was chosen for conversion scheme to chl concentration. Hereafter, chlorophyll fit factors will be referred to as chl proxy. Hence, neither correction nor conversion scheme was needed to be developed for this retrieval.

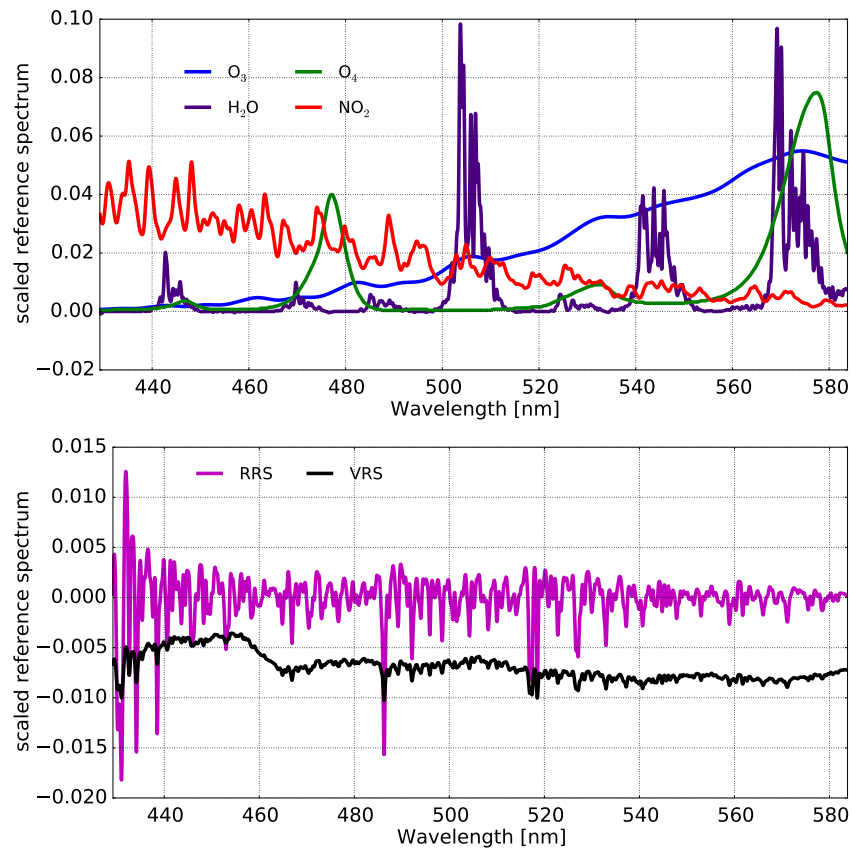


Figure 4.21: Absorption spectra of atmospheric absorbers included in the chl proxy retrieval (top panel) and the reference spectra of inelastic processes RRS and VRS (bottom panel), within the spectral window of the chl proxy retrieval.

Chapter 5

Observations of CDOM fluorescence with hyperspectral data

Two simple DOAS retrievals of CDOM fluorescence at two wavelengths regions (343 - 345.5 nm and 484 - 490 nm, see Section 4.2) were applied to two months of SCIAMACHY data (June and July 2009). As both spectral windows are very narrow and only one reference spectrum is fitted for each retrieval (which reflects all inelastic processes), the retrieved CDOM fluorescence fit factors can translate, in principle, into the overall strength of the filling-in of the investigated Fraunhofer lines. An example of a spectral fit for each DOAS retrieval (performed on the same SCIAMACHY pixel) is shown in Figure 5.1. Since for each retrieval only one spectrum (of CDOM fluorescence) was fitted, the fitted differential optical depth (DOD) corresponds directly to the scaled CDOM reference spectrum. The features of filling-in of Fraunhofer lines are clearly visible, and are well accounted for by the fitted CDOM fluorescence reference spectra. The bottom panels of Figure 5.1 show that the residuals are very small, which indicates that there are no additional narrow features in these spectral windows that should be additionally taken into consideration within the retrievals.

The global composite average of the CDOM fluorescence fit factors retrieved from SCIAMACHY for two-month period of June and July 2009 are presented in Figure 5.2a and b. The data points were gridded in 0.5° by 0.5° boxes, which roughly corresponds to two SCIAMACHY ground scenes at the equator. For comparison, the MODIS-Aqua product of absorption coefficient for dissolved and detrital particulate matter at 443 nm derived from the Garver-Siegel-Maritorena (GSM) algorithm (Garver & Siegel, 1997; Maritorena et al., 2002) for the same time period is additionally shown in Figure 5.2c.

A clear latitudinal pattern, with the minimal values found around 40°N , is seen in the results of the filling-in of the Fe I lines at 344 nm (Figure 5.2a). It reflects the spatial distribution of RRS signal, which in general increases towards higher SZAs and hence higher latitudes. The shift of the minimum signal towards northern latitudes is due to the time of measurements (boreal summer) and the fact that the SCIAMACHY measurements

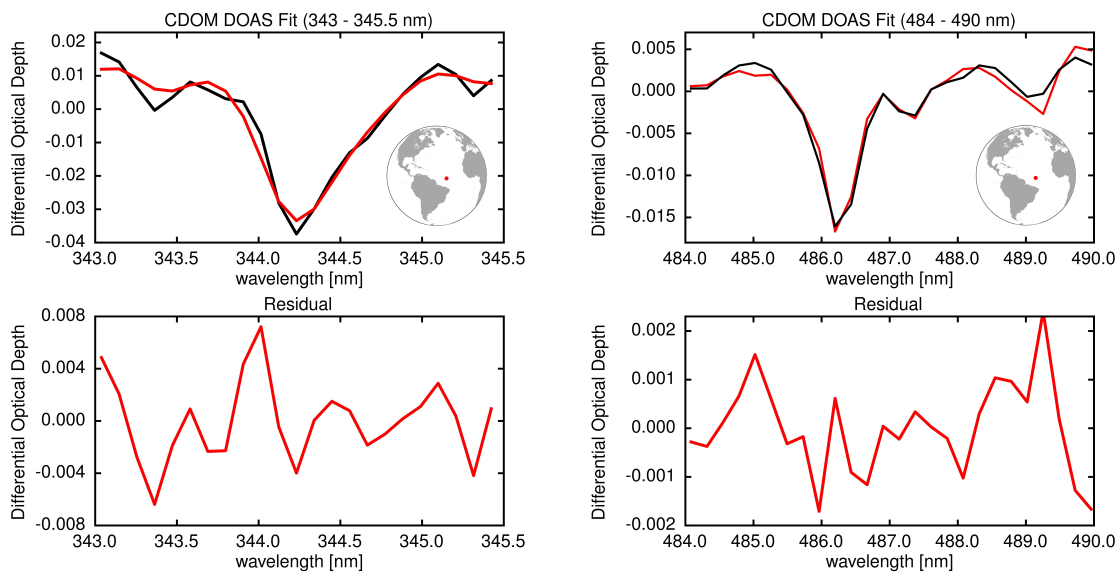


Figure 5.1: Examples of a SCIAMACHY CDOM Fluorescence DOAS Fits (7th July 2009; lat = 7° N, lon = 39° W).

- 1) Top left panel: the fitted DOAS DOD (red) and measured DOD (black) for CDOM fit in 343 - 345.5 nm.
- 2) Bottom left panel: the residual from the DOAS fit in 343 - 345.5 nm.
- 3) Top right panel: the fitted DOAS DOD (red) and measured DOD (black) for CDOM fit in 484 - 490 nm.
- 4) Bottom right panel: the residual from the DOAS fit in 484 - 490 nm.

are taken during the descending part of the orbit. RRS dominates the filling-in of the Fe I lines at 344 nm, which was also implied by the SCIATRAN simulations (Section 4.2.2). On top of this latitudinal pattern, some additional variations are observed, for example in the North Atlantic. These features are mainly due to the VRS spatial distribution, which is better captured by the retrieval focused on the filling-in of H β line at 486 nm, which is shown in Figure 5.2b. In the case of the retrieval around the H β line, the global composite of the retrieved fluorescence fit factors shows roughly an inverse picture of CDOM concentration, as retrieved by MODIS-Aqua GSM algorithm. This again supports the modeling results, which showed that VRS is the predominant effect in this wavelength region, which leads to the highest fit factors in the regions of the clearest waters (Section 4.2.2). The VRS signal is influenced not only by CDOM, but by all optical constituents of the water column. Hence, it does not exactly mirror the global CDOM distribution, but also shows features typical for chl *a* concentration (compare Figure 5.3a). It is especially true for the open ocean, where CDOM concentrations are smaller in regard to chl *a* concentration as compared to coastal waters. This relationship between CDOM and chl *a* concentrations can be observed globally by using the CDOM Index (Morel & Gentili, 2009), which shows values > 1 for excess and < 1 for deficit of CDOM as compared to chl *a* concentration for the mean conditions of the bio-optical model developed for Case 1 waters (Figure 5.3b).

In order to investigate if the enhanced signal originating from CDOM fluorescence can be observed from space at all, the inter-variability of the same parameters (SCIAMACHY fit

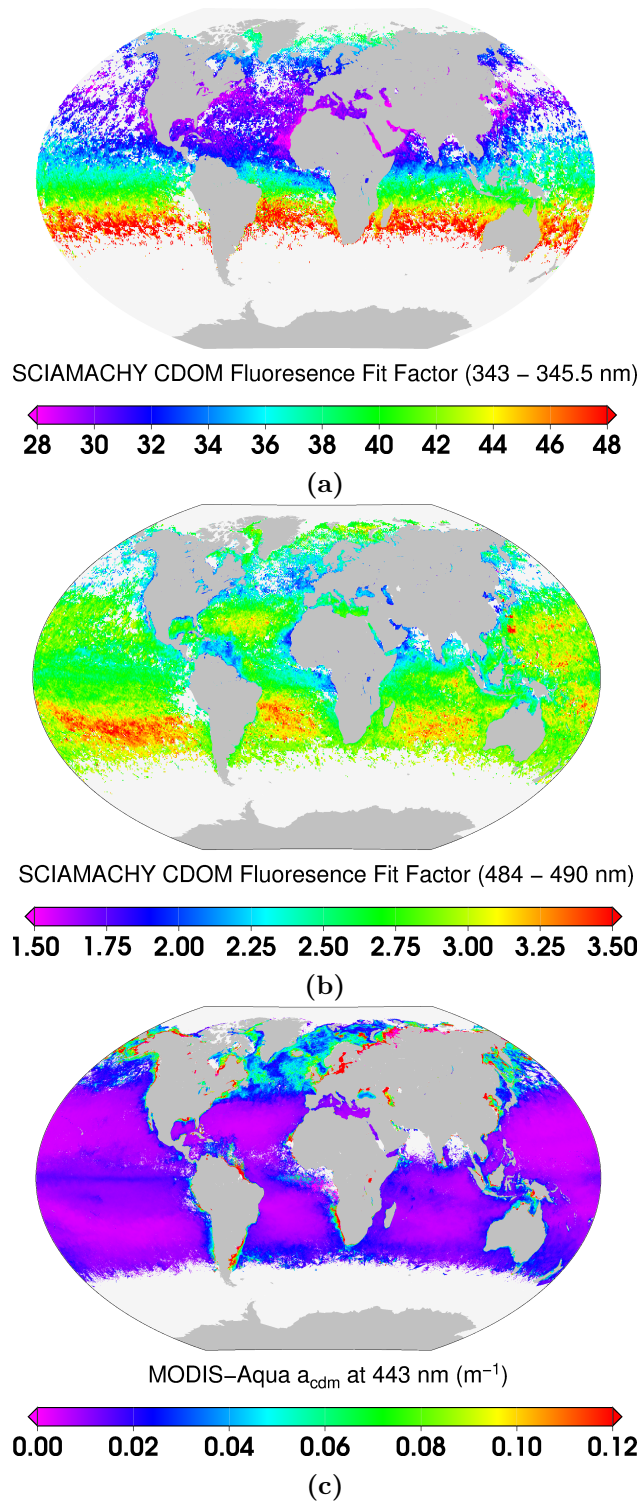


Figure 5.2: Global maps of SCIAMACHY CDOM fluorescence fit factors for two months (June and July 2009) in two different spectral regions (a,b) compared with MODIS-Aqua GSM absorption coefficient for dissolved and detrital particulate matter a_{cdm} at 443 nm [m^{-1}] (c).

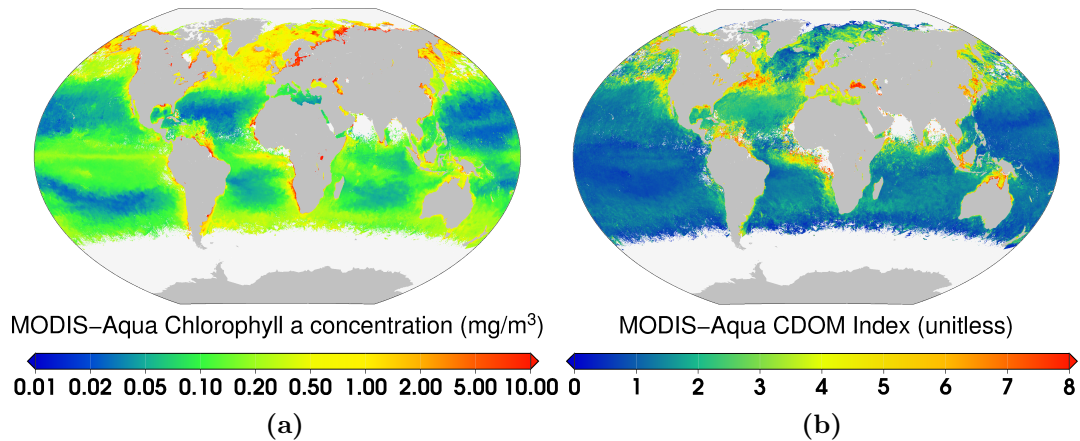


Figure 5.3: Global composites of (a) MODIS-Aqua Chlorophyll *a* concentration and (b) CDOM index for June and July 2009.

factors and MODIS-Aqua GSM a_{cdm}) for a region of especially high CDOM concentrations was studied in more detail (Fig. 5.4). The chosen region is located in the part of the Atlantic near the river mouth of the Amazon river, which is strongly affected by the high terrestrial CDOM loading the ocean, and where the highest CDOM absorption in surface waters of open ocean was found in the study by Nelson & Siegel (2013). Here, the spatial structure of the Amazon plum is not seen by the CDOM fluorescence retrieval around 345 nm (Fig. 5.4a), and the results are again dominated by RRS. In the case of the retrieval around 485 nm, the observed pattern is, as previously, reflecting inversely the CDOM distribution observed by the GSM a_{cdm} product (Fig. 5.4b). The influence of VRS variation is prevailing, despite the potentially strongest possible impact of CDOM fluorescence.

The presented results stress how difficult it is to apply the DOAS method to retrieve CDOM fluorescence from hyperspectral satellite data, despite it was previously proven possible to estimate other inelastic processes with similar approaches (e.g. Vountas et al., 1998, 2003, 2007). These difficulties arise mainly due to the overwhelming impact of other inelastic processes (RRS, VRS) in the spectral region of CDOM fluorescence. Still, for coastal areas, where VRS is weak, fluorescence of humic-like CDOM could be a significant source of filling-in. Comprehensive studies to retrieve CDOM composition via fitting of Fraunhofer lines, including a retrieval of amino acid-like fluorescence of DOM (which is excited in UV-wavelengths), are even more difficult.

In addition to looking at filling-in of individual Fraunhofer lines, it could be possible to compare broader spectral structures, as the reference spectra of different CDOM components are distinctly different from RRS and VRS (Fig. 4.1). However, due to diverse composition of CDOM worldwide, these spectral features vary significantly in time and space, and are not precisely known a-priori. Additional adequate EEM measurements, combined use of narrow and broad fluorescence features and an appropriate method to account for inelastic processes are necessary for further investigations of a retrieval of CDOM fluorescence with hyperspectral instruments.

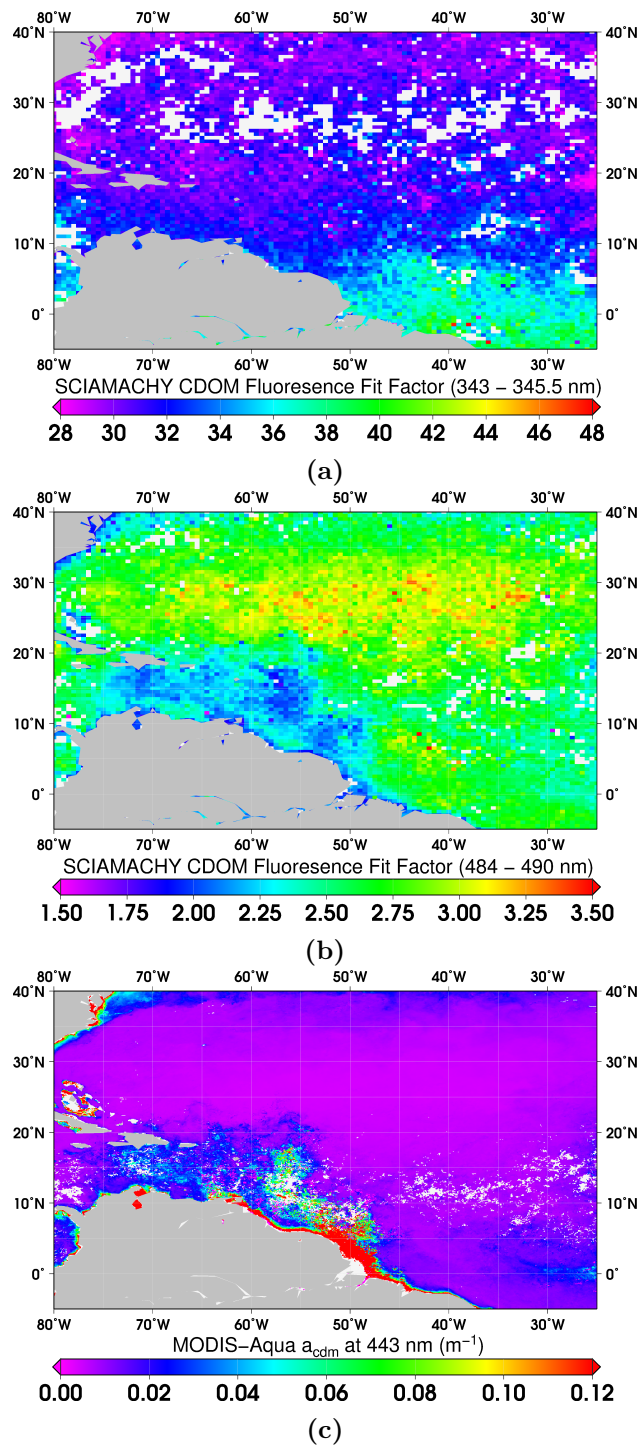


Figure 5.4: Maps of SCIAMACHY CDOM fluorescence fit factors for two months (June and July 2009) in two different spectral regions (a,b) compared with MODIS-Aqua absorption coefficient for dissolved and detrital particulate matter a_{cdm} at 443 nm [m^{-1}] (c), focused on the region near the Amazon discharge.

Chapter 6

Observations of chlorophyll *a* fluorescence and absorption

6.1 Observations of the red peak of chlorophyll *a* fluorescence

6.1.1 Marine chl *a* fluorescence

Chl *a* fluorescence observed with SCIAMACHY

An example of the spectral fit of the SCIAMACHY measurements over ocean, corresponding to one of the smallest chi-square values, is shown in Figure 6.1 (the SCIAMACHY measurements of extraterrestrial irradiance and backscatter radiance for the same scene are shown in Figure 4.5). It follows that the measured differential optical depth (DOD) contains spectral structures of fluorescence (upper right panel) and water vapor (upper left panel), and those are successfully discriminated. The top panels of Figure 6.1 clearly show that the residual of the fit is very low ($\sim 0.02\%$). This indicates that there are no strong unidentified features in the selected spectral window and provides an additional evidence for the validity of the developed retrieval.

The global yearly composite averages of the marine phytoplankton chl *a* fluorescence retrieved from SCIAMACHY for years 2004 - 2011 (Figure 6.2), and separately monthly climatologies calculated for these years are shown (Figure 6.3). In this thesis, all results of chl *a* fluorescence and chl proxy are presented for this period of eight years (2004-2011). Although retrievals were also performed on the measurements from the year 2003, these data were not included in the global composites. Many orbits of SCIAMACHY measurements during year 2003 have been excluded due to instrumental issues and adjustments in the first year of the SCIAMACHY mission (information on the operation of the SCIAMACHY instrument can be found on the website of the SCIAMACHY Operations Support Team at <http://atmos.caf.dlr.de/projects/scops/>). This resulted in a smaller number of pixels per grid cell for the year 2003 in the designed retrievals, as compared to other years (compare Figure 6.6 and 6.7, and see Figure 6.24). Since the data presented in the time series of

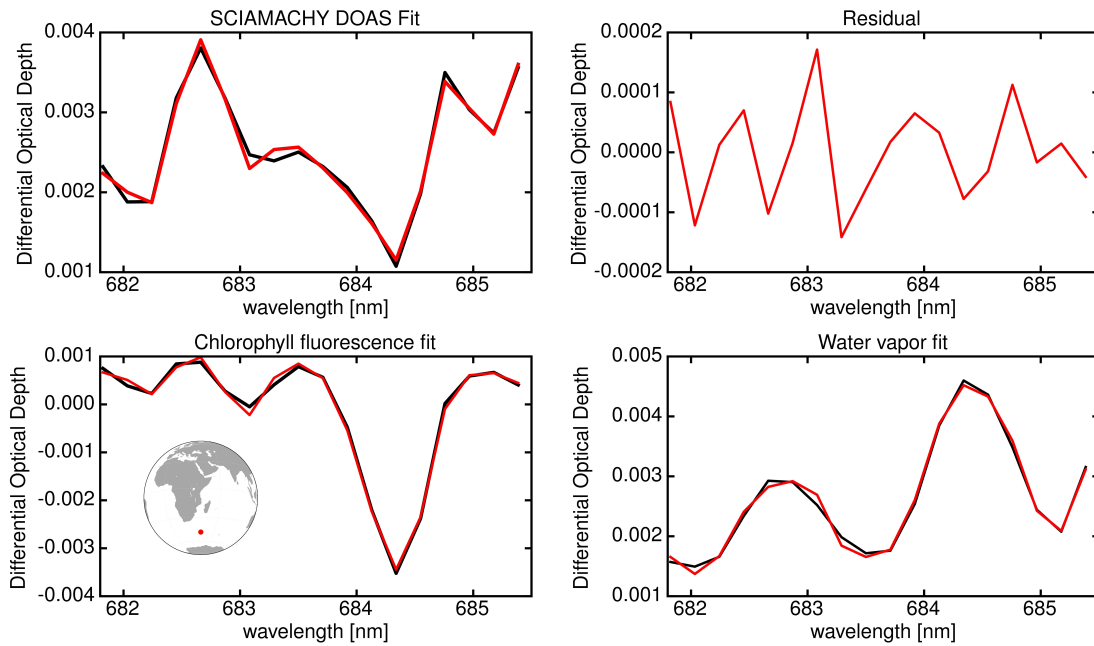


Figure 6.1: Example of a SCIAMACHY Fluorescence DOAS Fit over ocean (9th April 2009; lat = 47° S, lon =40° E). 1) Top left panel: the fitted DOAS DOD (red) and measured DOD (black). 2) Top right panel: the residual from the DOAS fit. 3) Bottom left panel: the scaled chl *a* fluorescence reference spectrum (red) and chl *a* fluorescence fit (black). 4) Bottom right panel: the scaled water vapor reference spectrum (red) and water vapor fit (black).

marine phytoplankton red chl *a* fluorescence in Section 6.1.1 were averaged over very big oceanic regions, the measurements from the year 2003 were also included in the time series to extend the yearly coverage. However, the terrestrial regions that were investigated in Section 7 are much smaller, and furthermore, the chl proxy retrieval had an exceptionally low number of pixels retrieved for year 2003 as compared to other years (Figure 6.24). Hence, the measurements from the year 2003 were excluded in case of the time series analysis over land in Section 7.

The data points were gridded in 0.5° by 0.5° boxes, which roughly corresponds to two SCIAMACHY ground scenes at the equator. The SCIAMACHY results are presented in the form of FLH as defined by Eq. 4.19. Yearly averages of chl *a* concentration from MODIS Terra (<http://oceancolor.gsfc.nasa.gov/cgi/l3>) for the same years are shown in Figure 6.4.

In general, strong fluorescence signal is observed in areas of high chl *a* concentration, although the relationship is not thought to be constant (Behrenfeld et al. 2009 and references therein). The highest fluorescence values are observed in the North Atlantic, the North Pacific, and in many coastal areas. Because of the coarse spatial resolution of SCIAMACHY data, small areas of high fluorescence very close to the shore are averaged across the larger scene, and thus are not well resolved. For larger coastal regions (e.g. Persian Gulf and the upwelling regions along the west coast of Africa) high fluorescence values are derived, but not for narrow marine regions, such as the Gulf of Ob (Northern

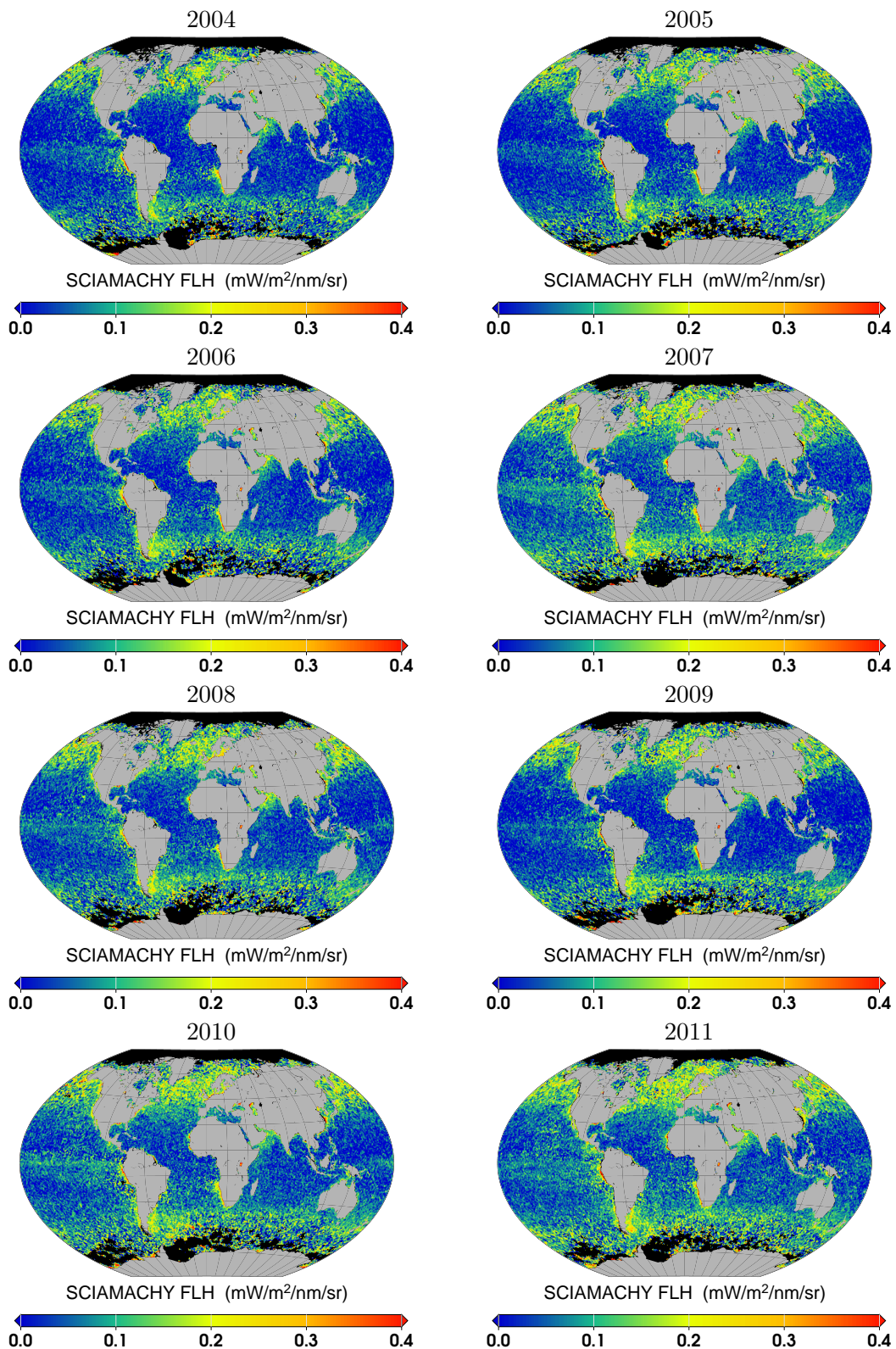


Figure 6.2: Global yearly composites of SCIAMACHY FLH for years 2004-2011.

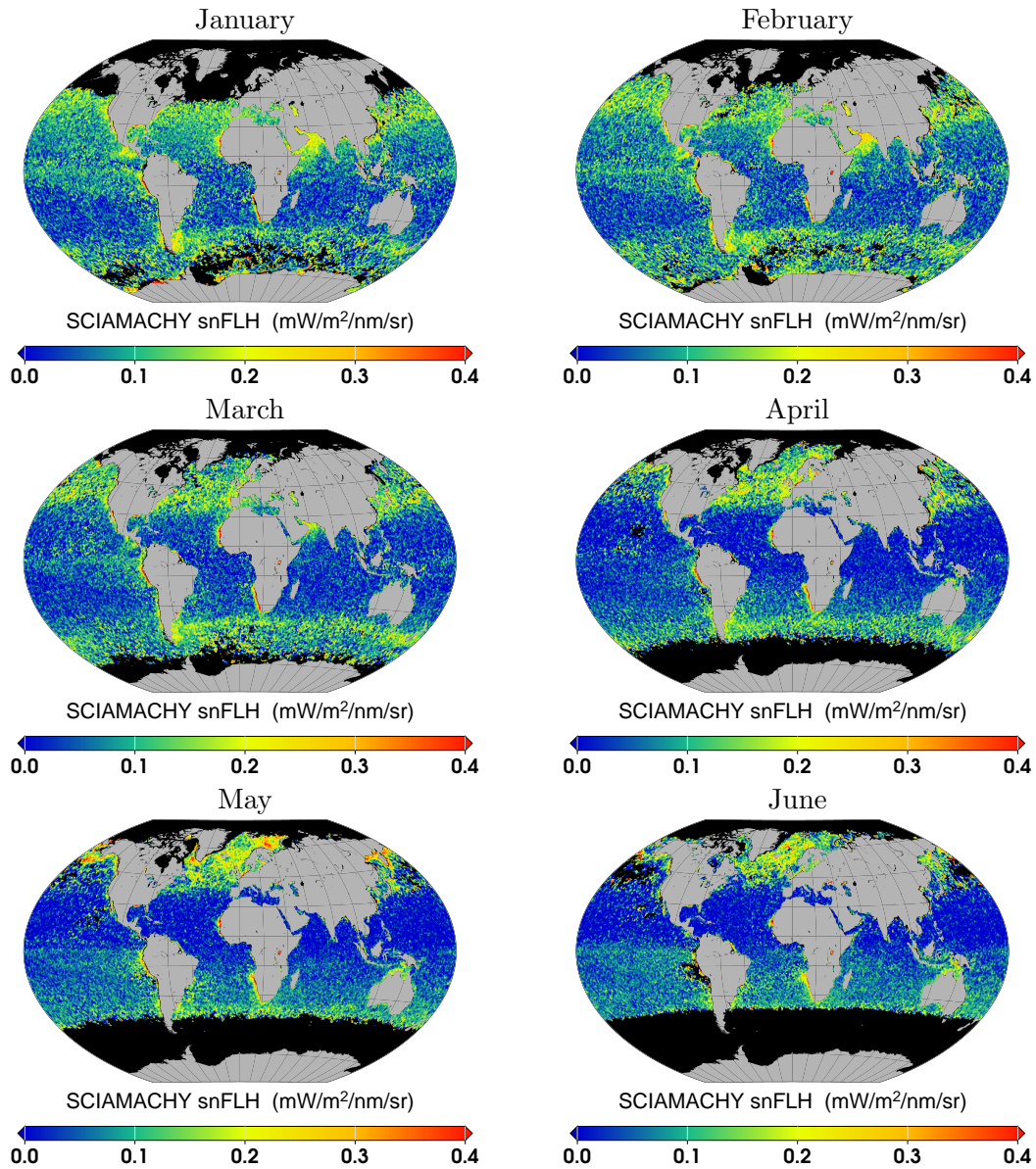


Figure 6.3: Global monthly composites of SCIAMACHY FLH for years 2004-2011.

Russia). The interannual variability is also readily observed in the SCIAMACHY FLH data, e.g. stronger phytoplankton blooms at the coast of Antarctica, which are observed in 2009 in MODIS Terra Chl *a* maps, are also clearly noticeable in the SCIAMACHY FLH results. Some values in the Atlantic east of Brazil are attributed to instrumental noise originating from the passage of the instruments through the South Atlantic Anomaly (SAA) (Soest et al., 2005). This effect is also visible in the chi-square values of SCIAMACHY (Figure 6.5a).

It is important to note when comparing the yearly global composites, that at high-latitude areas ground scenes are only available for measurements during a limited time of the year.

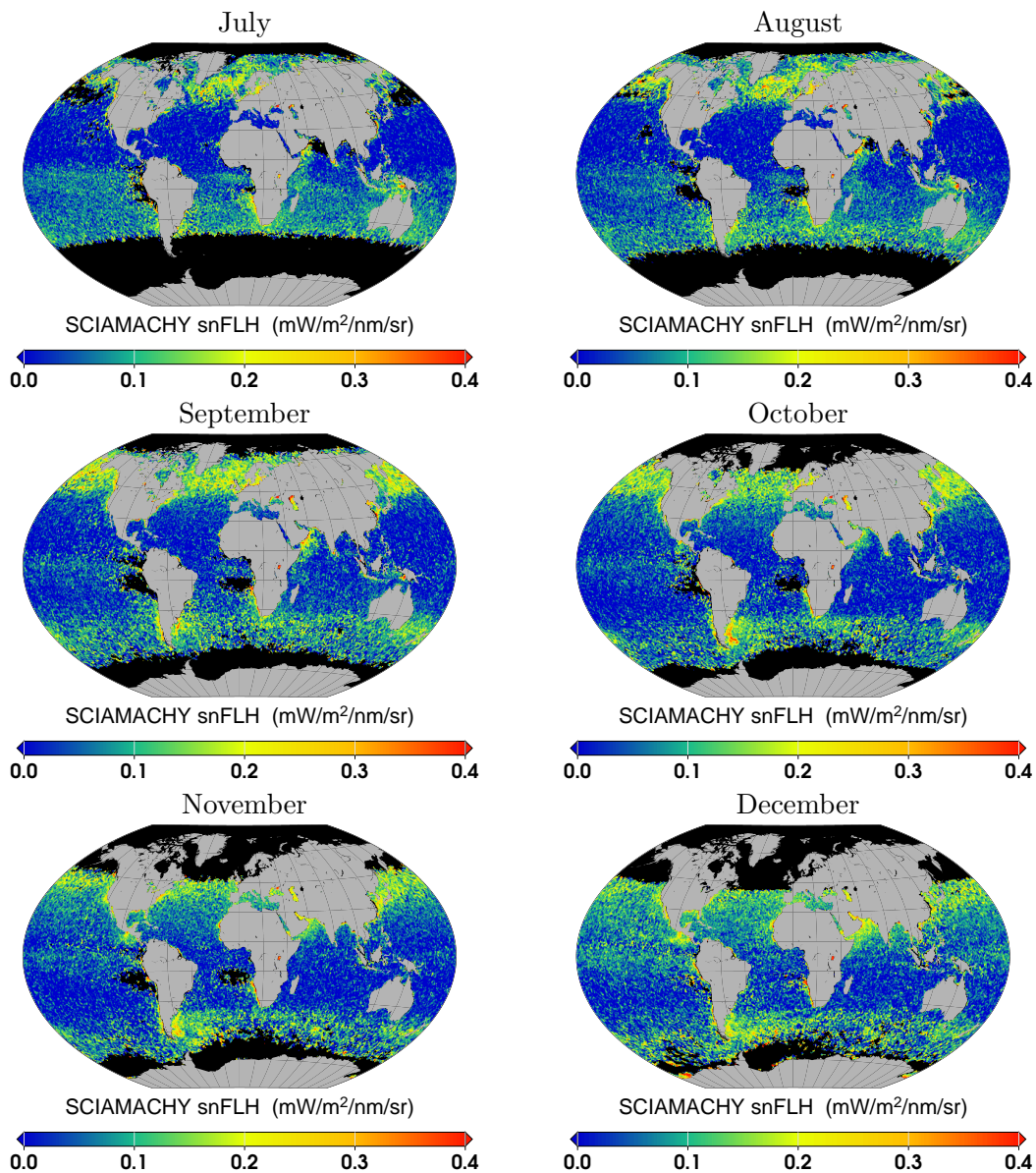


Figure 6.3: Global monthly composites of SCIAMACHY FLH nm for years 2004-2011.

Areas, which are covered by ice or clouds during some period in the year, are biased towards the cloud or ice free period (e.g. Indian monsoon region, which is mostly cloudy during the summer monsoon season). The number of data points of the retrieval per grid pixel for both instruments for year 2009 is compared with MODIS cloud fraction for year 2009 in Figure 6.6. In case of SCIAMACHY data, the number stays relatively similar for other years (Figure 6.7), although there were minor breaks in the data delivery in the first year of the SCIAMACHY operation time. The number of points is inversely proportional to the global cloud fraction (during daytime only) product from MODIS. Very cloudy regions are poorly-sampled and high latitudes are additionally limited by the

6. OBSERVATIONS OF CHLOROPHYLL A FLUORESCENCE AND ABSORPTION

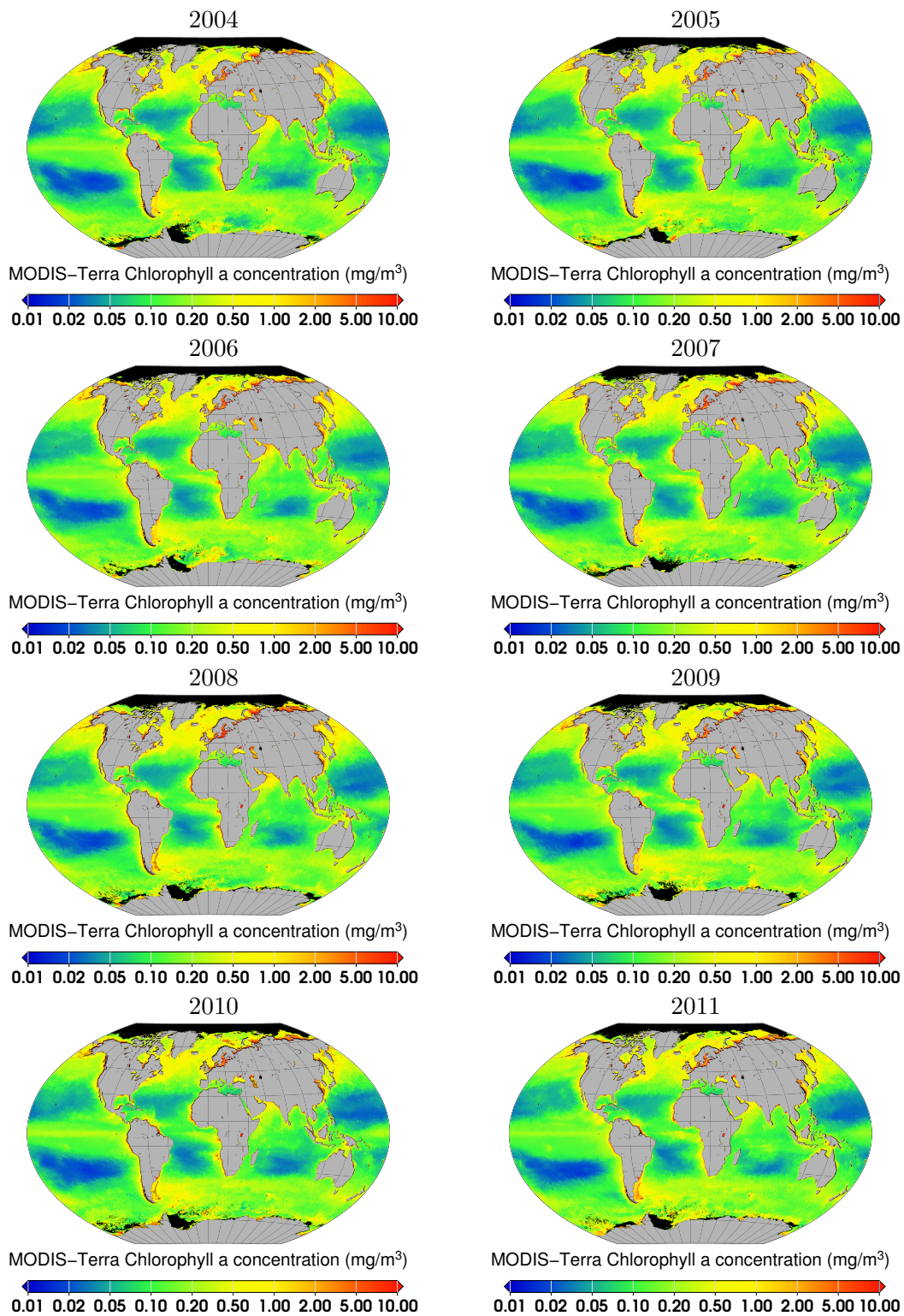
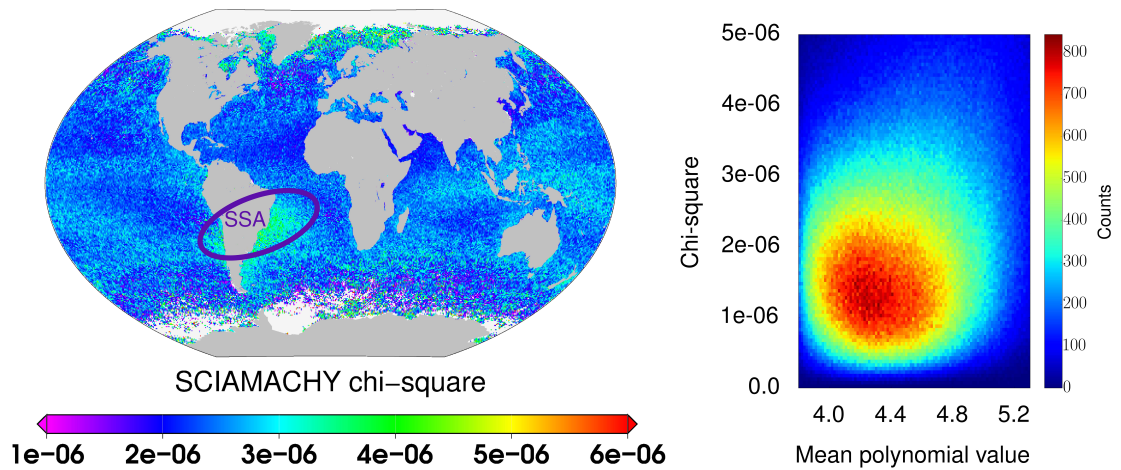
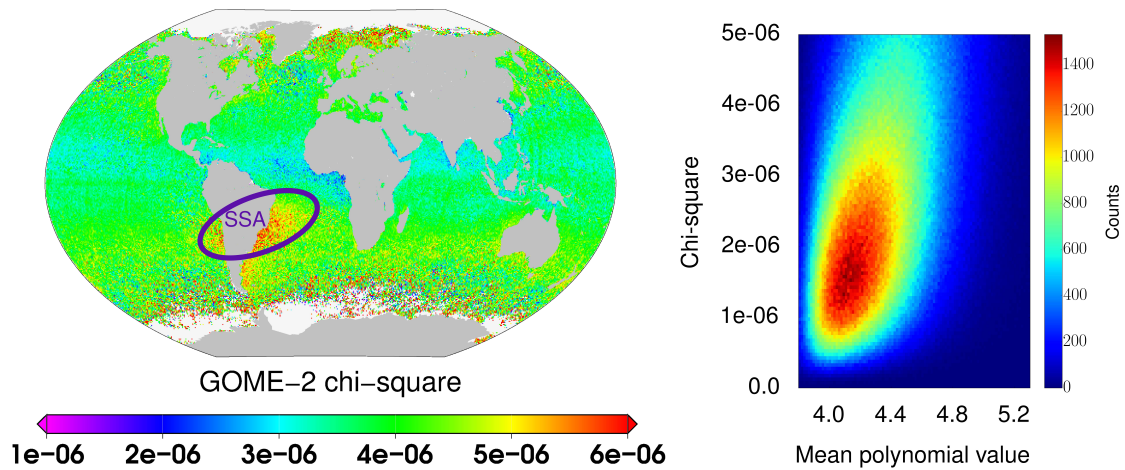


Figure 6.4: Global yearly composites of MODIS Terra Chl *a* concentration for years 2004-2011.



(a) SCIAMACHY chi-square values for year 2009



(b) GOME-2 chi-square values for year 2009

Figure 6.5: Global maps of chi-square for DOAS fluorescence retrieval applied to SCIAMACHY and GOME-2 for the year 2009, with the location of the South Atlantic Anomaly (SAA) circled (left panel).

high solar zenith angle. Because of the large pixel size and limb-nadir observation mode of SCIAMACHY, less cloud and ice free scenes are available as compared to multispectral sensors with higher spatial resolution.

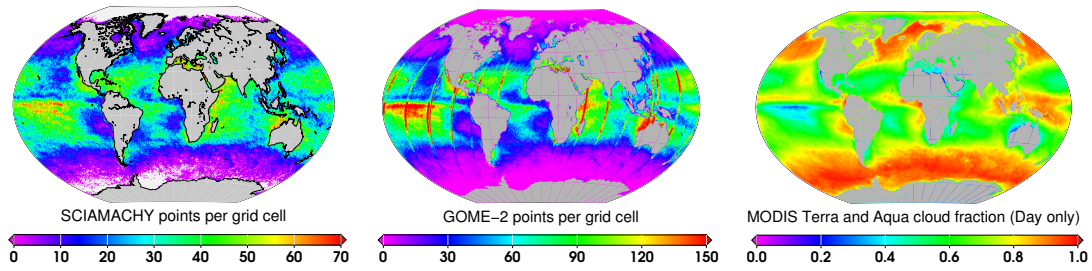


Figure 6.6: Global maps of SCIAMACHY and GOME-2 number of points per grid cell of the red chl *a* fluorescence retrieval compared with MODIS cloud fraction (Day only) for year 2009. Stripes in the GOME-2 figure result from measurements made with the narrow swath mode.

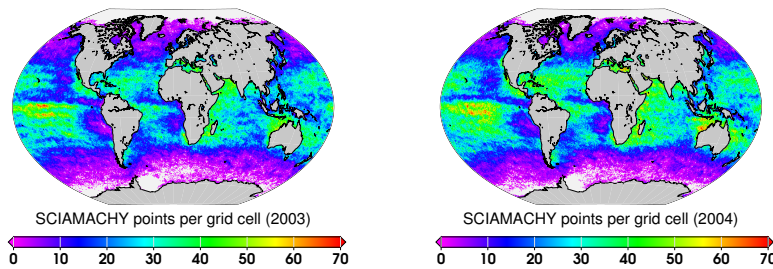


Figure 6.7: Global maps of SCIAMACHY number of points per grid cell of the red chl *a* fluorescence retrieval for years 2003 and 2004.

Comparison to MODIS Chl *a* and MODIS nFLH

The SCIAMACHY FLH data should be verified by performing a comparison with independent measurements of sun-induced chl *a* fluorescence. Both MERIS and MODIS instruments provide measurements in spectral bands designed to map the chl *a* fluorescence signal (Gower & King, 2012).

Mapped MODIS nFLH data are easily available online (at <http://oceandata.sci.gsfc.nasa.gov/>), whereas MERIS data need to be derived from the Level 1 product. Hence, it was decided to use MODIS data, as it was shown that MODIS and MERIS measurements of FLH agree closely (Gower & King, 2004). In particular, SCIAMACHY results were compared to MODIS Terra Level 3 standard product nFLH (<http://oceancolor.gsfc.nasa.gov/cgi/l3>). Although for such comparison the MODIS Aqua data can also be used, MODIS Terra was given preference, because the time of MODIS Terra overpass is similar to SCIAMACHY (~ 10.00 local time for ENVISAT; ~ 10.30 and ~ 13.30 for Terra and Aqua, respectively). Different overpass time of satellites impacts the retrieved fluorescence values, as the fluorescence increases as photochemistry saturates.

It is important to point out that the SCIAMACHY FLH corresponds to the fluorescence energy retrieved in the Fe I Fraunhofer band in the spectral window 681.8 nm to 685.5 nm, whereas the MODIS nFLH is the difference between the spectral band L_{14} and the mean of bands L_{13} and L_{15} . Thus the two retrievals are measuring fluorescence in different

ways and in different, but overlapping, spectral windows. Therefore, the amount of energy determined by the two techniques is not expected to be identical.

The yearly composite average nFLH values from MODIS Terra for the years 2004-2011 are presented in Figure 6.10. Comparing these data to the SCIAMACHY FLH and snFLH values presented in Figures 6.2 and 6.8, one can see a good spatial agreement between both data sets. After applying the simplified normalization, the values of SCIAMACHY snFLH are higher than SCIAMACHY FLH, especially snFLH close to the Antarctic coast is much more pronounced, and equatorial values are smaller as compared to high latitudes.

However, SCIAMACHY snFLH are also higher than MODIS nFLH. It is expected as the spectral window of the retrieval is placed exactly at the top of fluorescence emission, as opposed to the MODIS algorithm. The measured MODIS nFLH responds to only 57% of the actual fluorescence signal (Gower et al., 2004), as discussed in Section 2.2.3. Another possible reason of observed discrepancies can be the overestimated τ_a , used for calculating $E_{d,s}(0^+W_F)$. The slightly earlier time of overpass of SCIAMACHY can also lead to different values.

It is important to note that after applying all corrections some negative values for SCIAMACHY data were obtained. These negative values can be caused by random noise (especially in cases close to the fluorescence detection limit) and when the applied corrections (for water vapor and Raman scattering) are overestimated (see Eq. 4.14). Negative values occur also for the MODIS nFLH algorithm, where they are removed assuming bad atmospheric correction or cloud contamination (Behrenfeld et al., 2009). However, in a more recent study it was suggested that the negative values represent a normal distribution of the data and arise from noise in the sensor, as they were found to constitute an increasing part of pixels with decreasing chl *a* concentration (Huot et al., 2013). Following this recommendation negative fit values were included in the averages, except for measurements which were removed by the quality checks. Nevertheless, excluding negative values does not significantly change the results presented in Figures 6.2 and 6.8.

Comparing the multispectral MODIS and hyperspectral DOAS results, one has to keep in mind that the position of spectral bands used in MODIS fluorescence retrieval algorithm reflects an assumed spectral shape of fluorescence. In particular, the fluorescence band is centered at 678 nm near the maximum of the fluorescence signal located at 685 nm (see Section 2.2.3). However, as shown by Gitelson (1992) and Xing et al. (2007), the apparent peak in the water leaving radiance is shifted toward longer wavelengths with increasing chl *a* concentration, due to the strong chl absorption in red wavelengths (and re-absorption of chl *a* fluorescence). The impact of this shift on nFLH is discussed by Gower & King (2004), who suggested that for retrieving chl *a* fluorescence at high chl *a* concentrations, the measurements at longer wavelengths should be used additionally. Moreover, owing to the differences in light harvesting systems (pigment-protein binding in particular), especially in dinoflagellates and cyanobacteria (e.g., MacIntyre et al., 2010; Millie et al., 2002), the peak wavelength of fluorescence depends also on the species composition of phytoplankton. Thus, for example, phycocyanin-rich cyanobacteria have an additional emission peak at ~ 655 nm due to phycocyanin (Simis et al., 2012; MacIntyre et al., 2010), which is close to the first chosen baseline for the MODIS algorithm (667 nm). Therefore, in the case of multispectral retrievals the position of spectral bands for the nFLH retrieval can lead to a

smaller sensitivity and lower fluorescence values. It was also noted that during blooms of some cyanobacteria species the fluorescence signal is overwhelmed by scattering at longer wavelengths (peaks at 700-710 nm), which can lead to negative values of nFLH (Wynne et al., 2008). Hence, a computationally equivalent to the negative values of MODIS nFLH has been used to detect cyanobacteria blooms in Lake Erie, first with MERIS (Wynne et al., 2013b) and then with MODIS data (Wynne et al., 2013a).

In contrast to the multispectral retrievals, the hyperspectral method presented here uses a narrow spectral window for detecting the fluorescence emission, and subtracts a polynomial from the reference spectrum of fluorescence to account for broad-band features. The shape of the whole fluorescence emission band, and especially the apparent position of the fluorescence peak, is not relevant for the algorithm. It was demonstrated for terrestrial vegetation fluorescence retrievals using satellite hyperspectral data, that small changes in the fluorescence emission spectrum have indeed little impact on the estimated fluorescence values (Joiner et al., 2013; Fournier et al., 2012).

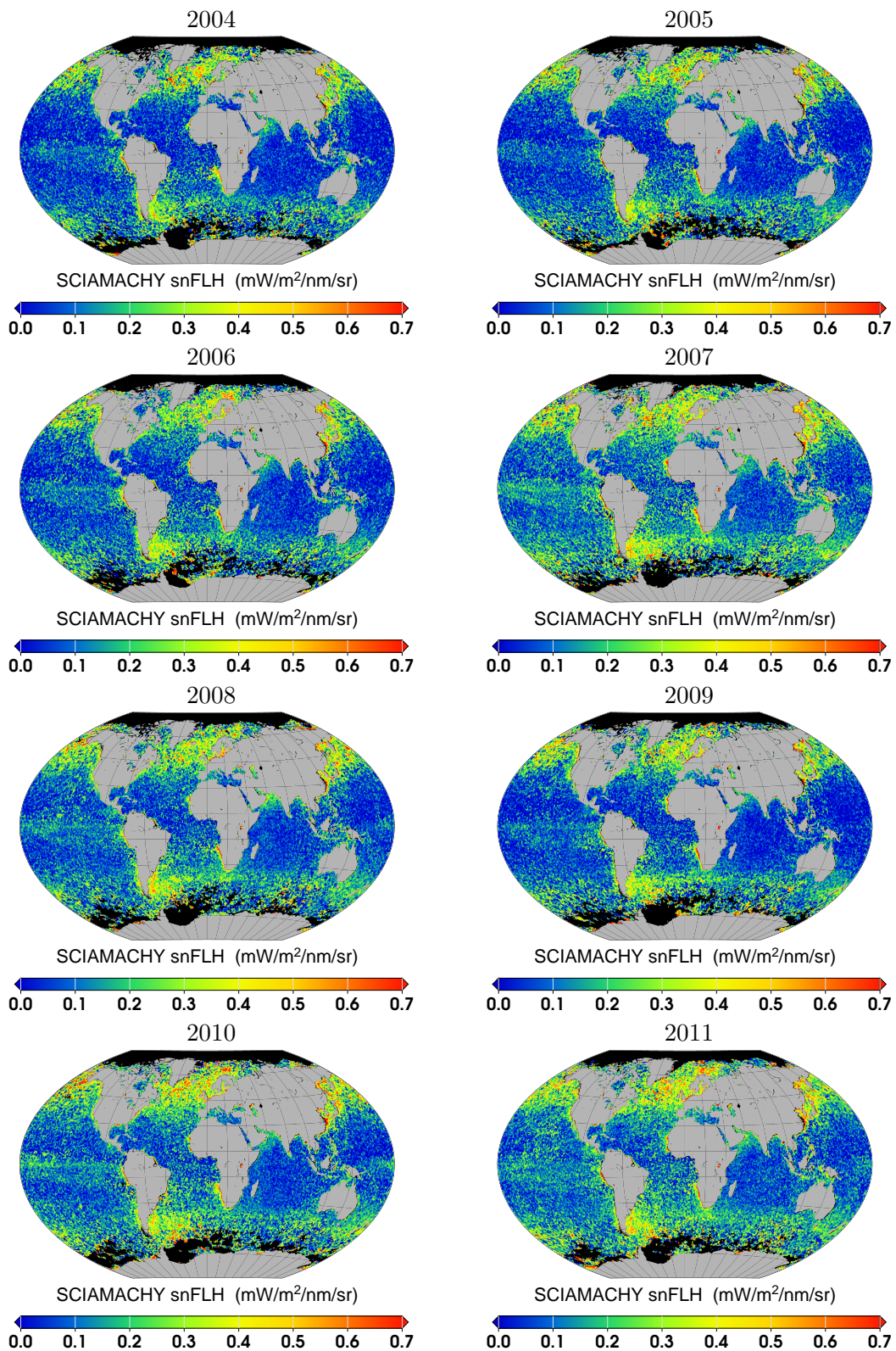


Figure 6.8: Global yearly composites of SCIAMACHY snFLH for years 2004-2011.

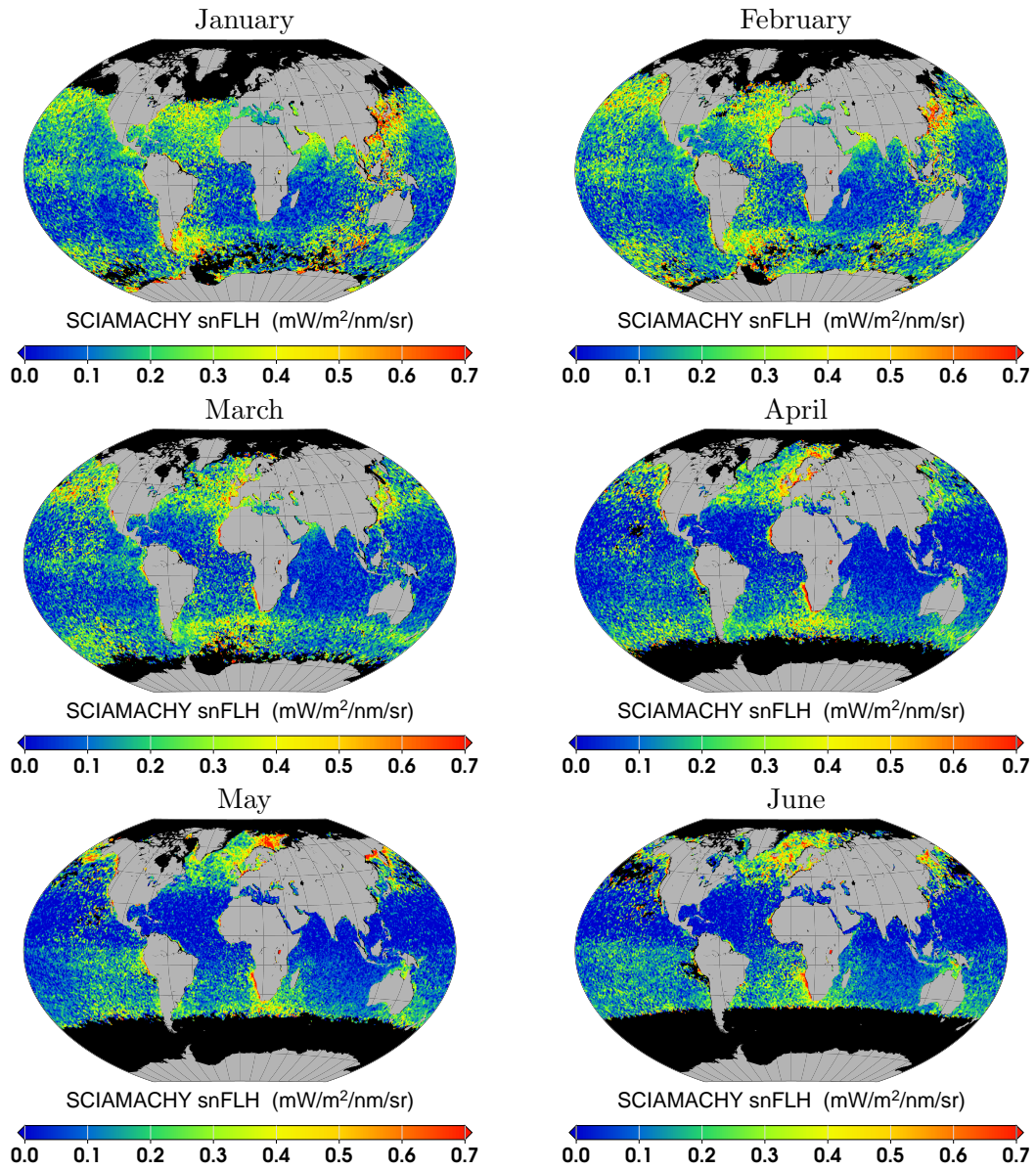


Figure 6.9: Global monthly composites of SCIAMACHY snFLH for years 2004-2011.

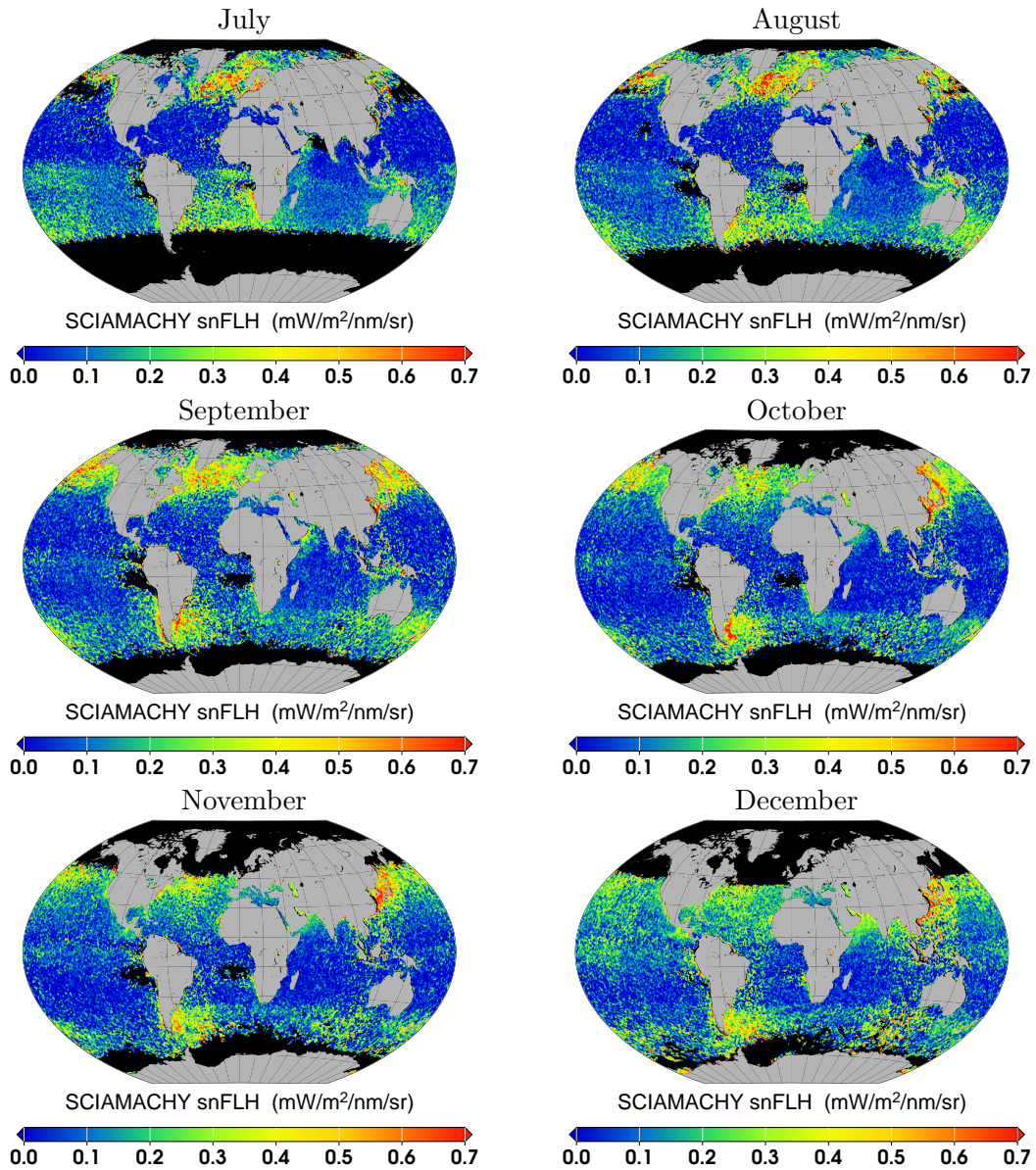


Figure 6.9: Global monthly composites of SCIAMACHY snFLH nm for years 2004-2011.

6. OBSERVATIONS OF CHLOROPHYLL A FLUORESCENCE AND ABSORPTION

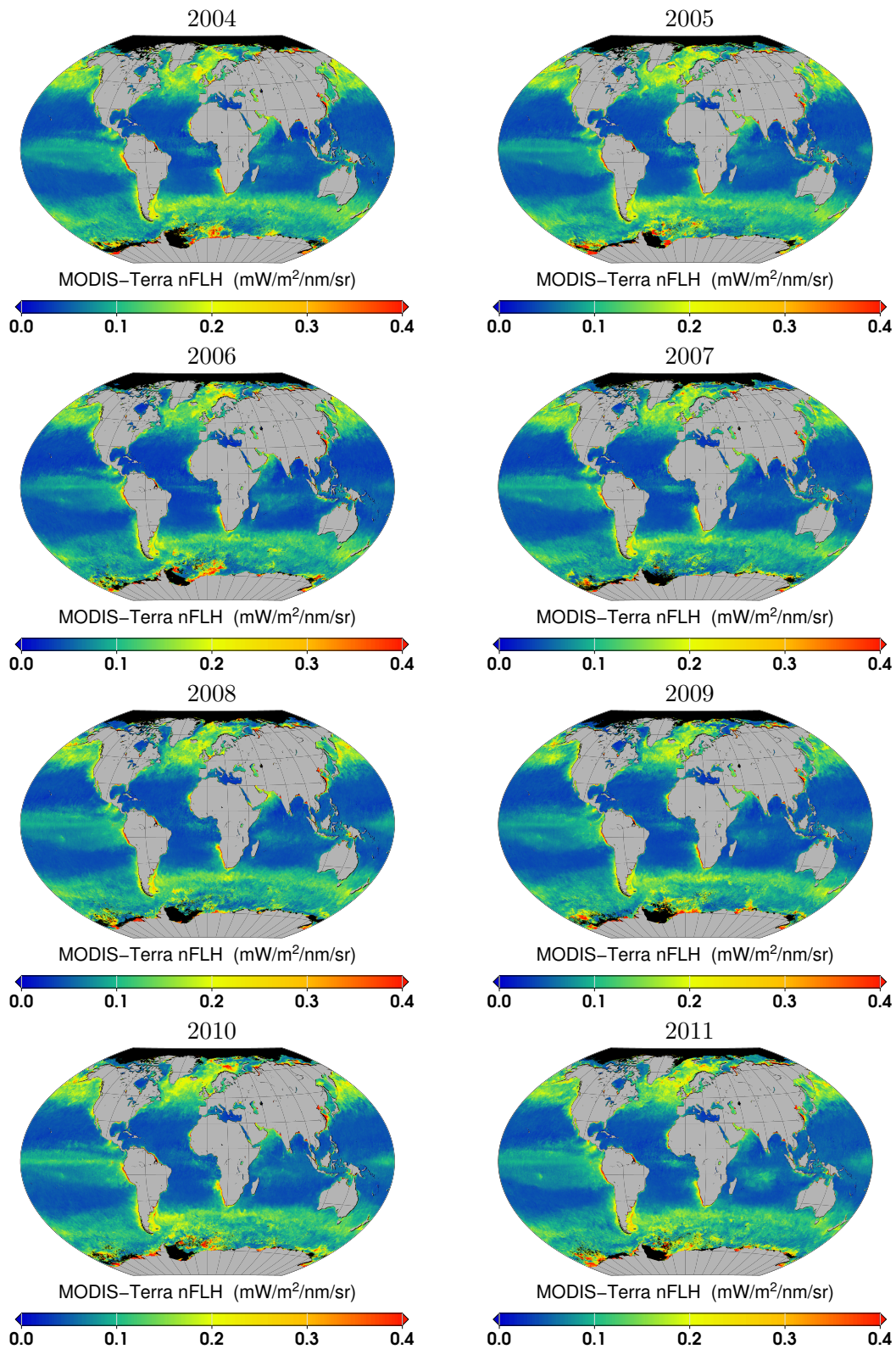


Figure 6.10: Global yearly composites of nFLH MODIS Terra for years 2004-2011.

Temporal variations in SCIAMACHY marine chl *a* fluorescence

As an example of possible application of SCIAMACHY chl *a* fluorescence results for open ocean waters, time series of monthly SCIAMACHY FLH values averaged over two regions were presented, in comparison to other satellite products and climate variables.

Firstly, the results from the region in the Indian Ocean near the coast of Madagascar are shown. This region exhibits low chl *a* concentrations ($< 0.1 \text{ mg/m}^3$, shown as MODIS Chl *a* in Figure 6.11 a), as it is located in the oligotrophic waters of the Indian Gyre. A seasonal cycle typical for all ocean gyres is observed, for which the common forcing factor is the change in surface thermal forcing that stimulates shallowing of mixed layers and increase of dynamic heights within the gyres. The higher dynamic height indicates strengthening of the gyre circulation and consequently promotes deepening of thermocline/nutricline, which combined with shallower mixed layer depths, reduces the transport of nutrients to the euphotic zone. As a result, chl *a* concentration is reduced during the austral summer, and the opposite occurs for the austral winter cooling period (Signorini & McClain, 2007, 2012). On top of this clear seasonal cycle, the additional

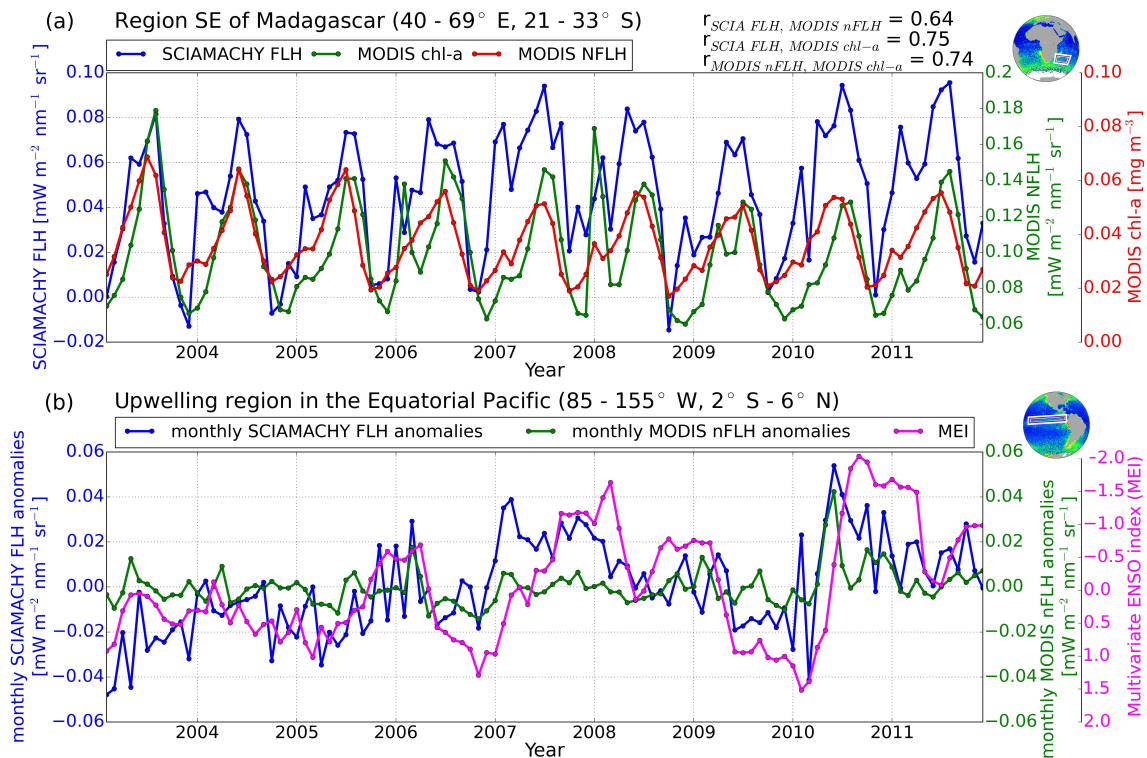


Figure 6.11: Time series of SCIAMACHY FLH for selected regions: a) compared with MODIS nFLH and MODIS Chl *a* concentration products for the region SE of Madagascar (40 - 69° E, 21 - 33° S); b) SCIAMACHY FLH monthly anomalies compared with monthly anomalies of MODIS nFLH and Multivariate ENSO index (MEI) for the upwelling region in the Equatorial Pacific (85 - 155° W, 2° S - 6° N). Correlations shown in (a) are significant at $p < 0.01$

Table 6.1: Correlation coefficients for variables shown as anomalies (an.) in Figure 6.11 b, for the upwelling region in the Equatorial Pacific (85 - 155°W, 2°S - 6°N). All correlations are significant at $p < 0.01$.

| | SCIA FLH an. | MODIS nFLH an. | MODIS Chl <i>a</i> an. | MEI | MODIS SST an. |
|------------------------|--------------|----------------|------------------------|---------|---------------|
| SCIA FLH an. | | 0.4418 | 0.3664 | -0.5624 | -0.5561 |
| MODIS nFLH an. | 0.4418 | | 0.7815 | -0.4188 | -0.4991 |
| MODIS Chl <i>a</i> an. | 0.3664 | 0.7815 | | -0.3211 | -0.5360 |
| MEI | -0.5624 | -0.4188 | -0.3211 | | 0.8362 |
| MODIS SST an. | -0.5561 | -0.4991 | -0.5360 | 0.8362 | |

impact of the Madagascar bloom is observed for most of the years. It occurs typically early in the year and then spreads eastward during the next weeks, creating a feature called a plankton wave (Srokosz, 2004). This feature is one of the largest phytoplankton blooms in the world ocean, and has received much attention in the recent years (e.g. Longhurst, 2001; Srokosz, 2004; Lévy et al., 2007; Uz, 2007; Raj et al., 2010; Huhn et al., 2012; Srokosz & Quartly, 2013). Interannual variability of this phytoplankton bloom is linked to the upwelling along the south coast of Madagascar, precipitation along the east coast of Madagascar, light limitation and local mesoscale circulation features (Raj et al., 2010). The time series of SCIAMACHY FLH and MODIS nFLH follow for most parts the variability of MODIS Chl *a* concentration. Correlation coefficients between the three parameters are high (similar for SCIAMACHY FLH and MODIS nFLH to MODIS Chl *a*: 0.75 and 0.74, respectively, and weaker between the two fluorescence variables). SCIAMACHY FLH values for this region indicate robustness of the retrieval, since both features, the seasonal cycle and the plankton wave, can be observed.

A second time series is presented for the equatorial Pacific region, for which the El Niño/Southern Oscillation (ENSO) is the dominant source of interannual climate variability (Figure 6.11b). During “normal” or La Niña conditions, the Pacific equatorial ecosystem is productive due to the supply of nutrients to the euphotic zone in the cold tongue of waters upwelled in the eastern equatorial Pacific and stretching westward to the date line (Wyrtki, 1981). During El Niño conditions, physical forcing dramatically reduces phytoplankton productivity, impacting food webs across the equatorial and coastal environments of the eastern tropical Pacific (e.g. Barber & Chavez, 1983; Barber & Chávez, 1986; Chavez et al., 1999; Strutton & Chavez, 2000; Ryan et al., 2002; Strutton et al., 2008). ENSO can be monitored with the Multivariate ENSO Index (MEI), which is based on the climate variables observed over the tropical Pacific (Wolter & Timlin, 1998). The MEI is positive in El Niño phase and negative in La Niña phase (data available at NOAA Earth Systems Research Laboratory, <http://www.esrl.noaa.gov/psd/enso/mei/>). The evident link between biology and the physical environment related to climate variability expressed by MEI has been shown for the Equatorial Pacific in the study by Rousseaux & Gregg (2012). In this study, high correlations between monthly anomalies of SCIAMACHY FLH and MEI and MODIS sea surface temperature product (MODIS SST) are also observed (Figure 6.11b and Table 6.1). MODIS SST data used in this study were produced with the Giovanni online data system, developed and maintained by the NASA GES DISC. SST is one of the input variables for calculating MEI and is directly related to the upwelling conditions. MODIS FLH and Chl *a* products are also significantly correlated to MEI and MODIS SST (Table 6.1). In essence, SCIAMACHY fluorescence can be used to observe seasonal variability in phytoplankton community and its response to climate fluctuations

for the equatorial Pacific.

Chl *a* fluorescence observed with GOME-2

The fluorescence signal from oceans was also retrieved with the data from GOME-2 onboard MetOp-A instrument for the year 2009 (Figure 6.12). MetOp-A has a slightly earlier overpass time than ENVISAT, $\sim 9:30$ a.m. As a result, the solar zenith angle of the ground scene is larger for GOME-2 than for SCIAMACHY and the observed fluorescence signal is expected to be weaker. Some regions of very strong fluorescence are retrieved from the measurements of both sensors, but it is noticeable that the negative values are more frequent for the GOME-2 results. This is attributed to the smaller fluorescence signal associated with higher SZA and the fact that the slit function is broader for GOME-2 than for SCIAMACHY, making the separation of spectral features of chl *a* fluorescence from water vapor absorption more difficult. While the retrievals' threshold for chi-square values is the same for both instruments, the chi-square values are substantially higher for GOME-2 than for SCIAMACHY (Figure 6.5 b). For SCIAMACHY, 82% of pixels of yearly composite for 2009 have a chi-square value smaller than $3 \cdot 10^{-6}$, while for GOME-2 it is only 23%. The number of high chi-square values increases for darker scenes (right panel of Figure 6.5 b). There are also larger errors for GOME-2 observed in the SAA region, as compared to SCIAMACHY retrieval results. It is difficult to remove those erroneous measurements from global composites by setting a lower chi-square threshold, because such observations are scattered globally. In addition, the GOME-2 ground scene used in this study is larger (40 km x 80 km) than SCIAMACHY, which further increases the chance of the cloud contamination and thus reduces the number of measurements available. Overall, the GOME-2 results are significantly noisier than the SCIAMACHY results.

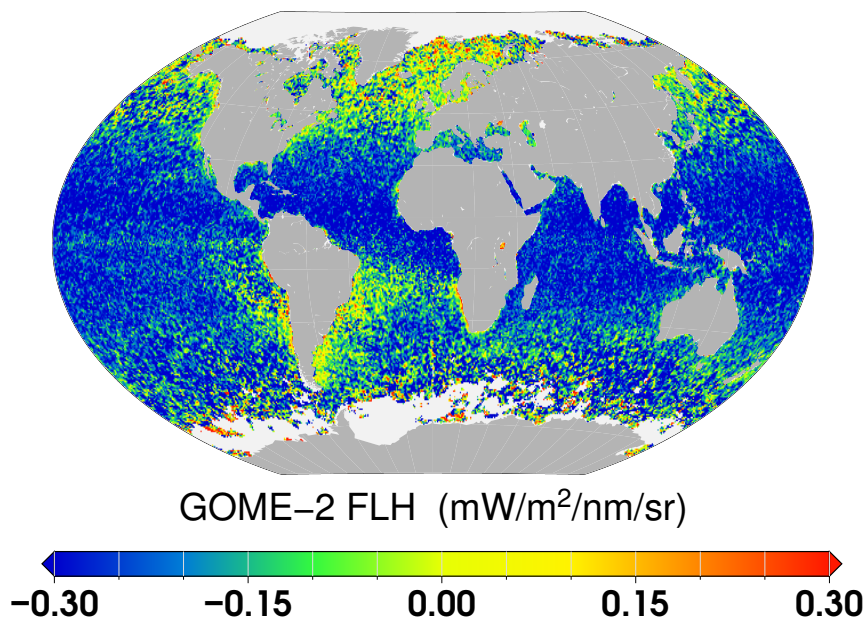


Figure 6.12: Global map of FLH from GOME-2 for year 2009

The regions of strong fluorescence are still readily identified in GOME-2 FLH, e.g., summer phytoplankton blooms in the North Atlantic Ocean, the Benguela Upwelling or the Peruvian Coastal Upwelling. The enhanced chl *a* concentration at the edges of the Antarctic coast is also observed. However, a lot of negative values for GOME-2 chl *a* fluorescence in most oceanic regions have been obtained. Some regions of increased chl *a* concentration, though discernible, still display negative values (e.g. the increased chl *a* at 40° S belt in Indian Ocean, or the upwelling in Equatorial Pacific).

It is advantageous to apply the fluorescence retrieval to GOME-2 data, because the satellites, which are already in orbit (MetOp-A, MetOp-B), and the upcoming satellite MetOp-C, provide potentially a long time series of chl *a* fluorescence data. Because of the broader slit function of the GOME-2 instrument, for future studies of the retrievals of chl *a* fluorescence at its red peak, it might be more advantageous to additionally make use of filling-in of telluric absorption lines, following the approach by Joiner et al. (2013). The application of the developed method to other hyperspectral instruments will also be possible after optimization for the particular instrument.

6.1.2 Terrestrial chl *a* fluorescence

The chl *a* fluorescence retrieval, designed in the first place for ocean application, can be also applied to retrieve the fluorescence signal originating from chl *a* of land vegetation. In general, the fluorescence over land is more intense than over the ocean because of the higher amount of chl *a* in terrestrial plants and lower variability in the spatio-temporal distribution of chl (as plants do not drift with water masses like phytoplankton does). In addition, fluorescence retrieved over land is not affected by VRS on water molecules.

Chl *a* fluorescence observed with SCIAMACHY

An example of the spectral fit of the SCIAMACHY measurements over land, corresponding to one of the smallest chi-square values, is shown in Figure 6.13, analogously to Figure 6.1. Spectral structures of fluorescence (upper right panel) and water vapor (upper left panel) are again successfully discriminated. The top panels of Figure 6.13 show that the residuals of the fit are very low ($\sim 0.02\%$), which again supports previous statement, that there are no strong unidentified features in the selected spectral window.

As shown for marine results, the global yearly composite averages of the terrestrial chl *a* fluorescence retrieved from SCIAMACHY for years 2004 - 2011 (Figure 6.14), and separately monthly climatologies calculated for these years (Figure 6.15) are shown. The data points were, as previously, gridded in 0.5° by 0.5° boxes.

Overall, yearly composites reflect typical global vegetation distribution. However, for earlier years, the boundaries of the highly vegetated regions are sharper, and get more blurred and noisy for later years. This issue might be related to the instrument degradation over time. The seasonal cycle of the vegetation in the Northern Hemisphere is very well captured in the monthly climatologies (Figure 6.15). A distinct pattern is less pronounced for the Southern Hemisphere, as values in South America are disrupted by SAA, and

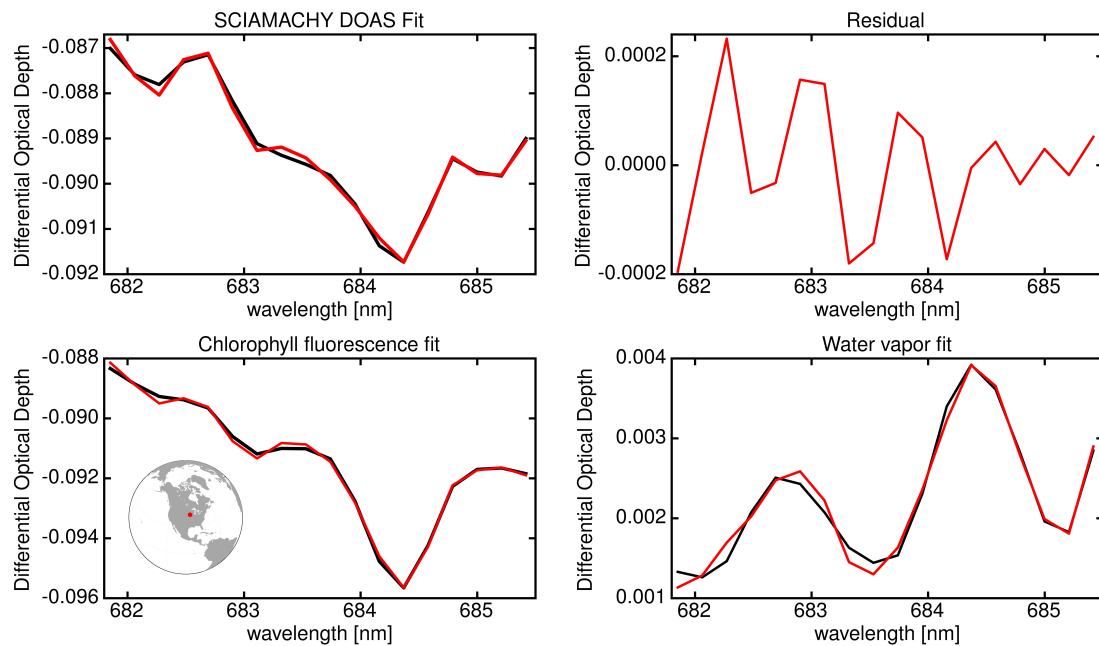


Figure 6.13: Example of a SCIAMACHY Fluorescence DOAS Fit over land (31st July 2009; lat = 42° N, lon =94° W). 1) Top left panel: the fitted DOAS DOD (red) and measured DOD (black). 2) Top right panel: the residual from the DOAS fit. 3) Bottom left panel: the scaled chl *a* fluorescence reference spectrum (red) and chl *a* fluorescence fit (black). 4) Bottom right panel: the scaled water vapor reference spectrum (red) and water vapor fit (black).

the vegetation cycle in Africa is mostly regulated by series of dry and wet seasons. The maximum values of the monthly composites are observed in July in the US croplands. Notably, values retrieved over most productive ecosystems of evergreen forests in Africa and Indonesia are not as high. Time series of the SCIAMACHY red chl *a* fluorescence for different biomes, together with other vegetation parameters retrieved from SCIAMACHY data, are further studied and discussed with reference to literature in Section 7.

6. OBSERVATIONS OF CHLOROPHYLL A FLUORESCENCE AND ABSORPTION

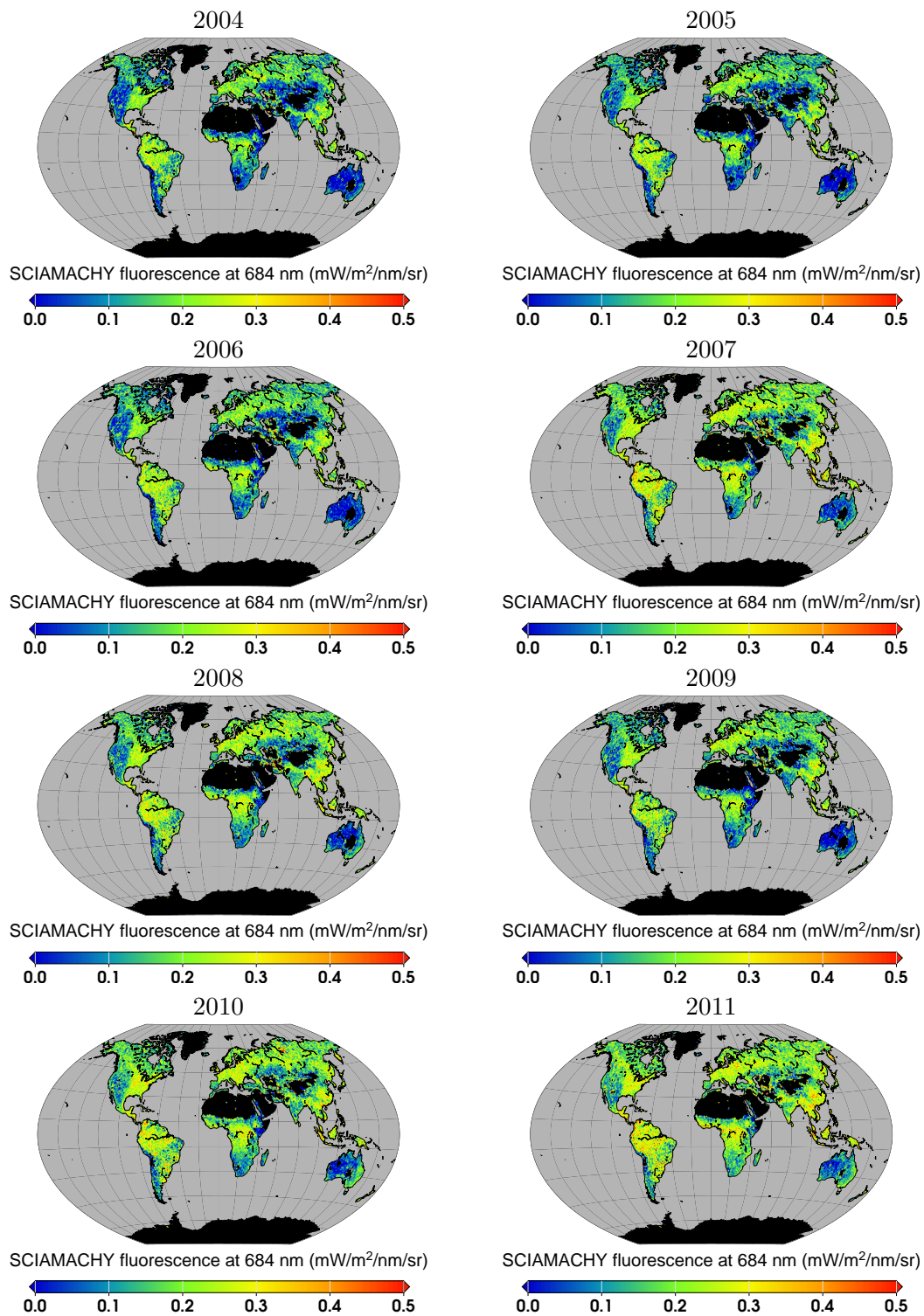


Figure 6.14: Global yearly composites of SCIAMACHY chl *a* fluorescence at 684 nm for years 2004-2011.

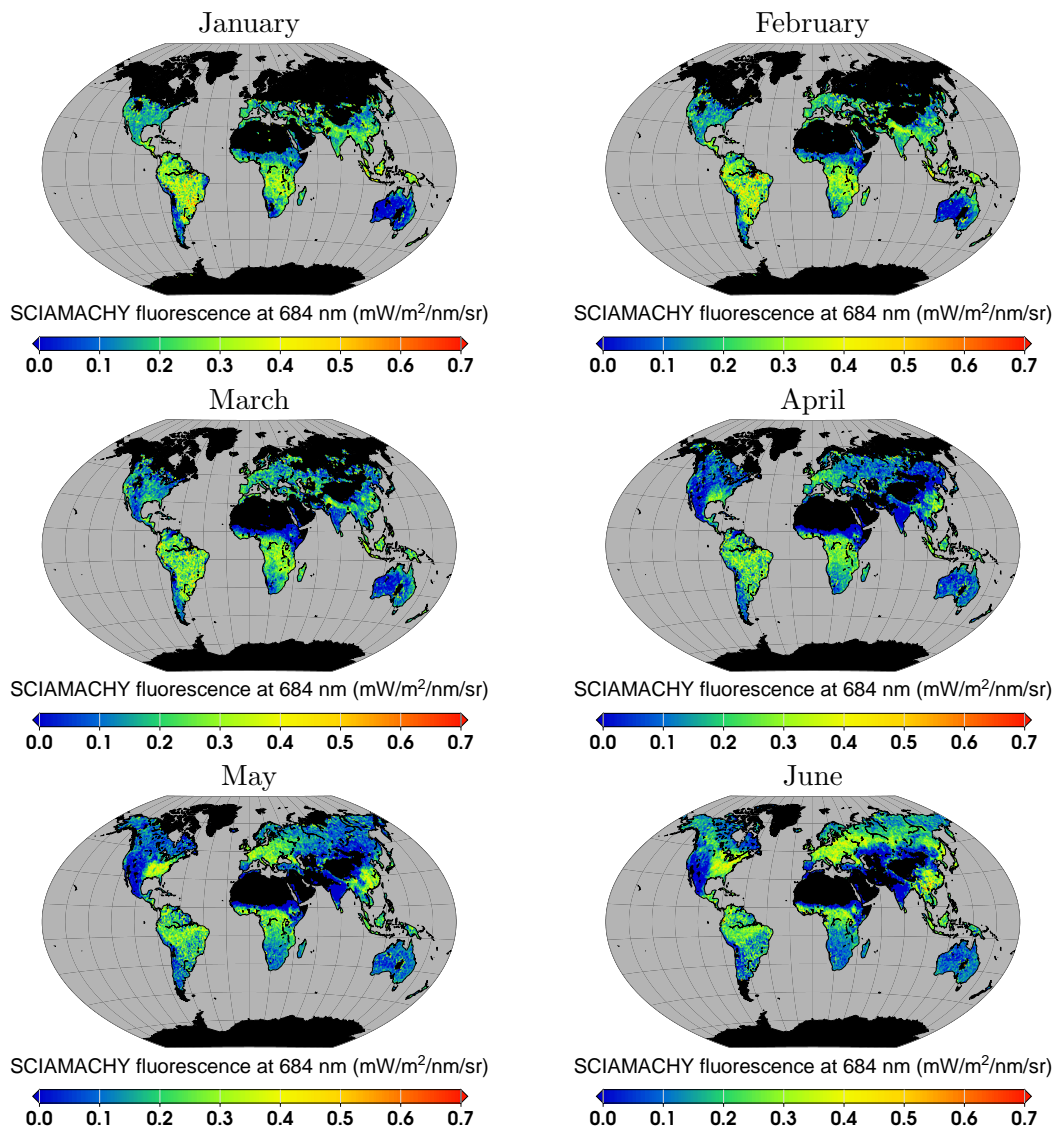


Figure 6.15: Global monthly composites of SCIAMACHY chl *a* fluorescence at 684 nm for years 2004-2011.

Chl *a* fluorescence observed with GOME-2

The red chl *a* fluorescence signal was also retrieved over land with GOME-2 data for July and December 2009 (Figure 6.16). GOME-2 results are noisier than SCIAMACHY, and show less pronounced vegetation distribution pattern. This can be attributed, as previously in case of marine observations (Section 6.1.1), to lower spectral and spatial resolution of the GOME-2 data. The GOME-2 results have a negative bias, as many pixels have negative values, but the spatial pattern for July 2009 is still observed. However, the results for December 2009 are much noisier and show little of the expected spatial distribution.

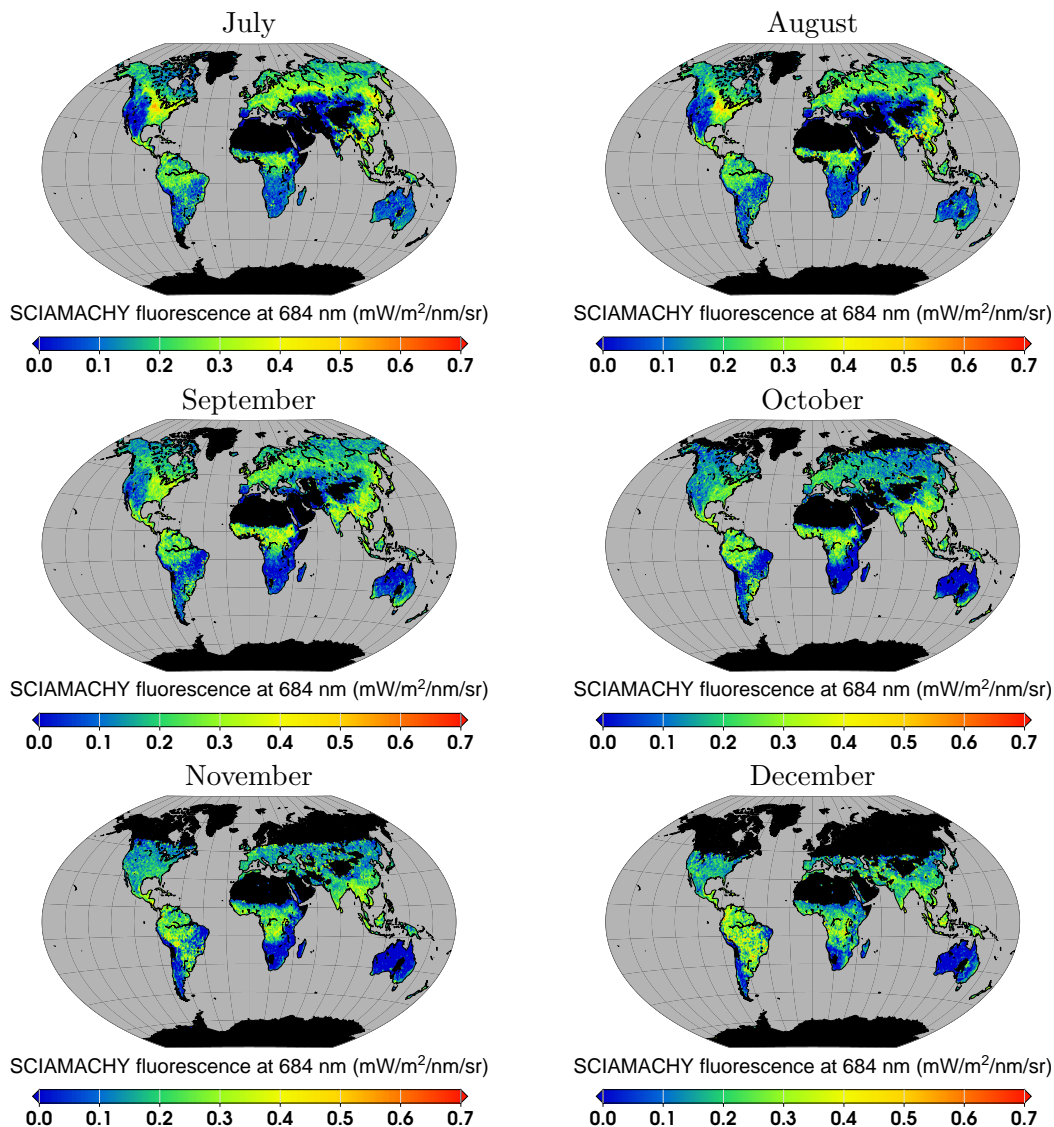


Figure 6.15: Global monthly composites of SCIAMACHY chl *a* fluorescence at 684 nm for years 2004-2011.

Comparison to other fluorescence retrievals and MODIS EVI

Figure 6.16 shows monthly mean values for July and December 2009 of terrestrial fluorescence emission retrieved by the DOAS algorithm for SCIAMACHY and GOME-2, compared with MODIS Terra Enhanced Vegetation Index (EVI) product, which is a popular greenness-based index. MODIS Terra EVI data used in this study were produced with the Giovanni online data system, developed and maintained by the NASA GES DISC.

Recently, two algorithms to retrieve terrestrial chl *a* fluorescence at its far-red peak have been applied to GOME-2 (Joiner et al., 2013) and GOSAT (Guanter et al., 2012) and showed good spatial agreement (Joiner et al., 2013). While the DOAS technique retrieves the red fluorescence features near 685 nm, the other two algorithms retrieve fluorescence

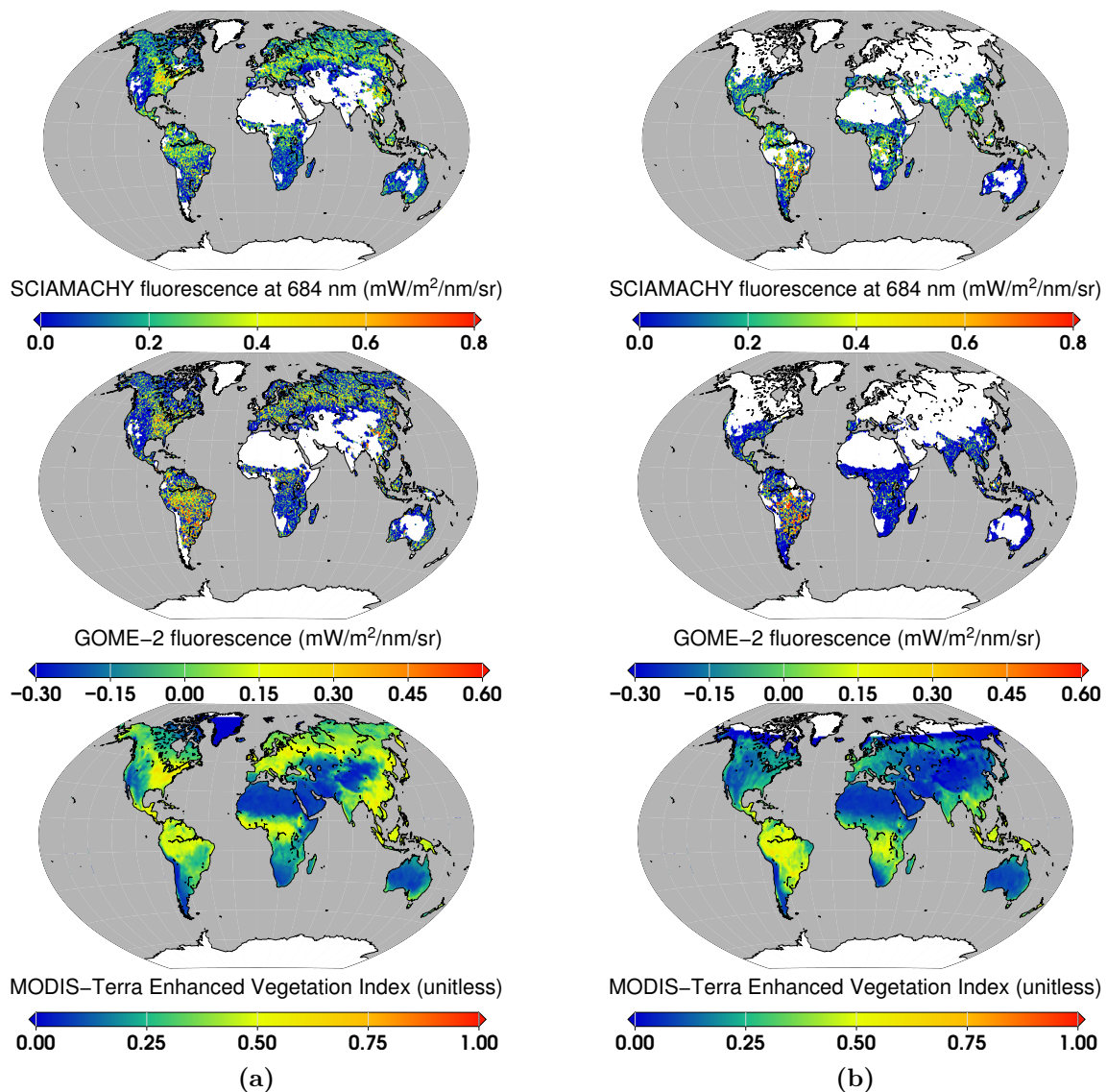


Figure 6.16: Global monthly mean for July (a) and December (b) 2009 of terrestrial chl *a* fluorescence radiance from SCIAMACHY (upper panel) and GOME-2 (middle panel) compared with MODIS EVI (MODIS Terra Enhanced Vegetation Index, lower panel).

in the far-red emission peak near 740 nm (736.8 nm for GOME-2, Joiner et al. 2013, and 757 nm for GOSAT, Guanter et al. 2012). The wavelength region used by Guanter et al. (2012) is ~ 17 nm shifted from the far-red fluorescence peak. To compare GOME-2 results with GOSAT, Joiner et al. (2013) multiplied the results of the fluorescence at 736.8 nm by a factor of 0.59, which is consistent with the spectral shape of the fluorescence emission they assumed. Assuming the same fluorescence shape for this study, values similar to those of Guanter et al. (2012) are expected to be retrieved using the DOAS technique at 685 nm. However, the ratio between two peaks of fluorescence cannot be assumed constant, and varied also for the top-of-canopy spectra simulated by Joiner et al. (2013).

All satellite terrestrial fluorescence retrievals (see Figure 15 a and b in Joiner et al.,

2013) show similar spatial patterns of high signals in areas of active vegetation and low signals in areas of barren land, as indicated by the MODIS EVI (Figure 6.16). Similar differences between the seasons for all fluorescence retrievals can also be observed. The highest values for July are retrieved in the east of North America in the area of US croplands. In December, fluorescence from this region is much weaker, and enhanced fluorescence in the Central and Southern Africa during the local rainy season for all retrievals. However, regional discrepancies between different retrievals are visible, e.g., the SCIAMACHY results show higher values in the high latitudes for July. Large errors in the SAA region are also observed in the SCIAMACHY results, in particular for the GOME-2 retrieval (Figure 6.16). In this region, the DOAS GOME-2 fluorescence emission values are substantially noisier than the GOME-2 retrieval results by Joiner et al. (2013), where the quality checks applied were more successful in removing erroneous measurements. Nevertheless, (Joiner et al., 2013) also obtained highest errors in the SAA area.

Overall, the SCIAMACHY and GOME-2 chl *a* fluorescence values are lower than values previously retrieved within the far-red wavelength region (Guanter et al., 2012; Joiner et al., 2013). This is particularly the case for the GOME-2 results. These data show many negative values, especially for December (note that color scales are different for GOME-2 and SCIAMACHY in Figure 6.16). Observed discrepancies are significant, and larger than expected considering different wavelengths of the spectral windows within which the fluorescence emission is retrieved. Some of the differences between the previous far-red land fluorescence algorithms were partly assigned to the coarser GOME-2 pixels and the low sampling of GOSAT (Joiner et al., 2013). Time of overpass (~ 13.00 for GOSAT) is also expected to lead to differences in fluorescence (Joiner et al., 2013).

Nevertheless, the qualitative spatial agreement of land fluorescence among the different fluorescence algorithms and MODIS EVI product, implies that it is plausible to retrieve a signal from the red chl *a* fluorescence peak of terrestrial vegetation as well. Observed differences also reflect, at least partially, a real variability in the fluorescence emission spectrum.

6.1.3 Global observations of the red peak of chl *a* fluorescence

The developed hyperspectral retrieval can be applied over both land and water, which enables simultaneous observations of chl *a* fluorescence from terrestrial vegetation and phytoplankton. Such chl *a* fluorescence measurements from the same instrument, and with the same algorithm have been never done before. A global average composite of SCIAMACHY chl *a* fluorescence for years 2004-2011 is shown in Figure 6.17. Observed fluorescence emission retrieved for land plants is in general higher than for marine phytoplankton, but the strength of both terrestrial and marine signals is of the same order. While concentration of chl *a* in terrestrial plants is usually higher as compared to marine phytoplankton, a lot of the originally emitted fluorescence signal is re-absorbed within the canopy, which probably leads to similar values observed for both land and aquatic realms.

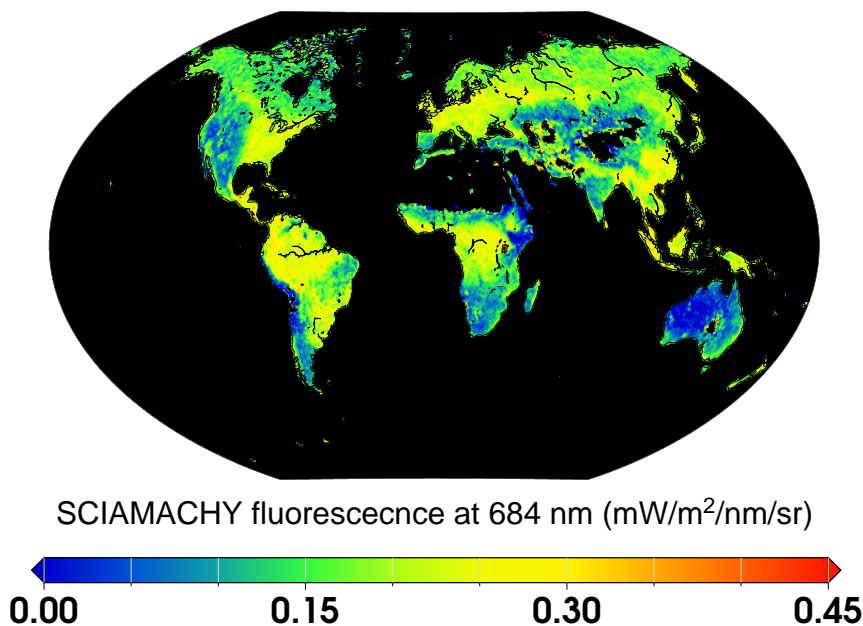


Figure 6.17: Global composite of SCIAMACHY chl *a* fluorescence at 684 nm for both land and ocean for years 2004-2011. The cloud threshold used for filtering the differs for ocean and land (0.08 and 0.4, respectively).

6.2 Observations of the far-red peak of chl *a* fluorescence

6.2.1 Chl *a* fluorescence observed with SCIAMACHY

Terrestrial chl *a* fluorescence at its far-red peak has been previously estimated from spaceborne platforms by a number of studies (Frankenberg et al., 2011b; Joiner et al., 2011; Guanter et al., 2012; Joiner et al., 2013). Here, it was demonstrated that, after necessary adjustments, the approach designed for observations of the red peak of chl *a* fluorescence can be extended to other spectral regions, in particular to the far-red peak of chl *a* fluorescence. The latest retrieval of far-red chl *a* fluorescence (Joiner et al., 2013, 2014), made use of broad spectral features and was applied to GOME-2 data. Here, the fit window was limited to a very narrow spectral region, which in case of the SCIAMACHY instrument, enables the use of the data at the best spatial resolution available (60 km by 30 km). If a broader fit window would have been applied, the data from clusters of lower spatial resolution would have needed to be included. The presented approach is conceptually similar to the first successful attempts of satellite-based observations of far-red chl *a* fluorescence, which were applied to the GOSAT instrument (Frankenberg et al., 2011b; Joiner et al., 2011; Guanter et al., 2012). However, GOSAT measurements have sparse spatial sampling and relatively low single-observation precision (Frankenberg et al., 2011b; Joiner et al., 2011; Guanter et al., 2012), which has encouraged development of retrievals for instruments with the lower spectral resolution like GOME- 2 (Joiner et al., 2012).

An example of the spectral fit of the SCIAMACHY measurements, corresponding to one of the smallest chi-square values, is shown in Figure 6.18. Spectral structures of

6. OBSERVATIONS OF CHLOROPHYLL *a* FLUORESCENCE AND ABSORPTION

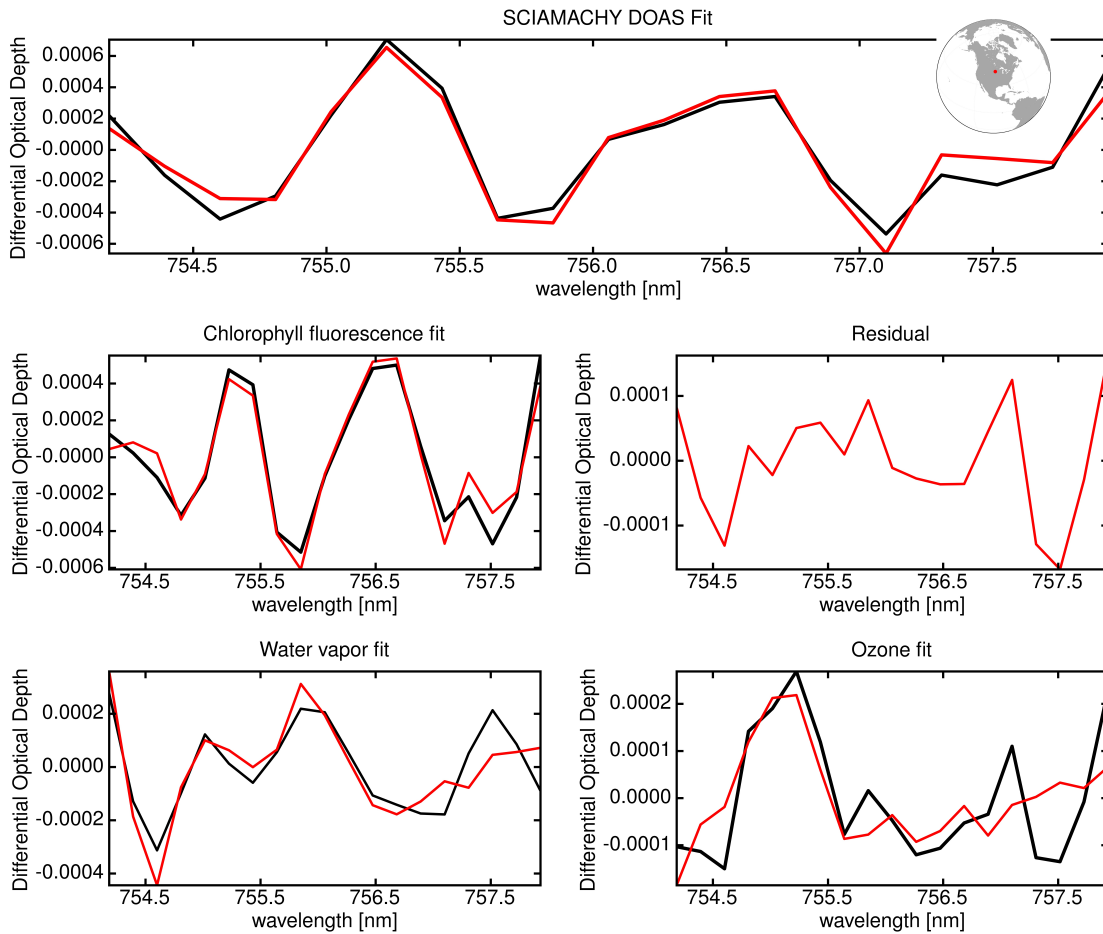


Figure 6.18: Example of a SCIAMACHY Fluorescence DOAS Fit over land (11th July 2009; lat = 45° N, lon =98° W). 1) Top panel: the fitted DOAS DOD (red) and measured DOD (black). 2) Middle left panel: the scaled chl *a* fluorescence reference spectrum (red) and chl *a* fluorescence fit (black). 3) Middle right panel: the residual from the DOAS fit. 4) Bottom left panel: the scaled water vapor reference spectrum (red) and water vapor fit (black). 5) Bottom right panel: the scaled ozone reference spectrum (red) and ozone fit (black).

chl *a* fluorescence and atmospheric absorbers (water vapor and ozone) are successfully discriminated, and the residuals of the fit are very low (< 0.02%). This again indicates that there are no strong unidentified features in the selected spectral window.

As for the red peak of chl *a* fluorescence, the global yearly composites of the far-red chl *a* fluorescence of terrestrial vegetation retrieved from SCIAMACHY for years 2004 - 2011 are shown (Figure 6.19). Additionally, monthly climatologies were calculated for these years (Figure 6.20). The data points were gridded, as previously, on a 0.5° by 0.5° grid. As for the case of red chl *a* fluorescence, similar spatial patterns (of high chl *a* fluorescence signal in areas of active vegetation and low signal in areas of barren land) are observed. The seasonal cycle of photosynthetic activities is well resolved and follows common expectations.

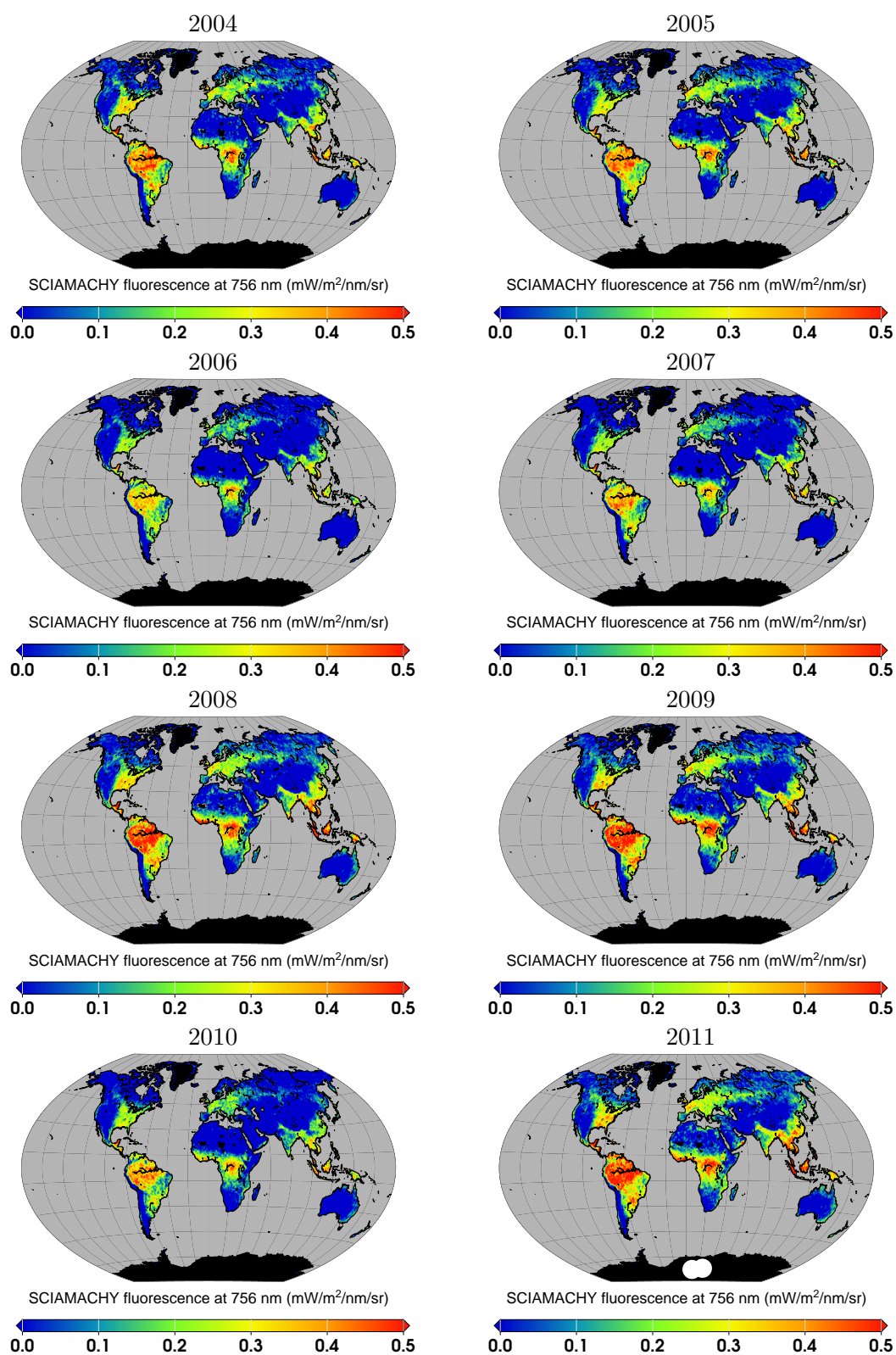


Figure 6.19: Global yearly composites of SCIAMACHY chl *a* fluorescence at 756 nm for years 2004-2011.

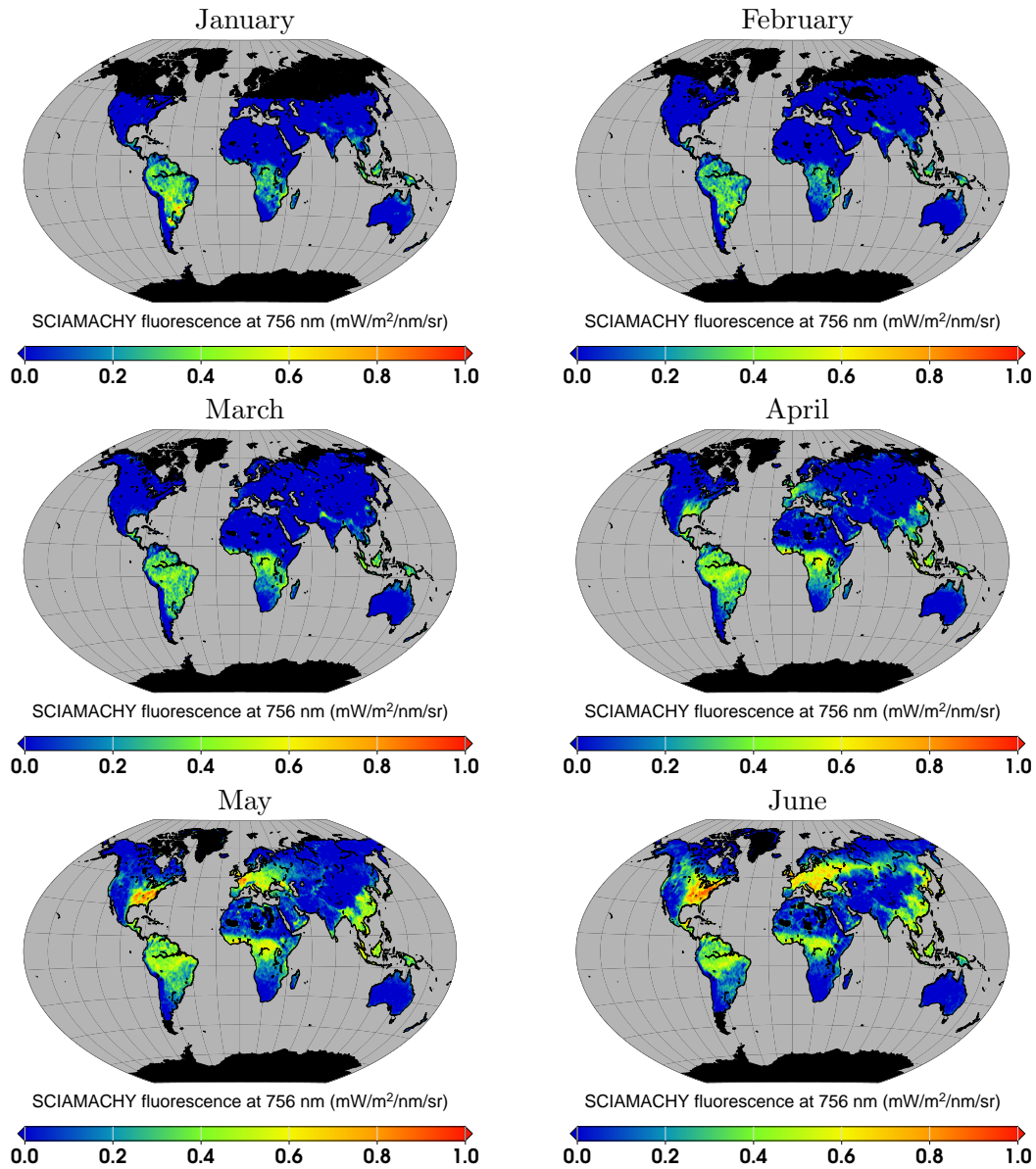


Figure 6.20: Global monthly composites of SCIAMACHY chl *a* fluorescence at 756 nm for years 2004-2011.

The far-red chl *a* fluorescence retrieval was performed globally, which also included ocean pixels. The global composite of SCIAMACHY chl *a* fluorescence at 756 nm for both land and ocean is shown in Fig. 6.21 for years 2004-2011. The only difference in the retrieval for the terrestrial and aquatic realms is the smaller cloud threshold applied to ocean scenes (0.08 and 0.4, for ocean and land respectively). Such a big difference is due to the strong water absorption and high reflectivity of vegetation in this spectral region. There is no fluorescence signal observed over the oceans, which is also because of strong liquid water absorption and hence very little radiation escaping the ocean surface. Liquid water absorption was significantly limiting the strength of the observed signal already in the shorter wavelengths (red peak) of chl *a* fluorescence. Here, for longer wavelengths, this

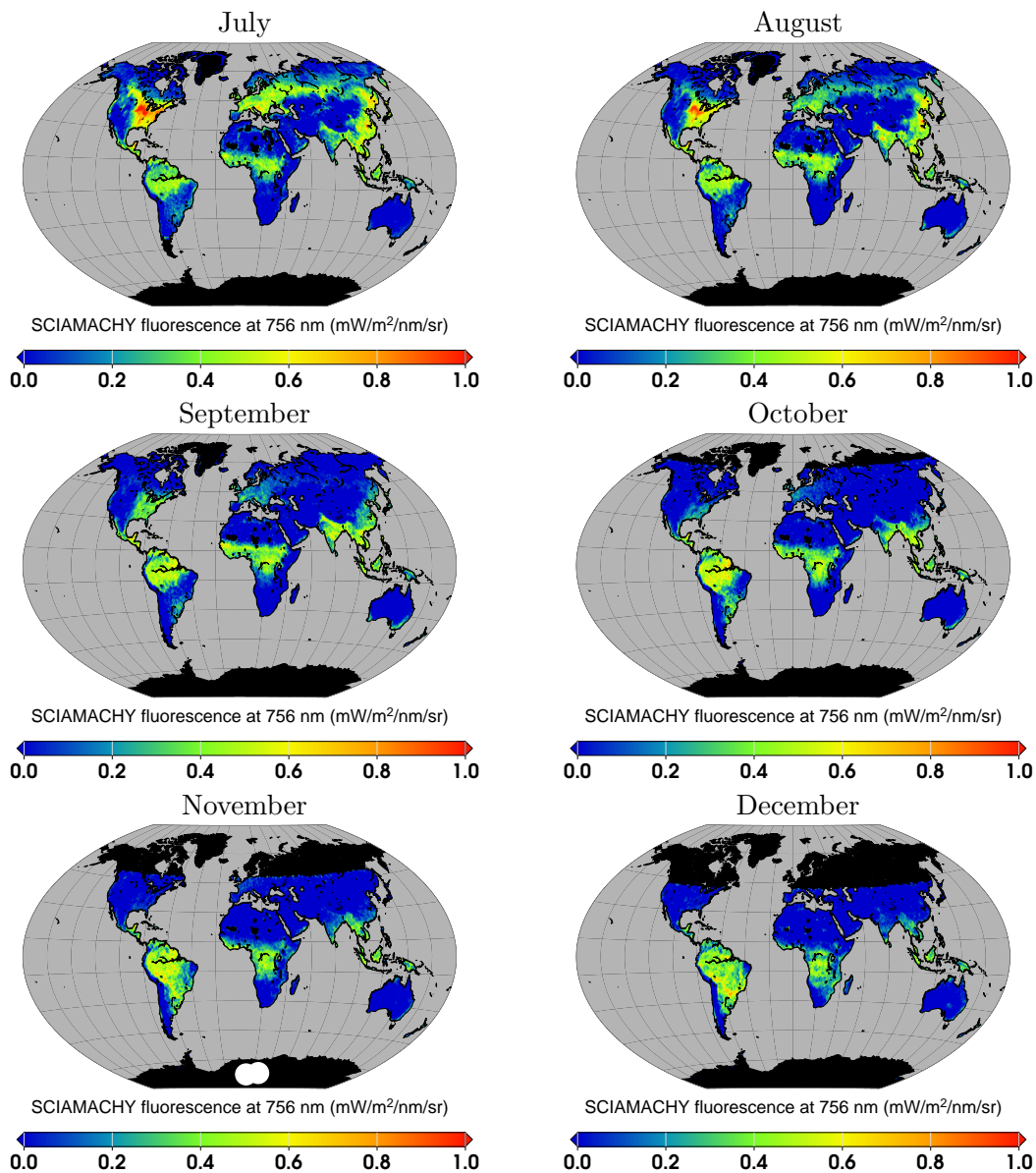


Figure 6.20: Global monthly composites of SCIAMACHY chl *a* fluorescence at 756 nm for years 2004-2011.

impact is much greater and no spatial pattern, resembling phytoplankton distribution, was observed. In the case of the recent far-red fluorescence retrieval developed for GOME-2 instrument by Joiner et al. (2013), also only instrumental noise was observed above the ocean surfaces (private communication).

6.2.2 Comparison with previous results

The SCIAMACHY results of chl *a* far-red fluorescence peak were compared with the GOME-2 far-red chl *a* fluorescence data from Joiner et al. (2013). There are currently two

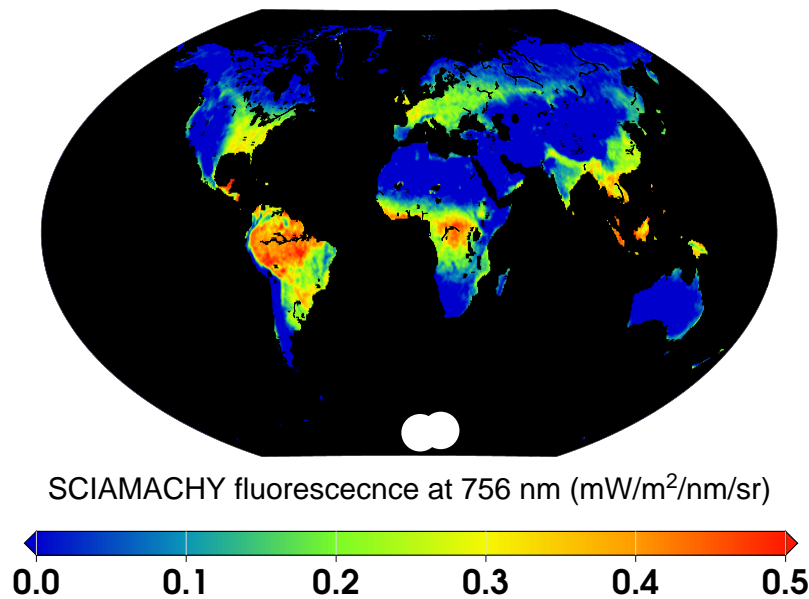


Figure 6.21: Global composite of SCIAMACHY chl *a* fluorescence at 756 nm for both land and ocean for years 2004-2011. The cloud threshold used for filtering the differs for ocean and land (0.08 and 0.4, respectively).

released versions of GOME-2 chl *a* fluorescence, where the main changes include reduction of the spectral window of the retrieval (from 712-783 nm to 734-758 nm), and decrease of the number of used principal components from 25 to 14. Additionally, the principal components analysis is applied to radiance spectra, as opposed to the logarithm of the radiance spectra (Joiner et al., 2014). Here, the latest released version, V25 (which is available online) was used for the comparison. Yearly composites of far-red fluorescence for year 2009 are compared in Fig. 6.22. The scatter plot of the corresponding data is shown in Fig. 6.23. The SCIAMACHY results are about half of the data obtained by Joiner et al. (2013). However, the global spatial distribution of both results is similar. A statistically significant correlation was obtained for the two datasets ($r^2=0.4871$, $p<0.001$).

One of the possible sources of the observed differences is a slight mismatch of the time of overpass of SCIAMACHY and GOME-2 instruments ($\sim 10:00$ a.m. for SCIAMACHY, as compared to $\sim 9:30$ a.m. for GOME-2). Other instrument-specific characteristics can also lead to further discrepancies, e.g., different spatial sampling and spatial resolution of the instruments. Additionally, due to the normalization of the measured spectra to the other earthshine spectra, and a use of data-driven statistical approach, Joiner et al. (2013) might be more effective in mitigating the problem of the zero-level offset. As the fitting window of the SCIAMACHY retrieval lies within the spectral window of Joiner et al. (2013), the obtained values were expected to have more similar values. The exact causes of the observed differences, in case of this comparison as well as the previous comparisons between the other fluorescence retrievals (e.g., Joiner et al., 2013), are still under investigation. Due to the lack of appropriate *in situ* fluorescence measurements available to perform a systematic validation, it is hard to accurately evaluate and verify the results.

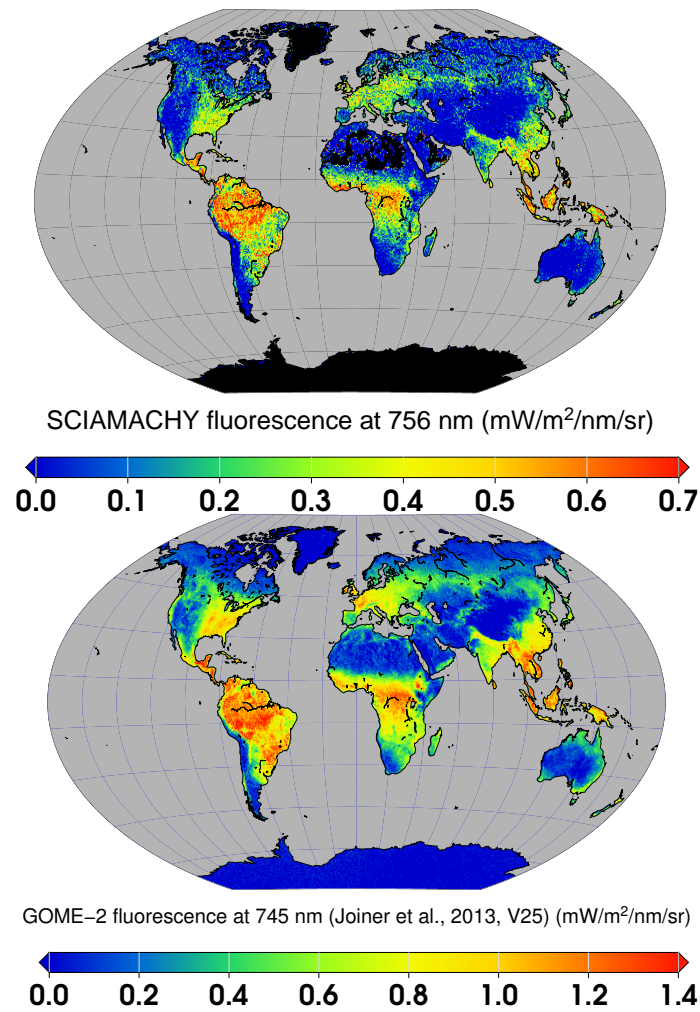


Figure 6.22: Comparison of yearly composites of far-red fluorescence for year 2009 of the SCIAMACHY results (this study) and Joiner et al. (2013).

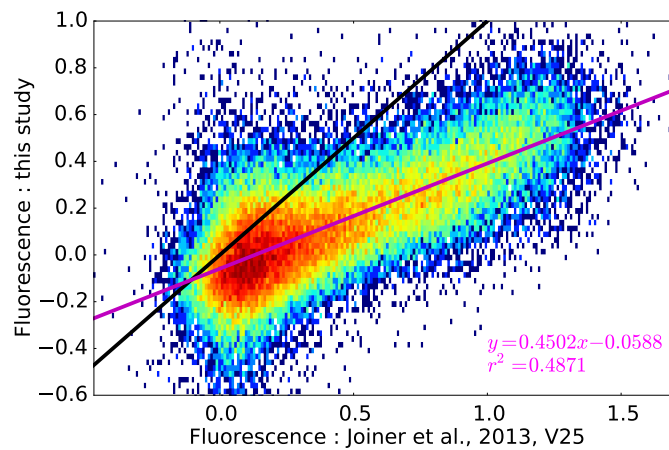


Figure 6.23: The scatter plot of yearly averages of far-red fluorescence for year 2009 of the SCIAMACHY results (this study) and Joiner et al. (2013).

6.3 Observations of the terrestrial chl proxy with SCIAMACHY

The retrieval of chl proxy of terrestrial vegetation was applied to the SCIAMACHY data for years 2004-2011. Since the fitting window is spectrally broad (429.2 - 583.8 nm), it covers many clusters of the SCIAMACHY radiance data. Hence, the pixels spatial resolution is 240 km across track and along track 30 km for most of the years. Such large pixel size is an undesirable limitation of applying such an algorithm to SCIAMACHY data. However, since April 2010, the resolution of the data has been improved, with the across track of the pixels being reduced to the nominal resolution of 60 km. Additionally, the chl proxy retrieval had an exceptionally low number of pixels retrieved for year 2003 as compared to other years (Figure 6.24) due to instrumental issues and adjustments in the first year of the SCIAMACHY mission (information on the operation of the SCIAMACHY instrument can be found on the website of the SCIAMACHY Operations Support Team at <http://atmos.caf.dlr.de/projects/scops/>).

Monthly climatologies of retrieved chl proxy are shown in Fig. 6.25. In general, a typical spatio-temporal pattern is clearly noticeable, with higher values for densely vegetated areas and low for barren land. Unfortunately, also negative value were retrieved for sparsely vegetated or non-vegetated areas, which possibly means that other broad-band surface spectral features might interfere in the algorithm. However, the seasonal cycle of photosynthetic activities for vegetated areas is well captured. For example, the onset of the chl build-up in the Northern Hemisphere in spring is well detected. It starts earlier in the southern regions, and subsequently spreads into the higher latitudes. Comparably high monthly maxima are observed for several regions worldwide, e.g., US crop belt and sub-Saharan savannas, but remain relatively low for very productive evergreen broadleaf forests in South America, Africa and Indonesia. This might be due to the strong evaporation and cloudiness over these regions throughout most of the year, which disrupts the measurements. In high latitudes, where snow cover is temporally present, the obtained results are additionally affected by snow precipitation and melt. In such cases, the observed timing of vegetation phenological events is strongly influenced by timing of snow cover build-up and decline (see more Section 7).

Nevertheless, the obtained global spatial pattern of vegetation follows common expecta-

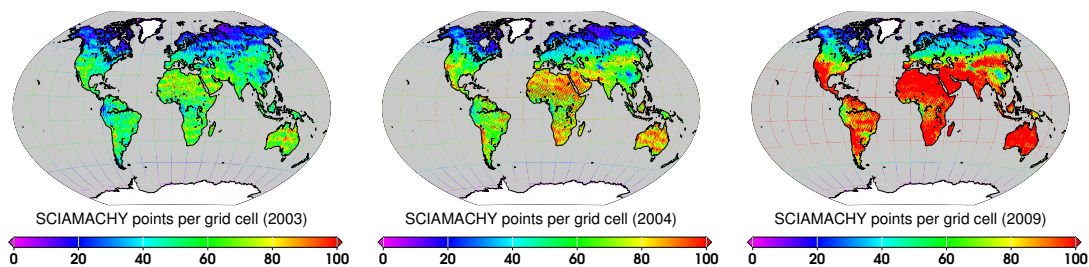


Figure 6.24: Global maps of SCIAMACHY number of points per grid cell for years 2003, 2004 and 2009 for the chl proxy retrieval.

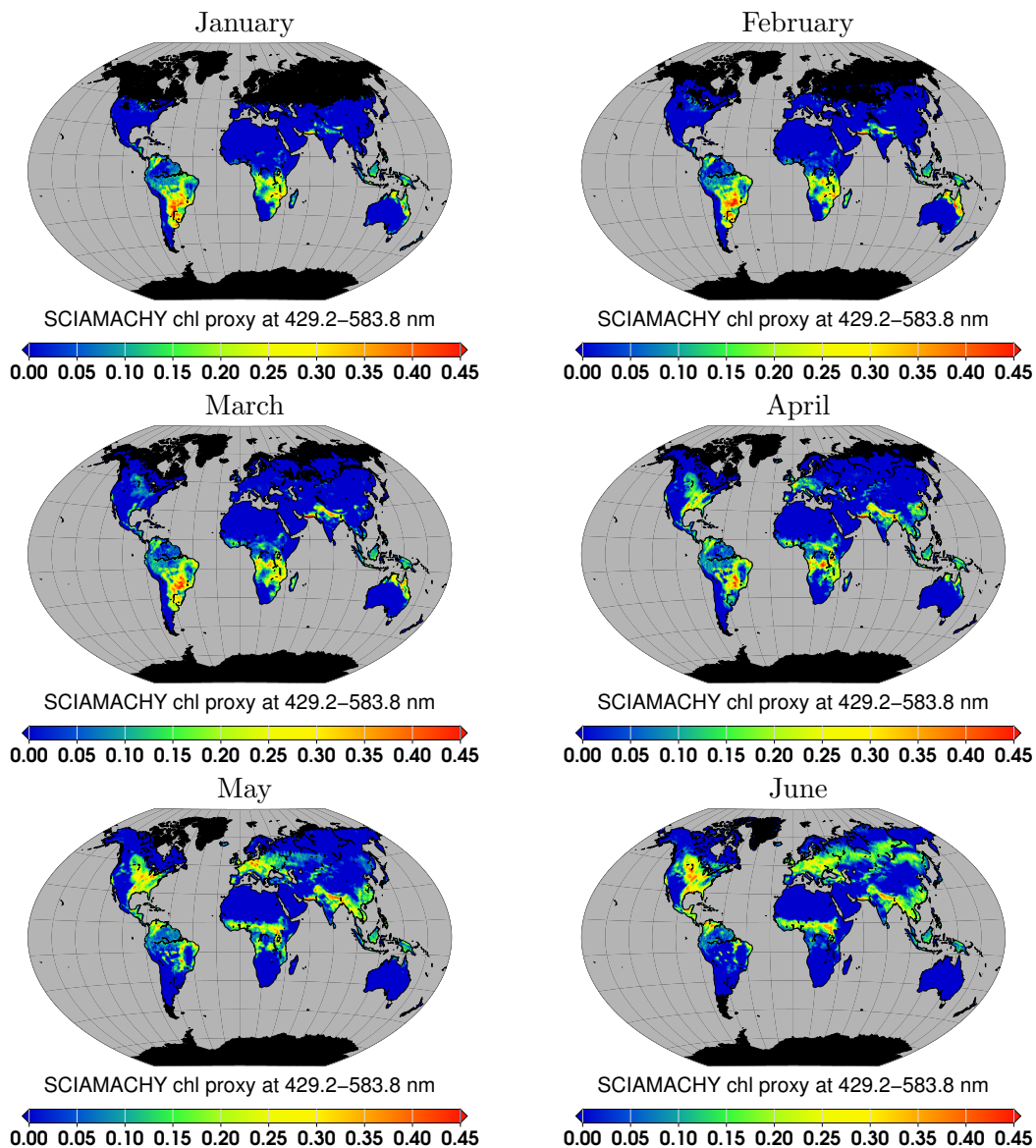


Figure 6.25: Global monthly composites of SCIAMACHY chl proxy at 429.2–583.8 nm for years 2004–2011.

tions, and seems more consistent than the fluorescence results. As only a small amount of absorbed light is re-emitted as fluorescence (typically 0.5–3%, see Section 2.2.2), the absorption signal is inevitably much stronger than the actively emitted fluorescence. However, as this retrieval is based on light absorption, it is expected to be more corrupted by the contamination of snow and clouds, as compared to fluorescence. The obtained chl proxy data are further applied in the study of the seasonal vegetation cycles for different biomes in Section 7.

Yearly composites of SCIAMACHY chl proxy and MODIS-Terra EVI for year 2009 are compared in Fig. 6.26. MODIS EVI data used in this study were produced with the Giovanni online data system, developed and maintained by the NASA GES DISC. MODIS

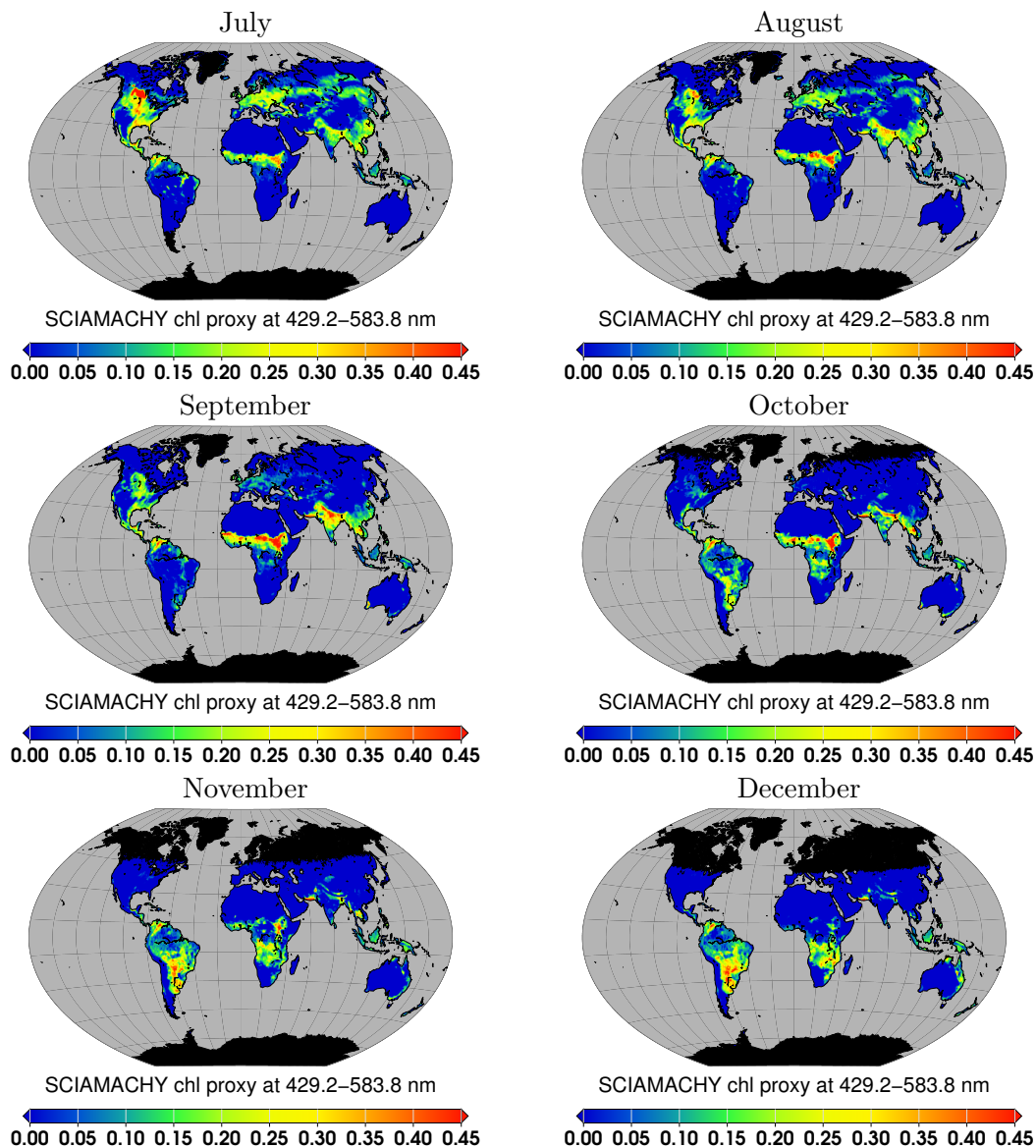


Figure 6.25: Global monthly composites of SCIAMACHY chl proxy at 429.2–583.8 nm for years 2004–2011.

EVI data are provided on the 1° by 1° grid, into which SCIAMACHY chl proxy data were re-gridded for comparison purpose. The areas of maximum values clearly vary between the two datasets. Very low values of SCIAMACHY chl proxy are obtained for rainy forests in the South America and Africa, and are probably related to the extensive cloud cover in these tropical regions. This issue is particularly problematic for the SCIAMACHY chl proxy retrieval because of the very big pixel size (240 km x 30 km). Hence, there is a low probability of obtaining cloud-free scenes, especially during rainy seasons. Significantly different original pixel sizes of these two datasets (250 m x 250 m in case of MODIS, and 30 x 240 km in case of SCIAMACHY) can be one of the main sources of discrepancies in spatial distributions of the obtained values. SCIAMACHY chl proxy retrieval is also based

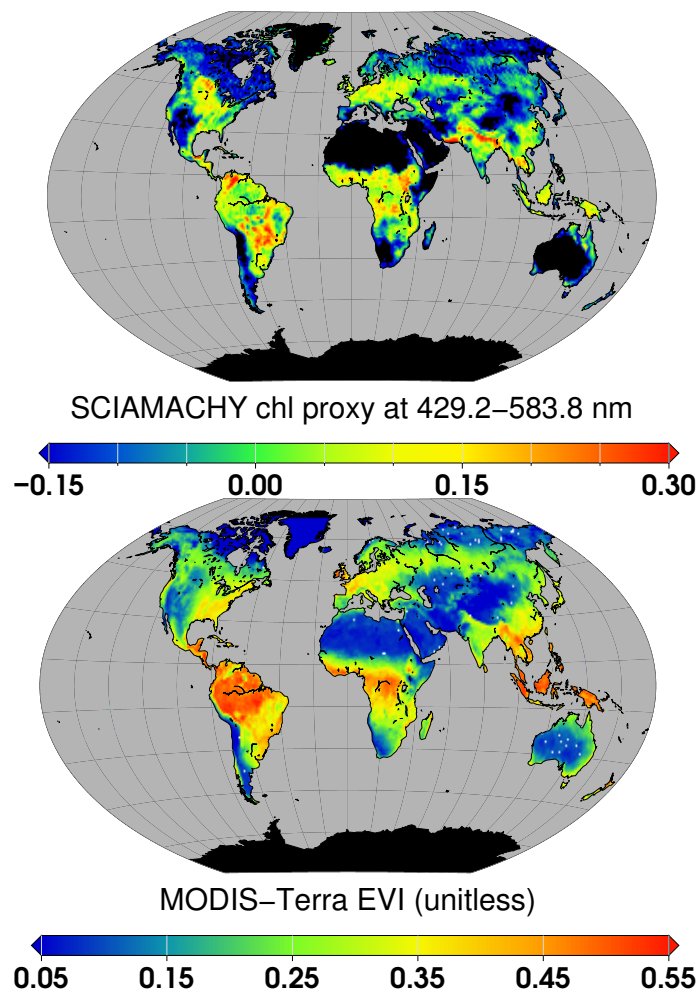


Figure 6.26: Comparison of yearly composites of SCIAMACHY chl proxy and MODIS-Terra EVI for year 2009.

on the chl *a* absorption in blue, as compared to EVI algorithms that are using the red edge wavelengths. Since in the blue region light is additionally absorbed by carotenoids, their concentration also influences retrieved chl proxy values (Buschmann & Lichtenthaler, 1998). Additionally, MODIS EVI data are in a form of a vegetation index and averaging them over the whole year leads to the values that are hard to interpret in physical terms. The scatter plot of the corresponding yearly averages is shown in Fig. 6.27. The points in the scatter do not produce a continuous scatter, but are clearly clustered in few groups. A small but statistically significant correlation was obtained for the two datasets ($r = 0.4380$, $p < 0.0001$)

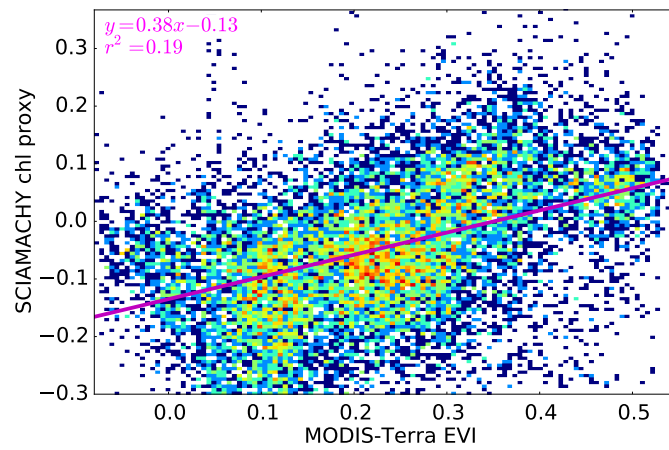


Figure 6.27: The scatter plot of yearly averages of SCIAMACHY chl proxy and MODIS-Terra EVI for year 2009.

Chapter 7

Observations of the seasonality of photosynthetic activity of vegetation using SCIAMACHY data

The potential application of the chl-related variables retrieved from the SCIAMACHY measurements (i.e. red and far-red chl *a* fluorescence, and chl proxy) to study the seasonality of the photosynthetic activity of vegetation, was investigated by analyzing the simultaneous changes of the SCIAMACHY parameters for different land vegetation biomes over the time period of eight years (2004-2011).

7.1 Vegetation seasonality

Vegetation phenology studies the timing of plant development phases, such as leaf onset, flowering, leaf senescence and leaf offset (so-called phenological events), and how they are impacted by both short- and long-term climatic variations. In turn, changes in vegetation properties and dynamics affect climate through a variety of pathways and over a range of spatial and temporal scales (Fig. 7.1). Since changes in vegetation dynamics could serve as an indicator of climate perturbations, the importance of phenology studies has been increasingly recognized over the last two decades (Richardson et al., 2013, and references therein).

Timing of vegetation photosynthetic activities can influence microclimate as well as ecosystem productivity (Fig. 7.1), through many processes, which are mediated by phenology (e.g., growth and productivity, evapotranspiration and runoff of water, decomposition and mineralization of nutrients). Vegetation is also one of the factors controlling surface-atmosphere exchanges of energy (short- and long-wave radiation), trace gases (mainly water vapor and carbon dioxide), and other substances (e.g., biogenic volatile organic compounds, BVOCs). Hence, besides its impact on the local conditions, phenology could

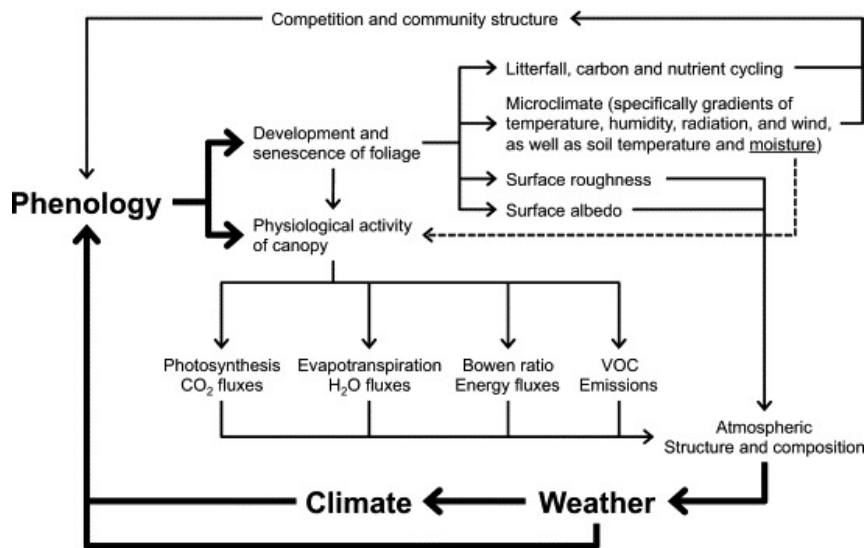


Figure 7.1: Conceptual model illustrating the primary feedbacks between vegetation and the climate system that are influenced by vegetation phenology. Source: Richardson et al. (2013).

also potentially influence weather patterns on larger scales, as well as global climate.

Photosynthetic activity plays an important role in regulating some vegetation feedbacks to the atmosphere and climate system through different processes and properties, including the albedo, the surface roughness length, the canopy conductance, and the water, CO₂, BVOCs and energy fluxes. The impacts on albedo can vary among ecosystems, e.g., through a lengthening of the growing season or changes in the duration of a snow cover. Surface roughness length is defined as the height above the surface where mean wind speed extrapolates to zero. It is related to the canopy height and the leaf area index, and has a direct link with the climate system by influencing the degree of coupling between the land surface and the atmosphere, thereby modulating surface energy fluxes. Canopy conductance is the product of the amount of the leaf area and the stomatal conductance per unit leaf area. It plays a role in regulating rates of transpiration and CO₂ uptake by plants. Surface energy balance and the partitioning of net radiation into latent, sensible, and ground heat fluxes, influence the composition and structure of the planetary boundary layer and thus atmospheric processes, including transport.

Vegetation influence on atmospheric CO₂ varies among ecosystem types according to shifts in the balance between canopy photosynthesis and ecosystem respiration, which is one of the most important feedbacks between vegetation and climate. Gross productivity by terrestrial vegetation is estimated to be $\sim 120 \text{ Pg C y}^{-1}$ (Beer et al., 2010), while the total carbon land sink is estimated to be $2\text{-}5 \text{ Pg C y}^{-1}$, as compared to the anthropogenic emission of 8 Pg C y^{-1} (Le Quéré et al., 2009). Hence, inter-annual variability in terrestrial ecosystems influences the annual growth rate of atmospheric CO₂, which can be clearly seen in the seasonal cycles of atmospheric CO₂, for examples in CO₂ data measured at Mauna Loa Observatory, which constitute the longest record of direct measurements of CO₂ in the atmosphere (Fig. 7.2). BVOC emissions, which are controlled mainly by environmental and phenological factors, play various roles in the photochemistry of the

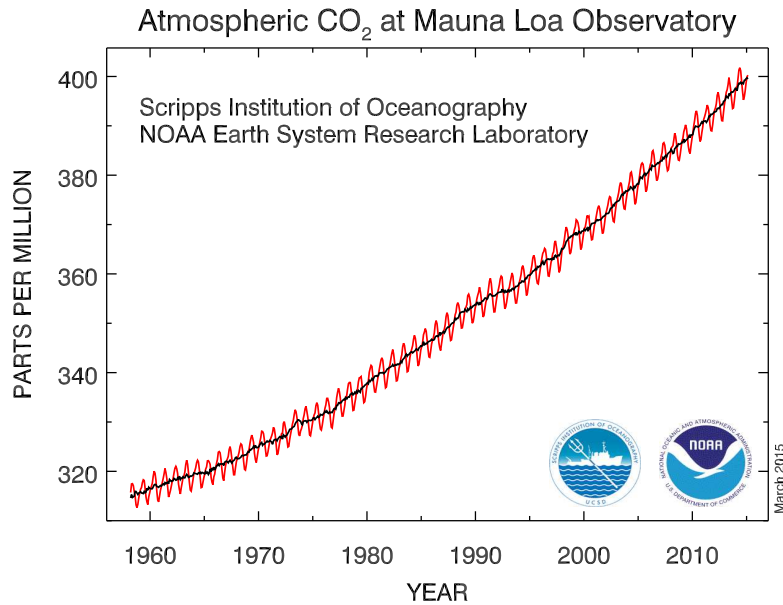


Figure 7.2: Monthly mean atmospheric carbon dioxide at Mauna Loa Observatory, Hawaii. Source: <http://www.esrl.noaa.gov/gmd/ccgg/trends/index.html>.

lower atmosphere. They control various mechanisms within the climate system, e.g., products of their reactions affect the radiative forcing of the atmosphere and increase the concentration of cloud condensing nuclei.

Major changes in timing of phenological events have been reported, together with the biological impacts of climate change, often related to warmer temperatures (IPCC, 2007). The key environmental drivers for phenology vary between major biomes: air temperature is thought to be the principal limiting factor to vegetation growth at temperate and higher latitudes, while in dry ecosystems it is rainfall (e.g. Zhang, 2005). Numerous studies have reported advances, particularly over the last four decades, in the timing of the spring onset in temperate trees, which was attributed to increasing temperature (Thompson & Clark, 2008). In some temperate tree species, photoperiod and winter chilling requirements also play a role in spring phenology (Richardson et al., 2013, and references therein). Some studies suggest rapid rates of advance (1.8-7.8 days/decade) of spring leaf-out in the recent decades. In the boreal forests, recent trends are similar to those observed in temperate forests, and these shifts have also been attributed to a warming climate. In high latitudes, earlier spring emergence has been observed, and linked as well to warmer temperatures and earlier snowmelt (Richardson et al., 2013, and references therein).

Perturbations in the timing of phenological events have also implications on land management, human health, and ecosystems services, on which humans depend (Schroter, 2005). These include agriculture, forestry, and invasive plants and pests, as well as nature conservation and the seasonal suitability of landscapes for recreational activities (e.g.,

Badeck et al., 2004). Recently, links have been postulated between phenology and disease transmission (e.g. Barrios et al., 2010).

7.2 Vegetation Indices

The use of vegetation indices (VIs) has been the most common method to infer vegetation phenological events from satellite sensors (e.g., White et al., 2009; Ganguly et al., 2010; Boyd et al., 2011). VIs relate reflectance from leaves or canopies with canopy characteristics, such as green leaf area and total green biomass. When derived from satellite-borne sensors, VIs provide unique observations of global-scale patterns of vegetation, with an exceptional spatial and temporal coverage. The most widely used VI, which also often serves as a benchmark for newly developed VIs, is the Normalized Difference Vegetative Index (NDVI) (Tucker & Sellers, 1986). NDVI is formulated as a normalized ratio of the NIR and red bands:

$$\text{NDVI} = \frac{\rho_{\text{NIR}} - \rho_{\text{RED}}}{\rho_{\text{NIR}} + \rho_{\text{RED}}}, \quad (7.1)$$

where ρ_{NIR} and ρ_{RED} are the reflectance measurements in the near-infrared (NIR) and red (RED) and spectral regions. NDVI was first applied to the satellite data of the Advanced Very High Resolution Radiometer (AVHRR) instruments deployed on NOAA satellites, and used for monitoring African vegetation (Tucker & Sellers, 1986). Since then, NDVI has been repeatedly retrieved from a new generation of satellites (e.g., VEGETATION, MODIS, and MERIS, see Fensholt et al. e.g. 2006). Nowadays, it is an official product of MODIS, referred to as the 'continuity index' (Huete et al., 1999).

The ratio nature of NDVI (and many other indices) reduces many of the signal variations, attributed to calibration, changing illumination and viewing conditions, topography, clouds/shadow, and atmospheric conditions (Fensholt et al., 2006). Residual effects still appear, due to sensor characteristics and atmospheric effects, such as aerosols, water vapor and residual clouds, which have different impact on different bands. One of the main disadvantages of the NDVI is the inherent nonlinearity of ratio-based indices. NDVI also exhibits scaling problems, saturated signals over high biomass conditions and high sensitivity to canopy background variations, especially at low vegetation cover (Huete & Jackson, 1988).

In order to optimize the vegetation signal (improve sensitivity in high biomass regions, decouple the canopy background signal, and reduce atmosphere influences), the enhanced vegetation index (EVI) was developed, originally for the MODIS sensor (Huete & Liu, 1994; Huete et al., 1999). EVI is formulated as follows:

$$\text{EVI} = G \frac{\rho_{\text{NIR}} - \rho_{\text{RED}}}{\rho_{\text{NIR}} + C_1 \rho_{\text{RED}} - C_2 \rho_{\text{BLUE}} + L}, \quad (7.2)$$

where constants C_1 , C_2 , L and G are empirically determined to be 6.0, 7.5, 1.0 and 2.5. The blue band (ρ_{BLUE}) is used in the EVI algorithm to correct for aerosol influence in the red band. Both indices, NDVI and EVI, have been widely applied to several vegetation

studies (Boyd et al., 2011, and references therein). They also together constitute an official MODIS vegetation indices product (MOD13).

There are multiple other VIs that are retrieved from satellite platforms. For example, there are two official vegetation index products for MERIS: the MERIS global vegetation index (MGVI, Gobron et al. 1999) and the MERIS terrestrial chlorophyll index (MTCI, Dash & Curran 2004). The MGVI is linearly related to the fraction of absorbed photosynthetically active radiation (fAPAR) by the canopy, and is computed using the top of atmosphere reflectance in blue, red and NIR MERIS bands, with the blue band being used to atmospherically correct red and NIR reflectances. The MGVI is computed as a polynomial function of the red and NIR reflectances (Gobron et al., 1999). The other MERIS index, MTCI is calculated using the ratio of the difference in reflectance between bands 10 and 9 and the difference in reflectance between bands 9 and 8. Despite its simplicity, it is sensitive to high values of chlorophyll content (Dash & Curran, 2004).

For this study, MODIS NDVI and EVI indices were used. The global data for years 2004-2009 were produced with the Giovanni online data system, developed and maintained by the NASA GES DISC. The data are provided on 1° by 1° grid.

7.3 Chl *a* fluorescence application for vegetation observations

As compared to chl absorption, chl *a* fluorescence is a much weaker signal, since fluorescence constitutes only ~0.5 to 3% of the light absorbed (see Section 2.2.2). Observations of the absorption features in the measured radiance data are the basis of the chl proxy retrieval. However, as shown in Fig. 1.3, fluorescence and absorption signals relate to different stages of the photosynthesis process, hence together they can provide more comprehensive information about the physiology and biomass of the vegetation than any of the parameters alone (Porcar-Castell et al., 2014). For example, Joiner et al. (2014) demonstrated that satellite-based fluorescence measurements show potential application of global observations of photosynthetic activity. They could possibly improve the seasonality of photosynthesis in simulations by global models, since reflectance-based indicators tend to overestimate the length of the photosynthetically-active period for forests and cropland sites (Joiner et al., 2014).

Recently, within the context of ESA's Earth Explorer 8 candidate mission, the FLuorescence EXplorer (FLEX), Mohammed et al. (2014) studied mechanistically-based models to link steady-state chl *a* fluorescence with photosynthesis, and investigated stress indicators derived from steady-state fluorescence signal. Their results indicated that the inclusion of fluorescence data leads to a substantive improvement in performance of the estimation of net canopy photosynthesis (NCP) and gross primary production (GPP) in unstressed vegetation. The use of both fluorescence bands was preferential for predicting GPP (which proves that the two bands do not carry the same information), but most of the information was contained within the red emission peak. However, the models were considerably overestimating fluorescence in the red band (five or eight times, depending on the chosen leaf biochemical module), and gave better agreement for the far-red band. In

contrast, neither reflectance data nor solely biophysical variables (Chl, LAI, fAPAR) led to meaningful relationships with NCP. However, Mohammed et al. (2014) suggested to take chlorophyll content into account because of its effects on light absorption (which influences photosynthesis and fluorescence radiance positively) and re-absorption (which decreases fluorescence emission). Surprisingly, one-variable models that use far-red fluorescence, were found to be non-predictive for any photosynthetic products, which is in contrast with the previously reported high correlation between far-red fluorescence and GPP derived from experimental data (e.g. Frankenberg et al., 2011b; Guanter et al., 2012). Furthermore, red and far-red chl *a* fluorescence peaks and their ratios were found suitable for detection of physiological strain from the investigated stresses. Photosynthesis can be hindered by the damage to critical cell or organelle membranes, denaturation of photosynthetic proteins or enzymes, impaired chloroplast function, destruction of chlorophyll or other pigments, blocked uptake or transport of water or other nutrients, buildup of toxic substances, and damage to protective mechanisms (Mohammed et al., 2014, and references therein). For example, water stress was associated with a decline in red and far-red chl *a* fluorescence measured at the leaf and canopy levels, and the ratio of red and far-red chl *a* fluorescence was, among the studied variables, the clearest indicator of nitrogen deficiency, as well as of temperature stress (Mohammed et al., 2014). However, Mohammed et al. (2014) stressed that while fluorescence may be diagnostic for the existence of stress, it usually would not be expected to diagnose the specific stress on its own (e.g., drought, salinity, pest etc.), given that different stresses can produce a similar result. Analysis by Mohammed et al. (2014) further indicated that acquisition of both red and far-red chl *a* fluorescence signals, with airborne and/or spaceborne sensors, will be beneficial for timely detection of plant stress events.

For the three stress categories considered by Mohammed et al. (2014) (water deficit, temperature extremes, nitrogen insufficiency), major knowledge gaps were identified. These included:

- temporal resolution required for reliable detection of fluorescence,
- influence of canopy structural complexity on fluorescence,
- detectability across plant functional types,
- influence of environmental spatial heterogeneity,
- impact of combined stressors on fluorescence,
- consistency of red and far-red fluorescence changes,
- consistency of active and passive data,
- consistency of fluorescence changes at leaf and canopy levels,
- influence of chlorophyll content.

These knowledge gaps clearly show that interpretation of fluorescence signal for stress identification and tracking is complicated, and certainly needs auxiliary information to

provide the full context for the stress diagnose. For example, under certain nutrient deficiencies, e.g., nitrogen, either an increase or a decrease of chl *a* fluorescence can be observed, depending on the particular circumstances and degree of advancement of stress. Furthermore, the relationship between both peaks is known to be significantly influenced by the strong re-absorption of red chl *a* fluorescence during its radiative transfer through the canopy (Daumard et al., 2012; Fournier et al., 2012).

Clearly, physiological interpretation of the chl *a* fluorescence and chlorophyll data is complex, and strongly depends on the environmental and physiological conditions, as well as structural and biochemical characteristics of vegetation, at both leaf and canopy levels. Considering the low spatio-temporal resolution of the data provided by the SCIAMACHY instrument, and the above-mentioned knowledge gaps, the full interpretation of the available data is a very difficult and error-prone task. However, by analyzing the time series of the SCIAMACHY results (i.e. red and far-red chl *a* fluorescence, and chl proxy), it was intended to investigate whether the retrieved signals can capture typical vegetation cycles, and furthermore, if the variability in timing and relations between the retrieved parameters can be discerned among the different seasons and biomes. The relationship between two chl *a* fluorescence peaks was also investigated, since it can reflect the effects of increasing re-absorption together with increasing chlorophyll content and biomass (Gitelson et al., 1999; Daumard et al., 2012; Fournier et al., 2012). The re-absorption effect was previously suggested to dominate the fluorescence signal (Fournier et al., 2012).

7.4 Biomes determination

Six biomes worldwide have been selected for the purpose of this study of biome-specific vegetation seasonality. The biomes were defined based on the MODIS vegetation data provided by Global Land Data Assimilation System (GLDAS, <http://ldas.gsfc.nasa.gov/gldas>), which uses modified IGBP land cover classification scheme (Friedl et al., 2002), to which three new classes of tundra have been added by the Land Team/EMC/NCEP. The dataset is provided on a 0.25° by 0.25° grid and adopts 20 vegetation types. For the purpose of this study, the vegetation type data were re-gridded into 0.5° by 0.5° grid, on which SCIAMACHY chl *a* fluorescence and chl proxy results are gridded. A given biome was assigned only to those new grid cells, for which all four input cells referred to the same vegetation type. The resulting gridded map is shown in Fig. 7.3 top panel. From the adjusted grid, homogeneous areas of relatively dense vegetation were selected, for which it was expected to observe a strong fluorescence signal for at least a few months of the year. Unfortunately, the most homogeneous areas represent non-vegetated ice or sand deserts (e.g. Greenland and Sahara), or sparsely vegetated open shrublands (e.g. Australia). Regions in South America were not considered, because of the impact of SAA on the retrieved fluorescence values (see Section 6.1.2). Eventually, five relatively homogeneous areas were chosen worldwide, each of which represents a different biome:

- croplands in the North America (C),
- evergreen needleleaf forest in Euroasia (ENF),

7. OBSERVATIONS OF THE SEASONALITY OF PHOTOSYNTHETIC ACTIVITY

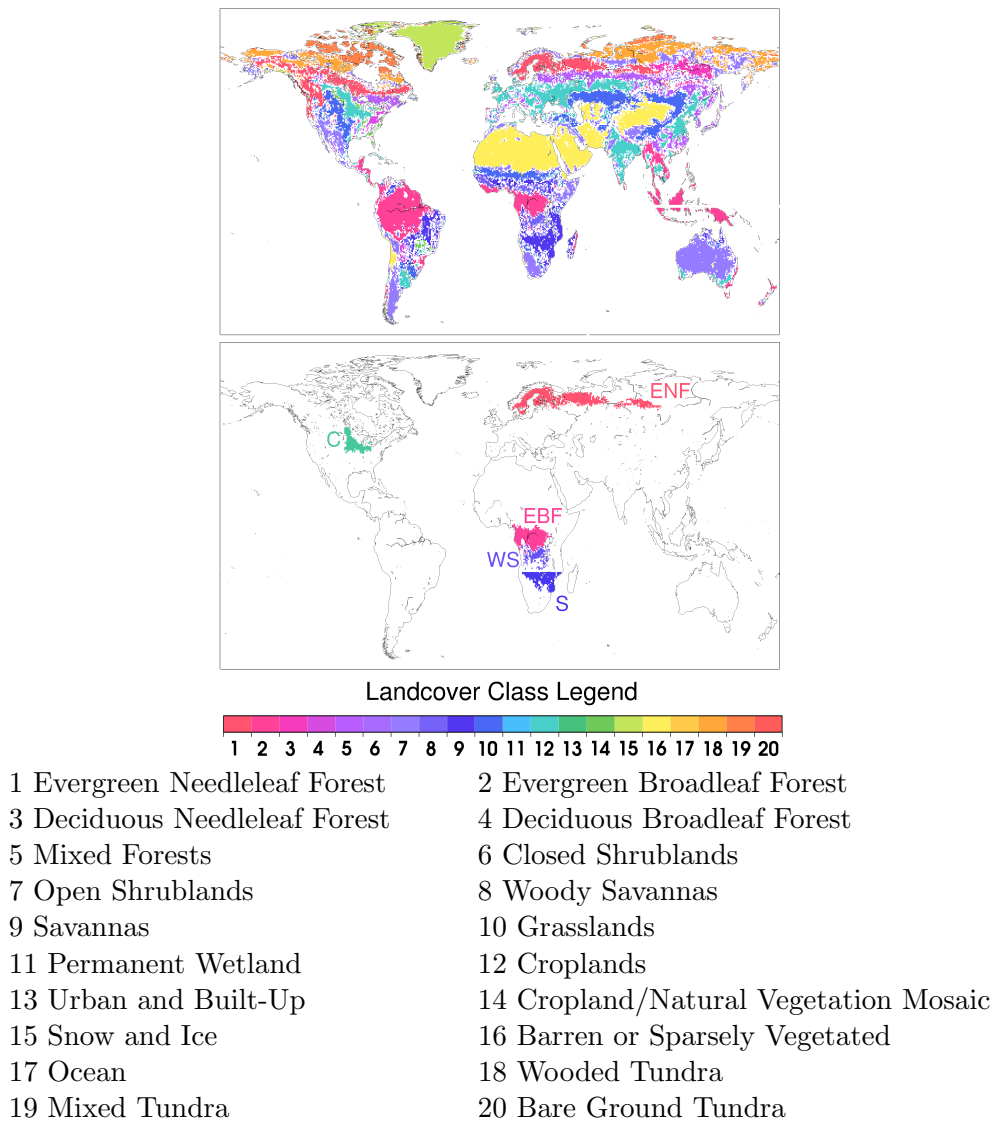


Figure 7.3: Top panel: regrided NOAHv3.3 Vegetation Dataset used in GLDAS2. Bottom panel: selected regions representing different biomes: croplands in the North America (C), evergreen needleleaf forest in Euroasia (ENF), evergreen broadleaf forest in Central Africa (EBF), woody savannas in Central Africa (WS), savannas in Southern Africa (S). Source of original dataset: <http://ldas.gsfc.nasa.gov/gldas/GLDASvegetation.php>

- evergreen broadleaf forest in Central Africa (EBF),
- woody savannas in Central Africa (WS),
- savannas in Southern Africa (S).

The locations of the selected regions are shown in Fig. 7.3 bottom panel.

7.5 Observations of seasonality of photosynthetic activity for different biomes

For every biome, time series of SCIAMACHY chl *a* fluorescence at red and far-red peaks and of the chl proxy were created. Additionally, the time series of the difference and the

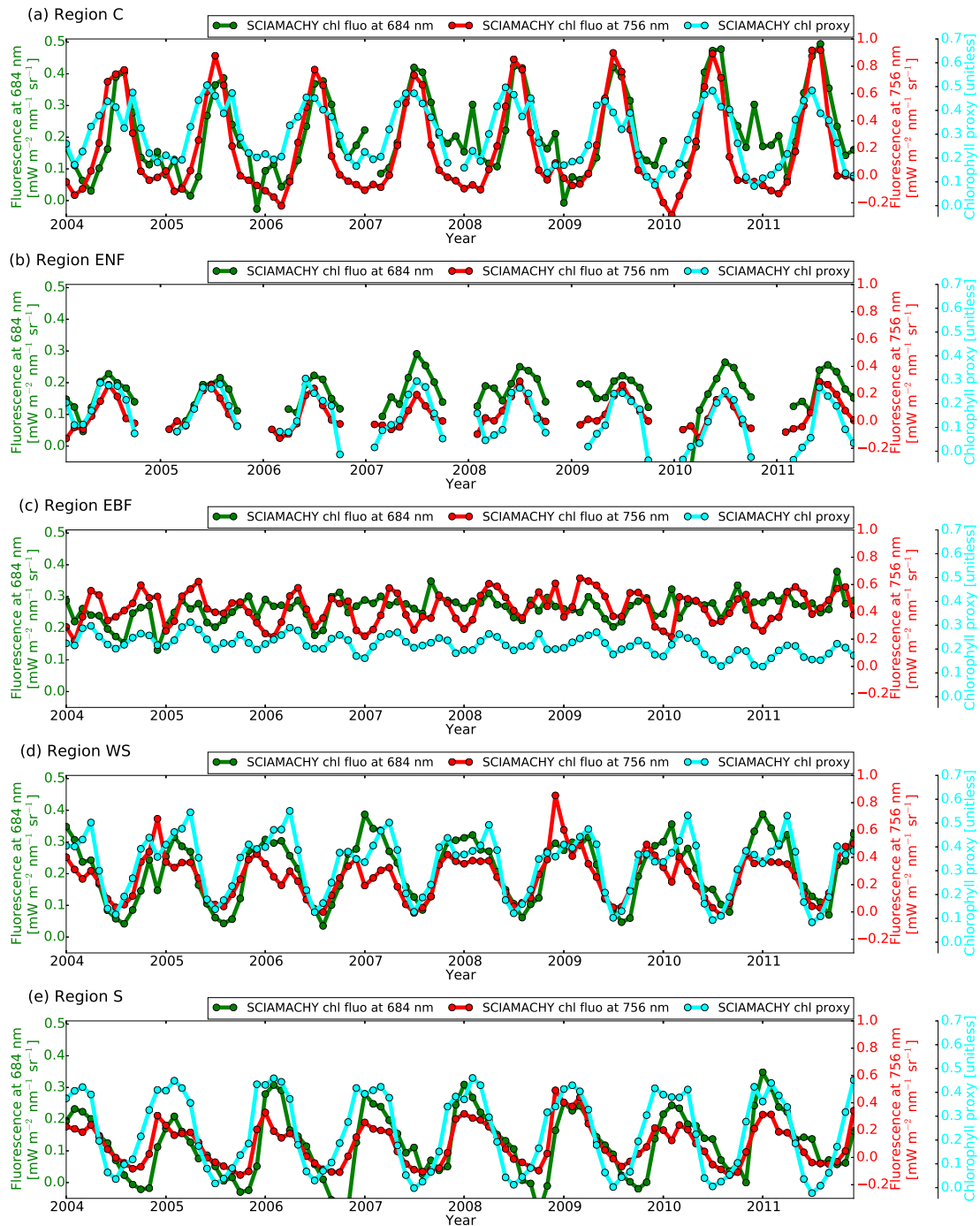


Figure 7.4: Time series of SCIAMACHY parameters (chl *a* fluorescence at 684 nm and at 756 nm, and chl proxy) for the years 2004–2011.

ratio of the two chl *a* fluorescence peaks are shown. The ratio between red fluorescence and far-red fluorescence has been proposed as a tool to detect differences and changes of chlorophyll content in plant species and leaf tissues, and to monitor chlorophyll content and photosynthetic activity caused by environmental conditions, strain and stress (Buschmann, 2007). In addition to the ratio, the difference between the two chl *a* fluorescence peaks is presented, as this parameter is expected to be more stable for small chl *a* fluorescence values, fluctuations of which can lead to rapid changes of the ratio.

For the variables retrieved from SCIAMACHY, a mean value of all available pixels within each defined biome for a given month was calculated. As MODIS NDVI and EVI indices data are provided on a 1° by 1° grid, in the case of their time series the mean was calculated for all pixels, for which the central coordinate overlapped the central coordinate of the pixel of the finer grid of land vegetation biomes map.

The mean annual time series, calculated from monthly climatologies of each parameter for SCIAMACHY and MODIS data are shown in Figures 7.5, 7.6, 7.7, 7.9 and 7.10 (for Regions C, ENF, EBF, WS and S, respectively). Additionally, the full eight-years long time series of monthly averages of chl *a* fluorescence at both red and far-red peaks and chl proxy retrieved from SCIAMACHY, are shown (Fig. 7.4). Boxplots of monthly averages of the retrieved SCIAMACHY parameters for different biomes are shown in Fig. 7.11.

7.5.1 Croplands in North America (region C)

The first investigated region is located in the US Corn Belt (region C), which is an important area of soybean and corn production. This area has been previously investigated by Guanter et al. (2014), since a remarkably high yearly maximum of far-red chl *a* fluorescence signal was retrieved over this region. Guanter et al. (2014) demonstrated that satellite chl *a* fluorescence measurements can be, without additional information, used for estimating GPP over the largest crop belts worldwide, such as the US Corn Belt. Joiner et al. (2014) compared seasonal cycles of GOME-2 chl *a* fluorescence data with the tower-based (tower gas exchange measurements) and upscaled Max Planck Institute for Biogeochemistry (MPI-BGC) GPP data for several sites worldwide, including various agriculture sites in the US. For the agriculture site US-Ne1 (a site in Nebraska, US), which is composed of continuous maize crops, monthly mean MPI-BGC upscaled GPP estimates showed a very good agreement with GOME-2 chl *a* fluorescence measurements.

Similarly to Guanter et al. (2014) and Joiner et al. (2014), a clear seasonal cycle for the croplands in North America can be observed with the SCIAMACHY chl *a* fluorescence and chl proxy data (region C, Fig 7.5). Results of Guanter et al. (2014), Joiner et al. (2014) and SCIAMACHY data all show that the photosynthetic activity increases in early spring, peaks in summer, and declines in autumn to be minimal in winter. Comparing time series of monthly climatologies for different parameters (Fig 7.5), it can be noticed that the month of the peak varies for different parameters: it is August for SCIAMACHY red chl *a* fluorescence, MODIS NDVI and EVI, July for SCIAMACHY far-red chl *a* fluorescence and June for SCIAMACHY chl proxy. The differences between the SCIAMACHY peak months are small, and can be only observed for some years (2005, 2006, 2010, see Fig. 7.4a). Furthermore, the increase of the red chl *a* fluorescence signal, as compared to the far-red,

7.5. OBSERVATIONS OF SEASONALITY OF PHOTOSYNTHETIC ACTIVITY

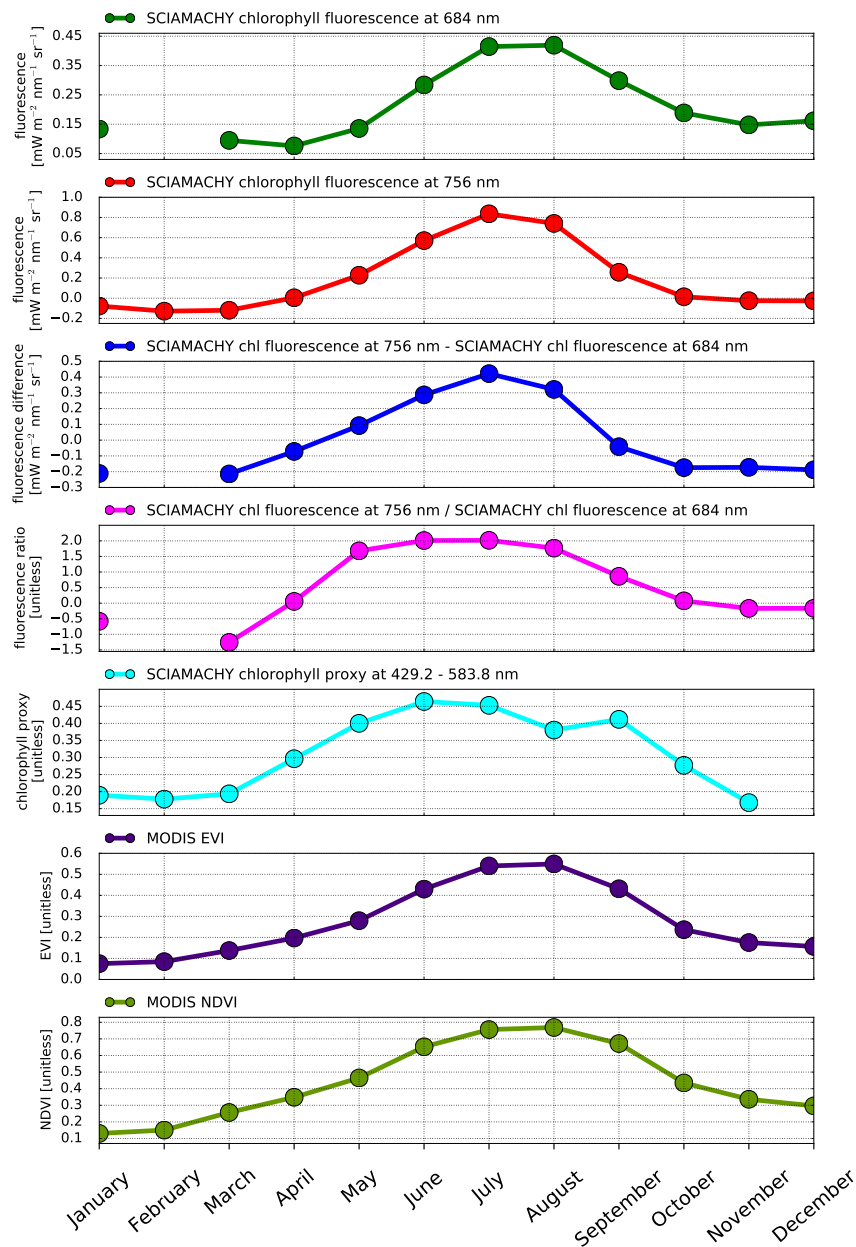


Figure 7.5: Mean annual cycle of SCIAMACHY parameters and MODIS VIs for the years 2004–2011 for region C.

is for some years delayed by a month (years 2004, 2005, 2010, Fig. 7.4a), while for other years chl *a* fluorescence signals of both peaks increase in the same time. They are usually preceded by the increase of the chl proxy. The red chl *a* fluorescence signal is noisier for the winter months, when it is expected to be exactly or close to zero. On the other hand, it is the far-red chl *a* fluorescence signal that starts declining first for most of the years, while the red chl *a* fluorescence and the chl proxy decline usually later. For many years a temporary decline of the chl proxy for August is observed, followed by an abrupt re-rising of the signal, and then by another decline towards winter. MODIS indices (only shown

climatology in Fig 7.5) show a big decrease in fall but tend to continue to decline rather slowly even further into the autumn and winter.

Previously, Joiner et al. (2014) noted a significantly earlier springtime rise and later autumn decline seen in MODIS-based APAR, as compared with GOME-2 far-red chl *a* fluorescence and the GPP estimates for the US-Ne1 agricultural site. Joiner et al. (2014) suggested that it is due to the MODIS (MOD15) fPAR sensitivity to pigments in vegetation and soil other than chlorophyll. A seasonal cycle more consistent with tower-based GPP for several tower sites in the US was obtained by using $fAPAR_{chl}$, a parameter accounting for the fAPAR linked to the chlorophyll-containing canopy fraction (Cheng et al., 2014). The chl proxy algorithm can be expected to be, similarly to fPAR, affected by these issues, and shows earlier rise and later decline than the SCIAMACHY fluorescence results. Joiner et al. (2014) also observed, that the upscaled GPP and GOME-2 far-red chl *a* fluorescence display a slightly wider growing season as compared with the tower-based GPP. In this study, the red peak of chl *a* fluorescence displays the shortest photosynthetically active season, which in turn agrees with previous suggestions, that it is the red peak of chl *a* fluorescence signal that contains most of the information regarding the vegetation productivity (Mohammed et al., 2014).

Both, the ratio and the difference of the two chl *a* fluorescence peaks, follow, in general, the same seasonal cycle (shown in climatologies in Fig 7.5). In agreement with previous studies (e.g., Buschmann, 2007), the ratio of far-red and red peaks increases with the increase in chlorophyll content (often it is the inverse ratio that is used; here this form was chosen to keep consistency of *an increase* of the ratio with *an increase* of the chlorophyll content). However, the difference of two chl *a* fluorescence peaks displays steeper changes in the onset and offset of the photosynthetic activities than the ratio, and mirrors mainly the red fluorescence signal. On the other hand, the ratio of the peaks, shows rapid increase in spring, an almost constant level for most of the summer months, and a slower decline towards winter. The ratio time series is more similar to chl proxy time series than the difference, but does not display a temporal decrease in August, and flattens earlier than the chl proxy signal (in May as compared to June).

Although all parameters follow, in principal, the same seasonal cycle, certain differences are noticeable. They can be driven by canopy structure, or physiological variability of plants over the season, but retrieval artifacts and others effects (e.g., cloud seasonality, directional effects) may well explain part of the differences seen in the seasonality of the studied parameters. The difference and ratio of the chl *a* fluorescence peaks follow the expected cycle, coinciding with the development and decline of the canopy. The red chl *a* fluorescence peak showed, at least for some years, the shortest growing season. The obtained results indicate that that different parameters carry different information about photosynthesis and canopy, and the complex observations, preferably of many parameters simultaneously, can certainly provide better understanding of vegetation dynamics than observations of one index or variable only. However, caution is recommended for the interpretation of the data, as the measurements have low spatio-temporal resolution, and only monthly averages are presented.

7.5.2 Evergreen needleleaf forest in Euroasia (region ENF)

A similar cycle, typical for the northern hemisphere, can be observed for evergreen coniferous forests (the ENF regions). ENF region is located more to the north as compared to region C, which is why no SCIAMACHY measurements were obtained for the winter months, due to the presence of snow cover and high SZAs (December-February, Fig. 7.6). In the case when measurements were obtained, these are often of erroneous value (see the unexpectedly high or negative values for some winters in Fig. 7.4b). MODIS indices

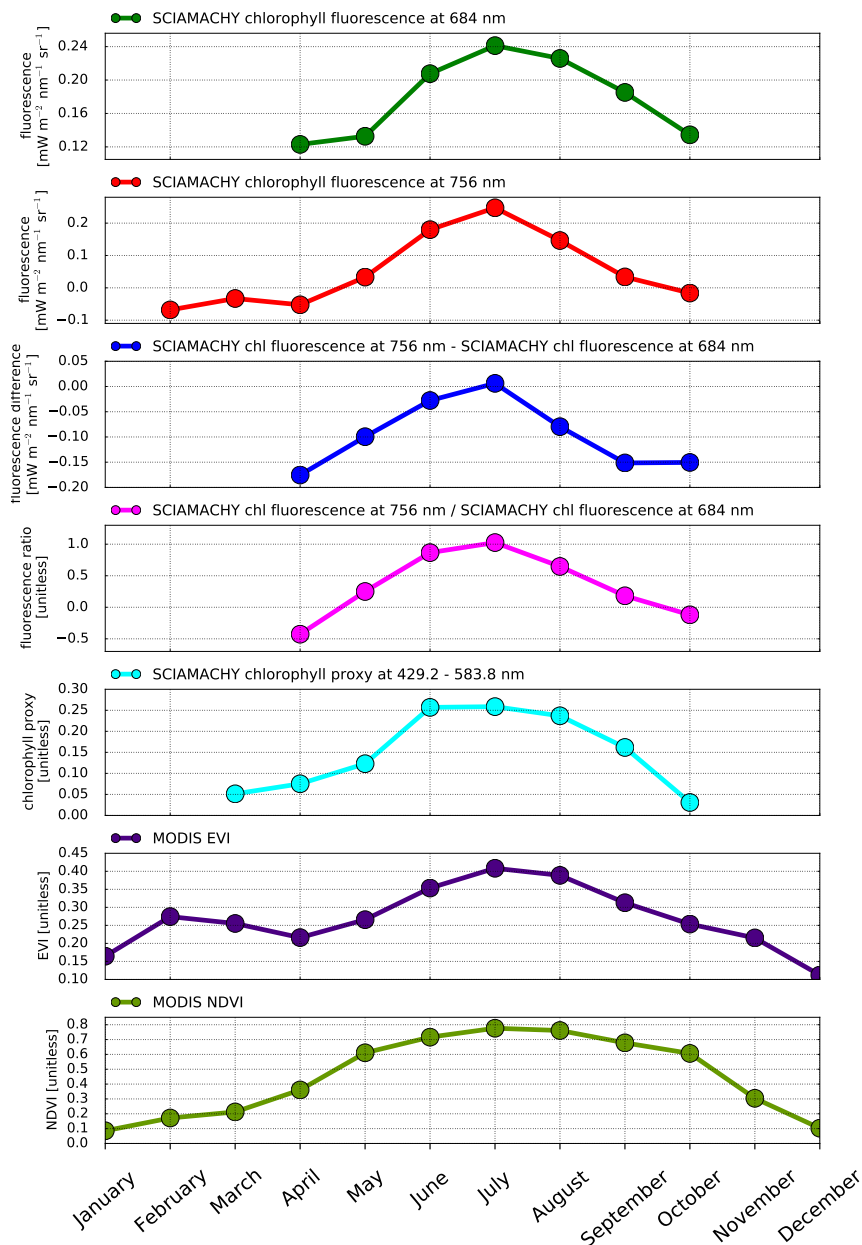


Figure 7.6: Mean annual cycle of SCIAMACHY parameters and MODIS VIs for the years 2004–2011 for region ENF.

provide values throughout the whole year, but at least EVI data seem not to be correct for winter season (see fluctuations of EVI for winter months in Fig. 7.6). Huete et al. (2002) noted that the presence of snow caused the NDVI values to dramatically decrease due to canopy background brightness influences, but in contrast, caused a false positive signal in EVI.

Comparing the time series of monthly climatologies (Fig. 7.6), it can be noticed that red chl *a* fluorescence shows a pronounced increase in the signal one month later than the far-red chl *a* fluorescence. However, this feature is mostly driven by a very small (and negative, hence probably erroneous) value calculated for April 2010 (Fig. 7.4b). Comparing the time series of all eight years (Fig. 7.4b), it can be seen that all three SCIAMACHY parameters have very similar timing of increase and decrease of the signal over the years. The chl proxy, similarly to region C, exhibits a rapid increase in spring, constant levels over the summer and a gradual decrease towards the winter. Chl proxy reaches zero, or even negative values, which is probably due to the effect of snow, as chl proxy is a parameter based on observations of chl absorption. The ratio and difference of chl *a* fluorescence show similar cycles as well.

MODIS indices show in principal similar annual cycles to the SCIAMACHY parameters. Still, as compared to the above discussed region C, more variability for the region ENF is clearly visible. MODIS EVI and NDVI show a more gradual rise and decline throughout the year than SCIAMACHY parameters. Additionally, EVI shows a small peak in February (which can be assumed to be erroneous, possibly because of changes in albedo due to snow cover, see above).

The needleleaf evergreen forests are particularly interesting regions to study the variability between different remote sensing variables, as monitoring of evergreen coniferous forests faces a lot of challenges. Coniferous species maintain a minimum greenness during winter, do not shed all of their needles each year (Fisher et al., 2006), new buds account only for a small proportion of the green biomass, and the shoot elongation process is relatively slow (Jönsson et al., 2010). Hence, the seasonal variation in the biomass is low. Observed changes in the estimated coniferous chlorophyll content are often primarily due to changes in chlorophyll concentration rather than leaf area index (LAI) (Boyd et al., 2011).

Jönsson et al. (2010) showed that evergreen vegetation does not have a sharp increase in greenness during spring, and the melting of snow can influence the vegetation indices at the timing of budburst in boreal forests. Jönsson et al. (2010) concluded that vegetation index threshold values, commonly used for monitoring of spring phenology, were not applicable to Swedish coniferous forests, and that seasonal changes in vegetation indices were more related to snow dynamics (approximately 90%) than to changes in needle biomass (approximately 10%). Furthermore, the recovery of photosynthetic activity can precede complete snow melt and changes in biomass (e.g. Richardson et al., 2009; Thum et al., 2009; Jönsson et al., 2010; Böttcher et al., 2014), which is before the error-free indices measurements are obtained.

7.5.3 Evergreen broadleaf forest in Central Africa (region EBF)

The third investigated region, the EBF region, covers the evergreen broadleaf forests located in the Congo Basin of central Africa. Previous studies have shown that the annual cycle of EVI for African forests within the Congo Basin demonstrates two peaks, which correspond to the two rainy seasons, one during March–May (short rainy season) and second in September–November (long rainy season). Rainy seasons alternate with two periods of lower EVI values, in December–February (long dry season) and in June–August

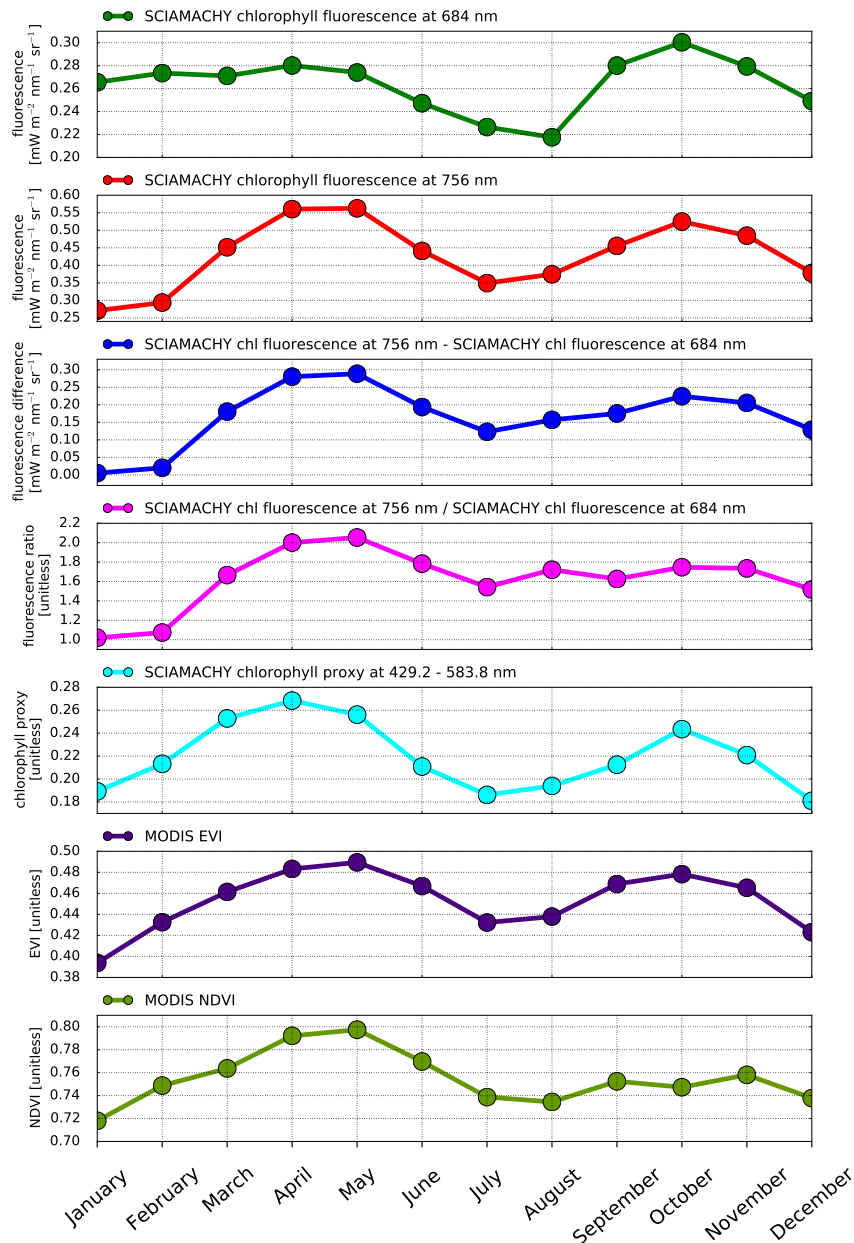


Figure 7.7: Mean annual cycle of SCIAMACHY parameters and MODIS VIs for the years 2004–2011 for region EBF.

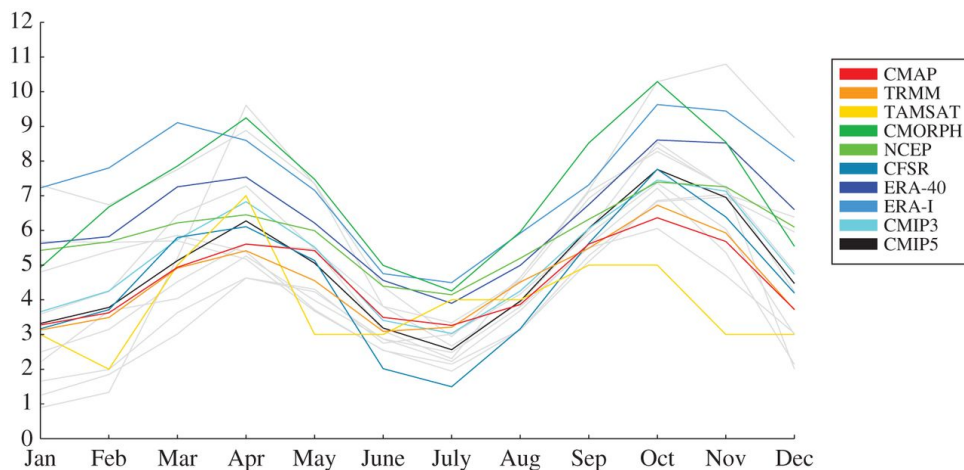


Figure 7.8: Long-term mean annual cycle of rainfall (mm d^{-1}) for Equatorial Central Africa over the region $5^{\circ} \text{ S}–5^{\circ} \text{ N}$, $12.5–30^{\circ} \text{ E}$ for the following datasets: CMAP, TRMM, TAMSAT, CMORPH, NCEP, CSFR, ERA-40, ERA-Interim, ensemble mean of CMIP3 and CMIP5. Individual CMIP5 models are shown in gray. Time period covers years 1961–1990 in the case of NCEP, ERA-40, CMIP3 ensemble and CMIP5 ensemble and 1979–1990 for ERA-Interim, CSFR and CMAP, 1998–2011 for TRMM and TAMSAT and 2002–2011 for CMORPH. Source: (Washington et al., 2013).

(short dry season) (Gond et al., 2013). Washington et al. (2013) computed long-term monthly rainfall means for satellite-based products, reanalyses data and climate models over the largely forested subregion of the Congo Basin, which are shown here for reference (Fig. 7.8). The rainfall seasonality is driven by the inter-tropical convergence zone (ITCZ), which crosses the study area twice a year during equinoxes. EVI was observed to lag the bimodal seasonal cycle of rainfall by about one month and to have a smoother seasonal variation than the rainfall (Zhou et al., 2014).

Gond et al. (2013) showed for similar regions within the Congo basin, that forest greenness, as expressed by EVI, was highly seasonal and strongly correlated with rainfall and, to a lesser extent, to light seasonality. Their EVI seasonal profiles were nearly the mirror images of the seasonal patterns of rainfall and light availability.

The same bimodal pattern is observed by all retrieved vegetation variables for the EBF region (Fig. 7.7). However, the pattern is least captured by the SCIAMACHY red chl *a* fluorescence results, for which the variability over the seasons is also very small. A much clearer and variable annual cycle is observed for the SCIAMACHY far-red chl *a* fluorescence, as well as for the SCIAMACHY chl proxy. There is a slight variability of the timing of the peaks in the first half of the year between the parameters (April or May). However, during the second half of the year all the SCIAMACHY data and MODIS EVI peak simultaneously in October. MODIS EVI follows well the seasonal pattern, while NDVI seems to respond to the first part of the cycle only and flattens for the second part. The time series of the difference and ratio of the chl *a* fluorescence peaks is somewhat similar to NDVI, as it flattens for the second half of the year as well. The constant values over the second half of the year are due to the similar pattern of the chl *a* fluorescence signal at both peaks at that time. In case of the SCIAMACHY far-red fluorescence and

7.5. OBSERVATIONS OF SEASONALITY OF PHOTOSYNTHETIC ACTIVITY

the SCIAMACHY chl proxy, the values are higher for the first peak of the year, which agrees with the EVI pattern. However, in the case of red chl *a* fluorescence signal, higher values are retrieved for the second peak of the year.

As compared to other biomes, the EBF region shows the highest median of both chl *a* fluorescence peaks, but not for the chl proxy (Fig. 7.11). This can indicate that chl *a* fluorescence observations are more applicable for observations of complex canopies. Since the broadleaf forests do not show such a strong seasonal cycle, the dynamic ranges of all the retrieved parameters are clearly smallest among all the biomes.

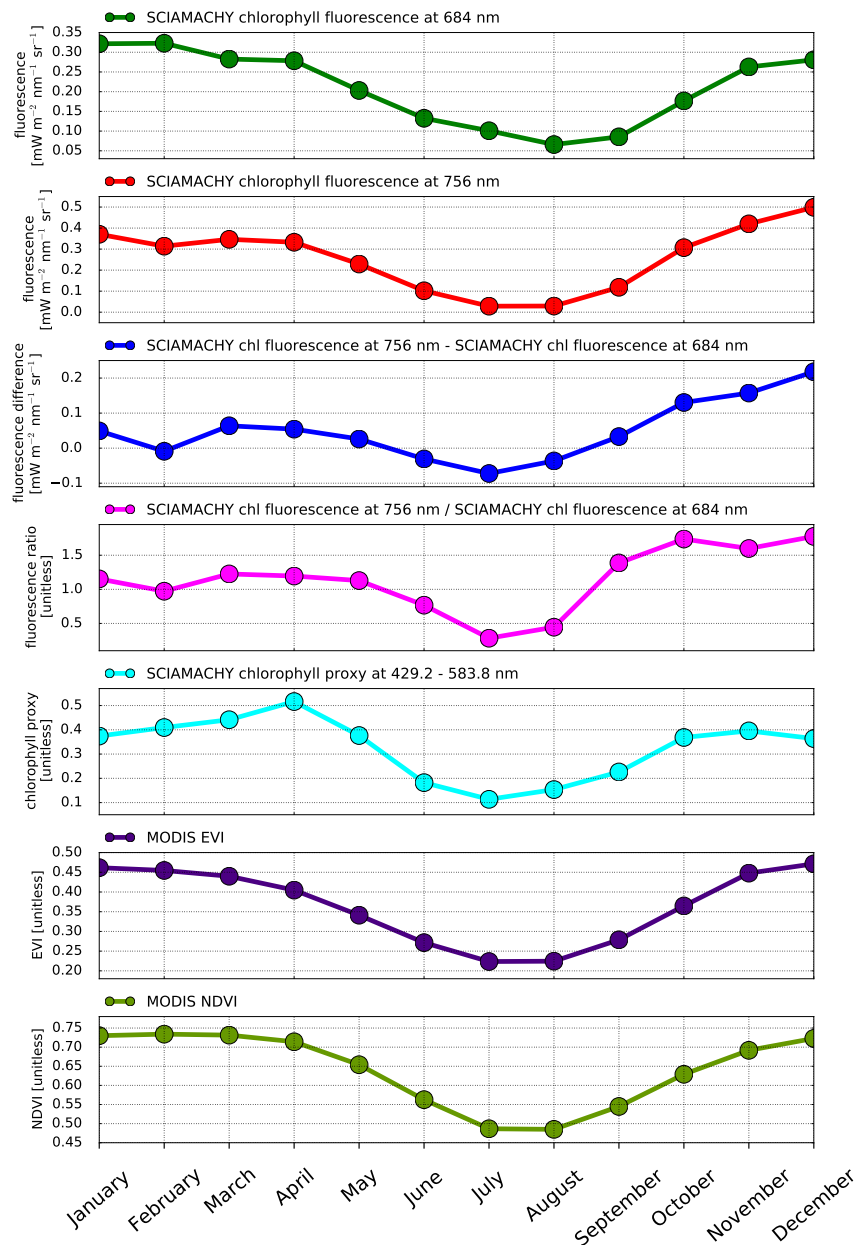


Figure 7.9: Mean annual cycle of SCIAMACHY parameters and MODIS VIs for the years 2004–2011 for region WS.

7.5.4 Woody savannas in Central Africa (region WS)

The time series of vegetation parameters for woody savannas show a strong seasonal cycle (Fig. 7.9), which was previously observed in other studies with the use of VIs (e.g. Hill et al., 2010). The cycle mirrors the pattern of the alternating rainy and dry seasons. In contrast to the case of evergreen forests, both MODIS indices have very similar, synchronized annual cycle. The EVI and NDVI cycles were mostly resembled by the time series of far-red chl *a* fluorescence of the SCIAMACHY results. The red chl *a* fluorescence shows a very similar, but less pronounced pattern. For most years, the chl proxy starts its slow increase earlier than all the other parameters. It peaks later in the season, and is followed by a rapid decrease. A similar cycle of difference and ratio of both peaks of chl *a* fluorescence (Fig. 7.9), with a steep increase of the ratio in the onset of rainy season, is observed.

Woody savannas show the highest maximum chl proxy values among all the biomes with a dynamic range of which is very similar to croplands (Fig. 7.11). However, maximum values for both chl *a* fluorescence peaks are smaller than for croplands (although the median values are higher, but variations are smaller over the years). This also could be explained by the natural (uncultivated) type of ecosystems in this area, which have higher biodiversity (also including trees) and for which all plants do not necessarily show a maximum productivity exactly in the same time.

7.5.5 Savannas in Southern Africa (region S).

Regions S shows a very similar seasonality of photosynthetic activity for rainy and dry seasons as the region WS (Fig. 7.10). The seasonal cycle is very much alike among most of the parameters. The red chl *a* fluorescence peak is less pronounced, and the chl proxy shows the most rapid decline at the end of the rainy season. Here, the difference between two chl *a* fluorescence peaks does not show the clear seasonal pattern. The ratio is considerably flat for most of the year, and shows a sudden increase in October. This is due to small variations of both fluorescence peaks values around zero, which leads to a sudden change of sign.

Overall, the seasonal cycle for both savannas regions (WS and S) are similar and well captured by the SCIAMACHY results (Fig. 7.9 and 7.10, and Fig. 7.4d and e). As regions S and WS cover very similar ecosystems, the values of SCIAMACHY parameters obtained for both regions are very similar. They are slightly higher for woody savannas, which might be because of the presence of deeper-rooted trees that stay longer green and productive due to possibility of using water from deeper ground layers.

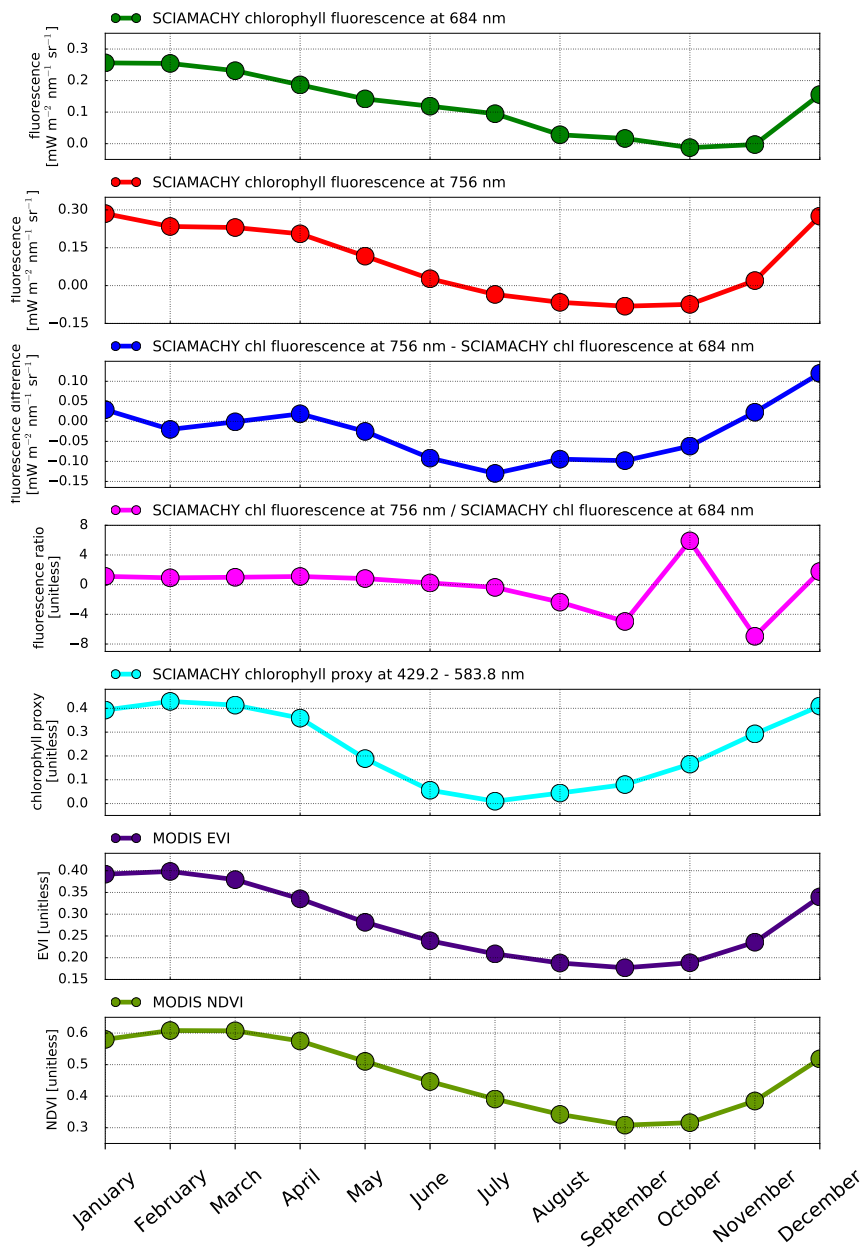


Figure 7.10: Mean annual cycle of SCIAMACHY parameters and MODIS VIs for the years 2004–2011 for region S.

7.6 Discussion and Summary

By showing the full-length time series of monthly averages of SCIAMACHY parameters for all the biomes plotted together on the same scale (Fig. 7.4), and comparing their boxplots (Fig. 7.11), the variability between the SCIAMACHY parameters for different biomes can be compared. First of all, the far-red chl *a* fluorescence is approximately two times stronger than the red chl *a* fluorescence for all the biomes investigated. The relationships

7. OBSERVATIONS OF THE SEASONALITY OF PHOTOSYNTHETIC ACTIVITY

Table 7.1: Correlation coefficients between the monthly averages of SCIAMACHY parameters, for all data together and for individual biomes. All shown correlation coefficients are significant at $p < 0.00001$. A red 'x' is given for the variables for which a significant correlation was not found.

| | All | | Reg C | | Reg ENF | |
|-----------------------|-----------------------|---------------------------|-----------------------|---------------------------|-----------------------|---------------------------|
| | chl <i>a</i> fluo red | chl <i>a</i> fluo far-red | chl <i>a</i> fluo red | chl <i>a</i> fluo far-red | chl <i>a</i> fluo red | chl <i>a</i> fluo far-red |
| chl proxy | 0.53 | 0.58 | 0.58 | 0.80 | 0.67 | 0.77 |
| chl <i>a</i> fluo red | | 0.77 | | 0.83 | | 0.70 |

| | Reg EBF | | Reg WS | | Reg S | |
|-----------------------|-----------------------|---------------------------|-----------------------|---------------------------|-----------------------|---------------------------|
| | chl <i>a</i> fluo red | chl <i>a</i> fluo far-red | chl <i>a</i> fluo red | chl <i>a</i> fluo far-red | chl <i>a</i> fluo red | chl <i>a</i> fluo far-red |
| chl proxy | x | 0.53 | 0.78 | 0.74 | 0.62 | 0.82 |
| chl fluo <i>a</i> red | | x | | 0.71 | | 0.80 |

between the chl *a* fluorescence signals and the chl proxy vary among the biomes. Monthly chl *a* fluorescence maxima at both peaks are overall strongest for US croplands, region C, which was observed for the far-red chl *a* fluorescence signal by Guanter et al. (2014). However, the chl proxy displays relatively similar maximum values for croplands (region C), as well as for the woody savannas and savannas (regions WS and S), although the maximum values of chl *a* are much smaller for regions WS and S than for region C. The chl proxy is exceptionally small in relation to chl *a* fluorescence for the evergreen broadleaf forests (region EBF), and is highest for savannas (Fig. 7.4). The smallest dynamic ranges of all SCIAMACHY parameters are observed for ENF and EBF regions, since both are evergreen forests. In contrast, the remaining biomes, which have strong seasonal cycle, show much higher dynamic range for all the parameters. Such variability suggests, that the retrieved parameters react differently to the canopy structure and vegetation type, and hence should be simultaneously used for the observations of the vegetation dynamics. As all parameters are responding to the changes in biomass and photosynthetic activity of the observed vegetation, they all are significantly correlated ($p < 0.00001$), for all regions besides the EBF region. However, the correlation coefficients vary between the different biomes (Table 7.1).

Additionally, monthly averages of SCIAMACHY parameters for different biomes are shown simultaneously in a 3D space in Fig. 7.12. The most apparent clustering is observed for the region EBF, the SCIAMACHY parameters of which clearly create one separate group. Although the measurements of the ENF region show higher scatter of values, they are still clearly distinctive from the other biomes. The points of the three other regions (C, WS and S) are at least partly intertwined, and cannot be easily separated. These regions are also more similar to each other, than to the forested regions. In general, savannas show smaller values of all SCIAMACHY parameters than woody savannas, while croplands show a great range of fluorescence values spreading over values observed for both savannas and woody savannas (see also Fig. 7.11).

The performed study suggests that comprehensive and simultaneous observations of many parameters can provide a better understanding of vegetation dynamics than observations of one variable only. The interpretation of the retrieved parameters depends on the biome investigated, its vegetation type and canopy structure, but also, e.g., on the dynamics of the snow cover. Croplands show the highest (while evergreen needleleaf forests the lowest) variability of chl *a* fluorescence relatively to the variability of chl proxy. However, for the ENF region, a lot of the observed changes could be driven by a snow cover.

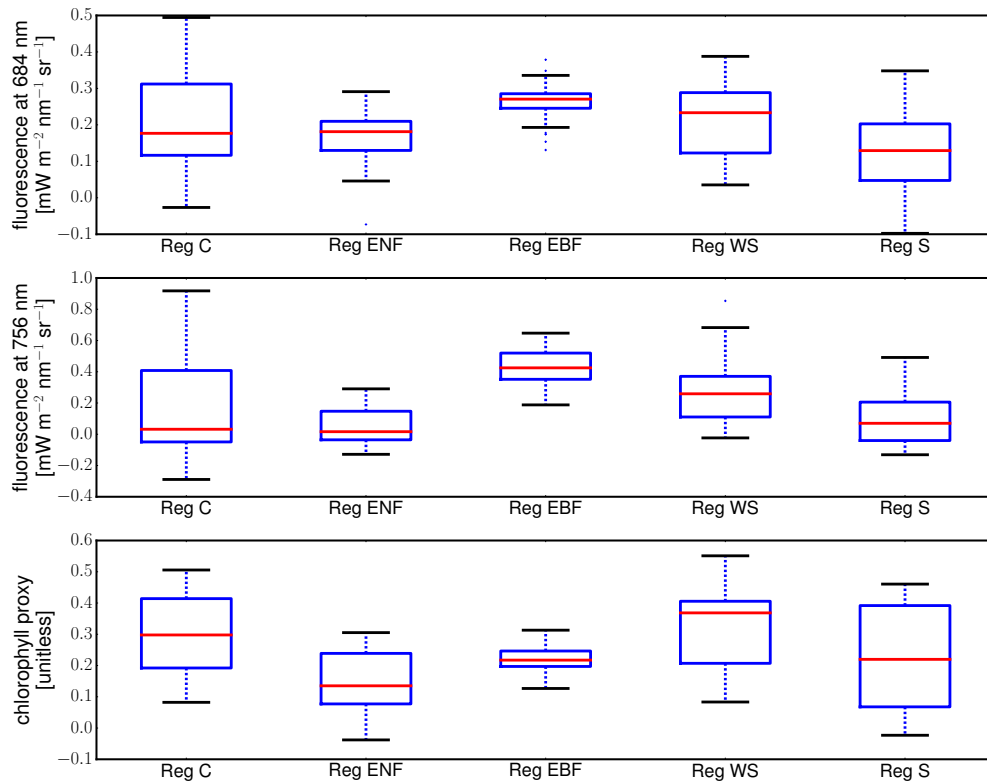


Figure 7.11: Boxplots showing distribution of monthly averages of SCIAMACHY parameters for years 2004–2011 for all regions. The bottom and top of the box are the first and third quartiles. The red horizontal line represents the median. The ends of the whiskers represent the smallest and the largest non-outliers in the data set. The outliers are plotted separately as points on the chart.

Furthermore, the ratio and the difference of the two peaks of chl *a* fluorescence follow the expected pattern of the signal increase with the build-up of chlorophyll and canopy development, as suggested previously by local leaf and canopy measurements and models (Gitelson et al., 1999; Daumard et al., 2012; Fournier et al., 2012). Hence, this study further suggests, that the ratio of two peaks could be used as a chlorophyll content indicator, though depending on the vegetation type. The obtained result here support the need of the further studies of the canopy effects on the retrieved fluorescence signal.

With current spatio-temporal resolution of the hyperspectral data, and the variability of the SCIAMACHY parameters among different biomes, the impact of stress on the retrieved parameters is difficult to observe and was out of scope of this work. Both active and passive optical chl *a* fluorescence measurements and further studies of the various stresses on the chl absorption and fluorescence properties are needed to better understand these signals when retrieved from air- and space-borne platforms.

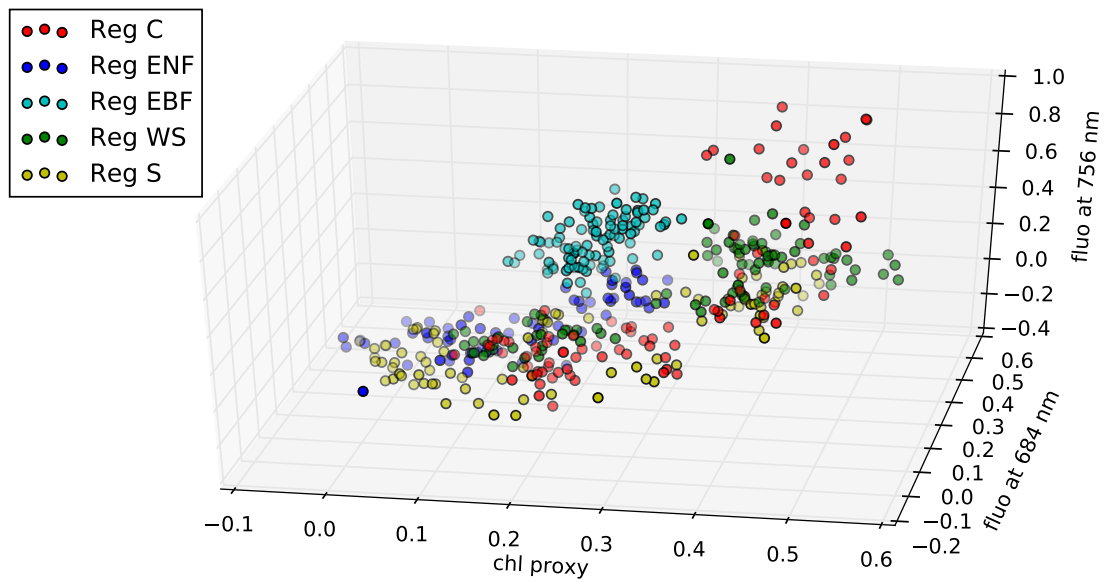


Figure 7.12: The 3D scatter plot of monthly averages of the SCIAMACHY parameters (chl *a* fluorescence at 684 nm and at 756 nm, and chl proxy) for regions C, ENF, EBF, WS and S. .

Chapter 8

Summary, conclusions and outlook

In this study, the hyperspectral data, mainly of the SCIAMACHY instrument, have been investigated in terms of application to the observation of the marine and terrestrial ecosystems. The research focused primarily on the retrieval of inelastic processes in the natural waters: CDOM and red peak of chl *a* fluorescence. Furthermore, the chl *a* fluorescence retrieval was applied to terrestrial vegetation, and expanded into the far-red peak of chl *a* fluorescence. Additionally, a simple algorithm to retrieve chl proxy for terrestrial vegetation was developed. The development of the retrievals included, among others, extensive modeling of inelastic processes in water and on land surface, and the investigation of different retrieval settings. The retrievals are based on the DOAS (Differential Optical Absorption Spectroscopy) technique, and involve fitting spectral features originating from the filling in of the Fraunhofer lines by fluorescence processes. The reference spectra of chl *a* and CDOM fluorescence, used in the DOAS fit, were calculated with the ocean-atmosphere coupled radiative transfer model SCIATRAN.

The preliminary CDOM fluorescence retrievals were unsuccessful in discriminating different CDOM components, and lead to the conclusion that the CDOM fluorescence signal is not strong enough to be retrieved with the proposed approach. The retrievals for both red and far-red peaks of chl *a* fluorescence were successfully developed, and were applied to both marine and terrestrial realms. Additionally, a chl proxy for land vegetation, based on the chl absorption features in the Soret band (blue spectral region), was retrieved. All the retrieved parameters were successfully applied to observations including the seasonality of both marine phytoplankton and terrestrial vegetation. In conclusion, this study has shown exceptional capacity of hyperspectral data for comprehensive observations of marine phytoplankton and terrestrial vegetation. Short summaries of consecutive parts of the study are given below.

Modeling CDOM fluorescence and initial CDOM fluorescence retrievals

CDOM fluorescence was implemented into the coupled radiative transfer model SCIATRAN, with a focus on possible CDOM fluorescence retrievals. However, the modeling studies, followed by preliminary retrievals applied to SCIAMACHY data, have not been successful in retrieving CDOM fluorescence from hyperspectral satellite data. It is mainly

due to the overwhelming effects of other inelastic processes (RRS, VRS) in the spectral region of CDOM fluorescence. Nevertheless, fluorescence of humic-like CDOM can be a significant source of fluorescence signal for coastal waters. Simultaneous retrievals of different fluorescent compounds of DOM would enable detailed studies of the global CDOM composition, but would be even more difficult (especially for amino acid-like components that have excitation spectrum in UV and hence a very weak emission signal in natural conditions).

Enabling the retrievals of chl *a* fluorescence and terrestrial chl proxy

Within this study the retrievals of red (~ 685 nm) and far-red (~ 755 nm) peaks of chlorophyll *a* fluorescence were developed. In case of the red peak of chl *a* fluorescence, two additional fits (688.0 - 700.0 nm and 615.9 - 620.9 nm) were performed, in order to take into account the effects of water vapor absorption and Raman scattering. The correction scheme, based on the modeling data, was developed and applied to SCIAMACHY (and partially to GOME-2) data. In case of far-red chl *a* fluorescence, the zero-offset problem was recognized and a data-driven correction was implemented to solve this issue. For both retrievals, the conversion schemes dependent on the elastically scattered radiance were developed with use of the radiative transfer simulations. The marine red chl *a* fluorescence results were additionally normalized to solar zenith angle, in order to be compared with the MODIS nFLH product. The DOAS technique was also implemented to retrieve a chl proxy of terrestrial plants, in a manner similar to previous algorithms aimed at observations of marine phytoplankton. The chlorophyll proxy retrieval was performed in the spectral window of 429.2 - 583.8 nm, which covers the Soret band of chl absorption. As most of the vegetation-related indices focus on the red edge, this spectral region can provide new information about terrestrial biomass.

Global observations of chl *a* fluorescence and terrestrial chl proxy

The newly developed red and far-red chl *a* fluorescence and chl proxy retrievals have enabled simultaneous observations of marine phytoplankton and terrestrial vegetation. The red peak of chl *a* fluorescence from terrestrial vegetation has never been observed from space before, and marine chl *a* fluorescence was retrieved for the first time with hyperspectral satellite-borne sensors. The obtained SCIAMACHY results showed good spatial agreement with other datasets, MODIS nFLH for marine chl *a* fluorescence, and MODIS EVI and GOME-2 far-red chl fluorescence (Joiner et al., 2013) for land vegetation. It was shown that these signals can be successfully retrieved from space with hyperspectral sensors. However, since chl *a* fluorescence is a weak signal, its observation with the spectral, spatial and temporal resolution of the current instruments remains challenging. The chl proxy retrieval, designed to observe terrestrial chl in the Soret band, showed promising preliminary results.

Application of the retrieved SCIAMACHY parameters to observations of phytoplankton and vegetation seasonality

For the marine realm, only observations of the red peak of chl *a* fluorescence can be applied to phenological studies of phytoplankton, as the far-red peak is invisible from space due to strong liquid water absorption. Two time series of chl *a* fluorescence retrieved from SCIAMACHY were presented: one for a subregion of the Indian Ocean near the coast of Madagascar, and one for the equatorial Pacific. The seasonal cycle and interannual variability of phytoplankton were well captured by the SCIAMACHY parameters. Good agreement with multispectral ocean color products (MODIS nFLH and MODIS Chl *a*) was obtained, and response of phytoplankton to climate fluctuations, as expressed by MEI, was well captured for the equatorial Pacific.

In case for land, all the retrieved parameters (SCIAMACHY red and far-red chl *a* fluorescence, and chl proxy) were applied to observations of the seasonality of the vegetation photosynthetic activity of five different biomes worldwide. SCIAMACHY data successfully captured the seasonal cycle of vegetation. Time series showed that the two peaks of the chl *a* fluorescence and chl proxy do not carry the same information about the physiology and biomass of vegetation, as they do not follow exactly the same seasonal pattern and their relationship varies over time and among biomes. The ratio and the difference of the two peaks of chl *a* fluorescence were calculated, which followed the increase of chlorophyll content and canopy development, as suggested previously by leaf and canopy *in situ* measurements and models. This study supports the argument, that the ratio of two peaks could be used as the chlorophyll content indicator, though not constant among the different vegetation types. Simultaneous observations of many parameters can provide better understanding of vegetation dynamics than observations of one index or variable only. However, with current spatio-temporal resolution of the hyperspectral data, the stress impact on the retrieved parameters of vegetation is difficult to estimate and was out of scope of this work.

Outlook for future studies

Based on this study, the following prospects for future research were identified:

- *Modeling of CDOM fluorescence* Implementing CDOM fluorescence with the PARAFAC model into the radiative transfer model is a novel approach and needs further investigation, especially regarding scaling of matrices into which the EEMs are decomposed. This can be improved by analyzing CDOM samples together with *in situ* radiometric measurements. Improved modeling of multiple fluorescent CDOM components within the water column will help to better understand the CDOM dynamics.
- *CDOM fluorescence retrievals* In addition to looking at filling-in of individual Fraunhofer lines, wider fit windows could be applied, as broad filling-in spectra of different CDOM components are distinctly different from RRS and VRS. Additional adequate EEM measurements, combined use of narrow and broad fluorescence features and an appropriate method to account for inelastic processes are necessary for further development of CDOM fluorescence retrievals for hyperspectral satellite-borne instruments.

- *Chl a red fluorescence retrieval* Chl *a* fluorescence is a very weak signal, and use of a broader window could in future decrease the noise within the retrieval. However, this would also mean that interactions of more atmospheric absorbers would need to be considered within the retrievals.
- *Chl a fluorescence retrievals at multiple wavelengths* It was shown that chl *a* fluorescence can be retrieved at both red and far-red peaks. However, chl *a* fluorescence could be retrieved in multiple small fit windows, which could derive information about the whole chl *a* fluorescence spectrum. This would be useful for studies of chl *a* fluorescence response to different environmental conditions.
- *Chl proxy retrieval* Chl proxy retrieval showed promising preliminary results. The retrieval can be substantially improved and should be tested in terms of sensitivity to environmental conditions and instrumental characteristics. Furthermore, it can also be applied to other hyperspectral sensors (e.g. GOME-2), and tested for future possible missions, including instruments with coarser spectral resolution (e.g. EnMAP).
- *Marine time series analysis* The obtained SCIAMACHY results showed significant correlation with MODIS nFLH and Chl *a* products, as well as climate fluctuations as expressed by MEI. Fluorescence results could be further compared with chl *a* data, to investigate if they provide an important additional source of information on phytoplankton, especially in the case of specific conditions (e.g. coastal waters, or where the chl *a* concentration varies primarily due to the photoacclimation, rather than changes in biomass).
- *Terrestrial time series analysis* It was shown that the red and far-red peaks of chl *a* fluorescence and chl proxy do not carry the same information on vegetation status. Satellite observations of multiple parameters for vegetation studies, preferably in parallel to *in situ* observations, will improve our understanding of observed signals and their practical application to monitoring phenology, health and stress resilience of vegetation.
- *Application to other satellite instruments* The proposed algorithms are generic and, after minor adjustments, can be applied to other current and future hyperspectral missions (e.g. TROPOMI) to provide long-term observations and better temporal and spatial coverage.
- *Chl a fluorescence knowledge gaps* The obtained SCIAMACHY results confirm that one of the main knowledge gaps of the chl *a* fluorescence observations is the understanding of the interplay between the different variables shaping the chl *a* fluorescence signal, e.g., vegetation type, environmental conditions, canopy structure. Especially the issue of the impact of canopy structure needs to be resolved before chl *a* fluorescence signal can be used for vegetation health and stress studies.

List of abbreviations

| | |
|-----------------------|--|
| aNN | Artificial neural network |
| ANOVA | Analysis of variance |
| ATP | Adenosine triphosphate |
| ATPase | ATP synthase |
| AVHRR | Advanced Very High Resolution Radiometer |
| BVOC | Biogenic volatile organic compounds |
| CET | Cyclic electron transport |
| chl | Chlorophyll |
| CDOM | Colored dissolved organic matter |
| DOC | Dissolved organic carbon |
| CH₄ | Methane |
| C | Croplands (region) |
| CarbonSat | Carbon Monitoring Satellite |
| CO | Carbon monoxide |
| CO₂ | Carbon dioxide |
| COS | Carbon sulfide |
| Cyt | Cytochrome |
| CZCS | Coastal Zone Color Scanner |
| DOAS | Differential optical absorption spectroscopy |
| DOD | Differential optical depth |
| DOM | Dissolved organic matter |
| EEMS | Emission matrix fluorescence spectroscopy |

| | |
|---------------|--|
| EBF | Evergreen broadleaf forest (region) |
| ENF | Evergreen needleleaf forest (region) |
| ENSO | The El Niño-Southern Oscillation |
| EVI | Enhanced vegetation index |
| fAPAR | Fraction of absorbed photosynthetically active radiation |
| Fd | Ferredoxin |
| FDOM | Fluorescent dissolved organic matter |
| FLEX | FLuorescence EXplorer |
| FLH | Fluorescence line height |
| FNR | Ferredoxin-NADPH reductase |
| FRR | Fast repetition rate fluorometry |
| FTS | Fourier transform spectrometer |
| FWHM | Full width at half maximum |
| GLDAS | Global land data assimilation system |
| GOME-2 | Global Ozone Monitoring Experiment–2 |
| GOSAT | Greenhouse Gases Observing Satellite |
| GPP | Gross primary production |
| Grend | Greenland |
| GSM | Garver-Siegel-Maritorea |
| IFOV | Instantaneous field of view |
| IOP | Inherent optical property |
| ITCZ | Inter-tropical convergence zone |
| LAI | Leaf area index |
| LET | Linear electron transport |
| LUE | Light use efficiency |
| nFLH | Normalized fluorescence line height |
| MEI | Multivariate El Niño Southern Oscillation index |
| MERIS | Medium Resolution Imaging Spectrometer |
| MGVI | MERIS global vegetation index |

| | |
|-------------------------|---|
| MODIS | Moderate Resolution Imaging Spectroradiometer |
| MPI-BGC | Max Planck Institute for Biogeochemistry |
| MTCI | MERIS terrestrial chlorophyll index |
| N₂ | Nitrogen gas |
| NADP⁺ | Nicotinamide adenine dinucleotide phosphate |
| NADPH | The reduced form of nicotinamide adenine dinucleotide phosphate |
| NASA | National Aeronautics and Space Administration |
| nAtln | North Atlantic |
| NCP | Net canopy photosynthesis |
| NDVI | Normalized difference vegetative index |
| NIR | Near infrared |
| nPac | North Pacific |
| NPP | Net primary production |
| NPQ | Non-photochemical quenching |
| O₂ | Oxygen gas |
| OCO-2 | Orbiting Carbon Observatory-2 |
| OEC | Oxygen-evolving complex |
| OLCI | Ocean Land Colour Instrument |
| PAM | Pulse amplitude modulation fluorometry |
| PAR | Photosynthetically active radiation |
| PARAFAC | Parallel factor analysis |
| PC | Plastocyanin |
| PCA | Principal component analysis |
| Pheo | Pheophytin |
| PLS | Partial least squares regression |
| P&P | Pump-and-probe fluorometry |
| PQ | Photochemical quenching |
| PS | Photosystem |
| Q_A | Quinone A |

| | |
|-------------------------|---|
| QAA | Quasi Analytical Algorithm |
| qE | Antennae quenching |
| qI | Reaction center quenching |
| ROS | Reactive oxygen species |
| RRS | Rotational Raman scattering |
| RTE | Radiative transfer equation |
| SCIAMACHY | Scanning Imaging Absorption Spectrometer for Atmospheric Chartography |
| S | Savannas (region) |
| snFLH | Simplified normalized fluorescence line height |
| sPac | South Pacific |
| SAA | South Atlantic Anomaly |
| Sah | Sahara |
| SST | Sea surface temperature |
| SZA | Solar zenith angle |
| VIS | Visible |
| VRS | Vibrational Raman scattering |
| UV | Ultraviolet |
| UVN | Ultraviolet visible near-infrared |
| VI | Vegetation index |
| VIIRS | Visible Infrared Imaging Radiometer Suite |
| W_F | The spectral window of red chl <i>a</i> fluorescence retrieval |
| W_R | The spectral window of Raman scattering retrieval |
| W_W | The spectral window of water vapor retrieval |
| WS | Woody savannas (region) |

Bibliography

- Abbott, M. R., & Letelier, R. M. (1999). Algorithm theoretical basis document chlorophyll fluorescence (MODIS product number 20). NASA (<http://www.modis.gsfc.nasa.gov/data/atbd>), .
- Aiken G.R., W. R. M. P., McKnight D. (1985). An introduction to humic substances in soil, sediment and water. In W. R. M. P. Aiken G.R., McKnight D. (Ed.), *Humic Substances in Soil, Sediment and Water*. John Wiley & Sons: New York.
- Babin, M. (2003). Variations in the light absorption coefficients of phytoplankton, nonalgal particles, and dissolved organic matter in coastal waters around Europe. *Journal of Geophysical Research*, 10.1029/2001JC000882{\it\bibinfo{volume}{108}\}, \bibinfo{pages}{2417--2448}.
- Babin, M. (2008). Phytoplankton fluorescence: Theory, current literature and in situ measurement. In R. C. Babin M., & C. J.J. (Eds.), *Real-time coastal observing systems for ecosystem dynamics and harmful algal blooms*. UNESCO.
- Babin, M., Morel, A., & Gentili, B. (1996). Remote sensing of sea surface sun-induced chlorophyll fluorescence: consequences of natural variations in the optical characteristics of phytoplankton and the quantum yield of chlorophyll a fluorescence. *International Journal of Remote Sensing*, 10.1080/01431169608948781{\it\bibinfo{volume}{17}\}, \bibinfo{pages}{2417--2448}.
- Badeck, F.-W., Bondeau, A., Bottcher, K., Doktor, D., Lucht, W., Schaber, J., & Sitch, S. (2004). Responses of spring phenology to climate change. *New Phytologist*, 10.1111/j.1469-8137.2004.01059.x{\it\bibinfo{volume}{162}\}, \bibinfo{pages}{295--309}.
- Baker, A. (2005). Thermal fluorescence quenching properties of dissolved organic matter. *Water Research*, 10.1016/j.watres.2005.08.023{\it\bibinfo{volume}{39}\}, \bibinfo{pages}{4405--4412}.
- Baldrige, A., Hook, S., Grove, C., & Rivera, G. (2009). The ASTER spectral library version 2.0. *Remote Sensing of Environment*, 10.1016/j.rse.2008.11.007{\it\bibinfo{volume}{113}\}, \bibinfo{pages}{711--715}.
- Barber, R. T., & Chavez, F. P. (1983). Biological consequences of El Niño. *Science*, 222, 1203–1210.
- Barber, R. T., & Chávez, F. P. (1986). Ocean variability in relation to living resources during the 1982–83 El Niño. *Nature*, 10.1038/319279a0{\it\bibinfo{volume}{319}\}, \bibinfo{pages}{279--285}.
- Barrios, J. M., Verstraeten, W. W., Maes, P., Clement, J., Aerts, J.-M., Haredasht, S. A., Wambacq, J., Lagrou, K., Ducoffre, G., Ranst, M. V., Berckmans, D., & Coppin, P. (2010). Satellite Derived Forest Phenology and Its Relation with Nephropathia Epidemica in Belgium. *International Journal of Environmental Research and Public Health*, 10.3390/ijerph7062486{\it\bibinfo{volume}{7}\}, \bibinfo{pages}{2486--2500}.

BIBLIOGRAPHY

- Battin, T. J., Kaplan, L. A., Findlay, S., Hopkinson, C. S., Marti, E., Packman, A. I., Newbold, J. D., & Sabater, F. (2008). Biophysical controls on organic carbon fluxes in fluvial networks. *Nature Geoscience*, 10.1038/ngeo101{\it\bibinfo{volume}{1}}{\it\bibinfo{pages}{95--100}}.
- Beer, C., Reichstein, M., Tomelleri, E., Ciais, P., Jung, M., Carvalhais, N., Rodenbeck, C., Arain, M. A., Baldocchi, D., Bonan, G. B., Bondeau, A., Cescatti, A., Lasslop, G., Lindroth, A., Lomas, M., Luyssaert, S., Margolis, H., Oleson, K. W., Rouspard, O., Veenendaal, E., Viovy, N., Williams, C., Woodward, F. I., & Papale, D. (2010). Terrestrial Gross Carbon Dioxide Uptake: Global Distribution and Covariation with Climate. *Science*, 10.1126/science.1184984{\it\bibinfo{volume}{329}}{\it\bibinfo{pages}{834--838}}.
- Behrenfeld, M. J., Westberry, T. K., Boss, E., O'Malley, R. T., Siegel, D. A., Wiggert, J. D., Franz, B. A., McClain, C. R., Feldman, G. C., Doney, S. C. et al. (2009). Satellite-detected fluorescence reveals global physiology of ocean phytoplankton. *Biogeosciences*, 10.5194/bg-6-779-2009{\it\bibinfo{volume}{6}}{\it\bibinfo{pages}{779--794}}.
- Blankenship, R. E. (Ed.) (2002). *Molecular Mechanisms of Photosynthesis*. Oxford, UK: Blackwell Science Ltd.
- Blondeau-Patissier, D., Gower, J. F., Dekker, A. G., Phinn, S. R., & Brando, V. E. (2014). A review of ocean color remote sensing methods and statistical techniques for the detection, mapping and analysis of phytoplankton blooms in coastal and open oceans. *Progress in Oceanography*, 10.1016/j.pocean.2013.12.008{\it\bibinfo{volume}{123}}{\it\bibinfo{pages}{123--144}}.
- Blough, N. (2001). Photochemical processes. In *Encyclopedia of Ocean Sciences* (pp. 2162–2172). Elsevier.
- Blum, M., Rozanov, V. V., Burrows, J. P., & Bracher, A. (2012). Coupled ocean-atmosphere radiative transfer model in the framework of software package SCIATRAN: selected comparisons to model and satellite data. *Advances in Space Research*, 10.1016/j.asr.2012.02.012{\it\bibinfo{volume}{49}}{\it\bibinfo{pages}{1728--1742}}.
- Bodhaine, B. A., Wood, N. B., Dutton, E. G., & Slusser, J. R. (1999). On Rayleigh optical depth calculations. *Journal of Atmospheric & Oceanic Technology*, 10.1175/1520-0426(1999)016<1854:ORODC>2.0.CO;2{\it\bibinfo{volume}{16}}{\it\bibinfo{pages}{1854--1861}}.
- Bovensmann, H., Buchwitz, M., Burrows, J. P., Reuter, M., Krings, T., Gerilowski, K., Schneising, O., Heymann, J., Tretner, A., & Erzinger, J. (2010). A remote sensing technique for global monitoring of power plant CO₂ emissions from space and related applications. *Atmospheric Measurement Techniques*, 10.5194/amt-3-781-2010{\it\bibinfo{volume}{3}}{\it\bibinfo{pages}{781--811}}.
- Bovensmann, H., Burrows, J. P., Buchwitz, M., Frerick, J., Noël, S., Rozanov, V. V., Chance, K. V., & Goede, A. P. H. (1999). SCIAMACHY: mission objectives and measurement modes. *Journal of the Atmospheric Sciences*, 56, 127–150.
- Boyd, D. S., Almond, S., Dash, J., Curran, P. J., & Hill, R. A. (2011). Phenology of vegetation in Southern England from Envisat MERIS terrestrial chlorophyll index (MTCI) data. *International Journal of Remote Sensing*, 10.1080/01431161.2010.542194{\it\bibinfo{volume}{32}}{\it\bibinfo{pages}{8421--8447}}.
- Bracher, A., Vountas, M., Dinter, T., Burrows, J. P., Röttgers, R., & Peeken, I. (2009). Quantitative observation of cyanobacteria and diatoms from space using PhytoDOAS on SCIAMACHY data. *Biogeosciences*, 6, 751–764.

- Bricaud, A., Ciotti, A. M., & Gentili, B. (2012). Spatial-temporal variations in phytoplankton size and colored detrital matter absorption at global and regional scales, as derived from twelve years of SeaWiFS data (1998-2009). *Global Biogeochemical Cycles*, 10.1029/2010GB003952{\it\bibinfo{volume}{26}\},\bibinfo{pages}{n/a--n/a}.
- Bricaud, A., Morel, A., & Prieur, L. (1981). Absorption by dissolved organic matter of the sea (yellow substance) in the UV and visible domains. *Limnology and oceanography*, (p. 43–53).
- Bro, R., & Vidal, M. (2011). EEMizer: automated modeling of fluorescence EEM data. *Chemometrics and Intelligent Laboratory Systems*, 10.1016/j.chemolab.2010.06.005{\it\bibinfo{volume}{106}\},\bibinfo{pages}{86--92}.
- Buchwitz, M., Reuter, M., Bovensmann, H., Pillai, D., Heymann, J., Schneising, O., Rozanov, V., Krings, T., Burrows, J. P., Boesch, H., Gerbig, C., Meijer, Y., & Löscher, A. (2013). Carbon Monitoring Satellite (CarbonSat): assessment of atmospheric CO₂ and CH₄ retrieval errors by error parameterization. *Atmospheric Measurement Techniques*, 10.5194/amt-6-3477-2013{\it\bibinfo{volume}{6}\},\bibinfo{pages}{3477--3500}.
- Burrows, J. P., Hölzle, E., Goede, A. P. H., Visser, H., & Fricke, W. (1995). SCIAMACHY—Scanning Imaging Absorption Spectrometer for Atmospheric Chartography. *Acta Astronautica*, 35, 445–451.
- Burrows, J. P., Weber, M., Buchwitz, M., Rozanov, V. V., Ladstätter-Weissenmayer, A., Richter, A., DeBeek, R., Hoogen, R., Bramstedt, K., & Eichmann, K.-U. (1999). The Global Ozone Monitoring Experiment (GOME): mission concept and first scientific results. *Journal of the Atmospheric Sciences*, 56, 151–175.
- Buschmann, C. (2007). Variability and application of the chlorophyll fluorescence emission ratio red/far-red of leaves. *Photosynthesis Research*, 10.1007/s11120-007-9187-8{\it\bibinfo{volume}{92}\},\bibinfo{pages}{261--271}.
- Buschmann, C., & Lichtenthaler, H. K. (1998). Principles and characteristics of multi-colour fluorescence imaging of plants. *Journal of Plant Physiology*, 10.1016/S0176-1617(98)80144-2{\it\bibinfo{volume}{152}\},\bibinfo{pages}{297--314}.
- Böttcher, K., Aurela, M., Kervinen, M., Markkanen, T., Mattila, O.-P., Kolari, P., Metsämäki, S., Aalto, T., Arslan, A. N., & Pulliainen, J. (2014). MODIS time-series-derived indicators for the beginning of the growing season in boreal coniferous forest — A comparison with CO₂ flux measurements and phenological observations in Finland. *Remote Sensing of Environment*, 10.1016/j.rse.2013.09.022{\it\bibinfo{volume}{140}\},\bibinfo{pages}{625--638}.
- Callies, J., Corpaccioli, E., Eisinger, M., Hahne, A., & Lefebvre, A. (2000). GOME-2-MetOP's second-generation sensor for operational ozone monitoring. *ESA bulletin*, 102, 28–36.
- Carder, K. L., Steward, R. G., Harvey, G. R., & Ortner, P. B. (1989). Marine humic and fulvic acids: Their effects on remote sensing of ocean chlorophyll. *Limnology and Oceanography*, 10.4319/lo.1989.34.1.0068{\it\bibinfo{volume}{34}\},\bibinfo{pages}{68--81}.
- Chavez, F. P., Messié, M., & Pennington, J. T. (2011). Marine primary production in relation to climate variability and change. *Annual Review of Marine Science*, 10.1146/annurev.marine.010908.163917{\it\bibinfo{volume}{3}\},\bibinfo{pages}{227--260}.
- Chavez, F. P., Strutton, P. G., Friederich, G. E., Feely, R. A., Feldman, G. C., Foley, D. G., & McPhaden, M. J. (1999). Biological and chemical response of the equatorial Pacific ocean to the 1997-98 El Niño. *Science*, 286, 2126–2131.

BIBLIOGRAPHY

- Cheng, Y.-B., Middleton, E., Zhang, Q., Huemmrich, K., Campbell, P., Corp, L., Cook, B., Kustas, W., & Daughtry, C. (2013). Integrating solar induced fluorescence and the photochemical reflectance index for estimating gross primary production in a cornfield. *Remote Sensing*, 10.3390/rs5126857{\it\bibinfo{volume}{5}\/}, \bibinfo{pages}{6857--6879}.
- Cheng, Y.-B., Zhang, Q., Lyapustin, A. I., Wang, Y., & Middleton, E. M. (2014). Impacts of light use efficiency and fPAR parameterization on gross primary production modeling. *Agricultural and Forest Meteorology*, 10.1016/j.agrformet.2014.01.006{\it\bibinfo{volume}{189-190}\/}, \bibinfo{pages}{187--197}.
- Coble, P. G. (1996). Characterization of marine and terrestrial DOM in seawater using excitation-emission matrix spectroscopy. *Marine Chemistry*, 10.1016/0304-4203(95)00062-3{\it\bibinfo{volume}{51}\/}, \bibinfo{pages}{325--346}.
- Coble, P. G. (2007). Marine optical biogeochemistry: The chemistry of ocean color. *ChemInform*, 10.1002/chin.200720265{\it\bibinfo{volume}{38}\/}.
- Collins, D. J., Kiefer, D. A., Soohoo, J. B., & Stuart McDermid, I. (1985). The role of reabsorption in the spectral distribution of phytoplankton fluorescence emission. *Deep Sea Research Part A. Oceanographic Research Papers*, 10.1016/0198-0149(85)90040-8{\it\bibinfo{volume}{32}\/}, \bibinfo{pages}{983--1003}.
- Conmy, R. N., Del Castillo, C. E., Downing, B. D., & Chen, R. F. (2014). Experimental Design and Quality Assurance. In P. Coble, J. Lead, A. Baker, D. M. Reynolds, & R. G. Spencer (Eds.), *Aquatic Organic Matter Fluorescence* (pp. 190–230). Cambridge: Cambridge University Press.
- Costanza, R., d'Arge, R., de Groot, R., Farber, S., Grasso, M., Hannon, B., Limburg, K., Naeem, S., O'Neill, R. V., Paruelo, J., Raskin, R. G., Sutton, P., & van den Belt, M. (1997). The value of the world's ecosystem services and natural capital. *Nature*, 10.1038/387253a0{\it\bibinfo{volume}{387}\/}, \bibinfo{pages}{253--260}.
- Crutzen, P. J. (2002). Geology of mankind. *Nature*, 415, 23–23.
- Curran, P. (1980). Multispectral remote sensing of vegetation amount. *Progress in physical geography*, 4, 315–341.
- Dash, J., & Curran, P. J. (2004). The MERIS terrestrial chlorophyll index. *International Journal of Remote Sensing*, 10.1080/0143116042000274015{\it\bibinfo{volume}{25}\/}, \bibinfo{pages}{5403--5413}.
- Daumard, F., Goulas, Y., Champagne, S., Fournier, A., Ounis, A., Olioso, A., & Moya, I. (2012). Continuous monitoring of canopy level sun-induced chlorophyll fluorescence during the growth of a sorghum field. *IEEE Transactions on Geoscience and Remote Sensing*, 10.1109/TGRS.2012.2193131{\it\bibinfo{volume}{50}\/}, \bibinfo{pages}{4292--4300}.
- Del Vecchio, R., & Blough, N. V. (2004). On the origin of the optical properties of humic substances. *Environmental Science & Technology*, 10.1021/es049912h{\it\bibinfo{volume}{38}\/}, \bibinfo{pages}{3885--3891}.
- Determann, S., Lobbes, J. M., Reuter, R., & Rullkötter, J. (1998). Ultraviolet fluorescence excitation and emission spectroscopy of marine algae and bacteria. *Marine Chemistry*, 62, 137–156.

- Dinter, T., Rozanov, V. V., Burrows, J. P., & Bracher, A. (2015). Retrieving the availability of light in the ocean utilising spectral signatures of vibrational Raman scattering in hyper-spectral satellite measurements. *Ocean Science*, 10.5194/os-11-373-2015{\it\bibinfo{volume}{11}\ /},\bibinfo{pages}{373--389}.
- Doerffer, R., & Schiller, H. (2007). The MERIS Case 2 water algorithm. *International Journal of Remote Sensing*, 10.1080/01431160600821127{\it\bibinfo{volume}{28}\ /},\bibinfo{pages}{517--535}.
- Eisinger, M., Richter, A., Ladstätter-Weissenmayer, A., & Burrows, J. P. (1997). DOAS Zenith Sky Observations: 1. BrO measurements over Bremen (53° N) 1993–1994. *Journal of atmospheric chemistry*, 26, 93–108.
- Esaias, W. E., Feldman, G. C., McClain, C. R., & Elrod, J. A. (1986). Monthly satellite-derived phytoplankton pigment distribution for the North Atlantic Ocean basin. *Eos, Transactions American Geophysical Union*, 67, 835–837.
- Falkowski, P., & Kiefer, D. A. (1985). Chlorophyll a fluorescence in phytoplankton: relationship to photosynthesis and biomass. *Journal of Plankton Research*, 7, 715–731.
- Falkowski, P. G., & Raven, J. A. (2007). *Aquatic photosynthesis*. (2nd ed.). Princeton: Princeton University Press.
- Fensholt, R., Sandholt, I., & Stisen, S. (2006). Evaluating MODIS, MERIS, and VEGETATION vegetation indices using in situ measurements in a semiarid environment. *IEEE Transactions on Geoscience and Remote Sensing*, 10.1109/TGRS.2006.875940{\it\bibinfo{volume}{44}\ /},\bibinfo{pages}{1774--1786}.
- Feret, J.-B., François, C., Asner, G. P., Gitelson, A. A., Martin, R. E., Bidel, L. P., Ustin, S. L., le Maire, G., & Jacquemoud, S. (2008). PROSPECT-4 and 5: Advances in the leaf optical properties model separating photosynthetic pigments. *Remote Sensing of Environment*, 10.1016/j.rse.2008.02.012{\it\bibinfo{volume}{112}\ /},\bibinfo{pages}{3030--3043}.
- Field, C. B. (1998). Primary production of the biosphere: Integrating terrestrial and oceanic components. *Science*, 10.1126/science.281.5374.237{\it\bibinfo{volume}{281}\ /},\bibinfo{pages}{237--240}.
- Fisher, J., Mustard, J., & Vadeboncoeur, M. (2006). Green leaf phenology at Landsat resolution: Scaling from the field to the satellite. *Remote Sensing of Environment*, 10.1016/j.rse.2005.10.022{\it\bibinfo{volume}{100}\ /},\bibinfo{pages}{265--279}.
- Fournier, A., Daumard, F., Champagne, S., Ounis, A., Goulas, Y., & Moya, I. (2012). Effect of canopy structure on sun-induced chlorophyll fluorescence. *ISPRS Journal of Photogrammetry and Remote Sensing*, 10.1016/j.isprsjprs.2012.01.003{\it\bibinfo{volume}{68}\ /},\bibinfo{pages}{112--120}.
- Franck, F., Juneau, P., & Popovic, R. (2002). Resolution of the Photosystem I and Photosystem II contributions to chlorophyll fluorescence of intact leaves at room temperature. *Biochimica et Biophysica Acta (BBA) - Bioenergetics*, 10.1016/S0005-2728(02)00366-3{\it\bibinfo{volume}{1556}\ /},\bibinfo{pages}{239--246}.
- Frankenberg, C., Butz, A., & Toon, G. C. (2011a). Disentangling chlorophyll fluorescence from atmospheric scattering effects in O₂ A-band spectra of reflected sun-light. *Geophysical Research Letters*, 10.1029/2010GL045896{\it\bibinfo{volume}{38}\ /}.

BIBLIOGRAPHY

- Frankenberg, C., Fisher, J. B., Worden, J., Badgley, G., Saatchi, S. S., Lee, J.-E., Toon, G. C., Butz, A., Jung, M., Kuze, A., & Yokota, T. (2011b). New global observations of the terrestrial carbon cycle from GOSAT: patterns of plant fluorescence with gross primary productivity. *Geophysical Research Letters*, 10.1029/2011GL048738{\it\bibinfo{volume}{38}\},\bibinfo{pages}{L17706}.
- Frankenberg, C., O'Dell, C., Berry, J., Guanter, L., Joiner, J., Köhler, P., Pollock, R., & Taylor, T. E. (2014). Prospects for chlorophyll fluorescence remote sensing from the Orbiting Carbon Observatory-2. *Remote Sensing of Environment*, 10.1016/j.rse.2014.02.007{\it\bibinfo{volume}{147}\},\bibinfo{pages}{1--12}.
- Friedl, M. A., McIver, D. K., Hodges, J. C., Zhang, X. Y., Muchoney, D., Strahler, A. H., Woodcock, C. E., Gopal, S., Schneider, A., Cooper, A., & others (2002). Global land cover mapping from MODIS: algorithms and early results. *Remote Sensing of Environment*, 83, 287–302.
- Ganguly, S., Friedl, M. A., Tan, B., Zhang, X., & Verma, M. (2010). Land surface phenology from MODIS: Characterization of the Collection 5 global land cover dynamics product. *Remote Sensing of Environment*, 10.1016/j.rse.2010.04.005{\it\bibinfo{volume}{114}\},\bibinfo{pages}{1805--1816}.
- Garver, S. A., & Siegel, D. A. (1997). Inherent optical property inversion of ocean color spectra and its biogeochemical interpretation: 1. Time series from the Sargasso Sea. *Journal of Geophysical Research*, 10.1029/96JC03243{\it\bibinfo{volume}{102}\},\bibinfo{pages}{18607}.
- Geddes, A., & Bösch, H. (2015). Tropospheric aerosol profile information from high-resolution oxygen A-band measurements from space. *Atmospheric Measurement Techniques*, 10.5194/amt-8-859-2015{\it\bibinfo{volume}{8}\},\bibinfo{pages}{859--874}.
- Gitelson, A. A. (1992). The peak near 700 nm on radiance spectra of algae and water: relationships of its magnitude and position with chlorophyll concentration. *International Journal of Remote Sensing*, 10.1080/01431169208904125{\it\bibinfo{volume}{13}\},\bibinfo{pages}{3367--3373}.
- Gitelson, A. A., Buschmann, C., & Lichtenthaler, H. K. (1998). Leaf chlorophyll fluorescence corrected for re-absorption by means of absorption and reflectance measurements. *Journal of Plant Physiology*, 10.1016/S0176-1617(98)80143-0{\it\bibinfo{volume}{152}\},\bibinfo{pages}{283--296}.
- Gitelson, A. A., Buschmann, C., & Lichtenthaler, H. K. (1999). The chlorophyll fluorescence ratio F_{735} / F_{700} as an accurate measure of the chlorophyll content in plants. *Remote Sensing of Environment*, 69, 296–302.
- Gobron, N., Pinty, B., Verstraete, M., & Govaerts, Y. (1999). The MERIS Global Vegetation Index (MGVI): Description and preliminary application. *International Journal of Remote Sensing*, 10.1080/014311699212542{\it\bibinfo{volume}{20}\},\bibinfo{pages}{1917--1927}.
- Gond, V., Fayolle, A., Pennec, A., Cornu, G., Mayaux, P., Camberlin, P., Doumenge, C., Fauvet, N., & Gourlet-Fleury, S. (2013). Vegetation structure and greenness in Central Africa from Modis multi-temporal data. *Philosophical Transactions of the Royal Society B: Biological Sciences*, 10.1098/rstb.2012.0309{\it\bibinfo{volume}{368}\},\bibinfo{pages}{20120309--20120309}.
- Gordon, H. R., & Clark, D. K. (1981). Clear water radiances for atmospheric correction of coastal zone color scanner imagery. *Applied Optics*, 20, 4175–4180.

- Gordon, H. R., & Voss, K. J. (2004). MODIS normalized water-leaving radiance algorithm theoretical basis document (MOD 18). *NASA* (<http://www.modis.gsfc.nasa.gov/data/atbd>), .
- Govindje, e. (1995). Sixty-Three Years Since Kautsky: Chlorophyll *a* Fluorescence. *Australian Journal of Plant Physiology*, 10.1071/PP9950131{\it\bibinfo{volume}{22}\}, \bibinfo{pages}{131}.
- Gower, J. F. R., Brown, L., & Borstad, G. A. (2004). Observation of chlorophyll fluorescence in west coast waters of Canada using the MODIS satellite sensor. *Canadian Journal of Remote Sensing*, 30, 17–25.
- Gower, J. F. R., & King, S. (2004). Satellite fluorescence as a measure of ocean surface chlorophyll. *Gayana (Concepción)*, 10.4067/S0717-65382004000200045{\it\bibinfo{volume}{68}\}.
- Gower, J. F. R., & King, S. (2012). Use of satellite images of chlorophyll fluorescence to monitor the spring bloom in coastal waters. *International Journal of Remote Sensing*, 10.1080/01431161.2012.685979{\it\bibinfo{volume}{33}\}, \bibinfo{pages}{7469--7481}.
- Grainger, J. F., & Ring, J. (1962). Anomalous Fraunhofer line profiles. *Nature*, 10.1038/193762a0{\it\bibinfo{volume}{193}\}, \bibinfo{pages}{762--762}.
- Granskog, M. A., Macdonald, R. W., Mundy, C.-J., & Barber, D. G. (2007). Distribution, characteristics and potential impacts of chromophoric dissolved organic matter (CDOM) in Hudson Strait and Hudson Bay, Canada. *Continental Shelf Research*, 10.1016/j.csr.2007.05.001{\it\bibinfo{volume}{27}\}, \bibinfo{pages}{2032--2050}.
- Green, S. A., & Blough, N. V. (1994). Optical absorption and fluorescence properties of chromophoric dissolved organic matter in natural waters. *Limnology and Oceanography*, 10.4319/lo.1994.39.8.1903{\it\bibinfo{volume}{39}\}, \bibinfo{pages}{1903--1916}.
- Guanter, L., Frankenberg, C., Dudhia, A., Lewis, P. E., Gómez-Dans, J., Kuze, A., Suto, H., & Grainger, R. G. (2012). Retrieval and global assessment of terrestrial chlorophyll fluorescence from GOSAT space measurements. *Remote Sensing of Environment*, 10.1016/j.rse.2012.02.006{\it\bibinfo{volume}{121}\}, \bibinfo{pages}{236--251}.
- Guanter, L., Zhang, Y., Jung, M., Joiner, J., Voigt, M., Berry, J. A., Frankenberg, C., Huete, A. R., Zarco-Tejada, P., Lee, J.-E., Moran, M. S., Ponce-Campos, G., Beer, C., Camps-Valls, G., Buchmann, N., Gianelle, D., Klumpp, K., Cescatti, A., Baker, J. M., & Griffis, T. J. (2014). Global and time-resolved monitoring of crop photosynthesis with chlorophyll fluorescence. *Proceedings of the National Academy of Sciences*, 10.1073/pnas.1320008111{\it\bibinfo{volume}{111}\}, \bibinfo{pages}{E1327--E1333}.
- Guéguen, C., Granskog, M., McCullough, G., & Barber, D. (2011). Characterisation of colored dissolved organic matter in Hudson Bay and Hudson Strait using parallel factor analysis. *Journal of Marine Systems*, 10.1016/j.jmarsys.2010.12.001{\it\bibinfo{volume}{88}\}, \bibinfo{pages}{423--433}.
- Halthore, R. N., & Caffrey, P. F. (2006). Measurement and modeling of background aerosols in remote marine atmospheres: Implications for sea salt flux. *Geophysical Research Letters*, 10.1029/2006GL026302{\it\bibinfo{volume}{33}\}, \bibinfo{pages}{L14819}.
- Haltrin, V. I. (2006). Absorption and scattering of light in natural waters. In *Light Scattering Reviews* (pp. 445–486). Springer.

BIBLIOGRAPHY

- Haltrin, V. I., & Kattawar, G. W. (1993). Self-consistent solutions to the equation of transfer with elastic and inelastic scattering in oceanic optic. *Applied Optics*, *32*, 5356–5367.
- Hawes, S. K. (1992). *Quantum Fluorescence Efficiencies Of Marine Fulvic And Humic Acids*. Msc-thesis University of South Florida.
- Hill, M., Román, M., & Schaaf, C. (2010). Biogeography and Dynamics of Global Tropical and Subtropical Savannas: A Spatiotemporal View. In M. Hill, & N. Hanan (Eds.), *Ecosystem Function in Savannas* (pp. 3–37). CRC Press.
- Hudson, N., Baker, A., & Reynolds, D. (2007). Fluorescence analysis of dissolved organic matter in natural, waste and polluted waters—a review. *River Research and Applications*, 10.1002/rra.1005{\it\bibinfo{volume}{23}\},\bibinfo{pages}{631--649}.
- Huete, A., Didan, K., Miura, T., Rodriguez, E. P., Gao, X., & Ferreira, L. G. (2002). Overview of the radiometric and biophysical performance of the MODIS vegetation indices. *Remote sensing of environment*, *83*, 195–213.
- Huete, A., & Jackson, R. (1988). Soil and atmosphere influences on the spectra of partial canopies. *Remote Sensing of Environment*, 10.1016/0034-4257(88)90043-0{\it\bibinfo{volume}{25}\},\bibinfo{pages}{89--105}.
- Huete, A., Justice, C., & Van Leeuwen, W. (1999). MODIS vegetation index (MOD13). *Algorithm theoretical basis document*, *3*, 213.
- Huete, A. R., & Liu, H. Q. (1994). An error and sensitivity analysis of the atmospheric-and soil-correcting variants of the NDVI for the MODIS-EOS. *Geoscience and Remote Sensing, IEEE Transactions on*, *32*, 897–905.
- Huhn, F., von Kameke, A., Pérez-Muñuzuri, V., Olascoaga, M. J., & Beron-Vera, F. J. (2012). The impact of advective transport by the south indian ocean countercurrent on the madagascar plankton bloom. *Geophysical Research Letters*, 10.1029/2012GL051246{\it\bibinfo{volume}{39}\},\bibinfo{pages}{n/a--n/a}.
- Huot, Y., & Babin, M. (2010). Overview of fluorescence protocols: Theory, basic concepts, and practice. In D. J. Suggett, O. Prášil, & M. A. Borowitzka (Eds.), *Chlorophyll a Fluorescence in Aquatic Sciences: Methods and Applications* (pp. 31–74). Dordrecht: Springer Netherlands.
- Huot, Y., Franz, B. A., & Fradette, M. (2013). Estimating variability in the quantum yield of sun-induced chlorophyll fluorescence: A global analysis of oceanic waters. *Remote Sensing of Environment*, 10.1016/j.rse.2013.01.003{\it\bibinfo{volume}{132}\},\bibinfo{pages}{238--253}.
- IOCCG (2006). *Remote Sensing of Inherent Optical Properties: Fundamentals, Tests of Algorithms, and Applications* volume No. 5 of *Reports of the International Ocean Colour Coordinating Group*. Dartmouth, Canada: IOCCG.
- IPCC (2007). *Climate Change 2007: Impacts, Adaptation and Vulnerability. Contribution of Working Group II to the Fourth Assessment Report of the Intergovernmental Panel on Climate Change*. Cambridge University Press.
- IPCC (2013). *Climate Change 2013: The Physical Science Basis. Working Group I Contribution to the IPCC 5th Assessment Report - Changes to the Underlying Scientific/Technical Assessment*. Cambridge University Press.

- Ishii, S. K. L., & Boyer, T. H. (2012). Behavior of Reoccurring PARAFAC Components in Fluorescent Dissolved Organic Matter in Natural and Engineered Systems: A Critical Review. *Environmental Science & Technology*, 10.1021/es2043504{\it\bibinfo{volume}{46}\ /},\bibinfo{pages}{2006--2017}.
- Jacquemoud, S., & Baret, F. (1990). PROSPECT: A model of leaf optical properties spectra. *Remote Sensing of Environment*, 10.1016/0034-4257(90)90100-Z{\it\bibinfo{volume}{34}\ /},\bibinfo{pages}{75--91}.
- Jerlov, N. G. (1976). *Marine optics* volume 14. Elsevier Science Ltd.
- Joiner, J., Guanter, L., Lindstrot, R., Voigt, M., Vasilkov, A. P., Middleton, E. M., Huemmrich, K. F., Yoshida, Y., & Frankenberg, C. (2013). Global monitoring of terrestrial chlorophyll fluorescence from moderate-spectral-resolution near-infrared satellite measurements: methodology, simulations, and application to GOME-2. *Atmospheric Measurement Techniques*, 10.5194/amt-6-2803-2013{\it\bibinfo{volume}{6}\ /},\bibinfo{pages}{2803--2823}.
- Joiner, J., Yoshida, Y., Vasilkov, A., Schaefer, K., Jung, M., Guanter, L., Zhang, Y., Garrity, S., Middleton, E., Huemmrich, K., Gu, L., & Belelli Marchesini, L. (2014). The seasonal cycle of satellite chlorophyll fluorescence observations and its relationship to vegetation phenology and ecosystem atmosphere carbon exchange. *Remote Sensing of Environment*, 10.1016/j.rse.2014.06.022{\it\bibinfo{volume}{152}\ /},\bibinfo{pages}{375--391}.
- Joiner, J., Yoshida, Y., Vasilkov, A. P., Middleton, E. M., Campbell, P. K. E., Yoshida, Y., Kuze, A., & Corp, L. A. (2012). Filling-in of near-infrared solar lines by terrestrial fluorescence and other geophysical effects: simulations and space-based observations from SCIAMACHY and GOSAT. *Atmospheric Measurement Techniques*, 10.5194/amt-5-809-2012{\it\bibinfo{volume}{5}\ /},\bibinfo{pages}{809--829}.
- Joiner, J., Yoshida, Y., Vasilkov, A. P., Yoshida, Y., Corp, L. A., & Middleton, E. M. (2011). First observations of global and seasonal terrestrial chlorophyll fluorescence from space. *Biogeosciences*, 10.5194/bg-8-637-2011{\it\bibinfo{volume}{8}\ /},\bibinfo{pages}{637--651}.
- Jönsson, A., Eklundh, L., Hellström, M., Barring, L., & Jönsson, P. (2010). Annual changes in MODIS vegetation indices of Swedish coniferous forests in relation to snow dynamics and tree phenology. *Remote Sensing of Environment*, 10.1016/j.rse.2010.06.005{\it\bibinfo{volume}{114}\ /},\bibinfo{pages}{2719--2730}.
- Jørgensen, L., Stedmon, C. A., Kragh, T., Markager, S., Middelboe, M., & Søndergaard, M. (2011). Global trends in the fluorescence characteristics and distribution of marine dissolved organic matter. *Marine Chemistry*, 10.1016/j.marchem.2011.05.002{\it\bibinfo{volume}{126}\ /},\bibinfo{pages}{139--148}.
- Kattawar, G. W., & Xu, X. (1992). Filling in of Fraunhofer lines in the ocean by Raman scattering. *Appl. Opt.*, 10.1364/AO.31.006491{\it\bibinfo{volume}{31}\ /},\bibinfo{pages}{6491--6500}.
- Kautsky, H., & Hirsch, A. (1931). Neue Versuche zur Kohlensaureassimilation. *Die Naturwissenschaften*, 10.1007/BF01516164{\it\bibinfo{volume}{19}\ /},\bibinfo{pages}{964--964}.
- Kiefer, D. A., Chamberlin, W. S., & Booth, C. R. (1989). Natural fluorescence of chlorophyll a: Relationship to photosynthesis and chlorophyll concentration in the western South Pacific gyre. *Limnology and Oceanography*, 34, 868-881.

BIBLIOGRAPHY

- Knyazikhin, Y., Martonchik, J. V., Myneni, R. B., Diner, D. J., & Running, S. W. (1998). Synergistic algorithm for estimating vegetation canopy leaf area index and fraction of absorbed photosynthetically active radiation from MODIS and MISR data. *Journal of Geophysical Research: Atmospheres (1984–2012)*, *103*, 32257–32275.
- Kowalczyk, P., Stoń-Egiert, J., Cooper, W. J., Whitehead, R. F., & Durako, M. J. (2005). Characterization of chromophoric dissolved organic matter (CDOM) in the Baltic Sea by excitation emission matrix fluorescence spectroscopy. *Marine Chemistry*, 10.1016/j.marchem.2005.03.002{\it\bibinfo{volume}{96}\}, \bibinfo{pages}{273--292}.
- Krause, G. H., & Jahns, P. (2004). Non-photochemical Energy Dissipation Determined by Chlorophyll Fluorescence Quenching: Characterization and Function. In G. C. Papageorgiou, & Govindjee (Eds.), *Chlorophyll a Fluorescence* (pp. 463–495). Springer Netherlands volume 19.
- Kumar, R., & Silva, L. (1973). Reflectance model of a plant leaf, .
- Lakowicz, J. R. (1999). *Principle of Fluorescence Spectroscopy*. Kluwer Academic/Plenum Publishers: New York.
- Le Quéré, C., Raupach, M. R., Canadell, J. G., Marland et al., G., Le Quéré et al., C., Le Quéré et al., C., Raupach, M. R., Canadell, J. G., Marland, G., Bopp, L., Ciais, P., Conway, T. J., Doney, S. C., Feely, R. A., Foster, P., Friedlingstein, P., Gurney, K., Houghton, R. A., House, J. I., Huntingford, C., Levy, P. E., Lomas, M. R., Majkut, J., Metzl, N., Ometto, J. P., Peters, G. P., Prentice, I. C., Randerson, J. T., Running, S. W., Sarmiento, J. L., Schuster, U., Sitch, S., Takahashi, T., Viovy, N., van der Werf, G. R., & Woodward, F. I. (2009). Trends in the sources and sinks of carbon dioxide. *Nature Geoscience*, 10.1038/ngeo689{\it\bibinfo{volume}{2}\}, \bibinfo{pages}{831--836}.
- Lee, Z., Carder, K., Arnone, R., & He, M. (2007). Determination of primary spectral bands for remote sensing of aquatic environments. *Sensors*, *7*, 3428–3441.
- Lee, Z., Carder, K. L., & Arnone, R. A. (2002). Deriving inherent optical properties from water color: a multiband quasi-analytical algorithm for optically deep waters. *Applied optics*, *41*, 5755–5772.
- Lee, Z. P. (2006). *Remote Sensing of Inherent Optical Properties: Fundamentals, Tests of Algorithms, and Applications*. Technical Report IOCCG Report Number 5, 2006.
- Lichtenthaler, H. K., & Rinderle, U. (1988). The role of chlorophyll fluorescence in the detection of stress conditions in plants. *C R C Critical Reviews in Analytical Chemistry*, 10.1080/15476510.1988.10401466{\it\bibinfo{volume}{19}\}, \bibinfo{pages}{S29--S85}.
- Longhurst, A. (2001). A major seasonal phytoplankton bloom in the Madagascar Basin. *Deep Sea Research Part I: Oceanographic Research Papers*, *48*, 2413–2422.
- Lévy, M., Shankar, D., André, J.-M., Shenoi, S. S. C., Durand, F., & de Boyer Montégut, C. (2007). Basin-wide seasonal evolution of the indian ocean's phytoplankton blooms. *Journal of Geophysical Research*, 10.1029/2007JC004090{\it\bibinfo{volume}{112}\}/.
- Ma, B. L., Dwyer, L. M., Costa, C., Cober, E. R., & Morrison, M. J. (2001). Early Prediction of Soybean Yield from Canopy Reflectance Measurements. *Agronomy Journal*, 10.2134/agronj2001.1227{\it\bibinfo{volume}{93}\}, \bibinfo{pages}{1227}.

- MacIntyre, H. L., Lawrenz, E., & Richardson, T. L. (2010). Taxonomic discrimination of phytoplankton by spectral fluorescence. In D. J. Suggett, O. Prášil, & M. A. Borowitzka (Eds.), *Chlorophyll a Fluorescence in Aquatic Sciences: Methods and Applications* (pp. 31–74). Springer Netherlands.
- Maier, S. (2000). *Modeling the radiative transfer in leaves in the 300nm to 2.5 μm wavelength region taking into consideration chlorophyll fluorescence - The leaf model SLOPE*. Phd-thesis Technical University Munich.
- Maier, S. W., Lüdeker, W., & Günther, K. P. (1999). SLOP: A revised version of the stochastic model for leaf optical properties. *Remote Sensing of Environment*, *68*, 273–280.
- Maritorena, S., Siegel, D., & Peterson, A. (2002). Optimization of a semianalytical ocean color model for global-scale applications. *Applied Optics*, *41*, 2705–2714.
- McKibben, S. M., Strutton, P. G., Foley, D. G., Peterson, T. D., & White, A. E. (2012). Satellite-based detection and monitoring of phytoplankton blooms along the oregon coast. *Journal of Geophysical Research*, 10.1029/2012JC008114{\it\bibinfo{volume}{117}\}, \bibinfo{pages}{3133--3147}.
- MEA (2005). *Millenium ecosystem assessment*. Washington, DC: World Resources Institute.
- Meroni, M., Rossini, M., Guanter, L., Alonso, L., Rascher, U., Colombo, R., & Moreno, J. (2009). Remote sensing of solar-induced chlorophyll fluorescence: Review of methods and applications. *Remote sensing of environment*, *113*, 2037–2051.
- Millie, D. F., Schofield, O. M., Kirkpatrick, G. J., Johnsen, G., & Evens, T. J. (2002). Using absorbance and fluorescence spectra to discriminate microalgae. *European Journal of Phycology*, 10.1017/S0967026202003700{\it\bibinfo{volume}{37}\}, \bibinfo{pages}{313--322}.
- Mobley, C. D. (1994). *Light and water: radiative transfer in natural waters*. San Diego, Calif. [u.a.]: Academic Press.
- Mohammed, G. H., Goulas, Y., Magnani, F., Moreno, J., Olejníčková, J., Rascher, U., van der Tol, C., Verhoef, W., Ač, A., Daumard, F., & others (2014). 2012 FLEX/Sentinel-3 Tandem Mission Photosynthesis Study, .
- Morel, A., & Bricaud, A. (1981). Theoretical results concerning light absorption in a discrete medium, and application to specific absorption of phytoplankton. *Deep Sea Research Part A. Oceanographic Research Papers*, 10.1016/0198-0149(81)90039-X{\it\bibinfo{volume}{28}\}, \bibinfo{pages}{1375--1393}.
- Morel, A., & Gentili, B. (2009). A simple band ratio technique to quantify the colored dissolved and detrital organic material from ocean color remotely sensed data. *Remote Sensing of Environment*, 10.1016/j.rse.2009.01.008{\it\bibinfo{volume}{113}\}, \bibinfo{pages}{998--1011}.
- Moreno, J. F. e. a. (2006). FLuorescence EXplorer (FLEX): an optimised payload to map vegetation photosynthesis from space. 10.2514/6.IAC-06-B1.3.04\bibinfo{publisher}{AmericanInstituteofAeronauticsandAstronautics}.
- Morrison, J. R., & Goodwin, D. S. (2010). Phytoplankton photocompensation from space-based fluorescence measurements. *Geophysical Research Letters*, 10.1029/2009GL041799{\it\bibinfo{volume}{37}\}, \bibinfo{pages}{L06603}.
- Munro, R., Eisinger, M., Anderson, C., Callies, J., Corpaccioli, E., Lang, R., Lefebvre, A., Livschitz, Y., & Albiñana, A. P. (2006). GOME-2 on MetOp. In *Proc. The 2006 EUMETSAT Meteorological Satellite Conference, Helsinki, Finland, EUMETSAT* (p. 48).

BIBLIOGRAPHY

- Murphy, K. R., Stedmon, C. A., Waite, T. D., & Ruiz, G. M. (2008). Distinguishing between terrestrial and autochthonous organic matter sources in marine environments using fluorescence spectroscopy. *Marine Chemistry*, 10.1016/j.marchem.2007.10.003{\it\bibinfo{volume}{108}\},\bibinfo{pages}{40--58}.
- Nelson, N. B., & Siegel, D. A. (2013). The Global Distribution and Dynamics of Chromophoric Dissolved Organic Matter. *Annual Review of Marine Science*, 10.1146/annurev-marine-120710-100751{\it\bibinfo{volume}{5}\},\bibinfo{pages}{447--476}.
- Neville, R. A., & Gower, J. F. R. (1977). Passive remote sensing of phytoplankton via chlorophyll α fluorescence. *Journal of Geophysical Research*, 10.1029/JC082i024p03487{\it\bibinfo{volume}{82}\},\bibinfo{pages}{3487--3493}.
- Nieto-Cid, M., Álvarez Salgado, X., Gago, J., & Pérez, F. (2005). DOM fluorescence, a tracer for biogeochemical processes in a coastal upwelling system (NW Iberian Peninsula). *Marine Ecology Progress Series*, 10.3354/meps297033{\it\bibinfo{volume}{297}\},\bibinfo{pages}{33--50}.
- Noël, S., Buchwitz, M., Bovensmann, H., & Burrows, J. P. (2005). Validation of SCIAMACHY AMC-DOAS water vapour columns. *Atmos. Chem. Phys*, 5, 1835–1841.
- Noël, S., Buchwitz, M., & Burrows, J. P. (2004). First retrieval of global water vapour column amounts from SCIAMACHY measurements. *Atmospheric Chemistry and Physics*, 4, 111–125.
- Noël, S., Mieruch, S., Bovensmann, H., & Burrows, J. P. (2008). Preliminary results of GOME-2 water vapour retrievals and first applications in polar regions. *Atmospheric Chemistry and Physics*, 8, 1519–1529.
- O'Malley, R. T., Behrenfeld, M. J., Westberry, T. K., Milligan, A. J., Shang, S., & Yan, J. (2014). Geostationary satellite observations of dynamic phytoplankton photophysiology. *Geophysical Research Letters*, 10.1002/2014GL060246{\it\bibinfo{volume}{41}\},\bibinfo{pages}{5052--5059}.
- Perner, D., & Platt, U. (1979). Detection of nitrous acid in the atmosphere by differential optical absorption. *Geophysical Research Letters*, 6, 917–920.
- Peters, E., Wittrock, F., Richter, A., Alvarado, L. M. A., Rozanov, V. V., & Burrows, J. P. (2014). Liquid water absorption and scattering effects in DOAS retrievals over oceans. *Atmospheric Measurement Techniques*, 10.5194/amt-7-4203-2014{\it\bibinfo{volume}{7}\}/,\bibinfo{pages}{4203--4221}.
- Porcar-Castell, A., Tyystjarvi, E., Atherton, J., van der Tol, C., Flexas, J., Pfundel, E. E., Moreno, J., Frankenberg, C., & Berry, J. A. (2014). Linking chlorophyll a fluorescence to photosynthesis for remote sensing applications: mechanisms and challenges. *Journal of Experimental Botany*, 10.1093/jxb/eru191{\it\bibinfo{volume}{65}\},\bibinfo{pages}{4065--4095}.
- Pozdnyakov, D., Grassl, H., Lyaskovsky, A., & Pettersson, L. (2002). Numerical modelling of transspectral processes in natural waters: Implications for remote sensing. *International Journal of Remote Sensing*, 10.1080/014311601170735{\it\bibinfo{volume}{23}\},\bibinfo{pages}{1581--1607}.
- Priour, L., & Sathyendranath, S. (1981). An optical classification of coastal and oceanic waters based on the specific spectral absorption curves of phytoplankton pigments, dissolved organic matter, and other particulate materials. *Limnology and Oceanography*, 26, 671–689.

- Raj, R. P., Peter, B. N., & Pushpadas, D. (2010). Oceanic and atmospheric influences on the variability of phytoplankton bloom in the Southwestern Indian Ocean. *Journal of Marine Systems*, 10.1016/j.jmarsys.2010.05.009{\it\bibinfo{volume}{82}\}, \bibinfo{pages}{217--229}.
- Richardson, A. D., Hollinger, D. Y., Dail, D. B., Lee, J. T., Munger, J. W., & O'keefe, J. (2009). Influence of spring phenology on seasonal and annual carbon balance in two contrasting New England forests. *Tree Physiology*, 10.1093/treephys/tpn040{\it\bibinfo{volume}{29}\}, \bibinfo{pages}{321--331}.
- Richardson, A. D., Keenan, T. F., Migliavacca, M., Ryu, Y., Sonnentag, O., & Toomey, M. (2013). Climate change, phenology, and phenological control of vegetation feedbacks to the climate system. *Agricultural and Forest Meteorology*, 10.1016/j.agrformet.2012.09.012{\it\bibinfo{volume}{169}\}, \bibinfo{pages}{156--173}.
- Richter, A., Burrows, J. P., Nüß, H., Granier, C., & Niemeier, U. (2005). Increase in tropospheric nitrogen dioxide over China observed from space. *Nature*, 10.1038/nature04092{\it\bibinfo{volume}{437}\}, \bibinfo{pages}{129--132}.
- Rockström, J., Steffen, W. L., Noone, K., Persson, A., Chapin III, F. S., Lambin, E., Lenton, T. M., Scheffer, M., Folke, C., Schellnhuber, H. J., & others (2009). Planetary boundaries: exploring the safe operating space for humanity. *Ecology and Society*, 14(2): 32.
- Rousseaux, C. S., & Gregg, W. W. (2012). Climate variability and phytoplankton composition in the pacific ocean. *Journal of Geophysical Research*, 10.1029/2012JC008083{\it\bibinfo{volume}{117}\}.
- Rozanov, V., Rozanov, A., Kokhanovsky, A., & Burrows, J. (2014). Radiative transfer through terrestrial atmosphere and ocean: Software package SCIATRAN. *Journal of Quantitative Spectroscopy and Radiative Transfer*, 10.1016/j.jqsrt.2013.07.004{\it\bibinfo{volume}{133}\}/, \bibinfo{pages}{13--71}.
- Rozanov, V. V., & Rozanov, A. V. (2010). Differential optical absorption spectroscopy (DOAS) and air mass factor concept for a multiply scattering vertically inhomogeneous medium: theoretical consideration. *Atmos. Meas. Tech.*, 10.5194/amt-3-751-2010{\it\bibinfo{volume}{3}\}, \bibinfo{pages}{751--780}.
- Rozanov, V. V., & Vountas, M. (2014). Radiative transfer equation accounting for rotational Raman scattering and its solution by the discrete-ordinates method. *J. Quant. Spectrosc. Radiat. Transfer*, 133, 603–618.
- Ryan, J. P., Polito, P. S., Strutton, P. G., & Chavez, F. P. (2002). Unusual large-scale phytoplankton blooms in the equatorial Pacific. *Progress in Oceanography*, 55, 263–285.
- Sadeghi, A., Dinter, T., Vountas, M., Taylor, B. B., Altenburg-Soppa, M., Peeken, I., & Bracher, A. (2012). Improvement to the PhytoDOAS method for identification of coccolithophores using hyper-spectral satellite data. *Ocean Science*, 10.5194/os-8-1055-2012{\it\bibinfo{volume}{8}\}, \bibinfo{pages}{1055--1070}.
- Sanders, A. F. J., & de Haan, J. F. (2013). Retrieval of aerosol parameters from the oxygen A band in the presence of chlorophyll fluorescence. *Atmospheric Measurement Techniques*, 10.5194/amt-6-2725-2013{\it\bibinfo{volume}{6}\}, \bibinfo{pages}{2725--2740}.
- Sathyendranath, S. (2000). *Remote Sensing of Ocean Colour in Coastal, and Other Optically-Complex, Waters*. Technical Report IOCCG Report Number 3, 2000.

BIBLIOGRAPHY

- Schallenberg, C., Lewis, M. R., Kelley, D. E., & Cullen, J. J. (2008). Inferred influence of nutrient availability on the relationship between sun-induced chlorophyll fluorescence and incident irradiance in the bering sea. *Journal of Geophysical Research*, 10.1029/2007JC004355{\it\bibinfo{volume}{113}\/}.
- Schroter, D. (2005). Ecosystem Service Supply and Vulnerability to Global Change in Europe. *Science*, 10.1126/science.1115233{\it\bibinfo{volume}{310}\/}, \bibinfo{pages}{1333--1337}.
- Shanmugam, P. (2011). New models for retrieving and partitioning the colored dissolved organic matter in the global ocean: Implications for remote sensing. *Remote Sensing of Environment*, .
- Shifrin, K. (1988). *Physical optics of ocean water*. American Institute of Physics (New York).
- Siegenthaler, U., & Sarmiento, J. L. (1993). Atmospheric carbon dioxide and the ocean. *Nature*, 10.1038/365119a0{\it\bibinfo{volume}{365}\/}, \bibinfo{pages}{119--125}.
- Signorini, S. R., & McClain, C. R. (2007). Large-scale forcing impact on biomass variability in the South Atlantic Bight. *Geophysical Research Letters*, 10.1029/2007GL031121{\it\bibinfo{volume}{34}\/}.
- Signorini, S. R., & McClain, C. R. (2012). Subtropical gyre variability as seen from satellites. *Remote Sensing Letters*, 10.1080/01431161.2011.625053{\it\bibinfo{volume}{3}\/}, \bibinfo{pages}{471--479}.
- Simis, S. G. H., Huot, Y., Babin, M., Seppälä, J., & Metsamaa, L. (2012). Optimization of variable fluorescence measurements of phytoplankton communities with cyanobacteria. *Photosynthesis Research*, 10.1007/s11120-012-9729-6{\it\bibinfo{volume}{112}\/}, \bibinfo{pages}{13--30}.
- Singh, S., D'Sa, E. J., & Swenson, E. M. (2010). Chromophoric dissolved organic matter (CDOM) variability in barataria basin using excitation–emission matrix (EEM) fluorescence and parallel factor analysis (PARAFAC). *Science of The Total Environment*, 10.1016/j.scitotenv.2010.03.044{\it\bibinfo{volume}{408}\/}, \bibinfo{pages}{3211--3222}.
- Sinnhuber, B.-M., Sheode, N., Sinnhuber, M., Chipperfield, M. P., & Feng, W. (2009). The contribution of anthropogenic bromine emissions to past stratospheric ozone trends: A modelling study. *Atmos. Chem. Phys.*, 9, 2863–2871.
- Soest, G. v., Tilstra, L. G., & Stammes, P. (2005). Large-scale validation of SCIAMACHY reflectance in the ultraviolet. *Atmospheric Chemistry and Physics*, 5, 2171–2180.
- Srokosz, M. A. (2004). A possible plankton wave in the Indian Ocean. *Geophysical Research Letters*, 10.1029/2004GL019738{\it\bibinfo{volume}{31}\/}.
- Srokosz, M. A., & Quartly, G. D. (2013). The Madagascar Bloom: A serendipitous study. *Journal of Geophysical Research: Oceans*, 10.1029/2012JC008339{\it\bibinfo{volume}{118}\/}, \bibinfo{pages}{14--25}.
- Stedmon, C., Markager, S., & Bro, R. (2003). Tracing dissolved organic matter in aquatic environments using a new approach to fluorescence spectroscopy. *Marine Chemistry*, 82, 239–254.

- Stedmon, C., & Álvarez Salgado, X. (2011). Shedding light on a black box: Uv-visible spectroscopic characterization of marine dissolved organic matter. In N. Jiao, F. Azam, & S. Sanders (Eds.), *Microbial Carbon Pump in the Ocean* (pp. 62–63). American Association for the Advancement of Science.
- Stedmon, C. A., & Bro, R. (2008). Characterizing dissolved organic matter fluorescence with parallel factor analysis: a tutorial. *Limnology and Oceanography: Methods*, 10.4319/lom.2008.6.572{\it\bibinfo{volume}{6}\},\bibinfo{pages}{572--579}.
- Stedmon, C. A., & Markager, S. (2001). The optics of chromophoric dissolved organic matter (CDOM) in the Greenland sea: An algorithm for differentiation between marine and terrestrially derived organic matter. *Limnology and Oceanography*, (p. 2087–2093).
- Stedmon, C. A., & Markager, S. (2005). Tracing the production and degradation of autochthonous fractions of dissolved organic matter using fluorescence analysis. *Limnology and Oceanography*, 10.4319/lo.2005.50.5.1415{\it\bibinfo{volume}{50}\},\bibinfo{pages}{1415--1426}.
- Stedmon, C. A., Thomas, D. N., Granskog, M., Kaartokallio, H., Papadimitriou, S., & Kuosa, H. (2007). Characteristics of dissolved organic matter in Baltic coastal sea ice: Allochthonous or autochthonous origins? *Environmental Science & Technology*, 10.1021/es071210f{\it\bibinfo{volume}{41}\},\bibinfo{pages}{7273--7279}.
- Strutton, P. G., & Chavez, F. P. (2000). Primary productivity in the equatorial Pacific during the 1997–1998 El Niño. *Journal of Geophysical Research*, 10.1029/1999JC000056{\it\bibinfo{volume}{105}\},\bibinfo{pages}{26089}.
- Strutton, P. G., Evans, W., & Chavez, F. P. (2008). Equatorial Pacific chemical and biological variability, 1997–2003. *Global Biogeochemical Cycles*, 10.1029/2007GB003045{\it\bibinfo{volume}{22}\}.
- Swan, C. M., Nelson, N. B., Siegel, D. A., & Fields, E. A. (2013). A model for remote estimation of ultraviolet absorption by chromophoric dissolved organic matter based on the global distribution of spectral slope. *Remote Sensing of Environment*, 10.1016/j.rse.2013.05.009{\it\bibinfo{volume}{136}\},\bibinfo{pages}{277--285}.
- Thompson, M. V., & Randerson, J. T. (1999). Impulse response functions of terrestrial carbon cycle models: method and application. *Global Change Biology*, 5, 371–394.
- Thompson, R., & Clark, R. (2008). Is spring starting earlier? *The Holocene*, 10.1177/0959683607085599{\it\bibinfo{volume}{18}\},\bibinfo{pages}{95--104}.
- Thum, T., Aalto, T., Laurila, T., Aurela, M., Hatakka, J., Lindroth, A., & Vesala, T. (2009). Spring initiation and autumn cessation of boreal coniferous forest CO₂ exchange assessed by meteorological and biological variables. *Tellus B*, 10.1111/j.1600-0889.2009.00441.x{\it\bibinfo{volume}{61}\},\bibinfo{pages}{701--717}.
- Tucker, C. J., & Sellers, P. J. (1986). Satellite remote sensing of primary production. *International Journal of Remote Sensing*, 10.1080/01431168608948944{\it\bibinfo{volume}{7}\},\bibinfo{pages}{1395--1416}.
- Twardowski, M., Boss, E., Sullivan, J., & Donaghay, P. (2004). Modeling the spectral shape of absorption by chromophoric dissolved organic matter. *Marine Chemistry*, 89, 69–88.
- Uz, B. M. (2007). What causes the sporadic phytoplankton bloom southeast of Madagascar? *Journal of Geophysical Research*, 10.1029/2006JC003685{\it\bibinfo{volume}{112}\}.

BIBLIOGRAPHY

- Vasilkov, A., Joiner, J., & Spurr, R. (2013). Note on rotational-Raman scattering in the O₂ A- and B-bands. *Atmospheric Measurement Techniques*, 10.5194/amt-6-981-2013{\it\bibinfo{volume}{6}\/}, \bibinfo{pages}{981--990}.
- Vasilkov, A. P. (2002). Ocean raman scattering in satellite backscatter UV measurements. *Geophysical Research Letters*, 10.1029/2002GL014955{\it\bibinfo{volume}{29}\/}.
- Vassiliev, S., & Bruce, D. (2008). Toward understanding molecular mechanisms of light harvesting and charge separation in Photosystem II. *Photosynthesis Research*, 10.1007/s11120-008-9303-4{\it\bibinfo{volume}{97}\/}, \bibinfo{pages}{75--89}.
- Vodacek, A. (1989). Synchronous fluorescence spectroscopy of dissolved organic matter in surface waters: Application to airborne remote sensing. *Remote Sensing of Environment*, 30, 239–247.
- Vodacek, A., Green, S. A., & Blough, N. V. (1994). An experimental model of the solar-stimulated fluorescence of chromophoric dissolved organic matter. *Limnology and Oceanography*, 39.
- Vogelmann, T. C., & Evans, J. R. (2002). Profiles of light absorption and chlorophyll within spinach leaves from chlorophyll fluorescence. *Plant, Cell & Environment*, 25, 1313–1323.
- Vountas, M., Dinter, T., Bracher, A., Burrows, J. P., & Sierk, B. (2007). Spectral studies of ocean water with space-borne sensor SCIAMACHY using differential optical absorption spectroscopy (DOAS). *Ocean Science*, 10.5194/os-3-429-2007{\it\bibinfo{volume}{3}\/}, \bibinfo{pages}{429--440}.
- Vountas, M., Richter, A., Wittrock, F., & Burrows, J. P. (2003). Inelastic scattering in ocean water and its impact on trace gas retrievals from satellite data. *Atmospheric Chemistry and Physics*, 10.5194/acp-3-1365-2003{\it\bibinfo{volume}{3}\/}, \bibinfo{pages}{1365--1375}.
- Vountas, M., Rozanov, V. V., & Burrows, J. P. (1998). Ring effect: impact of rotational Raman scattering on radiative transfer in Earth's atmosphere. *Journal of Quantitative Spectroscopy and Radiative Transfer*, 10.1016/S0022-4073(97)00186-6{\it\bibinfo{volume}{60}\/}, \bibinfo{pages}{943--961}.
- Wagner, T., Beirle, S., Deutschmann, T., Grzegorski, M., & Platt, U. (2007). Satellite monitoring of different vegetation types by differential optical absorption spectroscopy (DOAS) in the red spectral range. *Atmospheric Chemistry and Physics*, 10.5194/acp-7-69-2007{\it\bibinfo{volume}{7}\/}, \bibinfo{pages}{69--79}.
- Washington, R., James, R., Pearce, H., Pokam, W. M., & Moufouma-Okia, W. (2013). Congo Basin rainfall climatology: can we believe the climate models? *Philosophical Transactions of the Royal Society B: Biological Sciences*, 10.1098/rstb.2012.0296{\it\bibinfo{volume}{368}\/}, \bibinfo{pages}{20120296--20120296}.
- Westberry, T. K., Behrenfeld, M. J., Milligan, A. J., & Doney, S. C. (2013). Retrospective satellite ocean color analysis of purposeful and natural ocean iron fertilization. *Deep Sea Research Part I: Oceanographic Research Papers*, 10.1016/j.dsr.2012.11.010{\it\bibinfo{volume}{73}\/}, \bibinfo{pages}{1--16}.
- White, M. A., de BEURS, K. M., Didan, K., Inouye, D. W., Richardson, A. D., Jensen, O. P., O'Keefe, J., Zhang, G., Nemani, R. R., van LEEUWEN, W. J. D., Brown, J. F., de WIT, A., Schaepman, M., Lin, X., Dettinger, M., Bailey, A. S., Kimball, J., Schwartz, M. D., Baldocchi, D. D., Lee, J. T., & Lauenroth, W. K. (2009). Intercomparison, interpretation, and assessment of spring phenology in North America estimated from remote sensing for 1982–2006. *Global Change Biology*, 10.1111/j.1365-2486.2009.01910.x{\it\bibinfo{volume}{15}\/}, \bibinfo{pages}{2335--2359}.

- Wolanin, A., Rozanov, V., Dinter, T., & Bracher, A. (2015a). Detecting CDOM fluorescence using high spectrally resolved satellite data: A model study. In G. Lohmann, H. Meggers, V. Unnithan, D. Wolf-Gladrow, J. Notholt, & A. Bracher (Eds.), *Towards an Interdisciplinary Approach in Earth System Science* (pp. 109–121). Cham: Springer International Publishing.
- Wolanin, A., Rozanov, V., Dinter, T., Noël, S., Vountas, M., Burrows, J., & Bracher, A. (2015b). Global retrieval of marine and terrestrial chlorophyll fluorescence at its red peak using hyperspectral top of atmosphere radiance measurements: Feasibility study and first results. *Remote Sensing of Environment*, 10.1016/j.rse.2015.05.018{\it\bibinfo{volume}{166}\}, \bibinfo{pages}{243--261}.
- Wolter, K., & Timlin, M. S. (1998). Measuring the strength of ENSO events: how does 1997/98 rank? *Weather*, 53, 315–324.
- Wynne, T. T., Stumpf, R. P., & Briggs, T. O. (2013a). Comparing MODIS and MERIS spectral shapes for cyanobacterial bloom detection. *International Journal of Remote Sensing*, 10.1080/01431161.2013.804228{\it\bibinfo{volume}{34}\}, \bibinfo{pages}{6668--6678}.
- Wynne, T. T., Stumpf, R. P., Tomlinson, M. C., Fahnenstiel, G. L., Dyble, J., Schwab, D. J., & Joshi, S. J. (2013b). Evolution of a cyanobacterial bloom forecast system in western Lake Erie: Development and initial evaluation. *Journal of Great Lakes Research*, 10.1016/j.jglr.2012.10.003{\it\bibinfo{volume}{39}\}, \bibinfo{pages}{90--99}.
- Wynne, T. T., Stumpf, R. P., Tomlinson, M. C., Warner, R. A., Tester, P. A., Dyble, J., & Fahnenstiel, G. L. (2008). Relating spectral shape to cyanobacterial blooms in the Laurentian great lakes. *International Journal of Remote Sensing*, 10.1080/01431160802007640{\it\bibinfo{volume}{29}\}, \bibinfo{pages}{3665--3672}.
- Wyrтки, K. (1981). An estimate of equatorial upwelling in the Pacific. *Journal of Physical Oceanography*, 10.1175/1520-0485(1981)011<1205:AEOEUI>2.0.CO;2{\it\bibinfo{volume}{11}\}, \bibinfo{pages}{1205--1214}.
- Xing, X.-G., Zhao, D.-Z., Liu, Y.-G., Yang, J.-H., Xiu, P., & Wang, L. (2007). An overview of remote sensing of chlorophyll fluorescence. *Ocean Science Journal*, 10.1007/BF03020910{\it\bibinfo{volume}{42}\}, \bibinfo{pages}{49--59}.
- Yamashita, Y., Panton, A., Mahaffey, C., & Jaffé, R. (2010). Assessing the spatial and temporal variability of dissolved organic matter in Liverpool Bay using excitation–emission matrix fluorescence and parallel factor analysis. *Ocean Dynamics*, 10.1007/s10236-010-0365-4{\it\bibinfo{volume}{61}\}, \bibinfo{pages}{569--579}.
- Yamashita, Y., & Tanoue, E. (2003). Chemical characterization of protein-like fluorophores in DOM in relation to aromatic amino acids. *Marine Chemistry*, 82, 255–271.
- Zalasiewicz, J., Williams, M., Smith, A., Barry, T. L., Coe, A. L., Bown, P. R., Brenchley, P., Cantrill, D., Gale, A., Gibbard, P., Gregory, F. J., Hounslow, M. W., Kerr, A. C., Pearson, P., Knox, R., Powell, J., Waters, C., Marshall, J., Oates, M., Rawson, P., & Stone, P. (2008). Are we now living in the Anthropocene. *GSA Today*, 10.1130/GSAT01802A.1{\it\bibinfo{volume}{18}\}, \bibinfo{pages}{4}.
- Zhang, X. (2005). Monitoring the response of vegetation phenology to precipitation in Africa by coupling MODIS and TRMM instruments. *Journal of Geophysical Research*, 10.1029/2004JD005263{\it\bibinfo{volume}{110}\}.

BIBLIOGRAPHY

Zhou, L., Tian, Y., Myneni, R. B., Ciais, P., Saatchi, S., Liu, Y. Y., Piao, S., Chen, H., Vermote, E. F., Song, C., & Hwang, T. (2014). Widespread decline of Congo rainforest greenness in the past decade. *Nature*, 10.1038/nature13265{\it\bibinfo{volume}{509}\/}, \bibinfo{pages}{86--90}.